FRACTAL THEORY AND GROUNDWATER

FLOW IN FRACTURED MEDIA

by

Ali R. Nowroozi

A Dissertation Presented to the
FACULTY OF THE GRADUATE SCHOOL
UNIVERSITY OF SOUTHERN CALIFIRNIA
In Partial Fulfillment of the
Requirements for the Degree
DOCTOR OF PHILOSOPHY
(CIVIL ENGINEERING)

May 2003

Copyright 2003   Ali R. Nowroozi
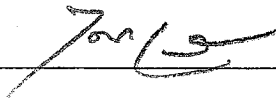
UNIVERSITY OF SOUTHERN CALIFORNIA
THE GRADUATE SCHOOL
UNIVERSITY PARK
LOS ANGELES, CALIFORNIA 90089-1695

This dissertation, written by

ALI R. NOWROOZI

*under the direction of h_is_ dissertation committee, and
approved by all its members, has been presented to and
accepted by the Director of Graduate and Professional
Programs, in partial fulfillment of the requirements for the
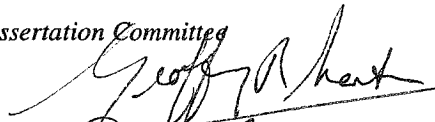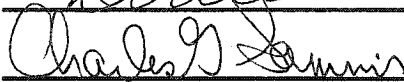degree of*

DOCTOR OF PHILOSOPHY

_____
Director

Date____May 16, 2003____

Dissertation Committee

_____
Chair

_____

_____

_____

DEDICATION

To my beloved wife

Mandana

and

Her precious gift,
to be born

ACKNOWLEDGEMENTS

It has been a great pleasure to study in the Geotechnical Engineering graduate program at Department of Civil Engineering. I am grateful to all the outstanding professors and colleagues who have supported and guided me during my entire graduate education.

First and foremost, my sincere appreciation goes to Dr. Geoffrey Martin, Chairman of my dissertation committee, for his scholarly guidance, encouragement, enthusiasm, and continuous support throughout my study.

My gratitude is extended to my other committee members: Dr. Jean-Pierre Bardet, Dr. James Moore, Dr. Charlie Sammis, and Dr. Dennis Williams, who provided me a better understanding of various aspects of geology, geohydrology, and geotechnics.

I wish to praise Professor Iraj Ershaghi, Department of Petroleum Engineering, for introducing me to fractals and their applications. I also forward my sincere appreciation to Professor Maged Dessouky, Department of Industrial Engineering, for his guidance in statistical aspects of this work. I would also like to acknowledge my friend Mr. Ali Rejaie, Mr. Andrew Dodds whose encouragements and assistances were truly helpful.

iii

Finally, my recognition and great appreciation go to four very special individuals: My mother with all her encouragement and her love; my father, who is my role model in being persistent and determined; my wife with all her love, patience, and support; and my late uncle Jahanbakhsh who helped me explore my talents and my passion for engineering and mathematics, early in my life.

iv

TABLE OF CONTENTS

v

LIST OF FIGURES

xiii

xv

ABSTRACT

Numerous statistical models have been developed to study fluid flow in fractured media. However, the randomness assumption in these models is difficult to rationalize. In fact, experimentally and theoretically, it has been shown that rock fractures have predetermined paths of growth. Rock fracturing is a self-similar process in which properties of new fractures are controlled by the existing fractures. Unlike engineering materials, rock fracturing cannot be described by simple mathematical equations, neither by statistical models.

This research aims to develop a fractal model that overcomes limitations of the current statistical models. Iterated function systems (IFS) can create fractal objects. An arbitrary fracture set can be created by four "background" transformations and one "condensation set". The challenge remains to identify the correct IFS whose attractor is "close" to limited field observations. An inverse fractal algorithm and associated graphical program provide the answer to this question. Subsequently, the fractal nature of fractures defines their hydraulic properties. Permeability tensors of all cells in a grid are calculated using "representative fractures". The flow problem is then solved using a finite difference program (FLAC^{2D}). Limitations of the finite difference technique are discussed, as applied to fractured media. For a highly heterogeneous fracture network, it is recommended to use a discrete network model, as opposed to an equivalent continuum model.

In a physical experiment based on a Hele-Shaw model, good agreement was observed between the experiment and the fractal model. 30% difference in discharge was predicted due to the considerably smaller number of fractures in the experiment and the observations confirmed this prediction. As a practical example, some initial work on Yucca Mountain Project (YMP) showed that fracture patterns at this site have a fractal nature. The "shadow theorem of fractals" was used to simulate a fracture set with a fractal pattern.

This work opens new opportunities for fractal theory to be used in characterization of fractured media. The proposed model is a simple and easy to use technique that proved to be effective and accurate.

CHAPTER 1 - INTRODUCTION

1.1 - RESEARCH NEED

Groundwater flow in rock media has been the subject of interest to geothechnical engineers, hydrologists, petroleum engineers, and chemical engineers for decades. Would the earth be composed of pure intact rocks free from any fissures or flaws, rock media could be simply a porous media with relatively low porosity. In reality, however, rocks are usually fractured due to stress heterogeneities in the earth crust. These fractures have an apparently irregular pattern in most cases. This makes it extremely difficult to use strictly theoretical solid mechanics and fluid mechanics to approach rock problems.

Due to the uncertainties involved in identification of rock discontinuities (fractures and primary surfaces), statistical and probabilistic approaches are usually used to characterize fracture patterns and to predict fluid flow behavior in these fractures. Each and every fracture network parameter (length, spacing, aperture, etc.) is defined by searching for the statistical density functions that fit best to the field data (e.g. Normal, Lognormal, Exponential, and Gamma distributions). Similarly, probabilistic approaches to flow modeling include statistical distribution of conductivity, percolation theory, and random walk.

1

Statistical simulation of fracture networks has several limitations. These limitations are summarized here and explained in more details in Chapter 3, after reviewing the related literature:

- Extensive data collection is necessary in order to develop a reliable statistical model and intensive computations are required.

- Statistical methods are associated with scale dependence. Identification of an appropriate scale is very difficult and, sometimes, impractical.

- Statistical model do not provide stable results. Various simulations of the exact same problem with the exact same assumptions and parameters may result in totally different outcomes.

- Fractures appear to have predefined paths to grow and they appear in clusters that are denser in some location. Fractures are not developed in a random manner.

- Fracture parameters interactions cannot be accounted for using the current statistical techniques.

As an alternative to statistical modeling, inverse hydraulic inversion technique has been developed and used by a number of scholars, as summarized in Chapter 3. Since this method makes no use of fracture data and the fractured pattern is back calculated from flow observations, detailed information is not available when the fracture pattern is heterogeneous and/or anisotropic. In addition, there is no

2

guarantee that simulation of some well test data would result in real filed-scale flow predictions.

1.2 - STUDY PURPOSE

The objective of this study is to address limitations of the current fracture network models and to propose an alternative approach that overcomes these limitations by using fractal theory. It has been proven, both conceptually and by field investigations, that fractured rock, like many other natural processes, has a fractal behavior. This study will show that fractal algorithm generates much more realistic fracture networks, compared to stochastic approaches. The ultimate goal of this study is to use fractal theory in order to characterize fractured media and develop a realistic fracture network that requires minimum fracture data collection effort. Subsequently, a flow model is developed that makes use of the "discrete"[1] nature of the proposed network model to develop the equivalent permeability tensor. Because of its discrete structure, with some modifications to the flow model, the proposed technique can be also applied to porous media or to a fractured media with considerable background porosity.

First, using essential fractal theorems, we develop a graphical technique that makes use of borehole observations to develop "Iterated Function System" (IFS) that

---

[1] The word "Discrete" refers to collection of numerous discrete dots to simulate a continuous fracture. This shall not be mistaken with discrete fracture network model.

3

generates the corresponding fracture pattern. Appropriateness of this iterated function system is evaluated by proximity of the simulated fracture network to the original field observations, measured by Hausdorff metric and/or fractal dimension. In the second stage of the study, this fractal network of fractures is translated into an equivalent porous media. Basic flow equations combined with a new regression technique are used to develop the permeability tensors based on fractal nature of the generated network. The proposed model is then verified by solving the flow problem in a finite difference program (FLAC^{2D}) and comparing with the outcomes of a physical model.

1.3 - DISSERTATION OVERVIEW

In order to understand nature and genesis of fractures, a summary of rock geology and sources of discontinuities is provided in Chapter 2. Chapter 2 provides an overview of rock geology, its properties, and rock fracturing process.

Chapter 3 reviews hydraulic properties of fractured media and current modeling approaches. Various parameters that contribute to fluid flow are studied and current modeling approaches are summarized, from simulation of individual fracture parameters to development of a complete flow model in fractured media. Some innovative fracture and flow modeling techniques are also discussed and the discussion of "self-similar / self-affined" property of fracture networks, that follow in the future Chapters, is initiated.

4

Chapter 4 provides an overview of field investigation methods for hydraulic characterization of fractured media. In the first part of Chapter 4, fracture detection techniques that provide information on fractures parameters are reviewed. In the second part of Chapter 4, hydraulic testing techniques are discussed. These tests use field discharge observations to predict flow behavior in fractured media.

Due to the importance and substantial value of fracture initiation and propagation process in this study, Chapter 5 provides an overview of fracture mechanics, as applied to rock media. Applicability and limitations of classical fracture mechanics to study rock fracturing are discussed. Chapter 5 reviews recent observations and investigations that justify self-similar nature of rock fractures initiation and propagation process. Influences of pre-existing fractures on a new neighboring crack are explained and the basis for application of fractal theory in rock fracture modeling is developed (Chapter 6).

In Chapter 6 fractal theory is explained. The most important fractal theorems that form the foundation for development of the proposed rock characterization model are discussed. Current applications of fractal theory to study fluid flow in fractured media are also reviewed.

5

In Chapter 7 a fracture network model is developed based on the fractal theory concepts that are explained in Chapter 6. Fractal theorems and mathematics are used to develop an inverse[2] algorithm that predicts fracture pattern using limited filed observations (borehole readings). The concept was used to develop the computer program "Interactive Fractal Program" (IFP)[3] that graphically seeks the most appropriate iterated function system for a given (partial) image.

The second part of Chapter 7 explains development of a numerical model that translates fractal pixels density (representing fractures) into rock permeability tensor. We will also take a look at a percolation algorithm that may be used for discrete network model to eliminate fractures that do not contribute to the flow network.

In the third part of Chapter 7, FLAC^{2D} (a finite difference program) is used to study flow behavior of the proposed model. To develop a good understanding of this program and its limitations, a brief summary of its backbone numerical model is provided and then simulation of the proposed model is explained.

Chapter 8 uses a physical model to verify results of the numerical model. Design and construction of the physical model and the experiment process are explained. The results of the experiment are then compared and contrasted with the proposed

---

[2] The word "inverse" refers to development of fractal codes for a (partially) given image. This should not be mistaken with current hydrologic inversion techniques.

[3] IFP is a Visual Basic program that was developed for the purpose of this study, only.

6

numerical model in order to validate the numerical model. In the second part of chapter 8, various sensitivity analyses verify stability of the proposed model.

In order to emphasize on practical applications of the proposed fractured rock characterization and flow model, Yucca Mountain project was initially selected as a field data source. Extensive site investigations and studies have been conducted at this site and a complete flow model is already developed that can be compared with the fractal model proposed in this study. However, due to sensitivity of Yucca Mountain Project, US Department of Energy removed all project data from public access, in the midst of this study, and it became impossible to collect any additional data. Various Projects have been investigated as alternatives, but none was found that would have as complete information as Yucca Mountain Project. The preliminary investigations and findings from the Yucca Mountain Project and the first steps to develop a fractal model for this project are summarized in Chapter 9.

Chapter 10 provides the conclusion of this dissertation and discusses applications, limitations, and future expansion of this work. Chapter 10 summarizes the most important findings of this study, provides recommendations for practical applications of this technique, explains expected improvements compared to current methods, and discusses areas of related studies in future.

7

CHAPTER 2 - ROCK, A DISCONTINUOUM

2.1 - ROCK GEOLOGY

This chapter aims to provide a brief summary of rock geology and the formation of rock discontinuities. This information is provided as an overview of the concepts that help us understand formation of rocks and then development of discontinuities in rocks.

I. Minerals

Oxygen, silica, aluminum, calcium, sodium, magnesium, and potassium, are the most common elements of nature. Elements or composite elements that have similar physical and chemical properties are categorizes as one group of minerals. A mineral is crystalline and inorganic. Among more than 2000 minerals in nature, the followings are the most common that form rocks (Figure 2.1):

- *Feldspars* are the most common minerals in rocks. They are plagioclases (aluminum calcium / aluminum sodium silicates) or orthoclases (Potassium). Feldspars have light color (white, pink, light green) with a hardness of 6. They have two perpendicular cleavages, glassy luster and no streak plate marks.

8

- *Quartz* is composed of silica and oxygen (SiO_2). In pure form, it is colorless or white and has glassy luster. It has no cleavage with a hardness of 7 and hexagonal crystalline form.

- *Pyroxenes* have a complex composition. Augite, for example, is composed of $Ca,NaMg,Fe(II),Fe(III)$. Pyroxenes have dark colors with 6 – 7 hardness. Their two cleavages are almost perpendicular. They have glassy luster and no streak marks.

- *Mica* has a well-bedded cleavage and it can be broken at parallel cleavage surfaces. It exists in two colors, depending on its composition. Biotite $[K(Mg,Fe)_3(AlSi_3O_{10})(OH)_2]$ is black mica and muscovite $[KAl_2(AlSi_3O_{10})(OH)_2]$ is white mica. It has large minerals and has several industrial applications. Mica's harness is between 2 and 4.

- *Clay Minerals* are hydrated aluminum silicates. They could contain K, Na, Fe, Mg. These minerals have light color, dull luster, and no streak marks. Their hardness is usually low.

- *Amphiboles* have very complex compositions. Hornblende, for example, is formulated as: $Ca_2Na(Mg,Fe)(Al,Fe,Ti)(Al,Si)_8O_{22}(O,OH)_2$. They are dark gray or dark green and have a hardness of 5 – 6. They two cleavages and can be distinguished from augites by their non-perpendicular cleavages.

- *Olivine* is $(Mg,Fe)SiO_4$. It has yellowish green (olive) color with almost glassy luster. It has no cleavage and a hardness of 6.5 or lower.
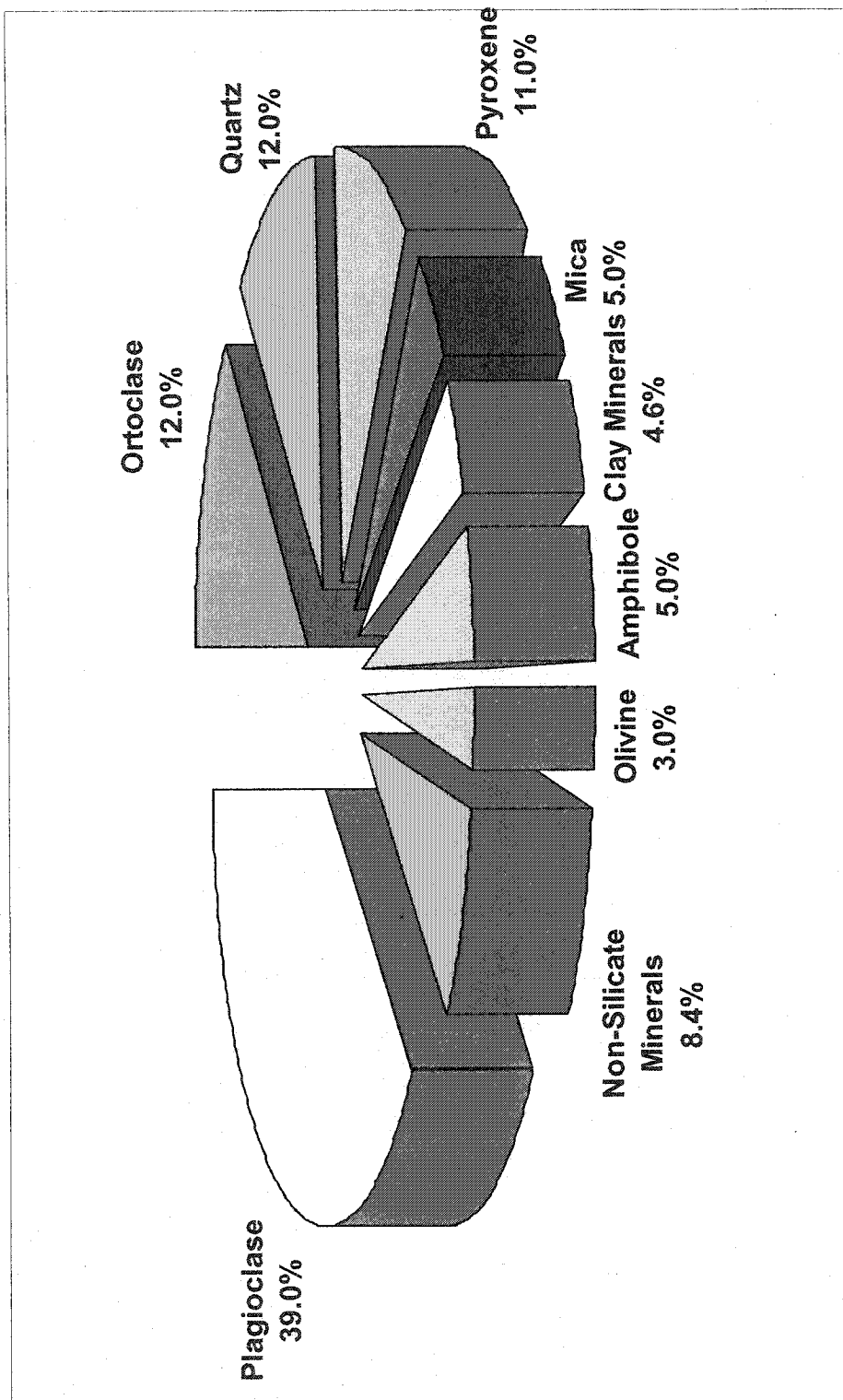
Figure 2.1 – Most Common Rock-Forming Minerals

Quartz 12.0%

Pyroxene 11.0%

Ortoclase 12.0%

Mica 5.0%

Clay Minerals 4.6%

Amphibole 5.0%

Olivine 3.0%

Non-Silicate Minerals 8.4%

Plagioclase 39.0%

10

II. Rocks Formation

"Rock" forms the earth crust and it is a composite of various minerals. It could be ultimately crushed and decomposed to the form that we call "soil". Rocks, based on their formation process, are categorized into three groups:

- About 56% of the earth crust is composed of *Igneous Rocks* that are formed as a result of liquid "Magmas" flowing from depth to the crust of the earth and cooling down.

  o <u>Intrusive</u> Igneous rock is formed as a result of sedimentation of the lava flow as it moves upwards and cools down, slowly. Gabbro, granite, diorite, and syenite are some intrusive igneous rocks. Gabbro is composed of feldspar calcites and some dark minerals, mostly aluminum and magnesium. In case of olivine presence it is called olivine gabbro. Granite has a visibly crystalline texture. It contains quartz, feldspar, and some mica. It is very course grained as a result of exceptionally slow cooling rate. Diorite is also course grained due to slow cooling. It contains feldspar (Plagioclase) with Calcium, Sodium, Iron, and Magnesium. Some dark kinds of diorite also contain pyroxenes (e.g. augites) and biotite. Syenite is formed like granite but it has less silica and very little quartz. Syenite has feldspar (plagioclases and orthoclase) and amphibole (hornblende).

11

o <u>Extrusive</u> igneous rock is formed by cooling of magmas that come to the earth surface as a result of volcanic activities. Basalt, felsite, and andesite are extrusive igneous rocks. Basalt is equivalent extrusive of gabbro, felsite is equivalent of granite, and andesite is equivalent of diorite.

- *Sedimentary rocks* are formed by sedimentation, decomposition, and fossilization of other rocks and beings, under natural forces (wind, rain, glacial ice, heat, etc). Despite their low quantity in the earth crust (8%), sedimentary rocks cover about 75% of the earth surface. Due to their formation process, layers of sedimentary rocks appear deposited on top of each other. These stratifications (beddings) range between a few centimeters to hundreds of meters. Based on their formation process and their composition (minerals contained in the original rock), sedimentary rocks are categorized in 3 groups. it has less silica and very little quartz. Syenite has feldspar (plagioclases and orthoclase) and amphibole (hornblende).

o <u>Clastic (fragmental)</u> sedimentary rocks are resulted from physical breakdown and consolidation of various rocks and organisms, cemented to each other by natural forces. Their properties are driven by their source (composition of the original rock), and sedimentation process (traveling length and slope, temperature, forces, and environment).

12

Conglomerate, Breccia, sandstone, silt and shale are sedimentary clastic rocks.

o Chemical/biochemical sedimentary rocks are formed by chemical decomposition of other rocks and organisms (fossils) and their sedimentation under environmental forces. Travertine, limestone, dolomite, and chalk are some sedimentary rocks in this category.

o Evaporitic rocks are formed by sedimentation of water solvents, after its evaporation. Halite (salt), Gypsum, and andride are evaporite rocks.

- Minerals in a rock may become subject to intense heat and/or pressure and change their crystalline formation. The deformed rock has completely different properties and it is called a *metamorphic rock*. For example, under high pressure/temperature, small particles of quartz in clay become parallel to the stress direction. This results in new crystalline formation and the new metamorphic rock is called schist. Metamorphic rocks are categorized in two groups. In foliated (Schistose) rocks minerals establish parallel planes and have smooth surfaces. Slate, schist, gneiss, and phyllite are examples of foliated metamorphic rocks. Metamorphism in non-foliated (massive) rocks is the result of long exposure to cooling magmas. As a result, their re-crystallization is less significant than foliated rocks and not much foliation is identified. Marble and quartz are the common massive metamorphic rocks.

13

III. Rock Evolution Cycle

Rock is continuously interchanging from one form to another (Figure 2.2). As a result of environmental forces, liquid moves from the earth mantle to the surface and creates intrusive or extrusive igneous rocks, depending on the cooling process. The igneous rock may come to the earth surface through erosion or explosion, it may go through sedimentation and create sedimentary rocks, may be exposed to intense heat and pressure and turn into metamorphic rock, or may melt back into magma. Similarly, sedimentary rock that usually appears at the earth surface, may go through a metamorphism process or may simply melt into magma. Metamorphic rocks also have the possibility of appearing on the earth surface or melting into magma.
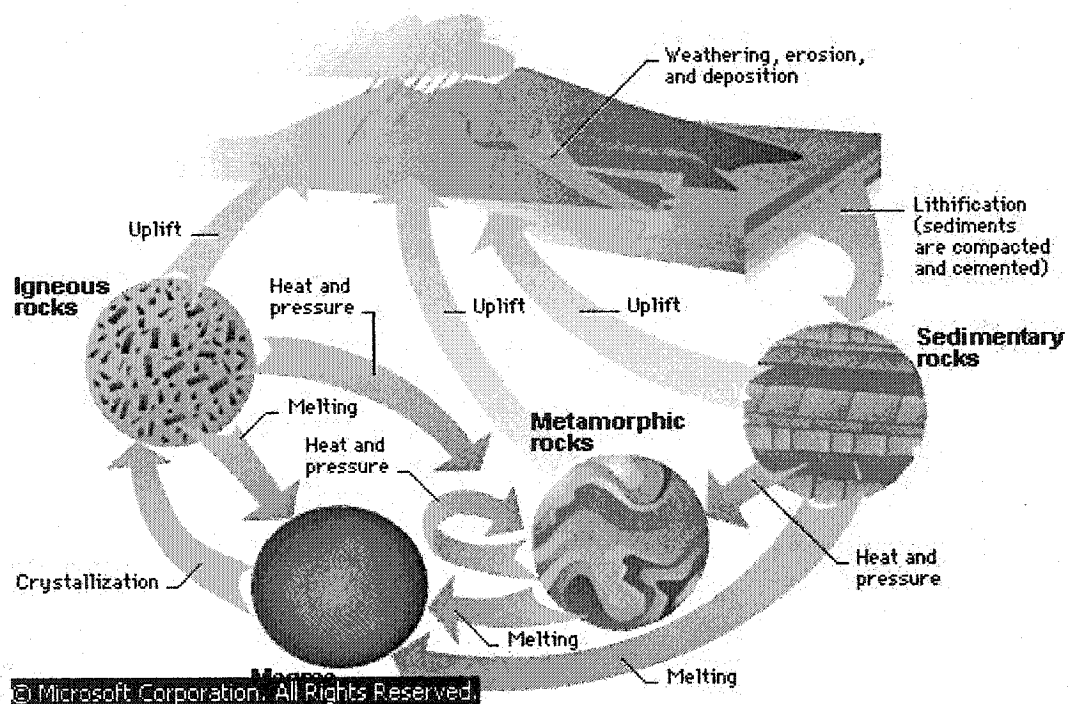
Figure 2.2 – Rock Evolution Life Cycle
(From Encrata Encyclopedia)

14

2.2 - ROCK DISCONTINUITIES

I. <u>Types and Geometries of Discontinuities</u>

Basics of rock geology (above) provide us with one important lesson: Rock is not a homogeneous medium and it is almost impossible to find a large piece of rock free from discontinuities. These discontinuities are major contributors to hydraulic properties of rock. At a minimum, closed discontinuities contribute to rock heterogeneity. Open discontinuities work as conduits for water to flow quickly and they enhance rock permeability, significantly. Discontinuities that are filled with other materials could enhance or reduce overall permeability, depending on the filling material properties. Discontinuity is formed either during formation of rock (primary surfaces), or afterwards as a result of filed stresses (Fractures).

- Depending on the rock type (igneous, sedimentary, or metamorphic), various types of *Primary surfaces* develop during rock formation:
  - Minerals, by themselves, are not homogenous. Due to their composition and crystallization, they have a tendency to be broken along specific planes defined by their crystal structure. These planes are called <u>cleavage</u>.
  - Sedimentary rocks are composed of layers of rock that are deposited on top of each other through time. As a result, each layer is separated from the others by <u>bedding</u> planes.

15

o <u>Foliation</u> is result of the metamorphism process. Because of rotation of mineral particles into one direction, in a metamorphic rock, foliation planes could be developed. In a foliated rock, mineral particles crystallize in parallel planes. This distinguishes foliation from bedding. When foliations planes are well-identifiable and the rock can be easily broken into thin layers along the foliation planes, These planes are also called schistosity.

• Earth crust is always subject to various kinds of stresses, from thermal forces to tectonic activities. These heterogeneous stresses occur at large range of scales. In order to release these stresses, rock may develop three types of *fractures*:

o <u>Dilating fractures/joints</u> *(Figure 2.3)* are formed as a result of normal stresses and, therefore, displacement is perpendicular to fracture plane. This is categorized as mode I (opening) fracture, in fracture mechanics (Figure 2.6). There is no relative movement in the direction of fracture planes. Joints usually intersect primary surfaces and have a plumose texture surface. In nature, joints appear in groups of semi-parallel fractures, called a joint set. These joints have the same origin and age and they are defined by spacing, length, and orientation. Presence of one joint set alters field stresses and, as a result zones of clustered joints are formed. Also, it is common to see joint sets intersecting each other

16

(almost) perpendicularly. Through time, hydrostatic state of stress results in interaction of nearby joints and development of network of joints.

| Joint Surface | Joint Set | Jointed Zone |
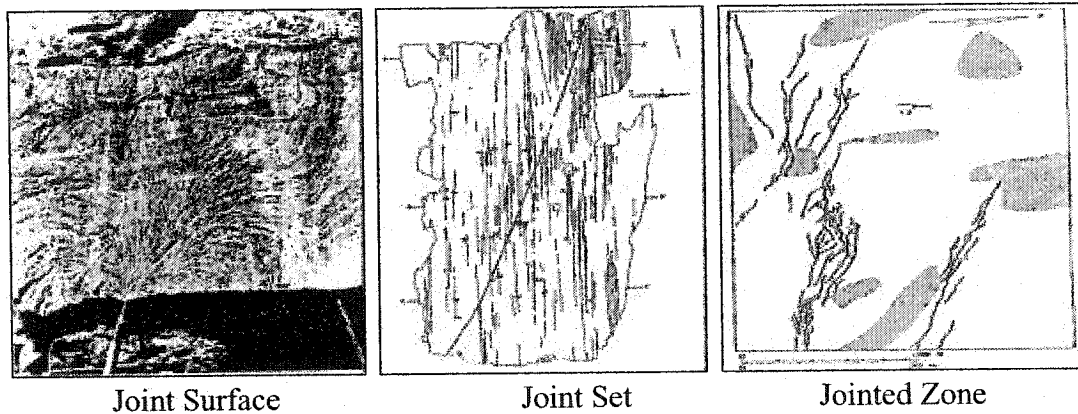
Figure 2.3 – Rock Joints Formation and Geometry

o <u>Shearing fractures/faults</u> *(Figure 2.4)* are formed as a result of shear stresses – stresses that develop in the plane of the fracture surfaces. These fractures are mode II or III in fracture mechanics (Figure 2.6). During the faulting process, the two surfaces of fracture make significant movements relative to each other. As a result, their surfaces are polished in the direction of movement and they are usually thicker than joints. Similar to joints, faults usually appear in semi-parallel sets, based on their age and origin. Length and spacing of the faults in one set may be related to magnitude and frequency of slip across the fault. Faulted zones appear in relatively irregular shapes and all kinds of fractures (mode I, II, and III) may be observed in a faulted zone. Secondary mode I fractures (joints) may develop in a fault zone, as a result of faults interaction and linkage. These joints that are parallel to the intermediate principal stress could act as significant fluid conductors. Because of high degree of heterogeneity in their pattern and composition, fault zones have very heterogeneous hydraulic properties.

17

Fault Formation Process   Fault Set   Faulted Zone
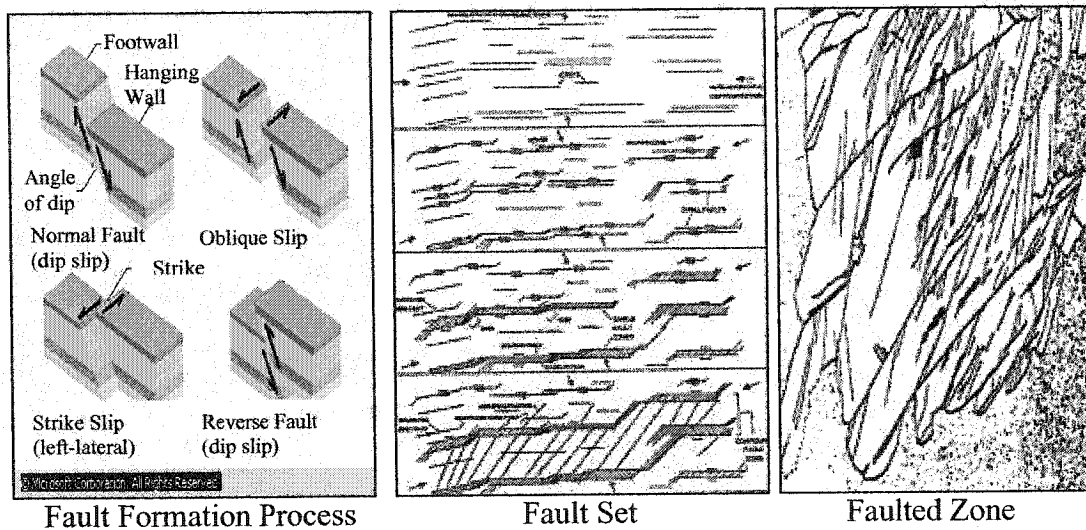
Figure 2.4 – Rock Faults Formation and Geometry

o <u>Closing fractures/pressure solutions or stylolites</u> *(Figure 2.5)* are the fractures in sedimentary rocks that are welded together by solution of grains at the fracture surface. These "anti-cracks"[4] are developed as a result of water-assisted diffusion of large grains at unexpectedly low temperatures. Some pressures solutions (incongruent) result in formation of a metamorphic banding in rocks.

---

[4]   Since these cracks act as barriers to flow (instead of conduits), they are called anti-cracks (Hudson et al. 1993).

18
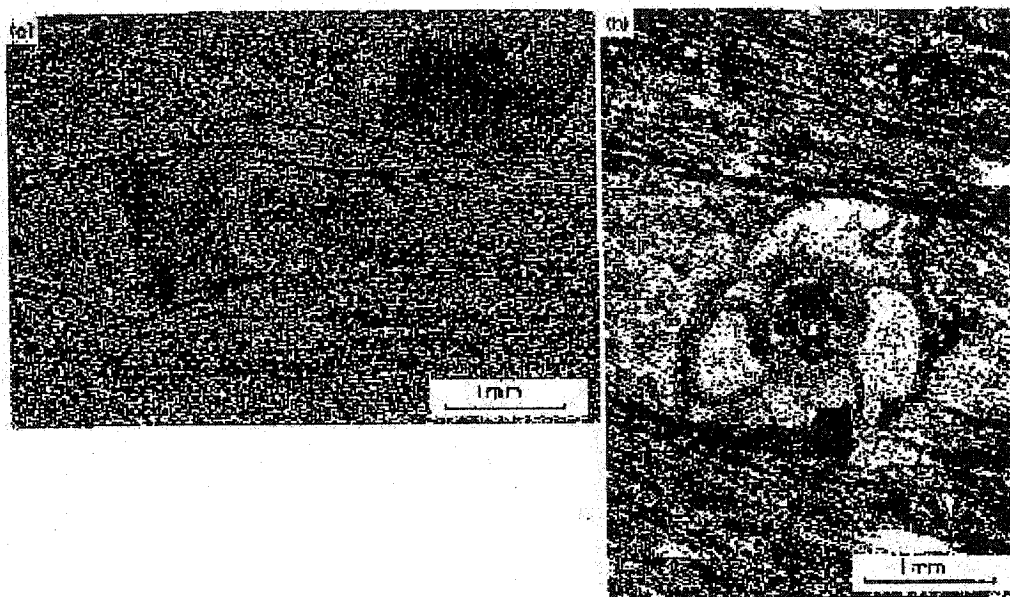
Figure 2.5 – Pressure Solutions Formation and Geometry

(from Hudson et al. 1993 – P.83)

Rock deformation by water-assisted diffusive mass transfer (pressure solution):

(a) Microstructural features of the flow of a naturally deformed crinoidal limestone (external zone of the Western Alps). The compression direction is vertical, and the material has been diffused away from the relatively stressed boundaries of the large angle crystal calcite fragments, leaving accumulation of nondiffusible residue (organic and intergranular clay minerals) as black stylolites. Diffused calcite is reprecipitated as a clear, impurity free overgrowth on each of the less stressed boundaries. Structural contiguity of the overgrowths is indicated by the prolongation of this twin lamellae between host and overgrowth. The same process has been operated on every grain of the finer matrix calcite , but is not evident at this magnification except for the pervasive development of stylolitic cleavage planes.

(b) Truncation of a foraminiferid by pressure solution, with diffused calcite forming fibrous Overgrowth on the relatively extended faces . The preservation of clear, undeformed calcite within the chambers of the fossil indicates that pressure solution takes place at stress levels too low to activate intracrystalline plasticity in calcite (photo J. G. Rumsay).

19
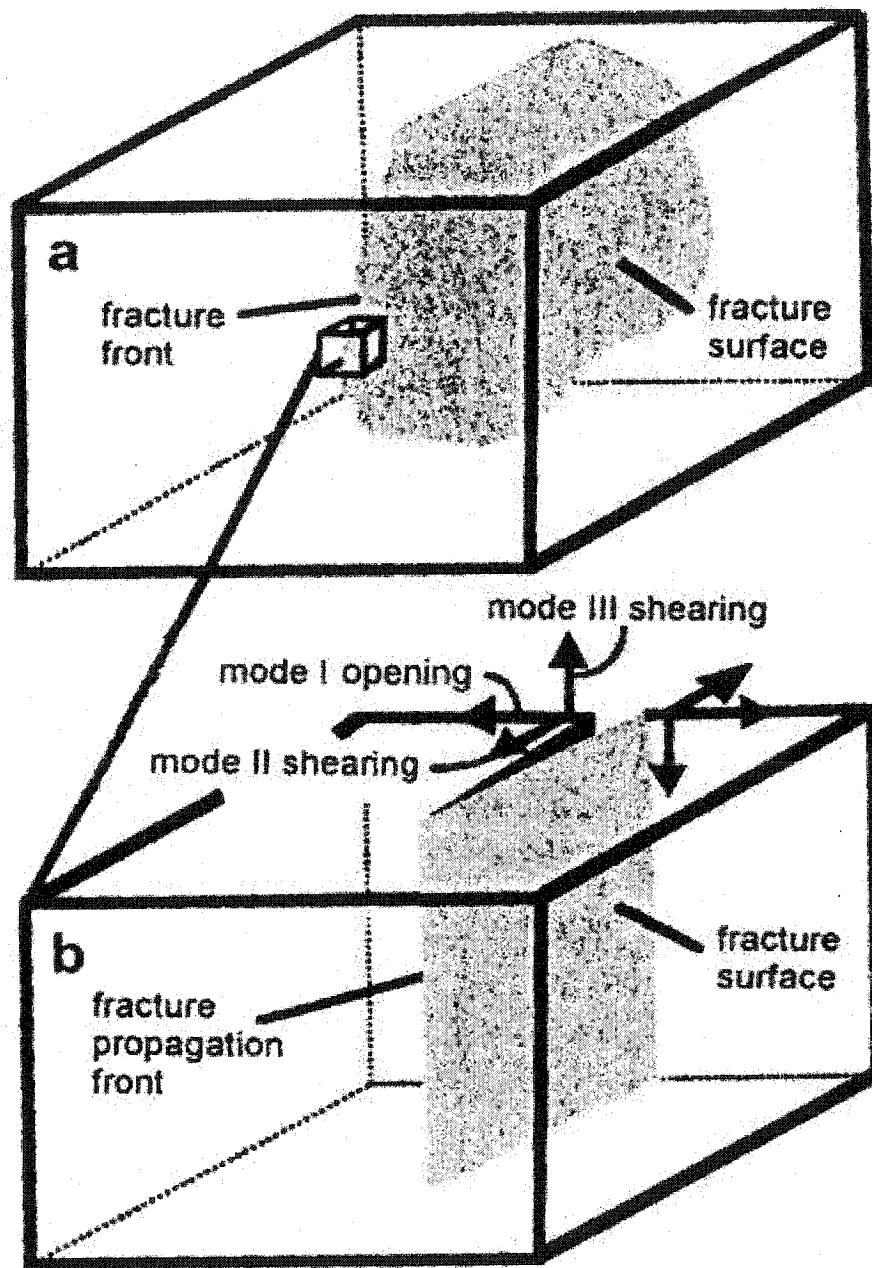
Figure 2.6 – (a) Block diagram showing a fracture and its propagation front. (b) Three fundamental modes of fractures corresponding to joints (mode I) and faults (mode II or III).

20

II. Genesis of Discontinuities

Considering a piece of intact rock with no discontinuities, would have field stresses remained constant, we would not expect too many fractures to develop. In reality, however, various environmental factors can alter filed stresses.

- Cooling of igneous rocks during and after formation generates thermal stresses. Polygonal fractures observed in extrusive igneous rocks are formed by thermal stresses. The well-known polygonal joint network in drying mud is a thermal fracturing process.

- Various earth forces result in stress heterogeneity and development of joints and faults in the earth crust:
    o Tectonic actions and seismic loads develop tremendous stresses that result in faulting and jointing of rocks.
    o Folding of earth crust and formation of synclines and anticlines as a result of continents movements, generate both shear and normal stresses and result in development of faults and joints.
    o Lithostatic forces such as uplift and erosion also cause stress heterogeneity

- Hydraulic forces such as flow of groundwater (or oil) in rock matrix and preexisting cracks develops pore pressure that could result in development of new cracks to release the pressure and develop a pathway for the fluid to flow. Hydro-fracturing, a technique with various applications such as stress

21

measurement and conductivity enhancement of production wells, is based on this phenomenon.

- Numerous other environmental forces such as Extraterrestrials impact and salt intrusion can cause development of fractures in rocks.

Appearance and characteristics of a fracture network can provide guidelines to hypothesize the causative geological process. A geo-mechanical analysis of the hypothesized stress heterogeneity sources can help us to establish a relationship between the observed fracture system and the proposed fracturing process. This would verify the hypothesized process, help us to understand the visible part of the fracture network, and predict the hidden fracture network pattern. The followings are some examples of predicting causative geological process by looking at the fracture pattern (outcrop):

- Polygonal fractures, perpendicular to cooling surface in extrusive volcanic rocks, indicate thermal stresses.

- Parallel fractures in intrusive igneous rocks (granite) are results of cooling down while subject to lithostatic and/or tectonic forces. Fracture system first starts by localized vertical micro-cracks and then interactions between them. Each micro-crack can influence the location of the next micro-crack.

- Buckling or banding stresses in synclines and anticlines originate radial joints.

22

- In porous sandstone, stress concentration at grains contact points controls fracturing process.

- In crystalline rocks structural defects (flaws) and grains mismatches initiate fractures.

- Based on the fracture surface patterns, fracturing of siltstone/sandstone beds may be described by a natural hydraulic fracturing mechanism.

- In sedimentary rocks, fault zones are generally created along the bedding planes.

- In igneous rocks, preexisting cooling joints and weakness plains (such as foliations and cleavages) are templates for fracture zones.

- Orthogonal joint sets are probably in the direction of principal stresses and have same age and properties.

- Non-orthogonal fracture sets indicate different stress fields for the two sets. The longer set is older and deflected when crossing. Lack of deflection may be result of high compressive stress on the older set.

- Joint orientation changes as stress regime changes in time.

- Fractures have a coalesce pattern in Marble, when under compression.

2.3 - DISCONTINUITIES CONDUCTIVITY

For the purpose of this study, we are only interested in the hydraulic properties of fractures. Depending on the geometry of individual fractures and the pattern of fracture network, hydraulic conductivity of fractured rocks could vary. A highly conductive single fracture that does not belong to a "connected" fracture network cannot contribute to fluid flow. Similarly, a well-connected fracture network that contains fractures that are filled by non-conductive minerals, may be blocked and not provide a continuous path for fluid to flow.

In order to predict fracture pattern and develop a realistic model that is true representative of hydraulic behavior of a fractured media, one should have a clear understanding of fractures properties and their connectedness. This would require good knowledge of rock composition and the causative geological process that resulted in development of the fracture pattern.

A large piece of intact rock with only a few large fractures (faults) would clearly need separate models for matrix permeability and fracture permeability. Open fractures work as long conduits for fluid and their contribution to flow is significantly larger than rock porosity. The flow model should consider these fractures as individual entities and then superimpose their effect on the global model (dual-porosity model).

24

A highly jointed piece of rock that shows similar patterns of fractures at various scales (self-similar) may be considered equivalent to a porous media with permeability values defined based on fractures density, superimposed on matrix permeability. In this case, it would be extremely difficult and impractical to study individual joints separately and fractures should be considered as inherent properties of the rock (single-porosity model).

It is noteworthy that it is possible to have non-conductive fractures in a fracture network. Various minerals with different porosities may fill the spacing of fractures (aperture). Detailed site investigations could predict percentage and distribution of open fractures and this knowledge will help in development of a more realistic model.

CHAPTER 3 - REVIEW OF CURRENT MODELING APPROACHES

3.1 - FRACTURE PROPERTIES

Numerous parameters contribute to the behavior of a fluid, flowing through a fractured rock. These include properties of individual fracture as well as the entire rock mass. Fracture properties are explained here and depicted in Figure 3.4:

I. Single Fracture:

- It is generally assumed that fractures have a planar surface *geometry*. Both "circular disks" (Beacher et al. – 1977) and "parallelograms" (Dershowitz and Einstain – 1988) have been used. In reality, however, fracture surfaces can be distorted. This may or may not be observed from fracture traces at the outcrop such as interactions and linkages. No study was found to take planes distortion into consideration.[5]

- *Size* is defined by fracture diameter. It is equivalent to twice the radii for circular geometry and $\sqrt{Area(ah)/\pi}$ for parallelogram geometry.

- *Persistence* is the lateral extent of a discontinuity plane and is described by "Trace Length" – the length of the fracture plane intersection with the observation surface.

---

[5] The proposed fractal model is 2D and assumes planar fracture surface. This model, if developed in 3D, is capable of accounting for planes distortion.

- *Roughness* is characterized by Joint Roughness Characteristic (JRC) index, a relative measure of jaggedness and deviation from perfect planarity. A standardized system of JRC has been developed that provides different values of JRC for different fracture surface geometries. Figure 3.1 shows a summary of various JRC values associated with various surface geometries.

Stepped		JRC_{20}	JRC_{100}	Undulating		JRC_{20}	JRC_{100}
I	Rough	20	11	IV	Rough	14	9
II	Smooth	14	9	V	Smooth	11	8
III	Slickensided	11	8	VI	Slickensided	7	5

Plannar		JRC_{20}	JRC_{100}
VII	Rough	2.5	2.3
VIII	Smooth	1.5	0.9
IX	Slickensided	0.5	0.4

Figure 3.1 – Joint Roughness Characterization Standards

- *Mechanical Aperture* is the physical gap between discontinuity walls. *Hydraulic Aperture* is the portion of the aperture that really contributes to hydraulic conductivity. Hydraulic Aperture (e) is always less than or equal to Mechanical Aperture (E) because of fracture surface roughness (Figure 3.2).

$$e = \frac{JRC^{2.5}}{\left(E/e\right)^2}$$

Barton et al. (1985)
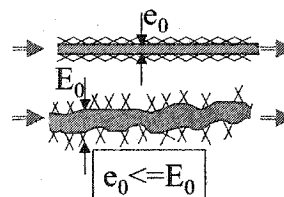
Figure 3.2 – Mechanical Aperture (E_0) and Hydraulic Aperture (e_0)

27

- Equivalent to aperture, *width* is the distance between walls of a filled discontinuity

- *Fracture Orientation* is defined by dip and azimuth of the individual fracture. Dip is the angle between the fracture surface and horizontal plane. Azimuth or Dip direction is the angle between normal to the fracture surface and geographic north.

II. Fractured Rock Mass:

- *Measured (Apparent) Spacing* $(S_{App.})$: The apparent distance between adjacent fractures, observed on scan-line that has an angle of θ with the face of the sample.

- *True Spacing* (S): Perpendicular distance between adjacent discontinuities.

$$S \approx S_{App.} \bullet Sin\theta$$

- *Average Spacing* $(S_{Avg.})$: Mean of all spacing values for one fracture set.

- *Frequency* (l): Number of fractures per unit length: $l = L / S_{Avg.}$; L =Sample size.

- *Volume Density of Fractures* (v): Number of fractures per unit volume.

- *Rock Quality Designation* (RQD): Percentage of the scan-line consisting of spacing values greater than or equal to a threshold (4 inches):

28

$$RQD = 100 \times \sum_{i=1}^{\#Fractures} \left(x_i \Big/ L \right) \% \quad ; \quad \begin{cases} If \quad S_i > 4^{in} \Rightarrow x_i = S_i - 4^{in} \\ If \quad S_i < 4^{in} \Rightarrow x_i = o \end{cases}$$

- *Fracture Sets Orientation* can be identified using pole plots (Figure 3.3).

a – Pole Plot of all Fractures

b – Identified Fracture Sets
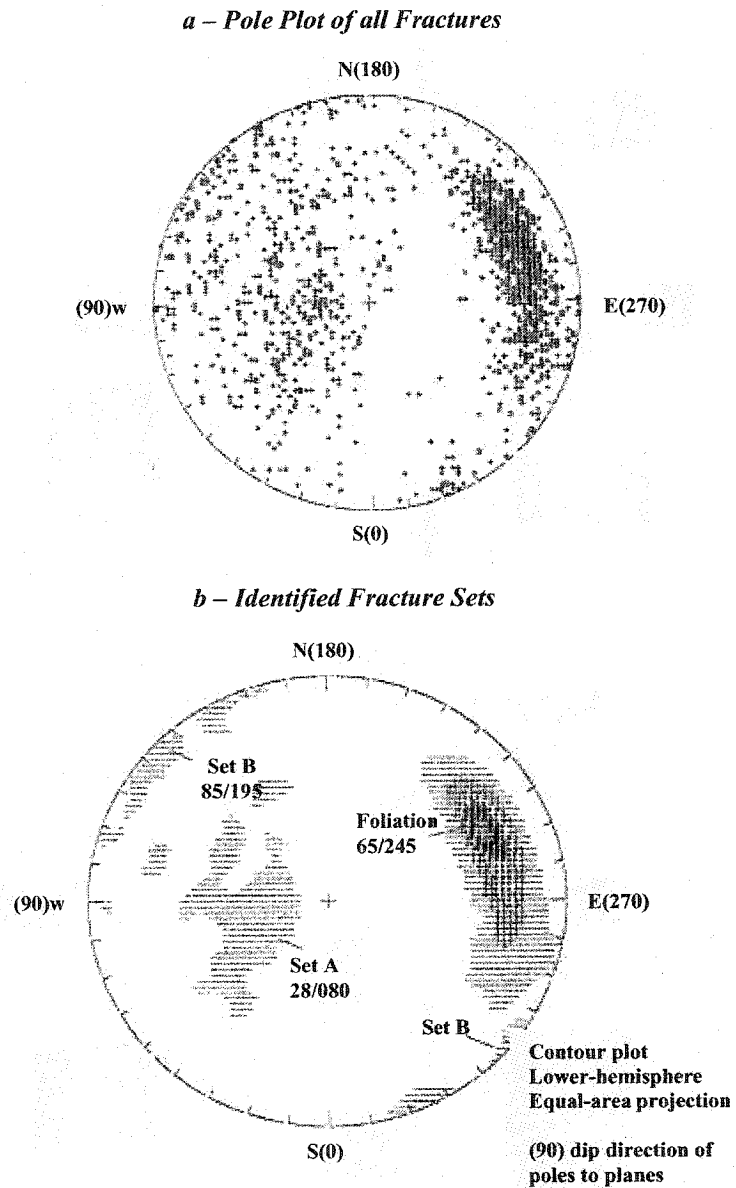
Figure 3.3 – Fracture Sets Orientation Prediction

29
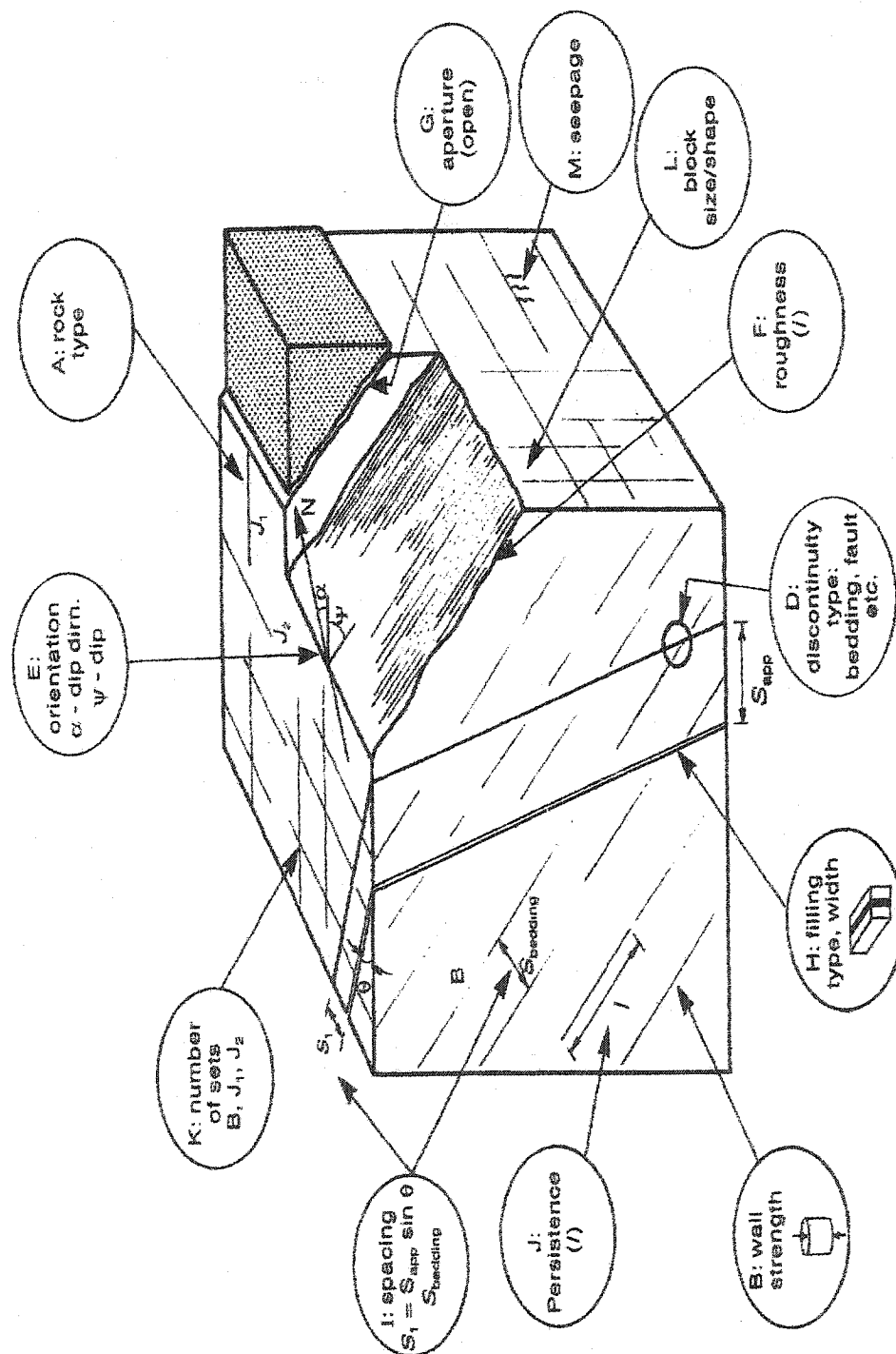
Figure 3.4 — Fractured Rock Parameters (From Myer et al. – 1995)

30

3.2 - CLASSIC ROCK CHARACTERIZATION TECHNIQUES

Numerous literatures have been published that look into characteristics of fractured rock and develop fracture network models based on observed behavior of individual fractures and rock mass. In general, individual fracture/rock mass properties are modeled based on limited observations that are generalized using statistical distribution of the field data as a guideline. The "Fanay-Augeres Mine" model [Billaux et al. (1989)] is a comprehensive example of 3D geostatistical modeling of a fracture network. In that study, fracture centers were modeled using a Poisson process that was modified as a Parent-Daughter Point process in order to account for fractures interactions and fractures clustering. In this technique, locations of the "parent" points are defined using a Poisson distribution and every new "daughter" point is defined randomly around every parent. Other similar techniques include Regionalized Poisson process, Regionalized Parent-Daughter process, Levy-Lee model, Nearest-Neighbor, and War Zone [Rock Fractures and Fluid Flow (1996) – P.363]. All of these models are statistical distributions based on statistical properties of limited observations. They are modified in one way or another to account for clustering nature of fractures.

Numerous studies have shown that specific statistical distributions are, in general, more applicable for specific rock parameters. Mathab et al. (1995) reviewed application of five statistical distributions (normal, lognormal, exponential, weibull,

31

gamma) in modeling of fractures spacing and extent (trace length). This study concluded that:

- The dominant best fit is provided by lognormal distribution.

- Normal and exponential distributions did not fit any of the clusters in their study.

- Weibull and gamma distributions provide the best fit in a limited number of cases.

- In 4 of the 12 cases, none of the five distributions provided an acceptable fit.

Wyllie (1999) referred to Priest and Hudson's (1981) work and concluded that, in general, for Trace Length distribution "While the Lognormal curve has the highest correlation coefficient, the exponential curve has a better fit at the longer discontinuity lengths".

Billaux et al. (1989) provided a good discussion on selection of point processes by looking at semi-variogram results.

A summary of the most common statistical distributions for fractures spacing and length within a rock mass was provided by Mathab et al. (1995) [Rock Fractures and Fluid Flow – P. 199]. Table 3.5 expands Mathab et al.'s work to account for statistical models used for other fracture parameters, as well as spacing and length.

32

Despite all the effort put into finding appropriate statistical distributions for various rock fractures parameters, there is little scientific evidence to validate these stochastic approaches. According to Hudson et al. (1993), *"Only the Negative Exponential distribution has any conceptual basis in that a random spatial distribution of lines means that spacings must follow a Poisson process"*.

Later on we will see that numerous hypothetical fracture patterns could result in the same statistical distributions for fracture network parameters. But they could have totally different flow properties. Therefore, there is little confidence that statistical models predict behavior of actual fracture flow problems, accurately.

33

Figure 3.5 – Statistical Distributions used to model fracture network properties[6]

Spacing		Length/Size		Spatial Distribution	
Distribution	Reference	Distribution	Reference	Distribution	Reference
Exponential	Baecher et al. (1977)	Exponential	Call et al. (1976)	Poison	Priest and Hudson (1976) (First Point Process Model)
	Call et al. (1976)		Cruden (1977)		Baecher et al. (1977)
	Hudson and Priest (1979)		Nordqvist et al. (1995)		Robinson (1984)
	Priest and Hudson (1976)		Priest and Hudson (1981)		Einstein et al. (1980, 1983)
	Rouleau and Gale (1985)		Robertson (1970)		Warburton (1980a,b)
	Sen and Eissa (1992)		Rouleau and Gale (1985)		Long et al. (1982,1985)
	Wallis and King (1980)	Gamma	Dershowitz (1984)		Dershowitz (1984)
	Nordqvist et al. (1995)	Hyperbolic	Segall and Polard (1983)		Herbert et al. (1991)
Lognormal	Barton (1978)	Lognormal	Baecher et al. (1977)	Parent-Dougher	Billaux et al. (1989)
	Bridges (1976)		Barton (1978)		Long and Billaux (1987)
	Sen and Eissa (1992)		Bridges (1976)	War-Zone Levy-Lee Nearest-Neighbor	Geier et al. (1989)
	Sen and Kazi (1984)		Cacas et al. (1990)		
Normal	Priest and Hudson (1981)		Garveis et al. (1995)	**Orientation (Dip/Azimuth)**	
	Rouleau and Gale (1985)		Herbert and Lanyon (1995)	Fisher-von-mises	Cacas et al. (1990)
Uniform	Gervais et al. (1995)		McMahon (1971)		Nordqvist et al. (1995)
	Chen and Harpalani (1995)		Odling (1995)		Mardia (1972)
Weibull	Bardsley et al. (1990)		Rouleau and Gale (1985)	Uniform	Billaux et al. (1989)
	Rouleau and Gale (1985)	Special Distribution	Grossmann (1995)	Random	Nordqvist et al. (1995)
					Gervais et al. (1995)
				Normal	Herbert Lanyon (1995)

[6] Expanded from Table 1 by Mathab et al. (1995)

34

The following assumptions build the backbone of all these stochastic techniques:

- Fracture properties are stationary random variables throughout the media.

- Each individual fracture/rock mass parameter can be isolated from the whole system and modeled individually, independent from the others.

- Representative Elementary Volume (REV), a volume above which hydraulic characteristics of the media remains constant, exists, can be determined, and has a reasonably small size.

Classical rock characterization methods, due to their statistical nature, have some limitations. In general, the following limitations are associated with current statistical techniques:

- Statistical simulation of individual parameters necessitates extensive data collection efforts. On the other hand, the sample size has to be large enough to have a statistically significant population (Hall 1991). It is, sometimes, very difficult and expensive to collect enough data to be able to generate a statistically representative distribution of parameters.

- Statistical techniques are computationally intensive and require numerous iterations and statistical calculations of every individual fracture network parameters. This issue becomes specifically critical when dealing with filed scale models for large projects such as Yucca Mountain repository Project.

35

- The scale at which site investigations are performed may not be an appropriate modeling scale. Studies and investigations have shown that different flow properties are achieved at different scales. However, flow properties become less sensitive to scale changes, as scale increases. Above a specific scale, called Representative Elementary Volume (REV), flow becomes almost insensitive to scale changes (Hudson et al. 1993). Usually, REV is very difficult to identify or too large to be practical:

> *Indeed, quantification of the scale dependence of hydraulic parameters presents one of the strong challenges to fracture hydrologists*
>
> *Hudson et al (1993)*

- The assumption of parameters randomness is not quite justifiable. In fact, fractures appear to have predefined paths to grow and they appear in clusters that are denser in some locations. While point processes have taken this effect into account, there is no conceptual justification for using these techniques. Fracture orientation, for example, is mainly controlled by history of field principal stresses and clearly is not a random variable. Rouleau and Raven (1995) recommended seeking a "non-random spatial distribution of fractures" to create a "more accurate fracture model".

> *Cracks seem to know where they want to go, and they do this in a systematic way*
>
> *Lajtai et al. (1990) – P.64*

36

- Fracture parameters, indeed, interact with each other and influence one another. Obviously presence, location, and orientation of fractures in proximity of a propagating fracture influence its behavior. This phenomenon is explained in detail in Chapter 5. Current Statistical techniques study fracture parameters in isolation from each other. Using statistical models, it is difficult, if not impossible, to truly account for interactions among various parameters. Current point processes, such as parent-daughter model, attempt to account for clustering nature of fractures spatial distribution, due to their interactions (coalescence). As explained above, there is no theoretical evidence that these processes truly simulate the actual fracture locations, consistent with fractures genesis.

Limitations of stochastic modeling of fracture networks are the main incentive for this work and its continuation – a deterministic approach to this problem and many other natural problems, based on fractal theory.

3.3 - CLASSIC FLOW MODELS FOR FRACTURED ROCK

In order to study behavior of fluid flow in a fractured media, numerous models have been developed. In general, all flow models can be categorized in 3 categories. All these models make the same assumptions about the fractured rock properties and they only "differ in their representation of the heterogeneity of fractured media"[7]. A

---

[7] Rock Fractures and Fluid Flow (1996)

37

good summary of various models is provided in Rock Fractures and Fluid Flow (1996) and presented in Table 3.7. Here we provide a brief description of each model, in order to pave the road for introduction of a new model that is developed based on fractal theory.

I.   Equivalent Continuum Model (ECM)

This technique assumes that the flow region is a continuum (porous media). Rock porosity may constitute "background" permeability or "matrix" permeability and presence of fissures, cracks, and faults, enhances permeability, variably. Due to their clustering nature (explained in chapter 5), rock discontinuities result is heterogeneity and anisotropy of overall permeability. ECM takes heterogeneity into account by regionalizing the entire media into numerous "cells", each assumed to be a homogenous porous medium. Rock anisotropy is approached by "permeability tensor" with different values in various directions. Permeability tensor for each cell is developed either through deterministic techniques (direct field measurements on every cell) or stochastic methods (statistical simulation model of hydraulic properties throughout the region). Sometimes geostatistical techniques are added to the stochastic method to define flow parameters (Issaaks and Srivastava 1989, Jones et al. 1985) and/or to improve stochastic flow theories (Gelhar and Axness 1983, Dagan 1987).

The important Consideration in this type of model is that the sample size should belarge enough in order to be "statistically representative" of the medium. Also, the

38

sample size should not be smaller than Representative Elementary Volume (REV) below which flow behavior is inconsistent and unpredictable. In addition, in order for the continuum assumption to be relevant, sample size should be considerably larger than fracture sizes. High fracture density is also desirable. Figures 3.6 shows an example of a fractured medium that can be well represented by a continuum model.
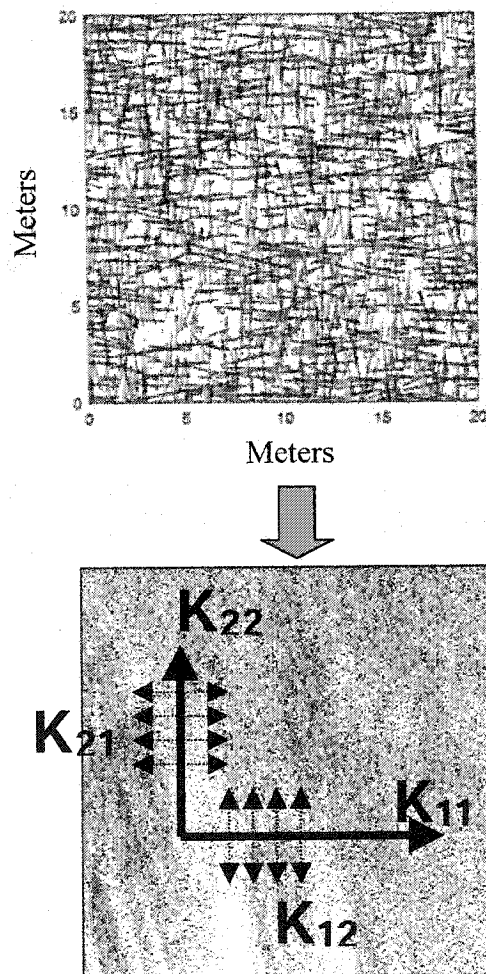
Figure 3.6 – Equivalent Continuum Model Application
(Fracture network from Rock Fractures and Fluid Flow (1996) – P.320)

39

Figure 3.7 – Fracture Flow Models (from Rock Fractures and Fluid Flow 1996)

Representation of Heterogeneity	Key Parameters that Distinguish Models	Recent Examples
Equivalent Continuum Models		
Single porosity	Effective permeability tensor	Carrera et al. (1990)
	Effective porosity	Davison (1985) Hsieh et SI. (1985)
Multiple continuum (double porosity, dual permeability, and multiple interacting continuum)	Network permeability and porosity	Reeves et al. (1991)
	Matrix permeability and porosity Matrix block geometry Nonequilibrium matrix/fracture interaction	Pruess and Narasimhan (1988)
Stochastic continuum	Geostatistical parameters for log permeability: mean, variance, spatial correlation scale	Neuman and Depner (1988)
Discrete Network Models		
Network models with simple structures	Network geometry statistics Fracture conductance distribution	Herbert et al. (1991)
Network models with significant matrix porosity	Network geometry statistics Fracture conductance distribution Matrix porosity and permeability	Sudicky and McLaren (199x)
Network models incorporating spatial relationships between fractures	Parameters controlling clustering of fractures, fracture growth, or fractal properties of networks	Dershowitz et al. (1991a) Lung and Billaux (1987)
Equivalent discontinoum	Equivalent conductors on a lattice	Long et al. (1992b)
Hybrid Models		
Continuum approximations based on discrete network analysis	Network geometry statistics	Cacas et al. (1990)
	Fracture transmissivity distribution	Oda et al. (1987)
Statistical continuum transport	Network geometry statistics Fracture transmissivity distribution	Smith et at. (1990)
Fractal Models		
Equivalent discontinuum	Fractal generator parameters	Long et al. (1992) Chang and Yortsos (1990)

40

II. Discrete Network Models (DNM)

Discrete networks account for each and every individual fracture as a conduit for water to flow. The important aspect of this technique is identification and simulation of individual fractures. The stochastic processes that were summarized in section 3.2 and Figure 3.5 are used to simulate individual fractures, based on limited field observations. Basic flow/transport equations are then solved to calculate flow/transport in individual fractures and in the overall system.

Obviously, DNM requires extensive data collection and intensive computations. Accuracy of the results depends on selection of the right statistical distributions for all fracture parameters (Figure 3.4). The flow part of the model is considerably accurate, since it uses proven laws of hydraulic and fluid transport. DNM is more appropriate for media with countable number of large fractures (Figure 3.8).
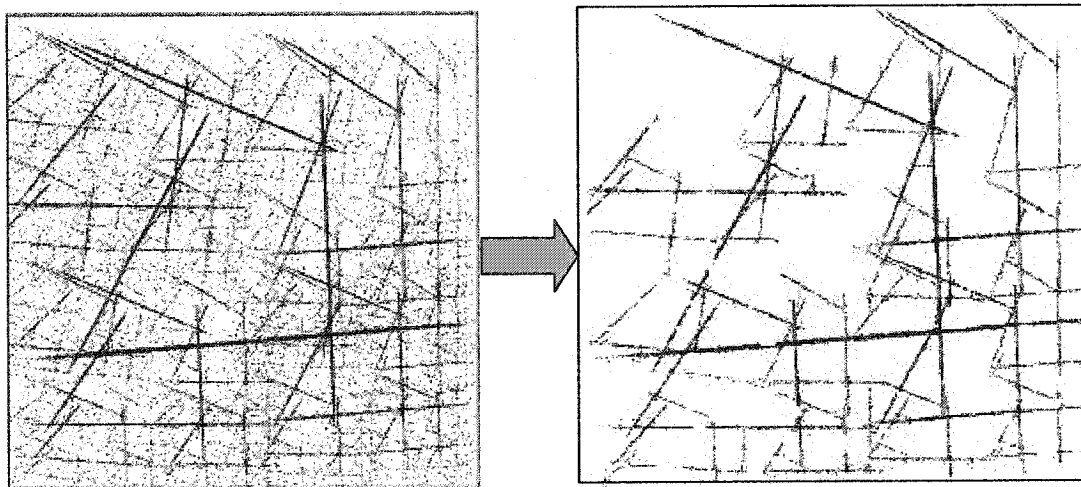
Figure 3.8 – Discrete Network Model Application

41

III. Hybrid Techniques

Hybrid techniques are developed to combine simplicity of ECM and accuracy of DNM to simulate permeability of large media. After regionalizing a medium, DNM is used to estimate permeability tensor of each cell which, by itself, contains numerous fractures. Analogous to Finite Element models, permeability tensors are assembled to solve the ECM for the overall system. Snow (1965) was one of the first studies that developed a relation between hydraulic conductivity and fractures properties in each cell and aggregation of them to estimate global permeability. Oda (1985) used simple flow equations to develop an analytical hybrid model. This model is widely applied to numerous practical problems in order to predict flow behavior. This technique, with some modification, was the basis of the flow model that is developed in this work and is explained in details in chapter 7.

3.4 - INNOVATIVE DEVELOPMENTS IN FRACTURE AND FLOW
      MODELING

Scholars have developed and implemented non-statistical techniques to overcome the limitations of stochastic models. "Hydrologic Inversion" technique has been developed and used by many. In this technique, a trial-error inversion algorithm searches for an arbitrary fracture pattern that produces the observed well test results [Rock Fractures and Fluid Flow – P. 373].

42

An innovative idea in this approach is the application of fractal theory to generate hypothetical fracture networks. Barker (1988), Chang and Yortsos (1990), and Acuna and Yortsos (1991) [Fractures and Fluid Flow – P. 371] introduced and constructed the backbone of an inverse algorithm to predict the fracture pattern using mathematical relations between fractal dimension and flow observations.

Hudson (1993) explained applications of "Iterated Function Systems (IFS)" to generate arbitrary fracture networks for hydrologic inversion study. Similarly, Acuna (1993) used IFS codes to generate fracture patterns that result in expected flow at well locations and studied the relation between flow properties and fractal dimension. This technique, in its current form, is a good tool to <u>guess</u> fracture patterns without conducting any fracture detection investigations. The predicted fracture pattern, however, may be far from the actual pattern. Therefore, while the flow estimates at large scale may be close to the actual values, internal behavior of fluid flow, at small scale, cannot be studied. Due to its close relation to this work, "Hydrologic Inversion" will be discussed in more details in chapter 6.

Percolation theory is another fractal/statistical-based concept that is widely used, especially in the petroleum industry. A brief review of percolation theory and its application to our study is also provided in chapter 6. Some practical applications of percolation theory include:

- Torelli and Scheidegger (1971) and Terolli (1972) were the first studies that looked into percolation process to develop "random maze" models of fractured/porous media.

- Sahimi (1994) provides a good discussion of percolation theory and its application in prediction of a fracture network connectedness and study of fluid flow behavior in porous and fractured media.

- Silliman and Wright (1988) used percolation theory combined with Monte Carlo simulation to investigate presence and pattern of a high conductivity flow path within a low conductivity media.

- Lenormand (1986) summarized various fluid displacement mechanisms and showed application of invasion percolation in drainage mechanism.

- Percolation theory was also used by Degregoria (1985) to simulate two-phased flow in porous media.

- Chelidze (1982) suggests a percolation model fracturing process which allows quantitative evaluation of the clustering phenomenon.

- Robinson (1983) & (1984) used a numerical model to predict percolation threshold as a function of fractures density and percolation probability.

- Robinson (1983) and Charlaix et al. (1987) studied the relation between correlation length (a percolation parameter) and REV.

- Gueguen et al. (1986) and Gueguen and Dienes (1989) looked into hydraulic properties of fractured media, using a mixture of percolation theory, statistics, and the permeability tensor definition by Dienes (1982).

44

- Hestir and Long (1990) used percolation theory and showed quantitatively that permeability decreases as shorter fractures are removed.

3.5 - FRACTAL BEHAVIOR OF FRACTURED MEDIA

Fractal theory is based on self-similarity behavior of natural phenomena. A detailed discussion of fractal theory and its applications to simulation of natural phenomena is provided in chapter 6. Validity and applications of fractal theory has been observed and studied extensively:

- Merely based on rock mechanics concepts, many studies [e.g. Lajtai et al. (1990), King and Sammis (1992)] showed that fracture initiation and propagation process in rock media is self-similar and has a fractal nature. More detailed discussion on this topic is provided in chapter 5.

- Ehlen (2000) showed that fracture patterns in granite have stable fractal dimensions, generally.

- Marrett et al. (1999) showed that fracture network at various sites have fractal pattern. Samples included Limestone and Sandstone (from Texas) and Tuff (From Yucca Mountain, Nevada).

- Barton and Hsieh (1989) showed that at Yucca Mountain, for fractures ranging from 20 cm to 20 m, D=1.6 – 1.7 and is stable.

- La Pointe (1988) calculated Fractal Dimension for simulated and natural fracture networks and studied sensitivity of Fractal Dimension with respect to

45

number of lines, mean line length, number of blocks, and block size. He concluded that fracture density, fracture pattern, and block density are all self-similar fractals.

Based on the wealth of available documentation, this study we does not attempt to prove fractal nature of fracture patterns, since it has been acknowledged unanimously. Instead, a new technique is developed that overcomes limitations of current models and searches for the fractal codes that would generate a fracture pattern with physical characteristics "close to"[8] field observations.

---

[8] Closeness is measured using fractal parameters and it can be improved by monitoring these parameters.

46

CHAPTER 4 - FIELD INVESTIGATIONS FOR ROCK MEDIA HYDRAULIC CHARACTERIZATION

4.1 - ROCK FRACTURE DETECTION TECHNIQUES

Field investigations assist geotechnical engineers to develop an understanding of characteristics of fractured and/or porous media. In fractured media, filed data can provide good approximation of fractures properties, number and interactions of fracture sets, and the overall fracture network pattern. Hereafter, we provide a summary of various fracture detection techniques:

I. Surface Observation Methods

- *Geological observations* at the rock surface (outcrop) provide a basic understanding of fractures genesis. The overall pattern of the subsurface fractures may be predicted from the outcrop observations. This method provides a basis for designing borehole locations for further investigations and better understanding of fracture patterns. La Pointe and Hudson (1985) provided a good example of using outcrop investigation to predict fracture pattern in Niagara dolomites. The topsoil was already removed at an abandoned query and this provided a good opportunity to observe fracture patterns from the rock surface (Figure 4.1). These observations, combined with various statistical models for different parameters, allowed the authors to interpreted and simulated the overall fracture network.

47

- *Seismic Reflection* is a widely used technique that predicts fractures location with a good level of accuracy. Fractures are sources of sudden heterogeneity in rocks. When energy waves, such as seismic and sound, are passed through the ground, they change their direction when hit a fracture. These anomalies, when return to the surface, can be detected and recorded to predict location, orientation, shape, and thickness of fractures. This kind of investigation may be conducted as 2D or 3D, depending on how the sources and receivers are set up.

Figure 4.1 – Geological Observations in the Niagara Dolomites, London, Wisconsin
(From La pointe and Hudson 1985)

- *Electrical/electromagnetic/Radar methods* follow the same principals as seismic reflection techniques. They are specifically appropriate for detecting

48

water-filled fractures, since water has high electrical conductivity, usually much more than intact rock.

- *Tiltmeters* are devices that measure volumetric strains in rocks. Fractured rock presents variations in volumetric strain as a result of water flowing through fractures. This concept is used to detect fractures properties in a rock mass. The region is subjected to hydraulic pressure and Tiltmeters measure volumetric strains at various locations. The results are used to predict fracture pattern, and sometimes to correct observations from borehole data (due to changes in principal stresses as a result of borehole excavation, fractures orientation may be altered from the original position).

II. Borehole Methods

The results of surface methods may be biased due to presence of overburden with properties completely different from the subsurface rock. In such cases we need to practically access the subsurface rock. For this purpose, boreholes are driven in the site, the rock samples are extracted, and the observed discontinuities on the borehole samples will guide us through prediction of the overall fracture pattern (*core inspection*). Sometimes images of the borehole walls may provide better description of the fracture pattern (*Borehole imaging logs*), specially when samples are extensively damaged during extraction. Alternatively, surface techniques may be used inside boreholes for more accurate data collection, although at a higher cost.

49

It is clear that core sampling is most effective for hard crystalline rocks (igneous rocks). Applying this technique to soft sedimentary rocks that easily damage during excavation requires special care and attention. Borehole imaging or wave emission techniques are more appropriate in this case.

In this study, we seek a technique to effectively predict fracture pattern, using limited fractured data from direct core inspection (Figure 4.2.a) or borehole imaging logs (Figure 4.2.b). While there are limitations to these technique, *"measurements made in the immediate vicinity of bore holes are very useful in characterizing fractures and fluid flow through fractures in a number of important applications".*

(Rock Fractures and Fluid Flow – P. 200)

50

(a)   (b)
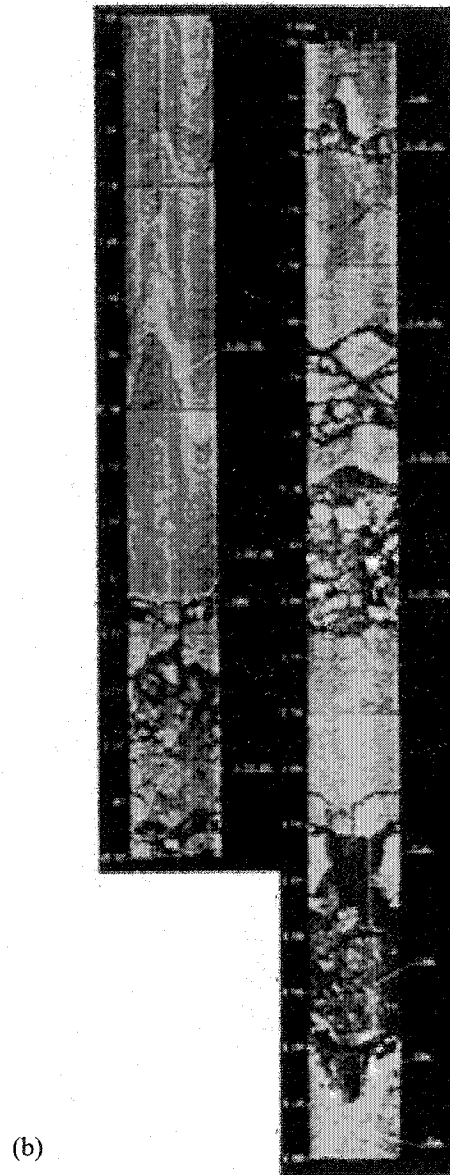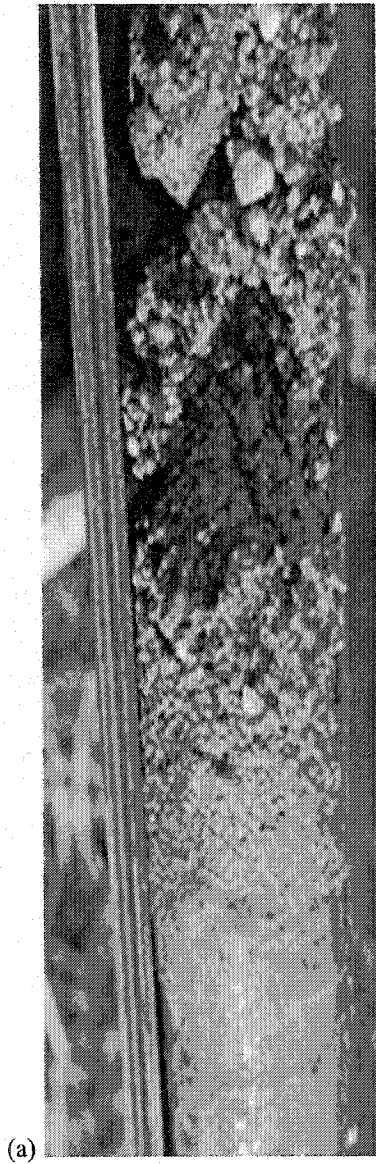
Figure 4.2 – (a) Core Inspection, (b) Borehole Imaging

51

4.2 - HYDRAULIC TESTING METHODS

Hydraulic and tracer tests are used to diagnose behavior of fluid flow at various location in fractured media and, based on that, develop a flow model that truly represents hydraulic properties of the overall rock mass. Hydraulic tests measure water flow by direct observation and tracer tests monitor concentration of a solute (tracer) at various locations, in order to collect flow information.

I. Hydraulic Tests

Hydraulic tests are based on observation of fluid flow through boreholes. To get faster and more economic results, *single borehole* tests may be adequate. To collect more information and develop more accurate flow models, one might conduct multiple boreholes experiments.

- In a *single borehole* test, when we are interested to calculate transmissivity of an entire aquifer, an open borehole would be sufficient. Open-single borehole test is the easiest and the least expensive hydraulic test. However, in the presence of numerous fractures and/or formations, we are interested in hydraulic properties of individual discontinuities and a packer test is more appropriate. In this case, two packers isolate the discontinuity under study, water is injected into or withdrawn from the isolated section, flow and hydraulic head are measured, and fracture transmissivity is calculated (Figure 4.3). In general, single borehole is used when the rock mass can be assumed

to be isotropic and homogeneous. In most cases that these assumptions do not hold, multi-borehole tests are performed.
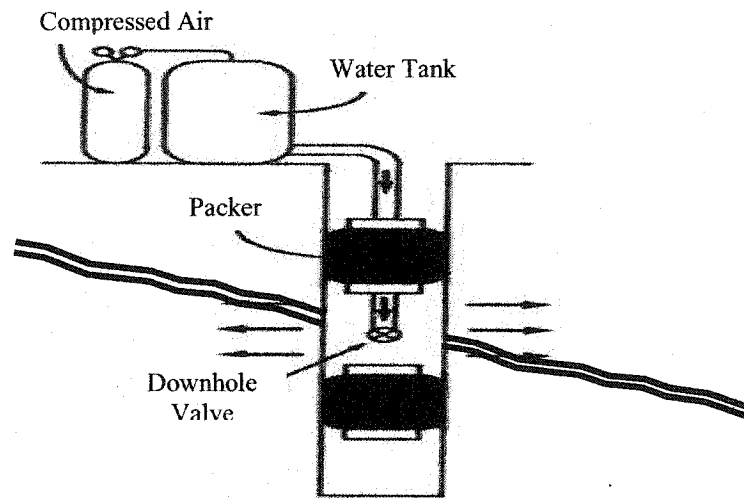
Figure 4.3 – Single Borehole Test (From Rock Fractures and Fluid Flow – 1996)

- *Multi-borehole* test works similar to single borehole test. In this case, water is injected into one borehole and monitored from another borehole. The boreholes can be open or isolated by packers, similar to single borehole. In multi-borehole tests, samples are usually much larger and the results are much more accurate, compared to single boreholes. In addition, Contribution of Individual fractures can be studied and the "isotropy" assumption in single borehole test can be removed. As an example, in the well-fractured rock mass of Figure (4.4.a), water is pumped into packer A at a constant rate and flow is observed at packers B and C. The readings from packers B represent transmissivity of the large fracture (e.g. fault) and the reading from packer C indicated transmissivity of the joints network that could be approximated by a continuous porous medium. As another example, the experiment that is set

53

up in Figure (4.4.b) provides permeability values and direction at various packers B. This test could provide a permeability tensor for the well-connected network of fractures (joints), for equivalent continuum medium model.

(a) A: pumped interval
B: observation interval straddling pumped fracture
C: observation interval straddling fractured rock

highly transmissive fracture
less transmissive fracture

(b)
A: pumped interval
B: observation interval
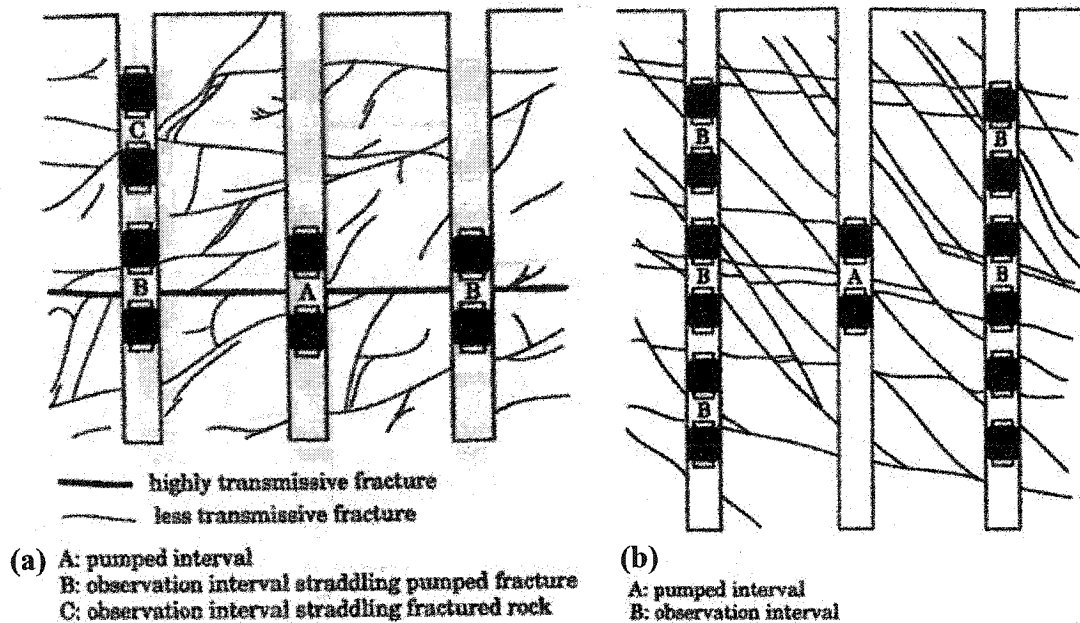
Figure 4.4 – Examples of Multi-borehole tests
(From Rock Fractures and Fluid Flow – 1996)

II. Tracer Tests

Tracer tests evaluate connectedness of fracture networks and solute transport properties of fractures. A water solute liquid (tracer) is injected from a series of injection wells and tracer concentration is monitored at another series of wells (monitoring wells) to understand flow behavior (Figure 4.5). This test is conducted in various forms: Natural gradient tracer test, Divergent flow tracer test, convergent

54

flow tracer test, two-well tracer test, and borehole dilution test. They vary in the way that injection wells and monitoring wells are networked to each other. They all follow the same principals of solute transport processes (advection and dispersion, channelized transport, diffusion, and adsorption).
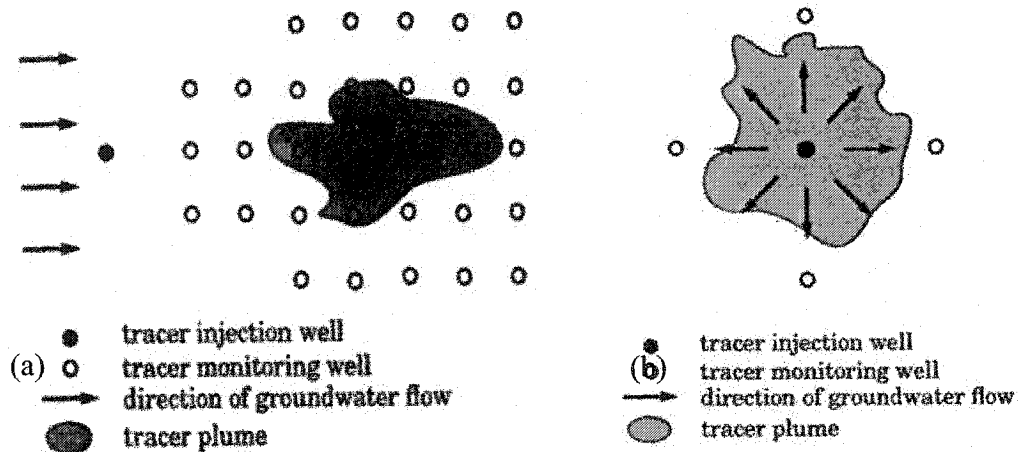
Figure 4.5 – Tracer Tests: (a) Natural Gradient, (b) Divergent Flow
(From Rock Fractures and Fluid Flow – 1996)

It is important to understand clearly applications of these tests. Flow observations at field are not intended to be considered as the "output". They are rather "input" parameters for flow models. A flow model that is supposed to predict overall flow at a region is evaluated by calculating local flow at test locations and comparing with test results. Would there exist a site investigation to provide overall flow properties of a region we would not need a flow mode.

55

CHAPTER 5 - FRACTURE MECHANICS IN ROCK MEDIA

5.1 - CLASSICAL THEORY OF FRACTURE MECHANICS

Fracture initiation and propagation study is the subject of fracture mechanics. The mathematical model is developed based on basic solid mechanics concepts and fundamentals of elasticity theory. Stress distribution and its concentration around a circular or elliptical hole is simulated. A crack is, ultimately, assumed to be an elliptical hole with a very high aspect ration (zero width). Stress intensity factor (K) is calculated that shows intensity of stress adjacent to the crack, compared to the overall field stresses.

Based on Linear Elastic Fracture Mechanics (LEFM), three modes of crack-tip deformation are identified in fracture mechanics:

I. <u>Mode I Crack-Tip Deformation (Opening Mode)</u>

Crack surfaces move directly apart from each other. This is a result of tension stresses perpendicular to the fracture surface (Figure 5.1). Stress intensity factor for mode I Fracturing is calculated as: $K_I = \sigma_0 \cdot \sqrt{\pi \cdot a}$ where, σ_0 is the overall field stress and a is half the size of the crack. Yielding theories of failure are then applied to investigate possibility and amount of fracture propagation.

56

Figure 5.1 – Mode I Fracture
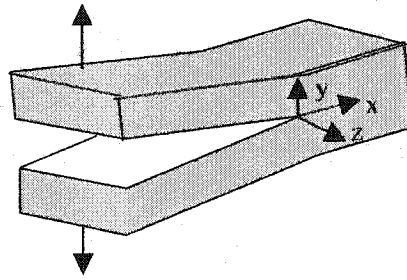
II. Mode II Crack-Tip Deformation (Sliding Mode)

Crack surfaces move in the plane of the fracture surface, as a result of shear stresses. This is also called in-plane shear mode. The direction of the crack surfaces movement is *perpendicular* to the leading edge of the crack (figure 5.2). Mode II stress intensity factor is calculated as: $K_{II} = \underset{r \to 0}{Lim} \ \tau_{xy}(r, \theta = 0)\sqrt{2\pi r}$ where,

$\underset{r \to 0}{Lim} \ \tau_{xy}(r, \theta = 0)$ is the shear stress in the xy plane, perpendicular to crack surface, at the crack tip and r is the distance from crack tip.

Figure 5.2 – Mode II Fracture
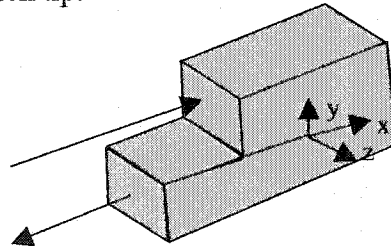
III. Mode III Crack-Tip Deformation (Tearing Mode)

This is also called anti-plane shear mode. Similar to the sliding mode, crack surfaces move in the plane of the fracture surface, as a result of shear stresses. However, the direction of the crack surfaces movement is *parallel* to the leading edge of the crack (figure5.3).

57

Figure 5.3 – Mode III Fracture
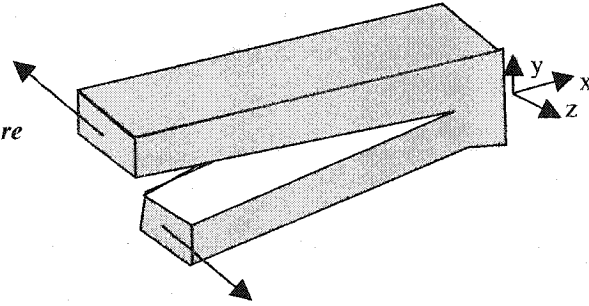
Sometimes a combination of failure modes may be observed in a material. For example, secondary joints in a fault zone are formed as result of a combination of failure modes I, II, and sometimes III.

IV. Yielding Theories of Failure

There are 5 yielding mechanisms that are commonly used in solid mechanics to predict failure of materials based on field stresses:

- *Maximum Principal Stress Theory (Rankine):* A material fails by yielding when the maximum principal stress exceeds the tensile yield strength, or when the minimum principal stress exceeds the compressive yield strength.

$$\sigma_1 \geq \sigma_{yp} \qquad , \qquad \sigma_1 > \sigma_2 > \sigma_3$$

- *Maximum Shear Stress Theory (Tresca):* Yielding will start when the maximum shear stress in the material equals the maximum shear stress at yielding in a simple tension test.

$$|\sigma_1 - \sigma_3| \geq \sigma_{yp} \qquad , \qquad \sigma_1 > \sigma_2 > \sigma_3$$

58

- *Maximum Principal Strain Theory:* A material fails by yielding when the maximum principal strain exceeds the tensile yield strain ($\varepsilon^{\grave{}}_{yp}$) or when the minimum principal strain exceeds the compressive yield strain ($\varepsilon^{\grave{}\grave{}}_{yp}$).

$$|\sigma_1 - \upsilon(\sigma_2 + \sigma_3)| \geq \sigma^{\grave{}}_{yp}$$

$$|\sigma_3 - \upsilon(\sigma_1 + \sigma_2)| \geq \sigma^{\grave{}\grave{}}_{yp}$$

- *Maximum Distortion Energy Theory (Von Mises):* Failure occurs when, at any point in the body, the distortion energy per unit volume in a state of combined stress becomes equal to that associated with yielding in a simple tension test.

$$(\sigma_1 - \sigma_2)^2 + (\sigma_2 - \sigma_3)^2 + (\sigma_1 - \sigma_3)^2 \geq 2\sigma^2_{yp}$$

- *The Octahedral Shear Stress Theory:* It predicts failure by yielding when the octahedral shearing stress at a point achieves a particular value.

$$\tau_{Oct} \geq \frac{\sqrt{2}}{3}\sigma^2_{yp}$$

V. <u>Crack initiation and propagation</u>

Based on fracture mechanics theories, fractures propagate as a result of stress concentration at their tips. Therefore, initiation of a fracture is nothing but extension of preexisting fissures in a solid. Material heterogeneity results in tiny cracks (fissures) at microscopic scale. Stress concentration at the tips of these fissures may result in their failure. As a result microscopic fissure grow to

59

macroscopic cracks. At some point, stress intensity may go below yielding stress and crack length may remain stable until next alteration of field stresses (figure 5.4).

In order to model this process, after identification of the fracture mode, stress at the initial crack (or fissure) tip is calculated using K_I, K_{II}, K_{III}, or a combination of them. One or more of the yielding mechanisms are analyzed and, if failure is predicted, plastic zone depth ($2r_y$) and the associated crack propagation (δ) are calculated. For example, for Mode I:

$$K_I = \sigma_0 \sqrt{\pi a} \quad \Leftrightarrow \quad YIELD? \quad \Leftrightarrow \quad \delta = \frac{K_I^2}{E \cdot \sigma_{Yield}}$$
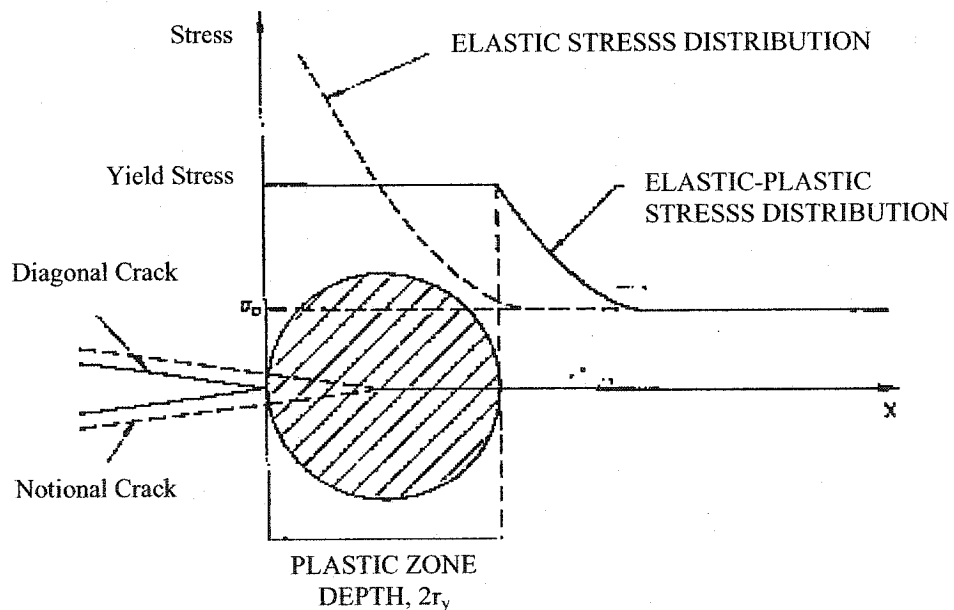
Figure 5.4 – Local Stresses and Crack Tip Propagation

VI. Improvements to classical Fracture Mechanics Models

Classical fracture mechanics that is based on application of stress intensity factors to finite element models, suffers some limitations. Particularly, mathematical derivation usually requires definition of complex functions and complicated calculations. The work by Nishioka and Atluri (1983) is a good example of a complicated fracture model for mixed-mode fracturing, using complex functions. In order to simulate fracture propagation, finite element model needs to be recalculated at every stage of fracture propagation. This requires intensive computations and long processing time.

Alternative approaches have been developed to overcome the above limitations. Swenson (1986) developed a numerical model for mixed mode stress. This model avoided complex functions by rotating coordinate system. The model predicted crack tip propagation displacement (w), its velocity (c), and stresses at crack tip.

Ghorbanpoor and Zhang (1990) discussed advantages of boundary element method (BEM) compared to finite element method (FEM) for fracture propagation modeling. In this model, crack growth direction was predicted using classical maximum principal stress model (see part IV above), but instead of stress intensity factors, crack surface relative displacement (CSRD) method was used to calculate displacement. The main advantage of BEM to FEM is its

61

speed and accuracy, since at each phase of crack propagation, re-meshing occurs only at the crack extension.

Guo et al. (1990) used classical Griffith-Irwin energy criterion to extend the classical crack propagation model to cracks with any arbitrary configuration and loading conditions. Displacement discontinuity model was used in this model and BEM approach was taken. Advantages of BEM to FEM were re-emphasized in this work.

Numerous other works searched for more appropriate and/or simplified fracture propagation models. While some of these models were great improvements to fracturing of engineering solids, they all present common limitations for rock media. The next section provides a brief discussion of applications and limitations of classical fracture mechanics to geotechnical fracturing process.

5.2 - APPLICATIONS AND LIMITATION OF CLASSICAL FRACTURE MECHANICS IN ROCK MEDIA

Fracture mechanics have been used to predict behavior of rock media in response to field stresses and understand development of fracture networks. Sammis and Ashby (1986) considered the initial flaws as penny-shaped objects with radius a and calculated fracture propagation length l at each stage, using classical stress intensity model for mode I fracturing (K_I). Direct effects of stress anisotropy (σ_3/σ_1) on fracture propagation were studied and it was shown that as long as $\sigma_3/\sigma_1 > 1/3$, there are little tensile stresses on the crack and therefore, the crack does not propagate. Relationships between normalized stress $\sigma_1/\left(\sqrt{\pi a}/K_{IC}\right)$ and normalized crack length l/a were developed and graphical presentations (such as figure 5.5) were proposed for prediction of crack propagation behavior. A physical experiment on a piece of glass showed good agreement between the model and the practical results.
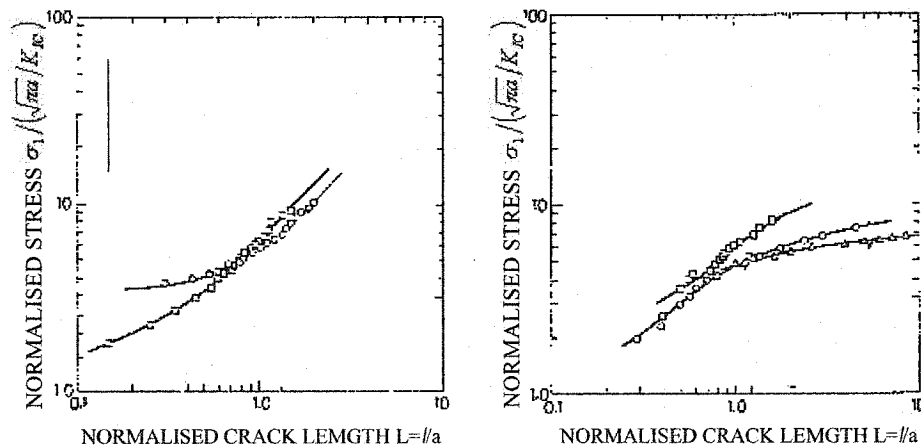
Figure 5.5 – Fracture Propagation Model from Sammis and Ashby (1986)

63

Sammis and Ashby (1986) continued with studying a group of such penny-shaped flaws and took into account interactions among these flaws during cracks propagation. These interactions were modeled using "beam" elements between neighboring cracks and studying failure criteria for these beams that are subject to rotation and shearing, knowing density of the flaws and remote stresses.

In another study, Ashby and Sammis (1990) used basic solid mechanics concepts to develop a damage model for a piece of material (e.g. rock) with numerous cracks interacting with each other. The study developed relations and charts for stress intensity factor (K_I) and normalized principal stresses $(\sigma_1/(\sqrt{\pi \cdot a}/K_{IC}), \lambda$, where $\lambda = \sigma_3/\sigma_1$).

In a similar work, Eberhardt et al. (1998) studied interactions among neighboring cracks using classical fracture mechanics. This study was motivated by lack of work on "how stresses surrounding coalescing cracks interact in terms of promoting or inhibiting crack propagation". A modified linear elastic fracture mechanics (LEFM) was used for the purpose of this study and elliptical cracks were assumed. Effects of neighboring cracks on stresses around a crack were simulated by "stress shadow" and it was concluded that stress shadows have significant effect on cracks extension; they either suppress or promote crack propagation. It was shown haw crack tips stresses interact and develop stress shadow, when two crack tips are close enough to each other. Several sensitivity analyses were performed to study effects of confining

64

stress, crack separation distance, and crack length on crack initiation stress. At the completion of their work, Eberhardt et al. (1998) acknowledged extreme complexity of crack propagation process when it belongs to a group of cracks, compared to when it is isolated. The classical fracture models "appear quite limited in simulating crack propagation in rock".

Yuan et al. (1993) assumed initial flaws to be parallel to principal compressive stress and have elliptical shape with finite width and a finite-width elliptical crack (FIWEC) model was developed. The classical zero-width fracture mechanics model was considered inappropriate for compressive mode (rock), since "sensitivity of the mathematical crack model to normal stress that is coaxial with the major axis of the crack is sacrificed". Based on the above assumption, classical solid mechanics concepts were used to calculate crack extension (a) as a function of fracture width (b), compressive pressure (P), and stress intensity factor at failure (K_{IC}).

Lajtai et al. (1990) argued that classical fracture mechanics, which is based on stress intensity factor calculation, neglects the normal stress parallel with the propagation direction. Therefore, these models become handicapped when applied to rock media in which fracturing occurs as a result of compressive stresses. Experience has shown that the dominant mode of fracturing in rocks is neither of the modes I, II, or III, but a compression mode.

65

According to Lajtai et al. (1990), Rock fractures usually develop parallel to principal stresses. This explains appearance of fractures in semi-parallel sets; "over 70 percent of cracks propagate within 10 degrees of the direction of far-field principal compressive stress", unless they are disrupted by pre-existing discontinuities such as beddings and cleavages. Clustering of fractures can be explained by the "shadowing effect". Two cracks that grow very closely influence local stresses and form a region (shadow) of intense stresses. This is a region in which we see "crack bunching". It is also observed that, around underground cavities, a "mother-daughter" relationship results in development of new fractures in the rock bridge between the two cracks. These new cracks have features similar to the "mother" and "daughter", the same process could be repeated over and over, and a self-similar pattern is observed.

Lajtai et al. (1990) also showed that rock fractures are not developed randomly, they "know were they want to go and they do this in the most systematic way". Lateral far-field stress has a very important role in the amount and rate of fractures extension. If this confining stress is high, it could prevent fractures propagation. Therefore, the crack propagation model should be based on both minimum and maximum principal stresses. A similar work by Carter et al. (1989) gave similar relations between principal stresses and crack growth and its direction.

5.3 - "SELF-SIMILARITY" OF THE ROCK FRACTURING PROCESS

Fracture initiation and propagation in rocks is very well explained as a self-similar (fractal) process. King and Sammis (1992) started with preexisting tiny flaws, which were assumed to have fractal distribution. They modeled fracturing process as a

66

series of rotations and bendings of hypothetical "beams" that are developed at each stage due to stress concentrations between fractures (flaws) of the previous stage.

The amount of beam rotation is controlled by the direction of principal stresses and by proximity and size of the cracks (beams) from the previous stage. As shown in figure 5.6, this model can very well explain the clustering nature of fractures, from fracture mechanics point of view. In fact, it was shown that the assumption of fractal distribution of the original flaws is not necessary, since after several stages of fracturing, a fractal geometry will appear, disregarding the original distribution of flaws (see also chapter 6 – fractal pattern is independent from the originator).

As the length of a beam extends, its aspect ratio increases and, as a result, it fails at some point. This is the time when the second generation of smaller beams is developed at the location of beams rupture. The new beams collapse again to fill the void space. This process repeats over and over and a self-similar fracture set is developed. This explains both irregularity and clustering that is observed in fractured rocks.
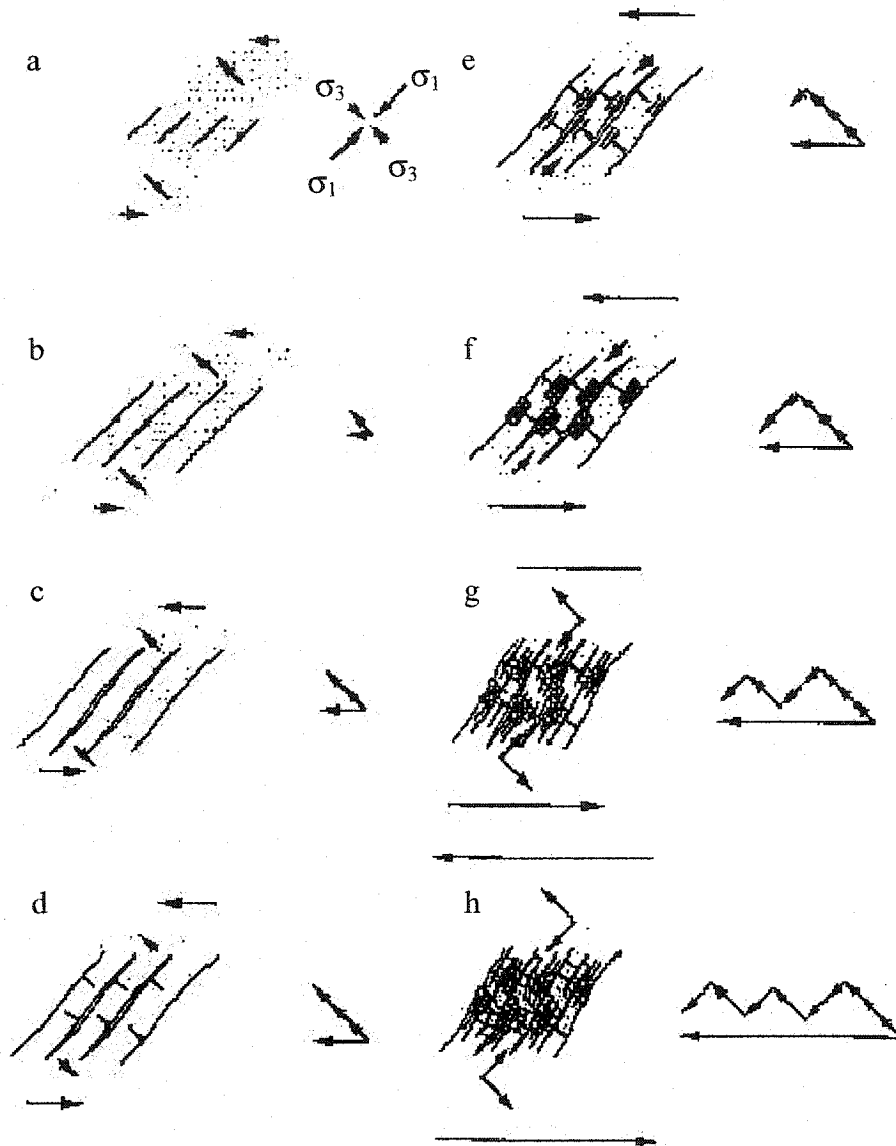
Figure 5.6 – Self-Similarity of Rock Fracturing Process (from King and Sammis - 1992)

A schematic evaluation that can lead from a few defects a multifractured material like fault gouge. Initially four defects are shown shedding tensile fractures (a). Displacement boundary conditions applied at a distance are shown by opposing arrows above and below each figure. As the tensile fractures create beams, motion close to the beams has an outward component. This is shown by angled arrows within the figures (a–d). When the beams start to fail similar arrows show inward motion (c, f). Further deformation involves repeated episodes of such expansion and contraction associated with dilation and collapse of the region being fragmented. Except for (a) where the initial stress conditions are shown, vector diagrams to the right of each figure indicate the cumulative displacement distant from the zone (horizontal arrows) and the corresponding displacements close to the zone (angled arrows). The zone cycles through episodes of expansion as voids are created and contractions as they are filled.

CHAPTER 6 - FRACTAL THEORY AND ITS APPLICATIONS

6.1 - FUNDAMENTAL CONCEPT, ESSENTIAL THEOREMS, AND MATHEMATICS

I. Fractal Concept:

Fractal is defined as a geometric shape that is complex and detailed in structure almost at any level of magnification. Benoit B. Mandelbrot (1982) was the first who introduced Fractals to describe geometric properties of apparently irregular (chaotic) fragments. This chaos is actually self-similar. That is, at any magnification scale, the image is a (sheared) replica of the overall object. Broccoli is a good example of a fractal. Each piece is similar to the whole object, rotated and/or stretched, but at a smaller scale.
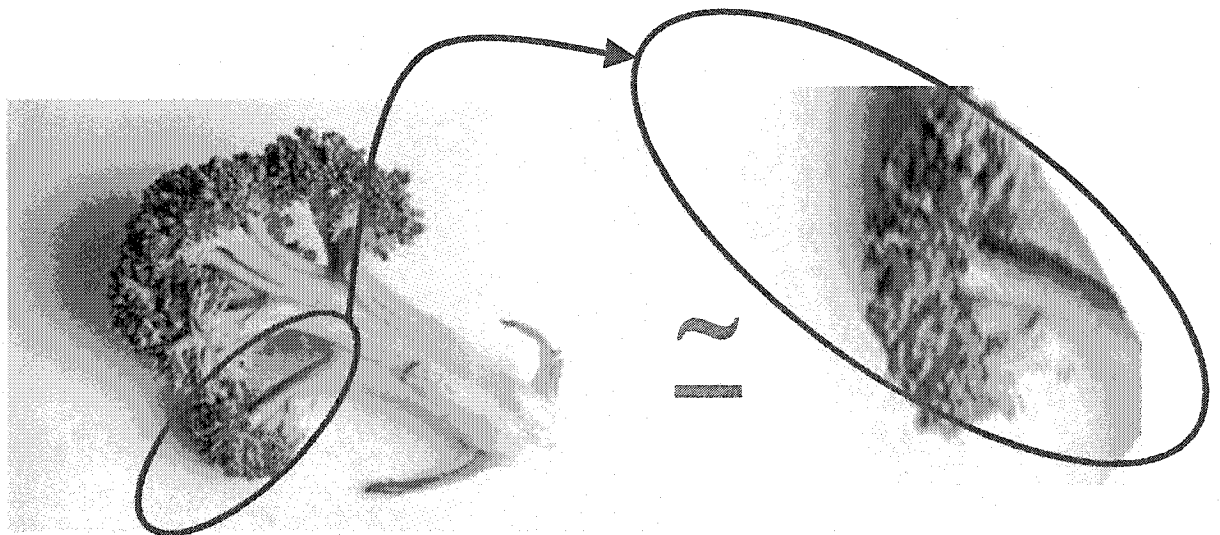
Figure 6.1.a – Broccoli is a fractal. Each piece is a rotated, stretched copy of the object

69

Fractal theory defines the geometry of nature. Despite classical geometry that defines every object in Euclidian space, fractal geometry uses partitions of the Euclidian space and fractal objects live in "fractal space". In the classical Euclidean space, an abject is one dimensional (line), 2 dimensional (plane), or 3 dimensional (space). In fractal space, objects can have fractional dimensions between 0 and 3:

Geometric Space	Fractal Space	
1 Dimensional (Line)	$0 \leq D \leq 1$	Cantor Sets: apparently segmented lines
	$1 \leq D \leq 2$	Koch: Non-differentiable curve
2 Dimensional (Plane)		Sierpinski Triangle: Partially filled plane
	$2 \leq D \leq 3$	Sierpinski Pyramid: Partially filled space
3 Dimensional (Space)		

The famous "Koch Curve" with a fractal dimension (D) of 1.262 is not a line (D=1) and is not a filled plane (D=2), it is somewhere in between. It is a continuous line with infinite length, apparently curvilinear but has no curvatures (non-differentiable)!

70
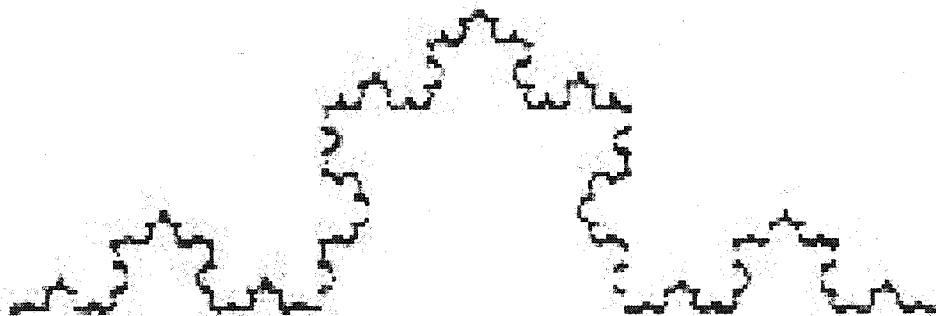
Some examples of natural fractals are shown in Figure 6.1.b. We will see later how an image can be evaluated for fractal behavior, by analyzing its fractal dimension stability.

Mountains

Trees / Clouds

Ocean Shoreline (Koch Curve!)

Figure 6..1.b – Some Natural Fractals

71

II. Fractal Definitions and Mathematics

The following are some essential definitions of fractal mathematics (Barnsley - 1993):

- A transformation $w : \Re^2 \rightarrow \Re^2$ of the form:

  (6-1) $\qquad w(x, y) = \{a \cdot x + b \cdot y + e \; ; \; c \cdot x + d \cdot y + f\}$

  where a, b, c, d, e, f are real numbers, is called a (two-dimensional) affine transformation. In this text, wherever we talk about a transformation, it refers to an affine transformation.

- Iterated Function System:

  A fractal image comes to life as a result of applying a series of transformations of the form (6-1) to an initial object over and over. Transformations may consist of rotation, transition, scaling, and/or shearing. This group of transformations is called iterated function system (IFS). In a 2D space, rotation, scaling, and shearing are presented by a 2x2 matrix and transition is presented by a 2x1 vector:

$$\begin{Bmatrix} x_{New} \\ y_{New} \end{Bmatrix} = \begin{bmatrix} a & b \\ c & d \end{bmatrix} \otimes \begin{Bmatrix} x \\ y \end{Bmatrix} + \begin{Bmatrix} e \\ f \end{Bmatrix}$$

  where:

$$\begin{bmatrix} a & b \\ c & d \end{bmatrix} = \begin{bmatrix} \rho_1 Cos\theta_1 & -\rho_2 Sin\theta_2 \\ \rho_1 Sin\theta_1 & \rho_2 Cos\theta_2 \end{bmatrix}$$

72

ρ_1, ρ_2 are the scaling factors of x and y and θ_1, θ_2 are counter-clockwise rotations with respect to x and y. $\begin{Bmatrix} e \\ f \end{Bmatrix}$ is the transition vector. Obviously, ρ_1, ρ_2 should be less than 1.0, in order for the sequence of transformations to converge (contractive transformation). IFS codes are usually shown in a tabular format. For example, consider the following 3 IFS codes:

IFS#	a	b	c	d	e	F	ρ_1	θ_1	ρ_2	θ_2
1	0.50	0.00	0.00	0.50	0.00	0.00	0.50	0.00	0.50	0.00
2	0.50	0.00	0.00	0.50	0.00	0.50	0.50	0.00	0.50	0.00
3	0.50	0.00	0.00	0.50	0.50	0.00	0.50	0.00	0.50	0.00

When they are applied to a square box 1x1 (Figure 6.2.a), we get 3 (½× ½) squares as shown in Figure 6.2.b. Applying the same IFS codes to each of the three squares breaks each into 3 new squares, half its size (1/4 original box). After large number of repetitions (27 in this case), the resulting object is a triangular shape fractal, called "Sierpinski" triangle (Figure 6.2.e). It is interesting to note that the shape of the fractal object is independent from the original object. Would we have used a triangle, a circle, or even a small point, the result would have been the same. This original object is called the initiator.
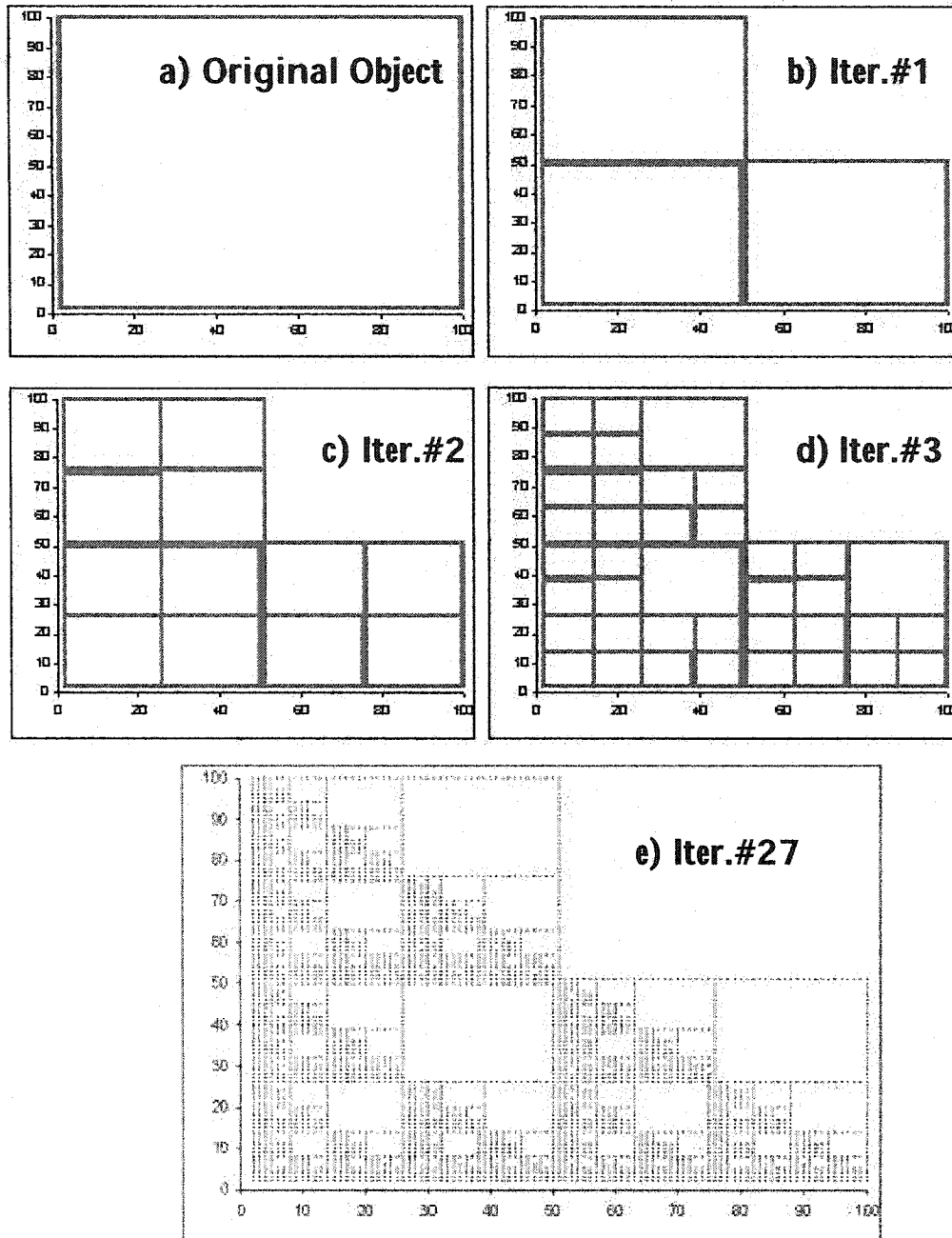
Figure 6.2 – Sierpinski Triangle Development Using Iterated Function System
(Deterministic Algorithm)

In practice, in order to generate realistic fractal images, a small dot is used as

the initiator. As long as this dot is small enough to identify object

74

boundaries, its size and position does not impact the final image. What is important is to apply all transformations equally, at every iteration. This is the basis of the random iteration algorithm that is explained later. Alternatively, by changing probabilities of various transformations, different fractal images can be generated from the same set of IFS codes. Figures 6.3.a and 6.3.b have the same IFS codes, but in Figure 6.3.b one of the Iterations is only applied 3.3% of time and the other two each has 48.3% probability (looks like a fracture set!).
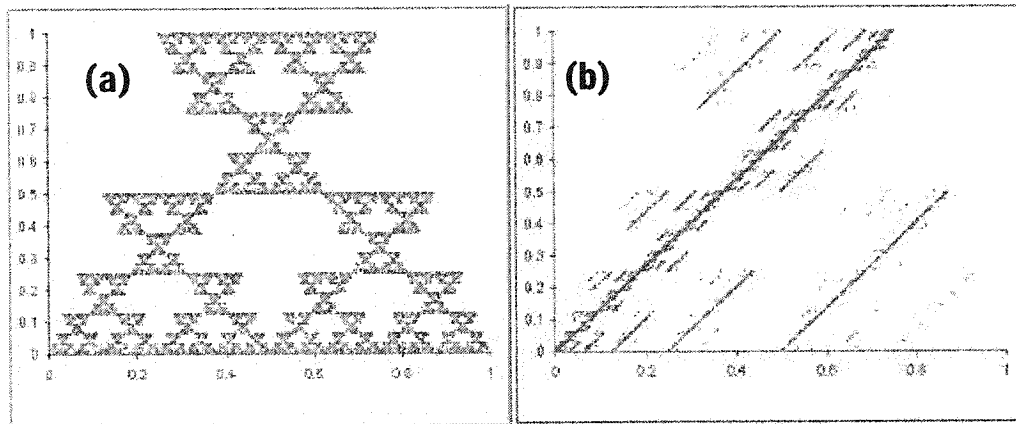
Figure 6.3 – Fractal Images: (a) and (b) have same IFS codes but different probabilities

- A transformation in which an object maintains its shape (but shrinks) at every iteration is called a *similitude (self-similar)*. In a similitude we have: $\rho_1 = \rho_2$ and $\theta_1 = \theta_2$. In Figure 6.4, transformation (2) is a similitude (square) and transformations (1) and (3) are self-affine (not similitude) transformations (parallelograms). Notion of similitude transformations in an attractor is very helpful to solve the reverse problem.

75
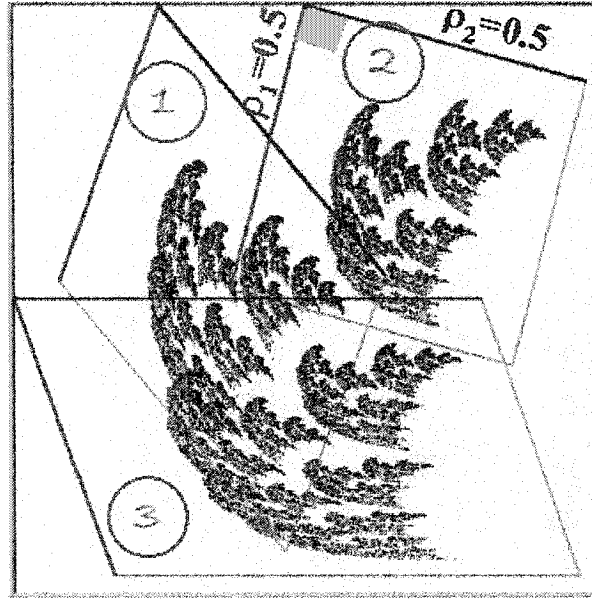
Figure 6.4 –Self-Affine (1 & 3) and Self-Similar (2) Transformations

- Fixed point of a transformation (X_f) is the point whose transformation is itself: $W(X_f)=X_f$. For a two dimensional transformation, X_f (x_f, y_f) is calculated as:

$$\begin{cases} x_f = \dfrac{bf - e(d-1)}{(a-1)(b-1) - bc} \\[2mm] y_f = \dfrac{ec - f(a-1)}{(a-1)(b-1) - bc} \end{cases}$$

In general, considering a transformation of the form $W(X) = A.X + B$, it can be shown that: $w^{on}(X) = A^n(X - X_f) + X_f$. In other words to estimate location of the nth transformation of a point X, one could use the following equations:

$$A^{on}(X) = A^n \quad \text{and} \quad B^{on}(X) = (I - A^n).X_f$$

The fifth transformation of the primary fracture at (0,0) in Figure 6.5, subject

to transformation: $\begin{bmatrix} 0.75 & 0.00 \\ 0.00 & 0.75 \end{bmatrix} \left| \begin{Bmatrix} 0.25 \\ 0.00 \end{Bmatrix} \right.$ is calculated as follows:

76

Fixed Point: $\begin{cases} 0.75x_f + 0.00y_f = x_f \\ 0.00x_f + 0.75y_f = y_f \end{cases} \Rightarrow \begin{cases} x_f = 1.00 \\ y_f = 0.00 \end{cases} \Rightarrow X_f = \begin{Bmatrix} 1.00 \\ 0.00 \end{Bmatrix}$

at 5th iteration: $A^{\circ 5} = A^5 = \begin{bmatrix} 0.75 & 0.00 \\ 0.00 & 0.75 \end{bmatrix}^5 = \begin{bmatrix} 0.237 & 0.000 \\ 0.000 & 0.237 \end{bmatrix}$ and

$B^{\circ 5} = (I - A^5) \cdot X_f = \left(\begin{bmatrix} 1.00 & 0.00 \\ 0.00 & 1.00 \end{bmatrix} - \begin{bmatrix} 0.75 & 0.00 \\ 0.00 & 0.75 \end{bmatrix}^5 \right) \otimes \begin{Bmatrix} 1.00 \\ 0.00 \end{Bmatrix} = \begin{Bmatrix} 0.763 \\ 0.000 \end{Bmatrix}$

This means that at the fifth iteration, the object is shrunk by 0.237 units and is

moved to the coordinates $\begin{Bmatrix} 0.763 \\ 0.000 \end{Bmatrix}$. From fractal concept, we know that this

simple transformation shrinks the object $(75\%)^n$ and moves it on x-axis

according to: $1 - 0.75^n$, (n = iteration number). Therefore, after 5 iterations,

the object is shrunk $(75\%)^5 = 23.7\%$ and it is moved to x $= 1 - 0.75^5 = 0.763$

and y=0.
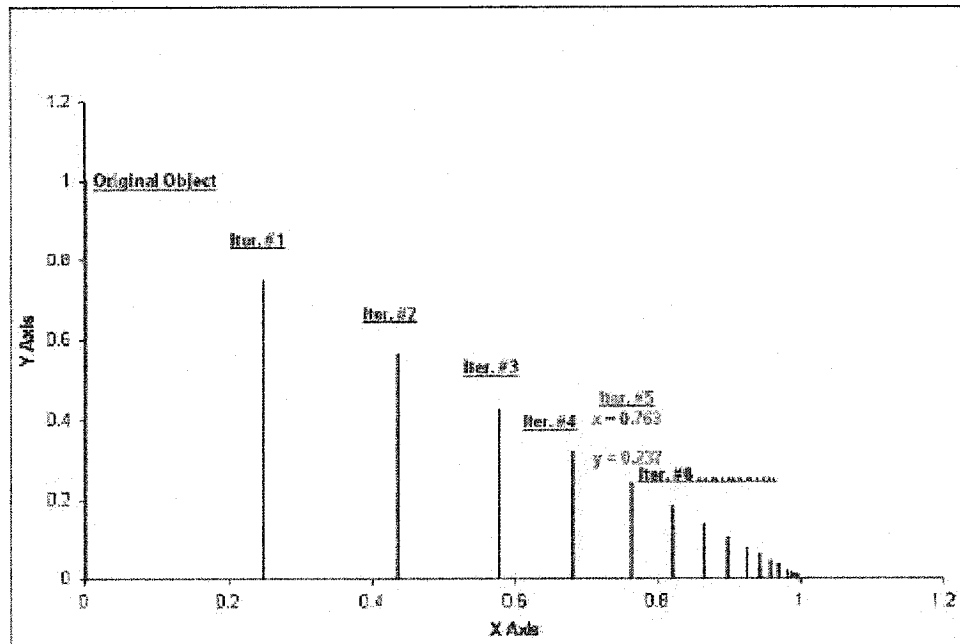
Figure 6.5 – Fixed Point of a Transformation and its Application

77

- Fixed point of a complete iterated function system $W(B)= \cup w_n(B)$ is also called its *attractor*. If B_0 is the attractor of an IFS, we have $W^{on}(B_0) = B_0$. The attractor of sierpinski is the equivalent triangle; the fractal image. The attractor of the cantor set: $IFS=\{R; 1/3x, 1/3x+2/3\}$ is the closed interval [0,1] on the x-axis.

- Each transformation in an iterated function system (each IFS Code) is also called a *Contraction Mapping*. The *Contractivity Factor (Scale Factor)* of a contraction map is the ratio of each iteration to the next one: $d(X'_1,X'_2)<s.d(X_1,X_2)$, where $X'_1=W(X_1)$ and $X'_2=W(X_2)$. This factor should be positive and smaller than 1 in order for the iterations to converge. For the Sierpinski triangle, for example, the contractivity factor is 0.5 for all transformations, since dimensions (x, y) of every iteration are half the dimensions of the previous one. If contractivity factors in x and y (and z) are different, system's contractivity factor is equal to the largest one (exceptionally for a condensation set, this rule does not apply: s=0). Also, contractivity factor of an iterated function system is equal to the largest contractivity factors of its transformations.

- *Condensation Set* is a contraction mapping with zero contractivity factor. In other words: $w_0(A)=A$. The fixed point of a condensation set is itself. The collage of an iterated function system $\{X;w_1,w_2,...,w_n\}$ with contractivity factor s and a condensation transformation w_0, is called an IFS with

78

condensation, with contractivity factor of s: {X;W, w_0}. In the example of Figure 6.5 above, the object A_0 could be simulated by condensation set: {$\rho_1=\varepsilon$ (width$\rightarrow$0), $\rho_2=1$ (height), $\theta_1=0$, $\theta_2=0$ (no rotation/shearing)} with contractivity factor of $\varepsilon\rightarrow0$.

In the example of Figure 6.6 (which is the basis for development of fractal network of fractures in the next chapter), the first 4 transformations are the IFS codes that define spatial distribution of copies of the primary fracture and the last IFS code is a condensation set, which is actually the image of the primary fracture. This fracture is the largest fracture of this set in the complete fractal image of the fracture set.

Define IFS Codes

w	a	b	c	d	e	f	θ1	r1	θ2	r2
1	0.48	0.00	0.00	0.48	0.01	0.01	0.00	0.48	0.00	0.48
2	0.48	0.00	0.00	0.48	0.01	0.51	0.00	0.48	0.00	0.48
3	0.48	0.00	0.00	0.48	0.51	0.01	0.00	0.48	0.00	0.48
4	0.48	0.00	0.00	0.48	0.51	0.51	0.00	0.48	0.00	0.48
5	0.35	0.00	0.61	0.02	0.30	0.30	60.00	0.70	0.00	0.02
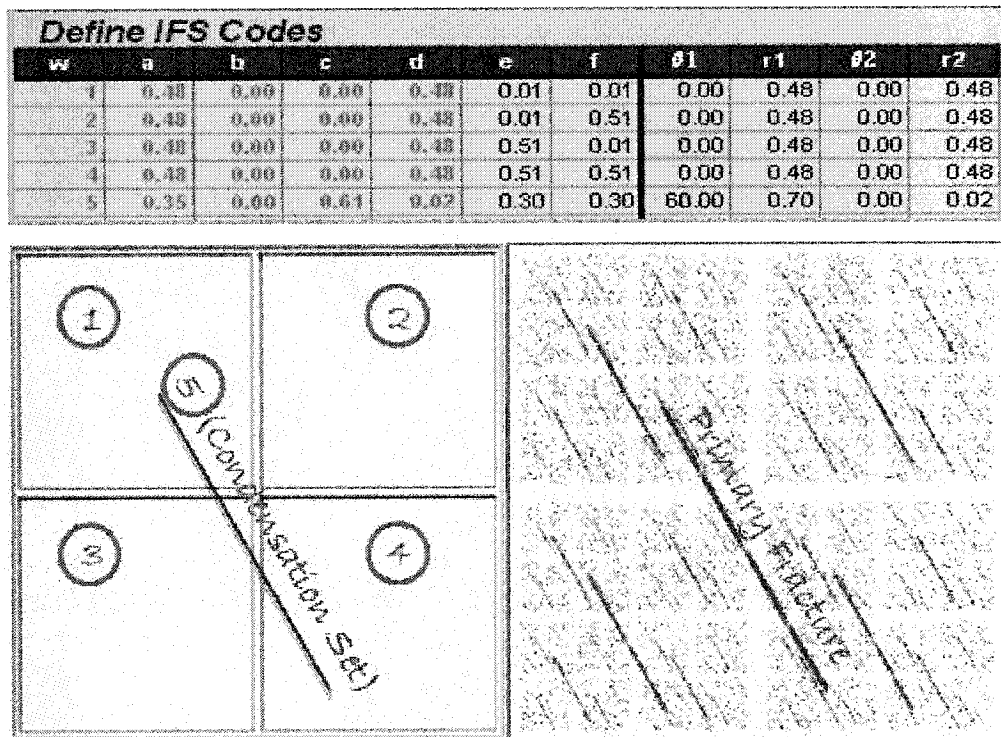
Figure 6.6 – Condensation Set and Fracture Set

79

- If two or more of transformations of an iterated function system are overlapping, their fractal images will be also overlapping. This system is called an *overlapping IFS* (Figure 6.7.a). Alternatively, an IFS may be *just-touching* (Figure 6.7.b) or *disconnected* (Figure 6.7.c). Overlapping IFS's are more difficult to analyze mathematically. Specifically, due to duplication of points at the same coordinates, their fractal dimension cannot be estimated very accurately.
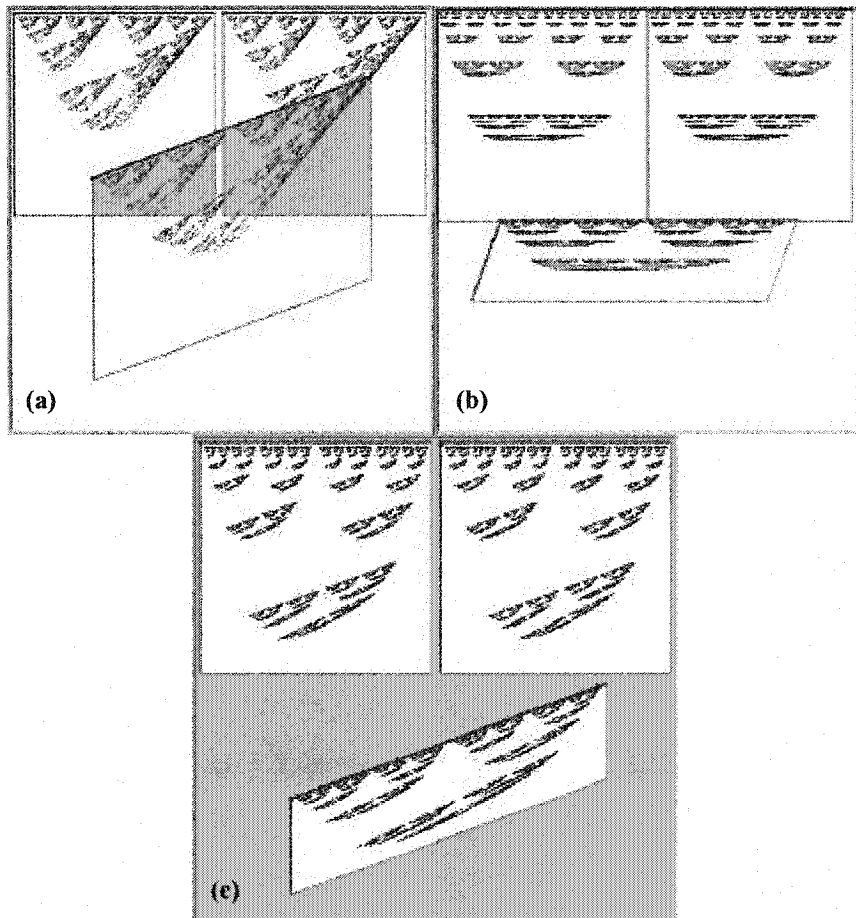
Figure 6.7 – (a) Overlapping, (b) Just-Touching, (c) Disconnected Fractals

- Fractal dimension is a measure of fractal behavior of an object compared to other fractals. Due to its importance in this study, fractal dimension is explained in details in part V of this section.

III. Fractal Theorems

The following theorems of fractal are particularly important in this study:

- *Contraction Mapping Theorem:* The union of transformations of an iterated function system ($\cup w_i$) in a metric space is a transformation in fractal space (W), by itself. The contractivity factor of W is the contractivity factor of the set of IFS transformations [that is, $\max(s_1, s_2, .., s_n)$]. The fixed point of the fractal space has the property: $A = W(A) = \cup w_i(A)$. This theorem is the basis of the classical deterministic algorithm that will be explained later.

- *Shadow Theorem:* If transformations of an iterated function system are invertible, the IFS can be projected on another system of coordinates to get a new fractal. An overlapping fractal can change to a disconnected fractal and visa versa. A 3D fractal can be projected on 2D and, subsequently, on 1D. In Figure 6.8 the two 1D cantor sets along x and y axes are projections of the 2D fractal object. Collage theorem can find IFS codes for the two 1D cantor sets easily and combine them to get the IFS codes the 2D fractal object.

81
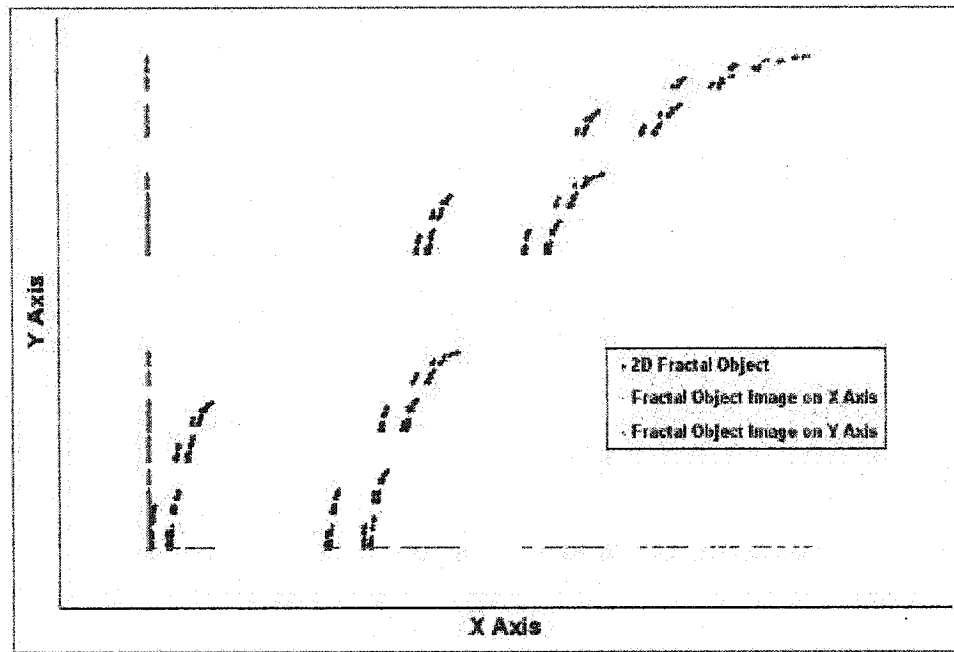
Figure 6.8 – Shadow Theorem

Shadow theorem is not used in this work, exclusively. However, it has a
great potential to help us define IFS codes of a fracture network based on
limited field observations of borehole date (y axis) and scan-line data (x
axis). A small example of possible application of shadow theorem is shown
in chapter 9, which simulates a fracture set at Yucca Mountain.

- *Collage Theorem:* In order to find an IFS whose attractor is similar to a given
  set, we need to find a set of transformations whose union (collage) is similar
  to the given set. Proximity of the IFS to the attractor is measured by
  Hausdorff metric [and/or fractal dimension]. In the following example, the
  three solid-border squares of Figure 6.9 represent the three transformations
  listed below:

IFS#	a	b	c	d	e	f	ρ_1	θ_1	ρ_2	θ_2	s
1	0.50	0.00	0.00	0.50	0.00	0.00	0.40	0	0.40	0	$\frac{2}{5}$
2	0.50	0.00	0.00	0.50	0.75	1.00	0.50	180	0.50	180	½
3	0.50	0.00	0.00	0.50	0.50	0.00	0.50	0	0.50	0	½

The fractal object is shown is red with a fractal dimension of 1.585 (box counting). The attractor of the IFS is shown in blue and its fractal dimension is 1.445 (Analytical). The above three transformations that encompass the attractor are shown as solid black squares, with a ☺ sign showing their orientations. In this case, it is clear that a little increase in ρ_1 and ρ_2 of transformation 1 would result in an attractor "closer" to the fractal object. In fact $\rho_1 = \rho_2 = ½$ in transformation 1, would result an attractor identical to the fractal image (the dashed-line gray square).
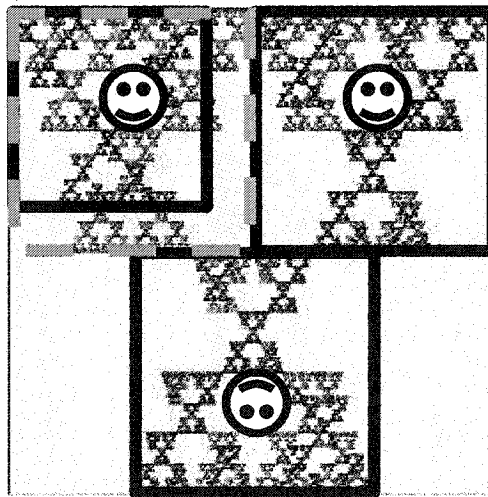
Figure 6.9 – Application of Collage Theorem

In practice, it is usually very difficult to identify the right IFS codes using the above technique. This study modifies collage algorithm and develops a more practical method to find the right IFS codes, specifically for fractal network

83

of fractures. Details of this technique and the associated computer program

are explained in the next chapter.

There are two other important theorems that relate to fractal dimension and are

explained in part V of this section.

IV. <u>Fractal Algorithms</u>

There are two classical "forward" fractal algorithms that are explained here:

- *Deterministic Algorithm:* Based on contraction mapping theorem, in every

  iteration, the fixed point remains unchanged: $W(A_f)=A_f$ ➜ $\cup w_i(A_f) = A_f$.

  Also, $A_f = \underset{n \to \infty}{Lim} \; W^{\circ n}(A)$, for any A. Therefore, if we start with an arbitrary

  object (lets say a 1×1 box), apply all transformations and unionize them into

  one object, we have done our first iteration. This process can repeat until a

  constant image is generated:

84
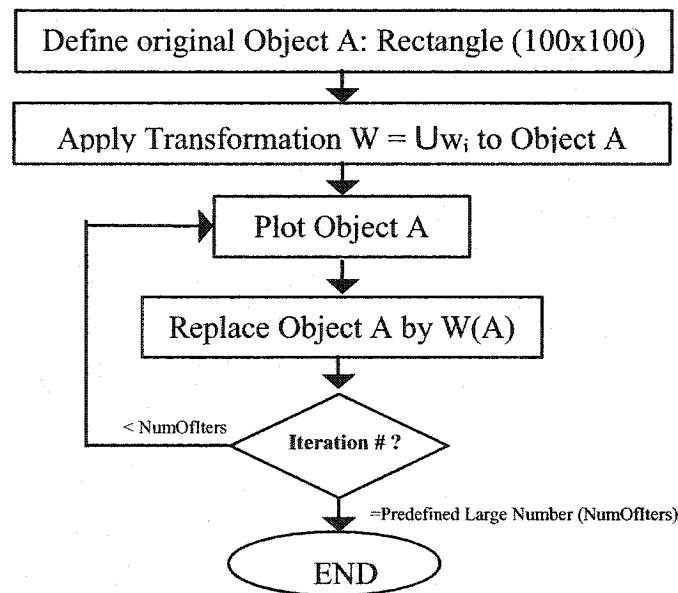
Deterministic algorithm is a quick way of understanding what happens at each stage of developing a fractal object using IFS codes. As we saw in Figure 6.2, after only 27 iterations, the image becomes stables and "looks like" the fractal attractor. However, in this form, this algorithm is not very efficient for the purpose of this study. In addition to other limitations, presence of transformations with condensation (primary fractures) results in ambiguity between the boundaries of A^{on} and the images of the initial fracture. For specific purpose of this study, this algorithm was modified as will be explained in Chapter 7.

- *Random Iteration Algorithm*

This algorithm is based on the notion that fractals (and in fact all natural phenomena) are collections of small particles. Images that are generated by this algorithm look much more realistic than the deterministic algorithm (Figure 6.6). Practically, this is the most appropriate algorithm to simulate rock permeability values at small regions of a finite difference model.

The idea behind random iteration algorithm is to apply one of the transformations to a single point, randomly, at each iteration. All transformations have equal probabilities of being selected. Therefore, after very large number of iterations, they are all used equally. If desired, this criterion can be modified for fractals that used different probabilities for

85

different transformations (Figure 6.3.b). The algorithm is very simple and is

summarized here:
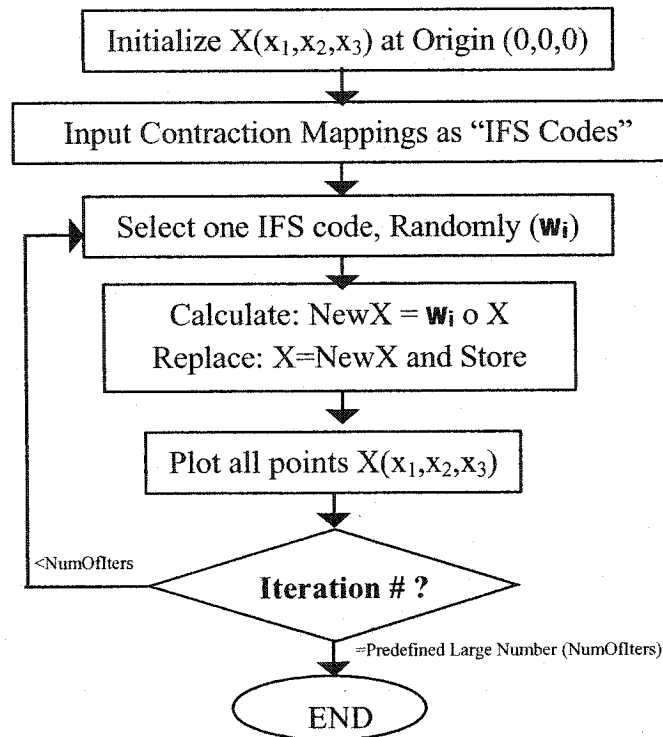
It would be more interesting to go the other way around. If we have an image that is

known to have a fractal nature (e.g. based on fractal dimension stability) what is its

iterated function system? A true mathematical answer to this question, in fact, could

open a whole new world of applications in image processing and compression:

*If, in the forward direction, fractal mathematics is good for generating
natural looking images, then, in the reverse direction, could it not serve to
compress images? Going from a given image to an Iterated Function System
that can generate the original (or at least closely resemble it), is known as
the inverse problem. This problem remains unsolved.*

Kominek (1977-1993)

86

The goal of this study is very similar to the above, and even broader than that. If we have limited field data on fracture network (borehole observations) that gives us a "partial" image of the network, would it be possible to find the correct iterated function system? For the purpose of this study, a "reverse" fractal algorithm was developed and implemented in a computer program. This reverse algorithm will be explained in details is chapter 7. The proposed reverse fractal algorithm is still based on trial-error approach. However, it is much more practical and effective compared to collage algorithm, specifically for borehole data imaging.

V. Fractal Dimension

Self-similarity of an image is evaluated by studying stability of its fractal dimension. Fractal dimension (D) is a number associated with a fractal image (*a measure*) that shows how well the fractal object fills the space and how it compares to other fractal objects. Great Britain coastline is a Koch curve with a fractal dimension of 1.2. Another shoreline with a fractal dimension of 1.1 should have a smoother, less jagged pattern and would be easier to travel, may be ?

Mathematically, fractal dimension, if exists, is defined as:

$$D = \lim_{\varepsilon \to 0} \left\{ \frac{Ln[N(A,\varepsilon)]}{Ln(1/\varepsilon)} \right\}$$

where, $N(A,\varepsilon)$ is the smallest number of closed balls of radius $\varepsilon > 0$, needed to cover fractal object "A".

For a totally-disconnected or just-touching similitude fractal, fractal dimension is mathematically calculated based on scale factors of its IFS codes as explained in the following theorem:

- Fractal dimension of a <u>similitude</u> IFS, which is <u>disconnected</u> or <u>just-touching</u>, is equal to the fractal dimension of its attractor and can be calculated as:

$$\sum_n |S_n|^D = 1 \Leftrightarrow D = D(A) = ? \quad ; \quad S_n = \text{Scale factor of n}^{\text{th}} \text{ transformation}$$

For a <u>similitude overlapping</u> IFS, fractal dimension of the object (D), calculated from the above equation, is larger than fractal dimension of the attractor [D(A)].

Two example applications of this theorem are explained hereafter:

- ➤ *Fractal Dimension of Sierpinski Triangle* – Mathematical Derivation: Consider the right angle Sierpinski triangle with the following IFS Codes and Scale factors:

IFS#	a	b	c	d	e	f	ρ₁	θ₁	ρ₂	θ₂	s
1	0.50	0.00	0.00	0.50	0.00	0.00	0.50	0.00	0.50	0.00	½
2	0.50	0.00	0.00	0.50	0.00	0.50	0.50	0.00	0.50	0.00	½
3	0.50	0.00	0.00	0.50	0.50	0.00	0.50	0.00	0.50	0.00	½

The fractal Dimension of this attractor is calculated as:

$$\sum_n |S_n|^D = 1 \quad , \quad D \geq 0 \quad \Rightarrow \quad S_1^D + S_2^D + S_3^D = 1$$

88

$$\Rightarrow \quad \frac{1}{2}^D + \frac{1}{2}^D + \frac{1}{2}^D = 1 \quad \Rightarrow \quad 3 \times \left(\frac{1}{2}^D\right) = 1 \quad \Rightarrow \quad D = \frac{Ln\left(\frac{1}{3}\right)}{Ln\left(\frac{1}{2}\right)} = 1.58496$$

> Single Fracture Set: For the <u>disconnected</u> and <u>similitude</u> fracture set of Figure 6.10 with the following IFS Codes and Scale factors:

IFS#	a	b	c	d	e	f	ρ_1	θ_1	ρ_2	θ_2	s
1	0.52	0.00	0.00	0.45	0.05	0.00	0.46	5.00	0.46	5.00	0.46
2	0.40	0.00	0.03	0.35	0.04	0.52	0.44	5.00	0.44	5.00	0.44
3	0.48	0.00	0.04	0.48	0.52	0.00	0.47	5.00	0.47	5.00	0.47
4	0.50	0.00	-0.01	0.42	0.50	0.55	0.42	6.00	0.42	6.00	0.42
Set #1	0.39	0.00	0.07	0.00	0.50	0.51	0.45	-8.00	0.00	30.00	0.00

Fractal Dimension is calculated as:

$$\sum_n |S_n|^D = 1 \;, \quad D \geq 0 \quad \Rightarrow \quad S_1^D + S_2^D + S_3^D + S_4^D = 1$$

$$\Rightarrow 0.46^D + 0.44^D + 0.47^D + 0.42^D + 0.00^D = 1 \quad \xrightarrow{\;Trial - Error\;} D = 1.7254$$
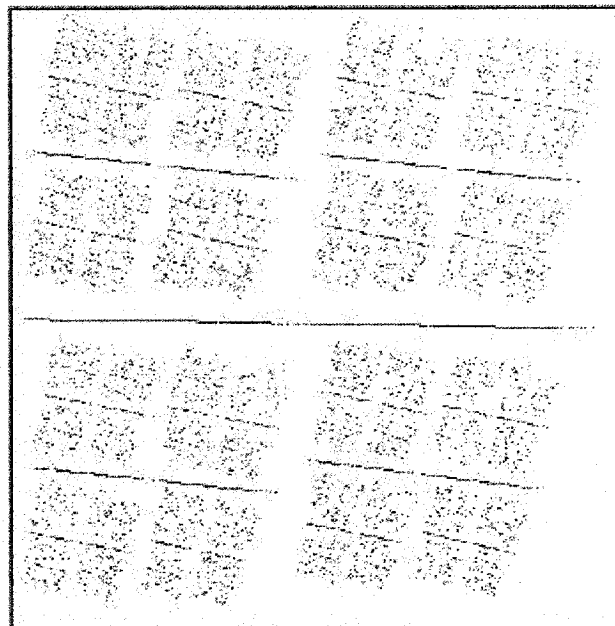
Figure 6.10 – Disconnected Fracture Set, Example

89

Another theorem approximates balls of radius ε by square boxes of edge ε:

- *Box Counting Theorem:* To evaluate whether an object is the attractor (A) of an IFS code, overlap the object by a $(2^n \times 2^n)$ grid, count the number of cells that intersect the object [N(A)]. Repeat this process with various n's and plot $Ln(N) - Ln(2^n)$ curve. If the slope of the curve remains constant and a good correlation exists, the selected object is the attractor of an iterated function system. This theorem is used to calculate fractal dimension of an object and its stability. Its application to fracture networks is explained and used in section 6.2.

This experimental theorem can be used to estimate fractal dimension of a totally-disconnected and/or just-touching object. The procedure of the box counting technique is very simple:

1. Cover image "A" by a rectangular mesh $2^n \times 2^n$ ($\varepsilon = \frac{1}{2}^n$).

2. Count the number and proportion of filled boxes [N(A,ε)].

3. Calculate $D = \dfrac{Ln(N)}{Ln(2^n)}$.

4. Change n and repeat the procedure for various n's.

5. If D remains relatively constant, the image is fractal and its fractal dimension is D.

The two examples of mathematical fractal dimension calculation are also analyzed by the box counting technique:

> Sierpinski Triangle: As shown in Figure 6.11, at $n=1$ (2×2 grid), 3 of the 4 boxes are filled. At $n=2$ (4x4 grid), 9 of the 16 boxes are filled, and at $n=k$ ($2^k \times 2^k$ grid), 3^k cells are filled. Therefore the fractal dimension is always calculated as: $D = \dfrac{Ln(3^k)}{Ln(2^k)} = 1.584962$. Fractal dimension is usually shown as the slope of the $Ln(N) - Ln(2^n)$ curve. If this slope remains relatively constant, the object is a fractal with a fractal dimension equal to the slope of this curve (Figure 6.13).

Usually, fractal objects are not as simple as Sierpinski triangle. Sometime it is difficult to identify which boxes are filled and which ones are empty. To overcome this difficulty, this study proposes to count the number of "points" in each box. The cell with maximum number of points takes number 1.0 and all other boxes are calculated as proportions of 1.

91

Mesh Size (n ➜ ε = $\frac{1}{2^n}$)	# of filled boxes (N)	Ln(2^n)	Ln(N)	Slope of Ln(N) – Ln(2^n)
1	3	0.69315	1.09861	1.58496
2	9	1.38629	2.19722	1.58496
3	27	2.07944	3.29584	1.58496
4	81	2.77259	4.39445	1.58496
5	243	3.46574	5.49306	1.58496
Fractal Dimension = Average of Slope of Ln(N) – Ln(2^n) curve:				1.58496
Variations of Fractal Dimension = Standard Deviation / Average:				0.00000

Figure 6.11 – Box Counting Method

When a computer processes an image, graphical deviations result in accounting for some points incorrectly. For example, for the graphical image of Sierpinski triangle, a Visual Basic program counted the number of points for a 2x2 (n=1) mesh (Figure 6.12.a). The 5 points in the upper right box of Figure 6.12.a are miscalculated. Some points close to the center of the box ($\frac{1}{2}$, $\frac{1}{2}$) may appear to belong to the upper right box, when analyzed by an image processor. This program identified 5 such points. The difference among the number of points in the other 3 boxes is rationalized similarly. In this case, the numbers are proportioned to the maximum number (3553) and rounded to the closest $(1/2^n)$, as shown in figure 6.12.b:
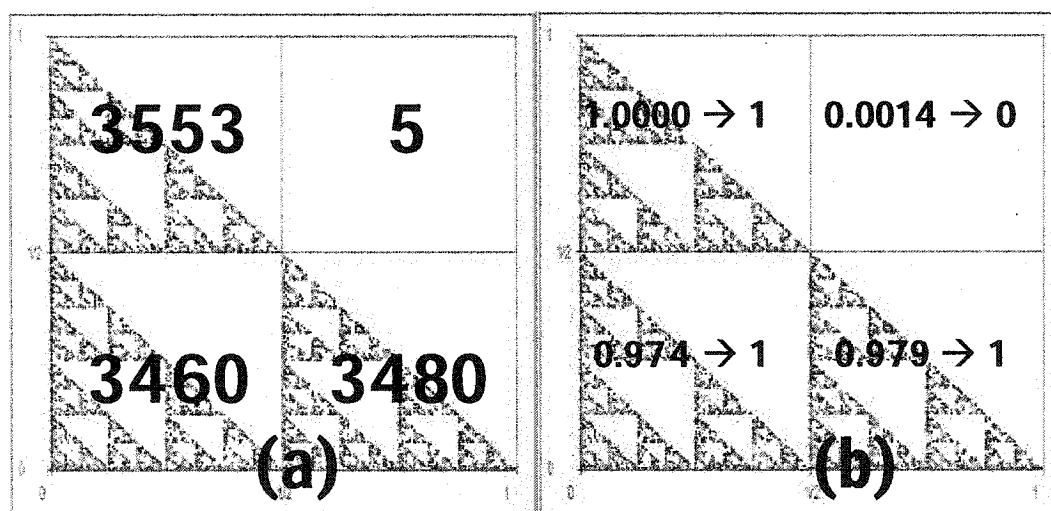
Figure 6.12 – Modified Box-Counting Technique: (a) Number of points from computer image processing, (b) Associated numbers for Box-Counting method

This results in the correct fractal dimension, with 100% accuracy. This accuracy, however, is not achieved regularly. There are usually some variations in the slope of the $Ln(N) - Ln(2^n)$ curve. The following example

93

shows a more practical application of the proposed modified box counting technique.

> > Similitude Fracture Set[9] – Box Counting Method: An image of the disconnected fracture set of Figure 6.10 was analyzed by a box counting Visual Basic program that resulted in the following values:

Mesh Size $(n \rightarrow \varepsilon = \frac{1}{2^n})$	# of filled boxes (N)	$Ln(2^n)$	$Ln(N)$	Slope of $Ln(N) - Ln(2^n)$
2	4	0.6931	1.3863	2.0000
4	12 1/4	1.3863	2.5055	1.8074
8	41 3/8	2.0794	3.7227	1.7902
16	120 1/16	2.7726	4.7880	1.7269
32	372 1/16	3.4657	5.9190	1.7079
64	993 3/4	3.4657	6.9015	1.6595
Fractal Dimension = Average of Slope of $Ln(N) - Ln(2^n)$ curve:				1.7384
Variations of Fractal Dimension = Standard Deviation / Average:				0.0349

Compared to the analytical method (1.7254) the value of D is about 0.7% more. As $Ln(N) - Ln(2^n)$ curve in Figure 6.13 shows, a very good correlation exists ($R^2 = 0.9925$). This, in addition to small variation ($\sim$3.5%), confirms stability of the fractal dimension. It is noteworthy that the value of the fractal dimension may be also estimated as the slope of the trend line. In this example, the estimated value from regression analysis (D=1.7045) is 1.2% less than the analytical estimate (D=1.7254). Other experiments

---

[9] Box counting can be also applied to a non-similitude fractal. This example is used merely to compare the results with the analytical method.

94

showed similar results. It could be concluded that average of the above two

approximations (average of D's and the slope of regression curve) provides a

more accurate estimate:

$$D_{BoxCounting} = (1.7383 + 1.7025)/2 = 1.7205 \quad \sim \quad D_{Analytical\ (Exact)} = 1.7254$$

Fractal Dimension Analysis for Similitude Fracture Set Model

$y = 1.7045x$
$R^2 = 0.9925$

Set Intercept=0

Ln[# of Filled Boxes (N)]

Ln[Grid Size (2^n)]
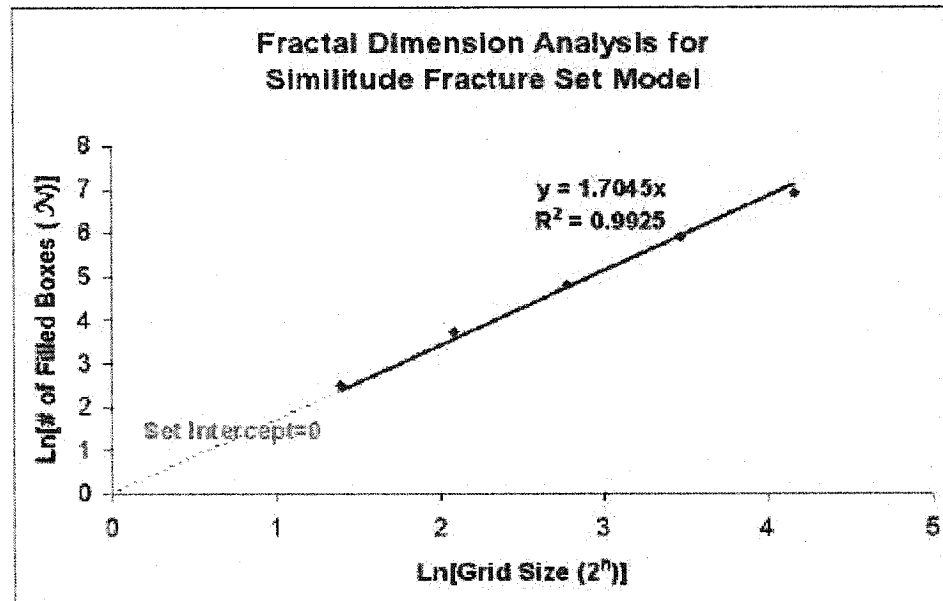
Figure 6.13 – Sample Ln(N) – Ln(2^n) Curve

In chapter 7 we will see the application of the above technique in an inverse

algorithm to: 1) estimate fractal dimension using partial image of a fractal and 2)

quantify proximity of an IFS attractor to a fractal image. One last word of caution in

using box counting technique is that for overlapping IFS's, this method

underestimates fractal dimension. In this case, fractal dimension of the attractor is

smaller than fractal dimension of the object, since graphical techniques may consider

two overlapping points as one point.

95

6.2 - CURRENT APPLICATIONS OF FRACTAL THEORY IN FRACTURED ROCK MODELING

I. Fractal Nature of Fracture Networks

It has been common to evaluate fractal nature of fracture networks using (modified) box counting. In this method, a grid of size (n) covers the image of the fracture network (outcrop). Number of fractures in each cell is considered as the level of cell occupancy and, based on that, $Ln(N) - Ln(n)$ {or $Log_{10}(N) - Log_{10}(n)$} curve is developed by changing the value of n and counting N. If the slope of this curve is relatively constant, it is concluded that the fracture network is a fractal with fractal dimension: $D = Ln(N) / Ln(n)$. La Pointe (1988) provided a good example. The number of fractures in the 3x3 mesh of the fracture network in Figure 6.14.a is provided in the 3D histogram of Figure 6.14.b. The normalized histogram, that represents the number of filled boxes is shown in Figure 6.14.c. In this case, fractal dimension is calculated as:

$$N = 15 , n = 3 \quad \Rightarrow \quad D = Log_{10}(N) / Log_{10}(n) = Log_{10}(15) / Log_{10}(3) = 2.465$$

This process was repeated for various values of (n) and the $Log_{10}(N) - Log_{10}(n)$ curve was developed as shown in Figure 6.14.d. The relatively constant slope of this curve confirmed fractal nature of the fracture pattern (D=2.48).

96
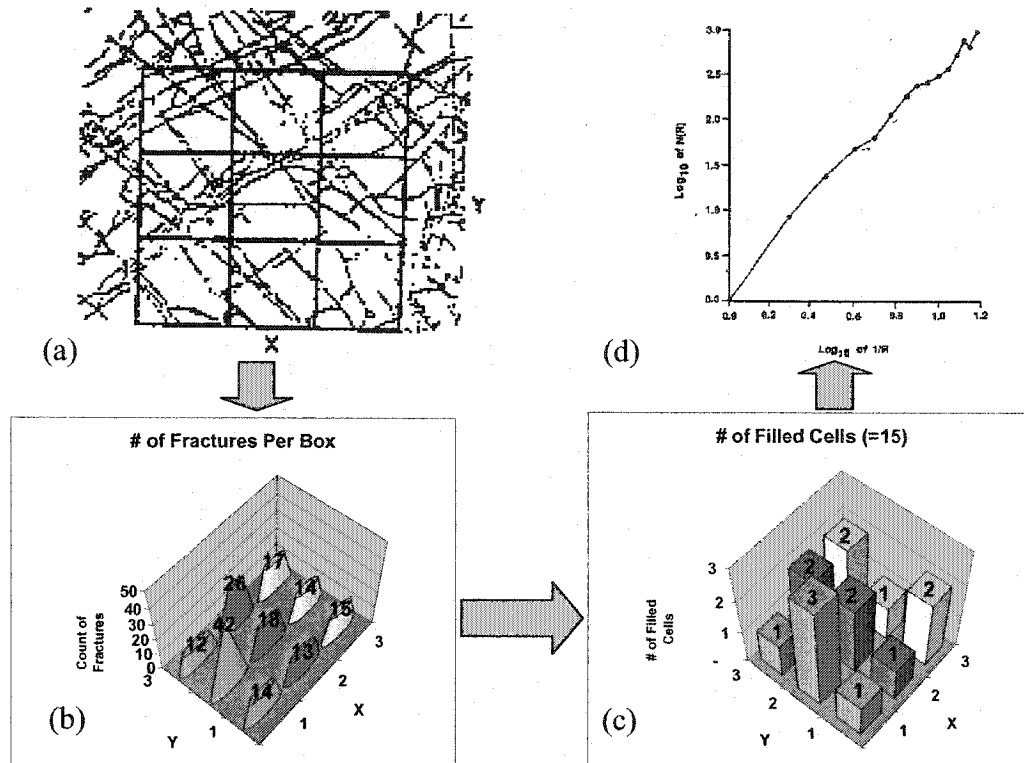
Figure 6.14 – Box Counting for Fracture Network

A big question here is why are we getting a fractal dimension larger than 2? As discussed before, D=1 represents a continuous line (–), D=2 represents a filled square (■), and D=3 represents a filled cube (▧). Therefore, a 2D fracture pattern such as Figure 6.14.a should have a fractal dimension between 1 and 2. It is not intended to overrule the above technique, but to improve it. For this purpose, the fracture network of Figure 6.14.a was scanned into computer and the modified box counting technique was applied to the "number of dots" that would cover the fractures. A preliminary test was conducted to confirm accuracy of the program. In this test, colors of the fractures (black to gray) were identified and they were filled by green dots (shown in lighter color). As Figure 6.15.a shows, the computer program identified almost all fractures. It is expected that the estimated D be just a

97

little less, since a few gray points are not identified and some points are deleted during elimination of the 3x3 grid, but this difference shouldn't be more than a few percentages. Ln(N) / Ln(n) curve for 79 grids (n=2, n=3, ..., n=80) is shown in Figure 6.15.b. The results confirm fractal behavior (D= 1.4118 and R^2 = 0.9864 ~ 1.000) for this fracture network. The conclusion by La Pointe (1981) was indeed correct. The value of D, however, was considerably overestimated.
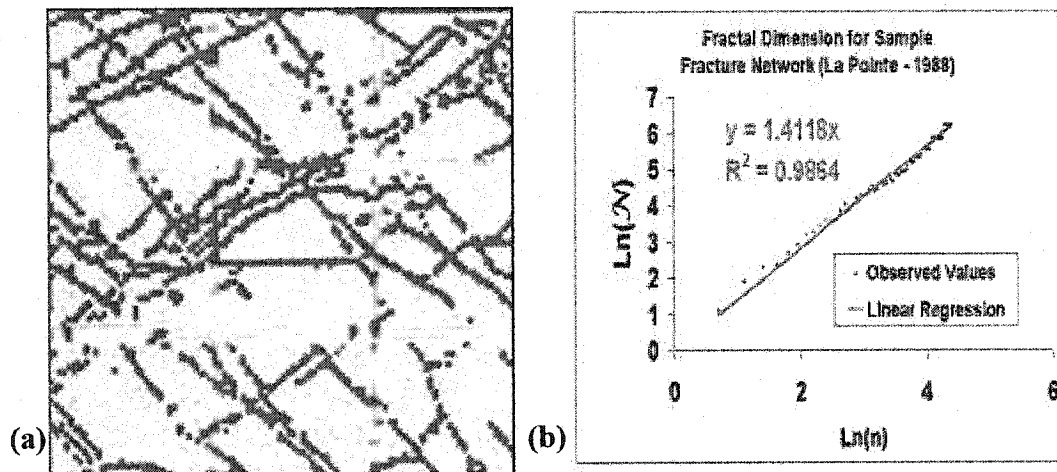
Figure 6.15 – Analysis of the fracture pattern from La Pointe (1988): (a) Fracture pattern, identified by image processing (Green/light Dots), (b) Box counting results

It is noteworthy that it may be more appropriate to analyze each fracture set individually. Intuitively, fracture sets that have different geological origins could be members of different fractal families (have different IFS Codes). If we analyze them all together, we may not be able to consider them as fractals, while they could be fractals, individually. If the fracture network of Figure 6.15.a did not have a stable fractal dimension, still it would be possible for each of the fracture sets to be fractals, with different fractal dimensions.

98

II. Fracture Parameters Estimation

Various fracture parameters are evaluated and shown to have fractal behavior. Burrough (1981) showed that fractal dimension of a fracture pattern can be calculated from its variogram. Variogram (or semi-variogram) is a geostatistical technique that relates the average squared difference in orientation to the separation distance (Hudson et al. 1993).

With information on a few points of a fracture surface profile, fractal interpolation can be used to simulate fracture surface and Joint Roughness Characteristic (JRC) can be estimated based on fractal dimension. There are still limitations associated with this technique as explained by Hudson et al. (1993):

1. JRC reference curves (figure 3.1) are Euclidian lines and non-fractal. Fractal dimension of such a curve and the associated fractal interpolation should be 1.0.

2. The resolution of fracture surface image on paper is much coarser than the finest jaggedness of the actual joint. Fractal dimension cannot be estimated accurately.

3. In general, as we saw in the box counting examples, fractal dimension cannot be estimated at the high level of accuracy that is needed for fracture surface profile.

99

Cantor sets have been used to simulate spacing values for a fracture set. For example, $IFS = \{\Re, w\,(x) = \tfrac{1}{2}x, w_2(x) = \tfrac{3}{4}x + \tfrac{1}{4}\}$ results in the joint set of Figure 6.16.a, in one run. It is noteworthy that another run may result in another configuration such as 6.16.b. These two joint sets have different statistical (and therefore hydraulic) properties. This is due to the very small number of iterations (100).
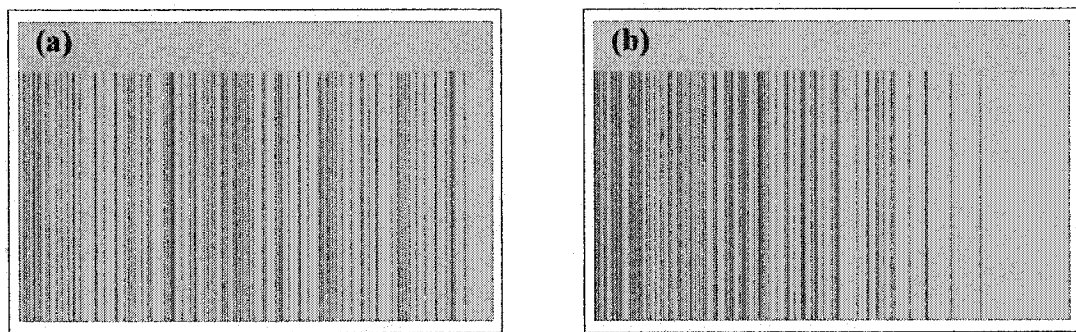
Figure 6.16 – Two alternative joints spacing distribution from one fractal model
with small number of iteration (100).

One important lesson can be learned from fractals. At very large number of iterations, when an attractor becomes stable, there is always an iterated function system that could produce a given statistical distribution that remains relatively stable at various runs. Figure 6.17 shows a good examples. The attractor of:

$$IFS = \{\Re, w\,(x) = 0.6x, w_2(x) = 0.5x + 0.3, w_3(x) = 0.4x + 0.22, w_4(x) = 0.4x + 0.14, w_5(x) = 0.5x + 0.19\}$$

was arbitrarily found to have a Normal distribution. Kolmogorov-Smirnov test accepts the hypothesis that the data distribution is Normal (K-S value = 0.0099 < K-S$_{(\alpha=0.01)}$ = 0.011), for 20,000 iterations and average of 1000 runs. It was also found that various simulations result on very similar (Normal) distributions, 95% of which being accepted by K-S test (the 5% rejections were marginal).

100

**Sample Fractal Model Histogram
Versus Normal Distribution**
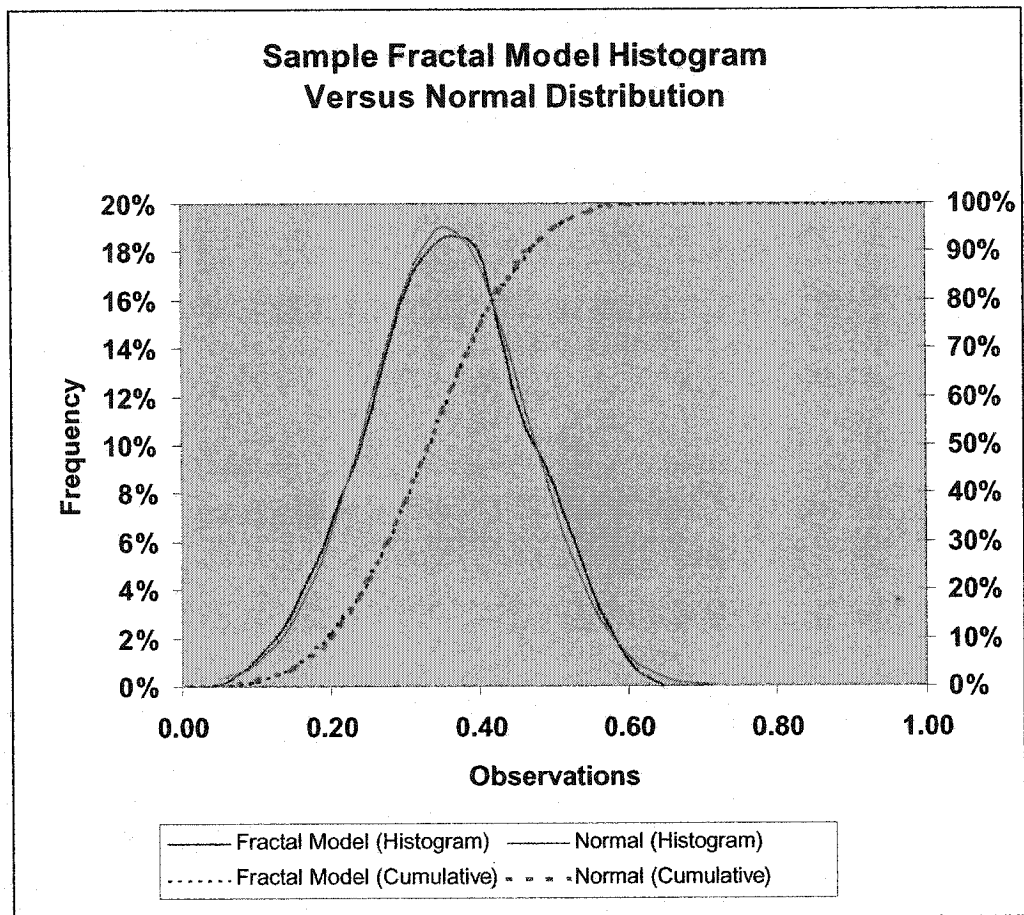
Figure 6.17 – A Normally Distributed Fractal Model

This example concludes that we can find an iterated function system that <u>always</u> produces a pattern with desired statistical distribution. The purpose of this discussion is to emphasize on the fact that statistical distributions are better <u>not</u> to be used as the "start point" in the process of rock characterization, but as a "verification tool" for fractal models.

101

III. Hydrologic Inversion

Let's forget about fractures characteristics for a minute. Would it be possible to identify flow characteristics of a rock medium using limited well-test data? This is a question that has been answered by "hydrological inversion". A trial-error inversion algorithm looks for an arbitrary fracture network that would produce the observed well-test values (Rock Fractures and Fluid Flow (1996) – P. 373), without going through any significant fracture network characterization.

An emerging concept in this field is the application of fractal theory to develop hypothetical fracture networks. An inverse algorithm looks for an iterated function system that produces a fracture pattern whose hydraulic properties agree with well test data. Self-similarity nature of this model can be used to extrapolate hydraulic properties of small test scale to large filed scale.

Acuna (1993) provided a good discussion on hydrological inversion and its algorithm. A brief overview of that work is provided here, in order to be compared with the current work and understand their similarities and differences:

Iterated function system (IFS) can be used to simulate the fragmentation process that is observed is fractured media. This work was motivated by the notion that:

"The necessary geometric and transport properties of a network of fractures to produce a particular well response remains a poorly understood topic. Is in this area where fractal geometry offers a theoretical frame to relate a large variety of pressure

102

transient responses to the geometric and dynamical properties of network of fractures".

Acuna included XY term in the IFS transformations to facilitate generating curvilinear fracture networks and applied these IFS codes to an "initial fracture". Figure 6.18 is an example fractal network of fractures. The number of largest fragments would equal to

the number of transformation and the study considered models with two transformations, only. A statistical distribution function for number of fragments was derived and, based on that, fractal dimension was calculated as a function of number of fragments and possibility of fracturing.
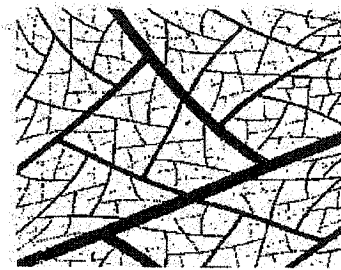
Figure 6.18 –Sample Fracture pattern from Acuna (1993)

Since each generation of fractures provides information on the next generation, Properties of the fracture network (number, size, and connectivity) are known, after a given number of iterations: "A network made with 2 transformations and n generations has $2^{n+1}-1$ fractures, including the original fracture". Acuna also proposed to systematically eliminate a proportion of fractures at some iterations, in order to control intact regions of the media, at a desired level. In the Sierpinski triangle of Figure 6.19, 25% of the fractures are eliminated, at the last two iterations.

103
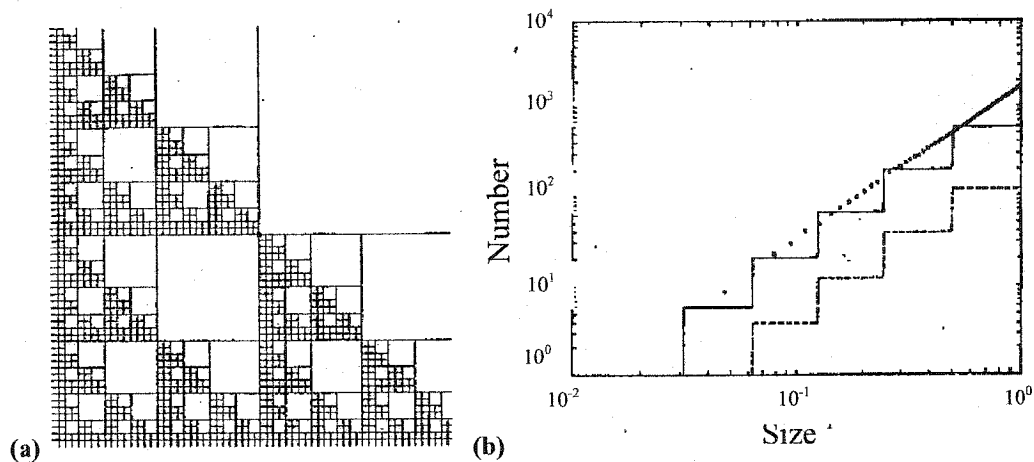
Figure 6.19 – (a) Modified Sierpinski Triangle (11 generation). (b) Box Counting (dot), Fracture Length (solid line), and Fragment Size (dashed line) Distributions. [From Acuna (1993)]

The above model was then linked to the conventional unsteady state transient flow model and a relation was developed between porosity at radius (r) from a well center and fractal dimension (D), size of the smallest fracture (r_0), and radius (r): $\phi(r) = \phi_0(r/r_0)^{D-d}$, where ϕ_0 = Constant. A similar relation was derived for permeability (K). Sierpinski triangle was used as the hypothetical fractured medium. Pressure transient response was simulated and various parameters (number of iterations, cut-off limit, Location of the well) were altered to conduct sensitivity analyses. Figure 6.20 shows one of these analyses as an example. It was observed that:

1. "More generations of fractures allows longer and clearer fractal pressure transient response" and "the boundary effects are felt sooner in the network with less generations".

2. "From the study of the cut-off sizes effects, it became clear that what actually controls the fractal behavior of a system is the separation between the upper

104

and lower cut-off sizes". Also "equally important is the presence of non-fractal features in the network that affect the pressure transient response".

3. Pressure response is also subject to properties of the fractures that are directly connected to the well. It was shown that changing location of the well influences pressure response of the system. "In deed, at early times, the higher value of the slope of pressure response [for the well not on the center] shows the fact that only a few long fractures are reaching the well".
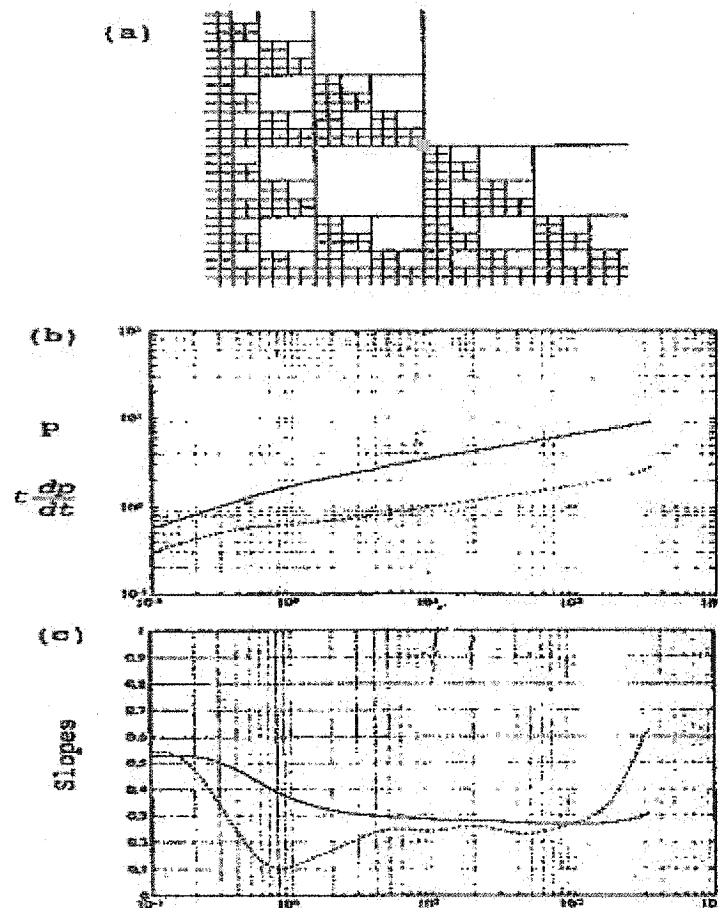
Figure 6.20 – (a) Modified Sierpinski Gasket (9 generations) with well position shown by small square. (b) Pressure transient response as pressure (solid) and pressure derivative (dashed). (c) Slope of curves.
[From Acuna (1993)]

105

The above results were used to interpret actual well test data. It is assumed that, in naturally fractured reservoirs, wells are connected to large networks of fractures that are dominant flow pathways. Based on well test observations, fractal dimension is back-calculated and a fractal network of fractures is hypothesized that would result in similar pressure transient response. Figure 6.21.b is an arbitrary fracture network that could produce the pressure response matching the well test result of Figure 6.21.a. The selected fracture network is only "one of infinite many possibilities", one of which may be even better than this one. There is no evidence that this model is similar to the actual geometry of the real network of fractures.
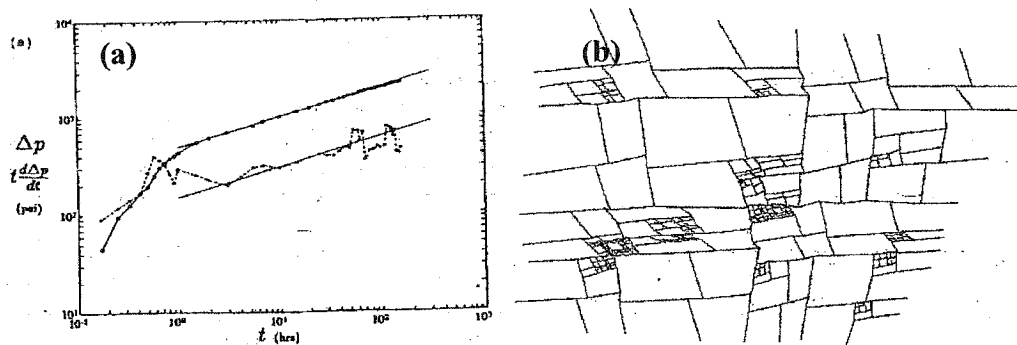
Figure 6.21 – (a) Well Drawdown for Pressure Transient test. (b) An Arbitrary Fractal Network of Fractures that Could Produce Pressure Response such as (a). [From Acuna (1993)]

Acuna concluded that, based on his fractal model, the classical transient flow model is, in general, acceptable. Also, large fracture networks are modeled better than small networks, using the proposed fractal concept. Fractal model, of the above form, offers a good alternative to other hydrological inversion methods, for naturally fractured rocks.

106

"The most important feature that distinguishes this study from conventional random methods is its ability to create geometrically complex networks in two and three dimensions by manipulating only a few parameters [fractal parameters]."

The fractal model proposed by Acuna (1993) and, in general, hydrologic inversion technique, provide good estimate of flow properties, based on limited well test results. These methods, however, have some limitations that could be overcome using an alternative fractal model, such as the one proposed in this study:

- An artificial fracture network developed by the above model is not necessarily the actual network. We may be able to get a fractal network to have the same pressure response as the observed values in specific well locations, there is no guarantee that overall hydraulic properties of the site are modeled accurately.

- Acuna's model is based on the assumption that rocks are well-fragmented. All fractures are connected to each other and contribute to flow. In reality there are many dead-end fractures that do not contribute to flow and fragments are not as organized as we see in Accuna's examples.

- According to the author, "Observation wells data are too site dependent to allow an unambiguous determination of fractal parameters".

- Since the initiator is a line (as apposed to a point), fracture roughness cannot be simulated in this technique.

107

- Since the model is developed based on "probability of fracturing", it is ultimately a statistical model and possesses statistical models limitations.

- As we discussed in section 6.2 – part I, two intersecting fracture sets may appear not to be fractal, but each could belong to a separate fractal family. Fracture sets cannot be analyzed separately, using Acuna's model.

- The model was not successful in simulating small scale fracture network. It was shown that it is more appropriate for large scale problems.

- Most of the well-test examples were based on Sierpinski triangle, or well-fragmented networks. It was acknowledged that additional arbitration of the networks (more realistic networks) result in "some additional problems regarding finite size effect".

This study attempts to develop a model in which the above limitations are addressed and eliminated. Fractal concepts and mathematics that are used in hydrologic inversion models, such as Acuna (1993), have a great potential to be combined with the proposed model in chapter 7 for improvement. For example, the modified iterated function system by Acuna (1993) could be used to simulate curvilinear fractures. Once the model is completely developed (as explained in chapter 7), any fracture pattern such as the ones by Acuna (1993) can be analyzed.

IV. Percolation Theory

Percolation theory is a statistical/fractal technique that provides a universal law that determines geometrical and physical properties of a system. Percolation is the process of fluid flow in a random medium and it is a measure of system connectivity. It was originally intended for porous media and later it was applied to fractured rocks, as well.

Percolation theory consists of numerous definitions such as percolation threshold, correlation length, cluster size and number of clusters, percolating cluster, accessible fraction and backbone fractures, and many more. Going through all these definitions and the complicated mathematics behind percolation theory is outside the scope of this work and does not serve any purpose for this study. We intend to proved a short description of percolation concept and study its possible applications in this work.

Percolation threshold is the fundamental concept of fractal theory. It is defined as the "*largest* fraction of occupied bonds below which there is no sample-spanning cluster of occupied bonds" [Sahimi (1994) – page 11]. In other words, in terms of number of clogged segments, it is the minimum number below which there is no fluid transmission (percolation). Percolation threshold has been estimated for various configurations. For example, it has been shown that for square networks (Figure 6.22), percolation threshold is 0.5927 for site percolation and 0.50 for bond percolation. That means, at least 50% of the bonds in Figure 6.22 must be open to

109

flow in order for fluid to be transmitted from left to right. In Figure 6.22.a 52.44% of the sites are open. and fluid can flow from left to right through one or more percolation clusters (blue/dark is one of them). In Figure 6.22.b only 44.44% of the segments are open and fluid cannot percolate from left to right.

(a)   **(b)**
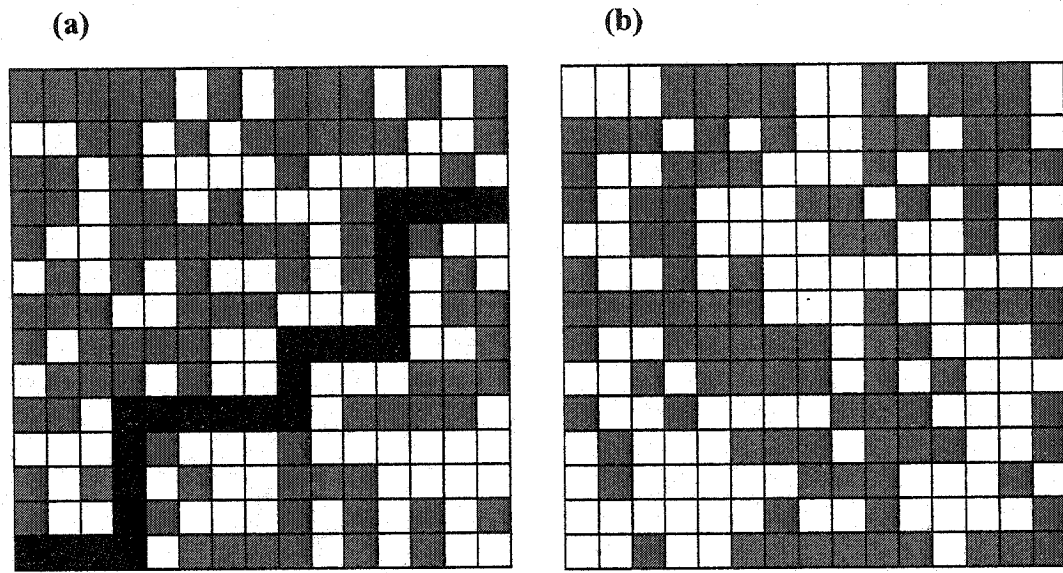
Figure 6.22 – Percolation Threshold: (a) Above Threshold (P=52.44% > P_c=50%), percolation occurs through percolation cluster (blue). (b) Below percolation threshold (P=44.44% < P_c=50%), no percolation occurs.

In percolation theory, all system parameters follow scaling laws and are of the form: $f(p) = (p - p_c)^\alpha$ where $f(p)$ is a system parameter and α is a constant which is *universal* (at least at some range). Universality means that these constants are independent from the system configuration. For example, Balberg (1987) used number of unclogged segments (N) instead of probability (P) and showed that volumetric water flow can be calculated as: $Q \propto (N - N_c)^\kappa$, where κ is independent from system configuration and complexity. Further, Berkowitz and Balberg (1993)

110

showed that system permeability can be modeled by: $K \propto (N/N_C - 1)^\alpha$. It was found that $\alpha=1.3$ for 2D and $\alpha=2.0$ for 3D.

At scales smaller than correlation length, a percolating system is heterogeneous and the sample-spanning (infinite) cluster is a fractal – it looks the same at all scales smaller than correlation length. Fractal dimension of the infinite cluster can be used to estimate various percolation constants. For example, Berkowitz and Balberg (1993) calculated a fractal dimension of 0.834 for a model of semi-rectangular boxes, separated at correlation length. Permeability of each box was modeled by: $K_\xi = K_0(P-P_c)^\zeta$, where ζ was estimated as $\zeta=D.\nu$ and for 2D: $\nu = 4/3$ and $D=0.834$ (above) therefore $\zeta= 1.11$.

Percolation theory is widely used in petroleum industry and is proven to be a good tool to predict fluids flow and transport behavior at macroscopic scale. This technique is ultimately a statistical approach and, once again, does not provide any information on the fracture system and microscopic flow behavior. In fact, due to universality of percolation theory, system configuration does not come into calculations.

While the concept of percolation, in general, is not much applicable to this study, a good use of "percolating cluster" was identified that will be explained in chapter 7.

6.3 - INTRODUCTION TO A NEW APPROACH FOR FRACTURE NETWORK CHARACTERIZATION

From what we learned about fractals, and fractal nature of fracture networks, it is quite possible to simulate a fracture network that realistically represents site characteristics, using fractal theory. All we need to do is to find the correct iterated function system. One that takes limited observations from site investigations and extrapolates them to develop the entire fracture network. If this goal is achieved, the next task would be to characterize flow behavior of such a fractal network of fractures.

The next chapter introduces a model with the above characteristics. Basic concepts and theorems of fractal are used to develop models and algorithms to simulate a fracture network, based on field observations. This network is not a hypothetical network, like the ones used in hydrologic inversion or in percolation models and it is not a random network. The proposed fracture network is aimed to be the most accurate one, the one that really exists in the field. The level of accuracy depends on the amount of available information and presence of a fractal nature in the system of fractures.

Noting that rock permeability is ultimately resulted from pores configuration, it can be assumed that fractures could be modeled as "collections of tiny pores" that are

112

configured in an apparently clustered pattern such as Figure 6.23. At the location of fractures, these pores get so close to each other that they form continuous lines. At microscopic scale, these lines are not straight lines, but corrugated lines whose grooves are defined by fracture roughness (JRC). These features can be simulated using fractal dots. In addition, matrix permeability could be accounted for, if the right IFS codes are selected. These simulated dotes are the backbone of the rock permeability tensor, at small scale. A finite difference program (such as $FLAC^{2D}$) can be used to model the complete system.
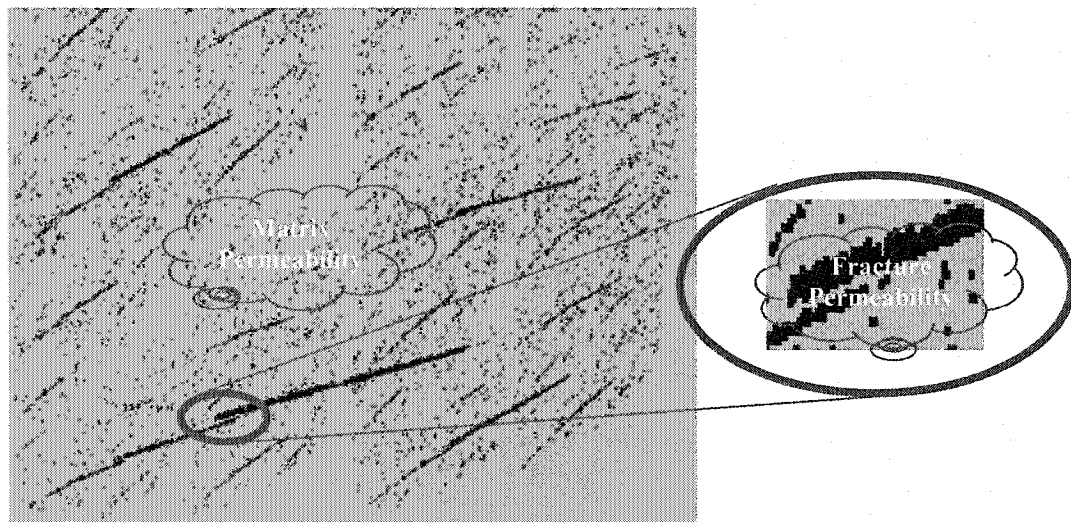
Figure 6.23 – Fractures are collections of tiny pores that are configures in a certain way. This perspective can help to account for fracture surface roughness.

113

CHAPTER 7 - A NEW APPROACH TO FRACTURE NETWORK AND FLOW MODELING USING FRACTAL THEORY

7.1 - FRACTAL BASED FRACTURE MODEL

I. Construction of Fractal Network of Fractures

Assuming that a fracture set has fractal behavior, iterated function system (IFS) with condensation can be used to simulate that fracture set. In this study we formalize this system in the following format (Figure 7.1):

Define IFS Codes

w	a	b	c	d	e	f	θ1	r1	θ2	r2
1	0.48	0.00	0.00	0.48	0.01	0.01	0.00	0.48	0.00	0.48
2	0.48	0.00	0.00	0.48	0.01	0.51	0.00	0.48	0.00	0.48
3	0.48	0.00	0.00	0.48	0.51	0.01	0.00	0.48	0.00	0.48
4	0.48	0.00	0.00	0.48	0.51	0.51	0.00	0.48	0.00	0.48
5	0.35	0.00	0.61	0.02	0.30	0.30	60.00	0.70	0.00	0.02
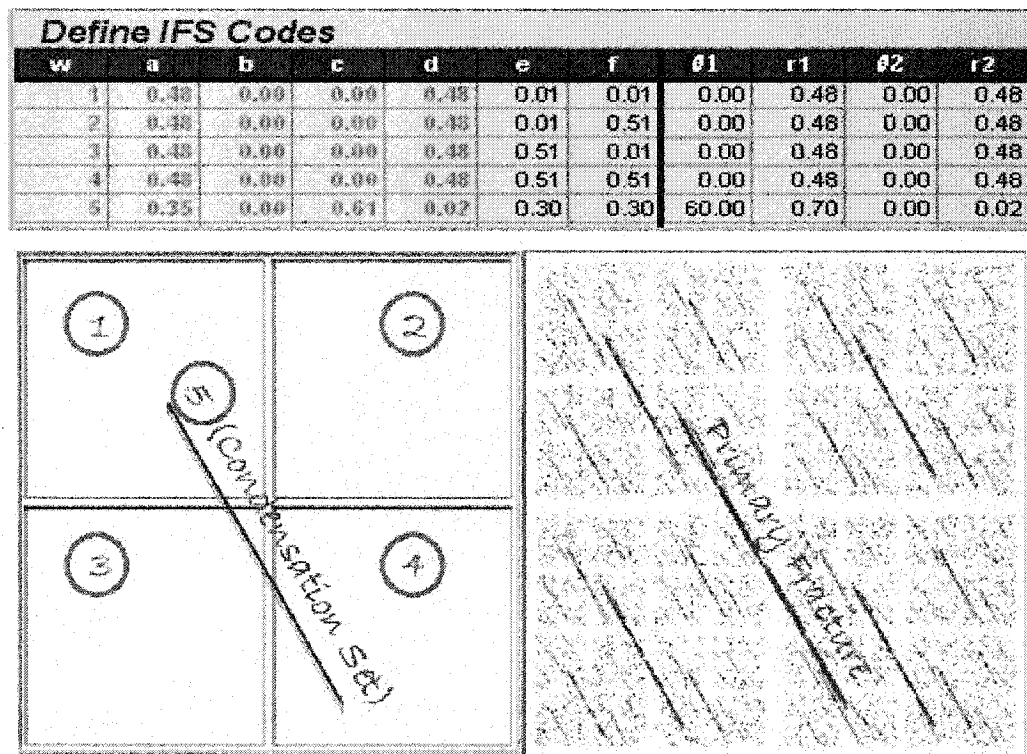
Figure 7.1 – Condensation Set and a "Perfect" Fracture Set

114

The first 4 transformations build the background and define properties of the fracture set, as a group. We call these "background sets". The last transformation is a condensation set that is defined based on the properties of the initial (primary) fracture. Initial fracture is the largest fracture in the system and copies on the map of the "condensation set".

The 4 background sets can be altered to generate alternative fracture networks, all based on the same initial fracture. If they are perfect squares (0.5x0.5) with no rotation and/or overlapping, the fracture set is a perfect set whose fractures are exactly parallel. At every iteration, 4 new fractures half the size of each previous fracture are copied at the center of the previous square. This doesn't do any good for us! Fracture sets are not so perfect in real world. They look more like Figure 7.2 in which the background sets are altered from (0.5x0.5) squares to arbitrary parallelograms. The properties of the fracture set obey the parameters of the first 4 transformations, as well as the condensation set.

There are many other ways to simulate fractured media using iterated function systems. One alternative is manipulating transformations probabilities (Figure 6.3). Figure 7.3 shows another alternative that could be used to simulate a single fault, for example. In this study, for simplicity, we only apply the above model (Figures 7.1 and 7.2). This simplification, however, does not limit applicability of the other models.

115

Define IFS Codes

w	a	b	c	d	e	f	θ1	r1	θ2	r2
1	0.48	0.00	0.13	0.50	0.00	-0.10	15.00	0.50	0.00	0.50
2	0.60	0.00	0.05	0.48	0.00	0.50	5.00	0.60	0.00	0.48
3	0.49	0.00	-0.09	0.60	0.50	0.00	-10.00	0.50	0.00	0.60
4	0.50	0.00	-0.04	0.40	0.60	0.60	-5.00	0.50	0.00	0.40
5	0.35	0.00	0.61	0.02	0.30	0.30	60.00	0.70	0.00	0.02
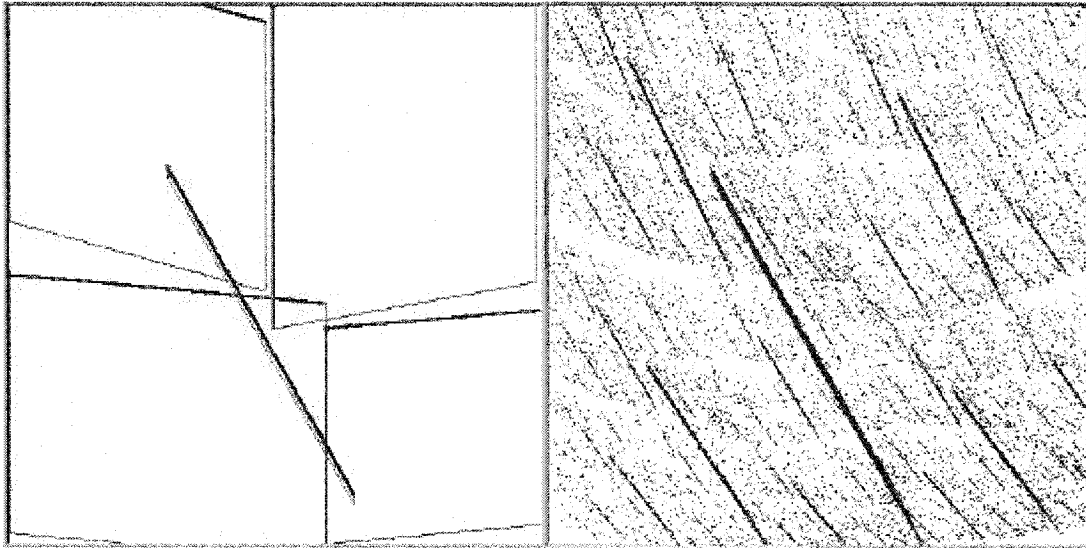
Figure 7.2 – A "Realistic" Fracture Set
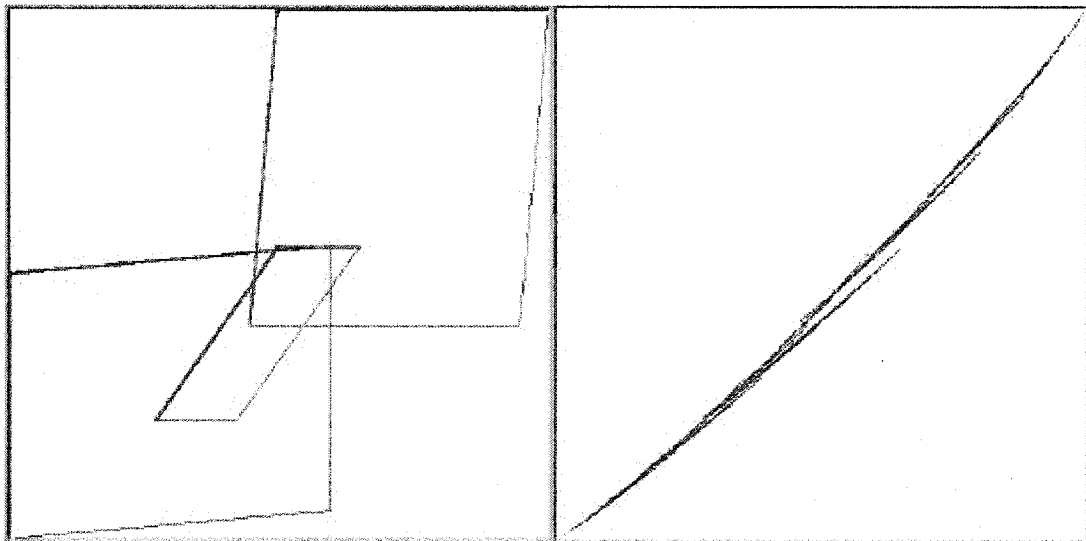
Figure 7.3 – Simulation of a Single Fault using 3 Transformations

116

It is important to note the relations between fracture network parameters. Despite conventional statistical models, a fractal model of the above form takes into account dependence of one parameter to the others. Fractures spatial distribution, length, orientation, aperture, and surface roughness, all depend on one set of parameters: the IFS codes. As a simple example, lets generalize the example discussed in Figure 6.5. A transformation of the form $\begin{bmatrix} \alpha & 0 \\ 0 & \alpha \end{bmatrix} \left\{ \begin{bmatrix} \beta \\ \gamma \end{bmatrix} \right\}$ is applied to a vertical fracture at origin. It can be shown mathematically that at iteration i, the fracture is α^i smaller than the original fracture and it is moved to: $\dfrac{1-\alpha^i}{1-\alpha} \begin{bmatrix} \beta \\ \gamma \end{bmatrix}$. In other words, there is a direct relationship between fractures size and their spacing:

$Spacing = f(Size, \alpha, \beta, \gamma)$

II. Forward Algorithm

Chapter 6 introduced two classical algorithms to create fractal images; deterministic algorithm and random iteration algorithm. In the forward simulation (i.e. generation of a fractal image from a given set of IFS codes), random iteration algorithm is appropriate, without any modification.

A deterministic algorithm is also needed to validate the outcome of the flow model (Chapter 8). The classical deterministic algorithm was found not to be quite sufficient and it was modified as follows:

117
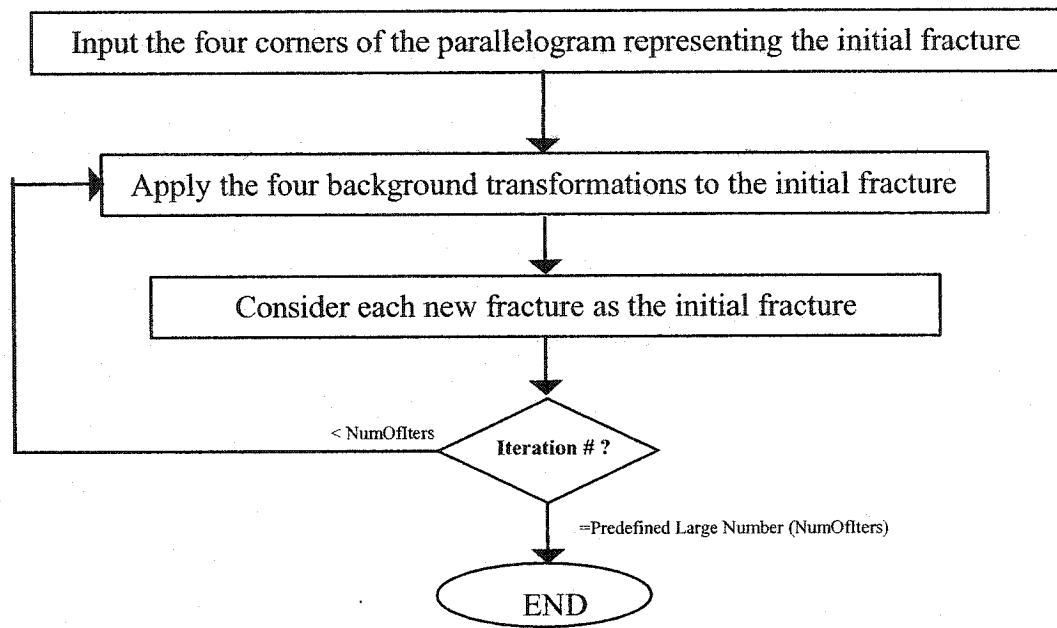
Figure 7.4.b shows the result of applying this algorithm to the fracture set of Figure 7.4.a. This model is developed only to study statistical distribution of parameters and evaluate flow simulation results compared to the classical equivalent continuum flow model. It does not provide any additional information.
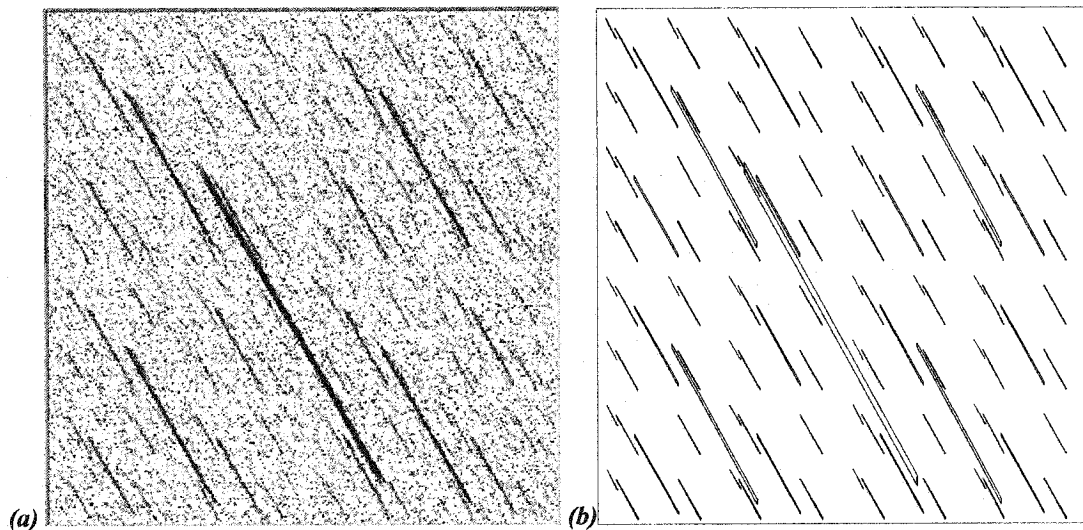
Figure 7.4 – (a) A Sample Fracture set using Random Iteration Algorithm.
(b) Same Fracture Set, using Deterministic Algorithm.

118

III. Reverse Algorithm

In order to find an iterated function system whose attractor is close to a given (partial) image, a reverse algorithm is needed. It has been a practical challenge to find appropriate IFS codes for an image and still there is no numerical model that could achieve this goal. Based on the collage theorem, however, it is possible to analyze an image and identify its IFS codes, approximately. Some Images that can be modeled using disconnected and/or just-touching IFS are easy to analyze. Figure 6.3.a in Chapter 6 was a good example. But this is more an exception than a rule. We need an algorithm that could be applied to a wider range of fractal images, specifically (partial) fractal network of fractures.

To develop such an algorithm, we need to look at the process of creating a fractal image. We start with the deterministic algorithm, which provides a good understanding of this process. Assume we have n transformations $(w_1, w_2, w_3, \ldots, w_n)$. At the first iteration, n copies of the original image (A) are created $\{w_1(A), w_2(A), w_3(A), \ldots, w_n(A)\}$. Based on the collage theorem, the union of these n images equals the original image. Therefore, if the image boundaries are approximated by a polygon P_0 with m corners, the n copies of P_0 should also approximate the fractal image segments boundaries, in the same manner. If the number of transformations (n) is correct, the union of images of P_0 should also cover the boundaries of the overall image (i.e. P_0).

119

Let's name the n copies of P_0 at iteration ① as $P_1^{①}, P_2^{①}, P_3^{①}, ..., P_n^{①}$. The relation

between $P_i^{①}$ and P_0 is clear: $P_i^{①} = w_i(P_0)$.

For each (background) transformation, w_i has 6 unknowns $(a_i, b_i, c_i, d_i, e_i, f_i)$, or in

polar coordinates: $(\rho_{1i}, \theta_{1i}, \rho_{2i}, \theta_{2i}, e_i, f_i)$. Therefore we need 6 equations to

identify these parameters. P_0 and $P_i^{①}$ can be described as:

$$P_0 = \{C; (x_1, y_1), (x_2, y_2), (x_3, y_3), ..., (x_m, y_m)\} \quad ; \quad P_i^{①} = \{C; (x_{1i}^{①}, y_{1i}^{①}), (x_{2i}^{①}, y_{2i}^{①}), (x_{3i}^{①}, y_{3i}^{①}), ..., (x_{mi}^{①}, y_{mi}^{①})\}$$

where, $(x_{ki}^{①}, y_{ki}^{①}) =$ node k of polygon i in Cartesian plane xy

The relation between P_0 and $P_{i}^{(1)}$ can be organized as the following matrix relation:

$$T' \rightarrow \begin{bmatrix} x_1 & y_1 & 0 & 0 & 1 & 0 \\ 0 & 0 & x_1 & y_1 & 0 & 1 \\ x_2 & y_2 & 0 & 0 & 1 & 0 \\ 0 & 0 & x_2 & y_2 & 0 & 1 \\ x_3 & y_3 & 0 & 0 & 1 & 0 \\ 0 & 0 & x_3 & y_3 & 0 & 1 \\ \vdots & \vdots & \vdots & \vdots & \vdots & \vdots \\ \vdots & \vdots & \vdots & \vdots & \vdots & \vdots \\ x_m & y_m & 0 & 0 & 1 & 0 \\ 0 & 0 & x_m & y_m & 0 & 1 \end{bmatrix} \times \begin{Bmatrix} a_i \\ b_i \\ c_i \\ d_i \\ e_i \\ f_i \end{Bmatrix} = X' \rightarrow \begin{Bmatrix} x_{1i}^{①} \\ y_{1i}^{①} \\ x_{2i}^{①} \\ y_{2i}^{①} \\ x_{3i}^{①} \\ y_{3i}^{①} \\ \vdots \\ x_{mi}^{①} \\ x_{mi}^{①} \end{Bmatrix}$$

$$(7.1) \qquad T^{①} \qquad \times \quad IFS_i = X_i^{①}$$

Therefore, IFS_i can be calculated using 6 of the above equations. In other words, If

we have coordinates of three corners of polygon P_0 and the corresponding three

corners of the polygon $P_i^{①}$, we can derive IFS_i:

120

$$(7.2) \qquad IFS_i = \left[T'^{\text{\textcircled{1}}}\right]^{-1}_{6 \times 6} \times \left\{X_i'^{\text{\textcircled{1}}}\right\}_{6 \times 1}$$

Equation 7.2 is the basis of the inverse algorithm that is developed for this study and explained below:

1. Consider an image that is expected to have fractal behavior (Figure 7.5.a)

2. Draw a polygon that defines a specific characteristic of the image (for example its boundary or an outstanding feature of the image) (P_0 in Figure 7.5.b)

3. Try to find three corners of a copy of this polygon (copy i) scaled down, rotated, and/or sheared (e.g. $i = 1 \Rightarrow P_1$ in Figure 7.3.b).

4. Use equation (7.2) to find IFS_1 based on the first three corners of P_0 and P_1.

5. Apply IFS_1 to equation (7.1) to find coordinates of other corners of P_1

6. If P_1 appears to be close to the boundaries of a portion of P_0, alter coordinates of its corners and go back to 4 to optimize P_1 or go to 7 if the proximity is acceptable, otherwise go back to 3 for the same i.

7. Increment i and go back to 3. Repeat until the entire image is covered by the transformations $(1,2,3,\ldots,i = n)$.

121
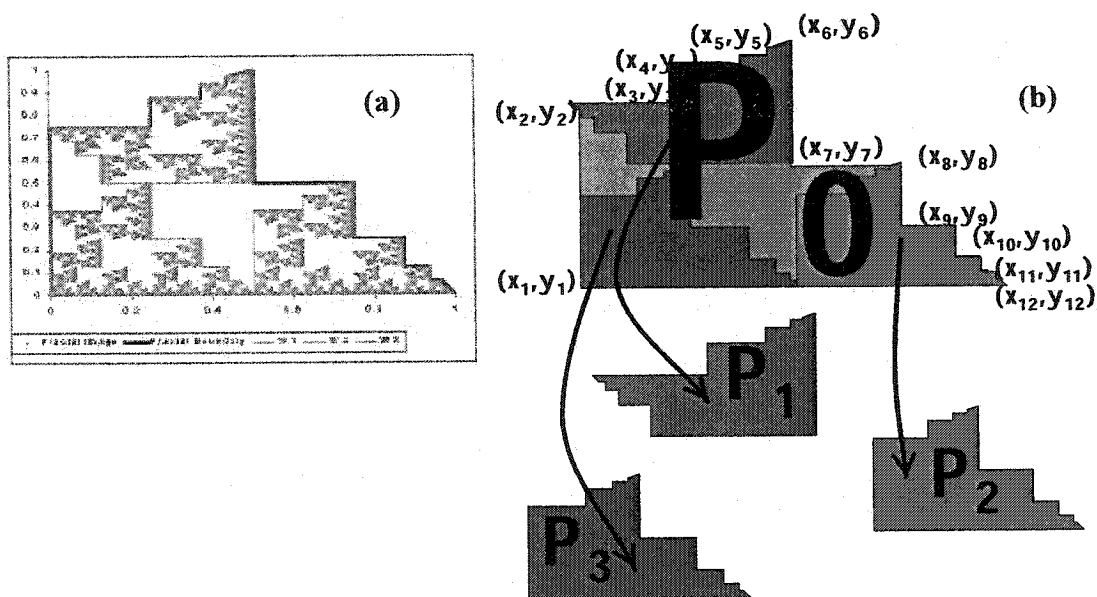
Figure 7.5 – Application of Fractal Inverse Algorithm (b) to a Fractal Image (a)

Using the above inverse algorithm in a computer program, the appropriate IFS codes can be found after just a few trials. The implementation of this algorithm in a graphical computer program will be explained in part V of this section.

In the case that a complete image of the fractal object is not available, the outstanding features of the image can be used, instead of its boundary. This becomes particularly important when we try to complete a fracture network based on limited borehole data from site investigations. An example of this case is also provided in part V of this section.

122

IV. Validation of Iterated Function System for a (Partial) Fractal Image

An iterated function system that is developed by the above inverse algorithm can be as accurate as eyes can see. In order to quantify proximity of an IFS attractor to a given image and improve it, a measure of comparison is needed, a single value that describes fractal properties of the two images and compares them.

Figure 7.6.a shows a fractal image in red/light color (it is a fractal image, for fact). The proposed inverse algorithm was implemented and the attractor of an "approximate" iterated function system is shown in blue/dark color (with some intentional error). Figure 7.6.b shows the same image overlapped by the attractor of another IFS, which is also "close" to the original image. But which one is a better model? How "close" are they to the image and which one is "closer"?
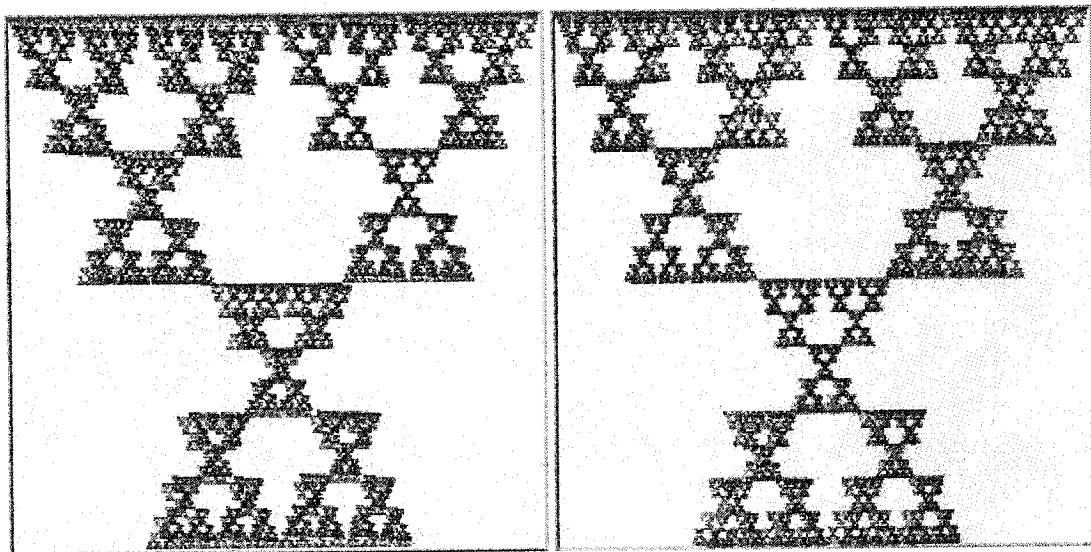
Figure 7.6 – Two Erroneous Attractors (blue/dark) for a Fractal Image (red/light).
Which one is better?

123

Barnsley (1993) used collage algorithm and quantified this "proximity" by Harsdorff metric, a value that shows the average distance between an image and its attractor. Though, determination of this value is very difficult and requires a lengthy process to measure the distance of every point on the attractor from every point on the image. Noting that some fractal images have hundreds of thousands of points, this would be a tedious process and would require extensive computations.

In Chapter 6 we introduced a simpler measure for fractals; fractal dimension. A real number between 0 and 3 that indicates how well a fractal image covers the Euclidian space. Fractal dimension is a simple tool that can be used to compare two fractal images, although it is not as accurate as Harsdorff metric. Two images that are totally different may have the same fractal dimensions (Figure 7.7). This limitation, however, is not a major factor in this work. It is almost impossible to find an iterated function system that has an attractor close to a given image and has the correct fractal dimension, but is a wrong one.
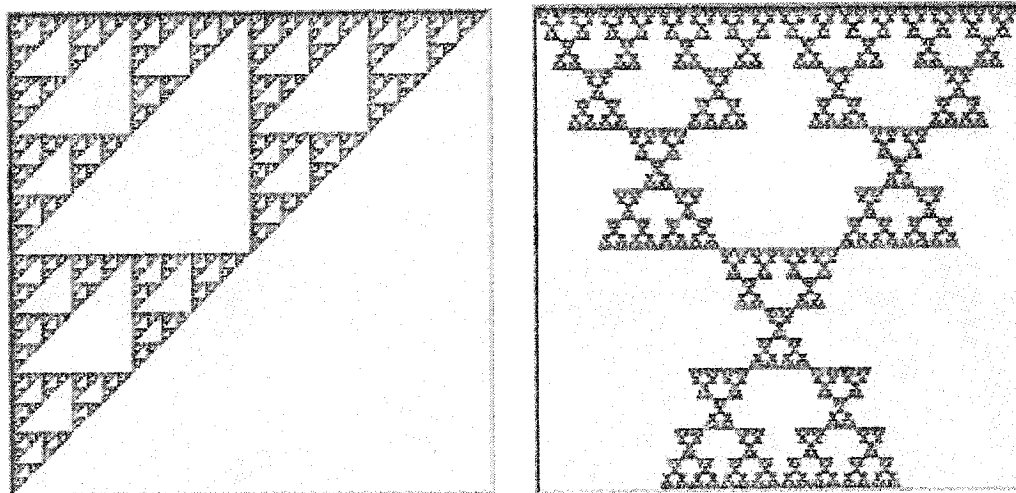
Figure 7.7 – Two Different Fractal Objects with the Same Fractal Dimensions (D=1.5849)

124

Fractal dimension of images that are created using random iteration algorithm can be estimated using the modified box counting technique, introduced in Chapter 6. The notion that these images are collections of numerous dots, allows us process them using a simple algorithm that counts the number of dots in each box. Fractal dimension stability can be estimated by repeating this process for various grid sizes (which could be different from 2^n). Despite the classical box counting that relies on visual inspection and can provide limited number of points on the $Ln(N) - Ln(n)$ curve, the new algorithm can generate numerous points on this curve and provide a more confident answer about fractal dimension stability and its value. In Chapter 6, we saw an example with 79 points on the $Ln(N) - Ln(n)$ curve (figure 6.15). Figure 7.8.a is the image of a fracture pattern found on the columns at the top of Dome tower in Florence. This image was analyzed using the proposed box counting algorithm and it became clear that it is not a fractal image. A rational for non-fractal behavior of these fractures is the fact that the column has been under (non-geological) structural loads for years and the pattern cannot be described by the self-similarity identified in rock fracture mechanics (Chapter 5).
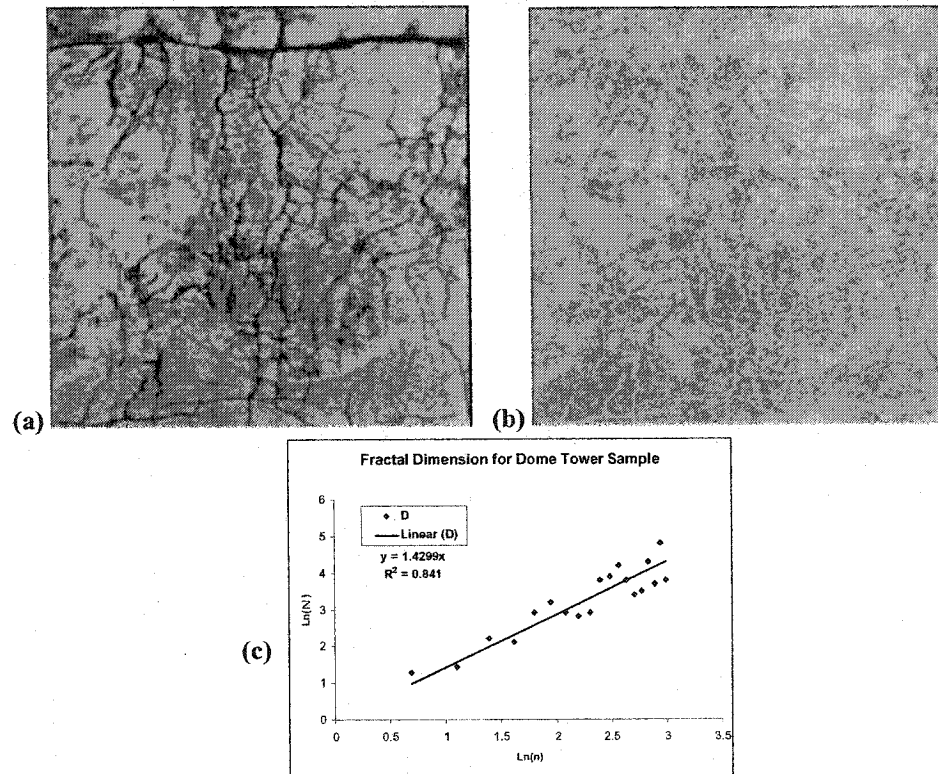
Figure 7.8 – (a) Fracture Pattern form Dome Tower Column, Florence, Italy.
(b) Identified Fractures by Box Counting Algorithm (green/light).
*(c) Ln(**N**) – Ln(n) Curve: It is not a fractal!*

V. Interactive Fractal Program (IFP V1.5 – SEP 2002)[10]

A visual basic program was developed for the purpose of this study. Both forward algorithm and reverse algorithm are incorporated in this program which interactively develops fractal images from given IFS codes and finds appropriate IFS codes for a given fractal image. The user interface is very simple, as shown in Figure 7.9.

---

[10] IFP was developed for the purpose of this study, only. It is not a commercial program and it is not used for any other purposes.

126
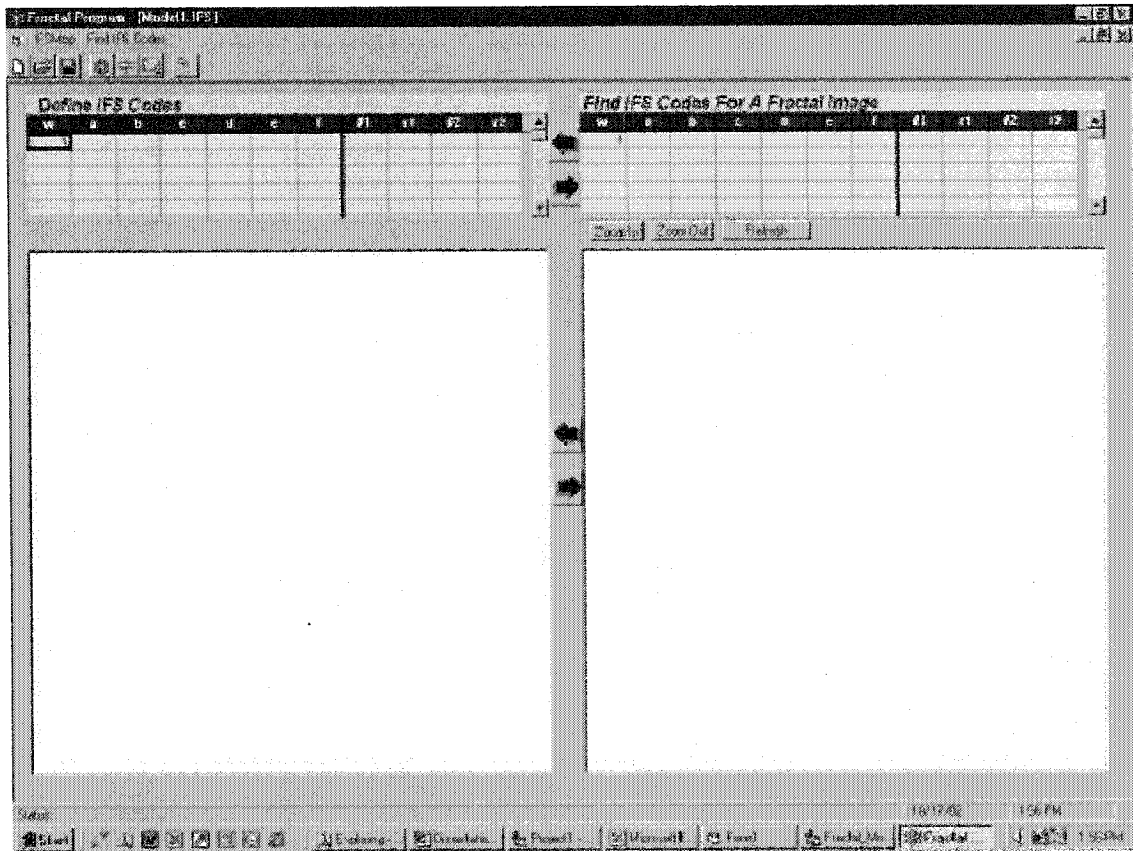
Figure 7.9 – Interactive Fractal Program – User Interface

IFS codes are defined in the left window. They can be entered either directly into the "Define IFS Codes" spreadsheet, or could be drawn as parallelograms on the left window, graphically. Transformations can be also sheared, rotated, and/or resized in the graphical window. After definition of all IFS codes, a random iteration algorithm can be applied to draw the attractor of the IFS, on the right window (Figure 7.10)

127
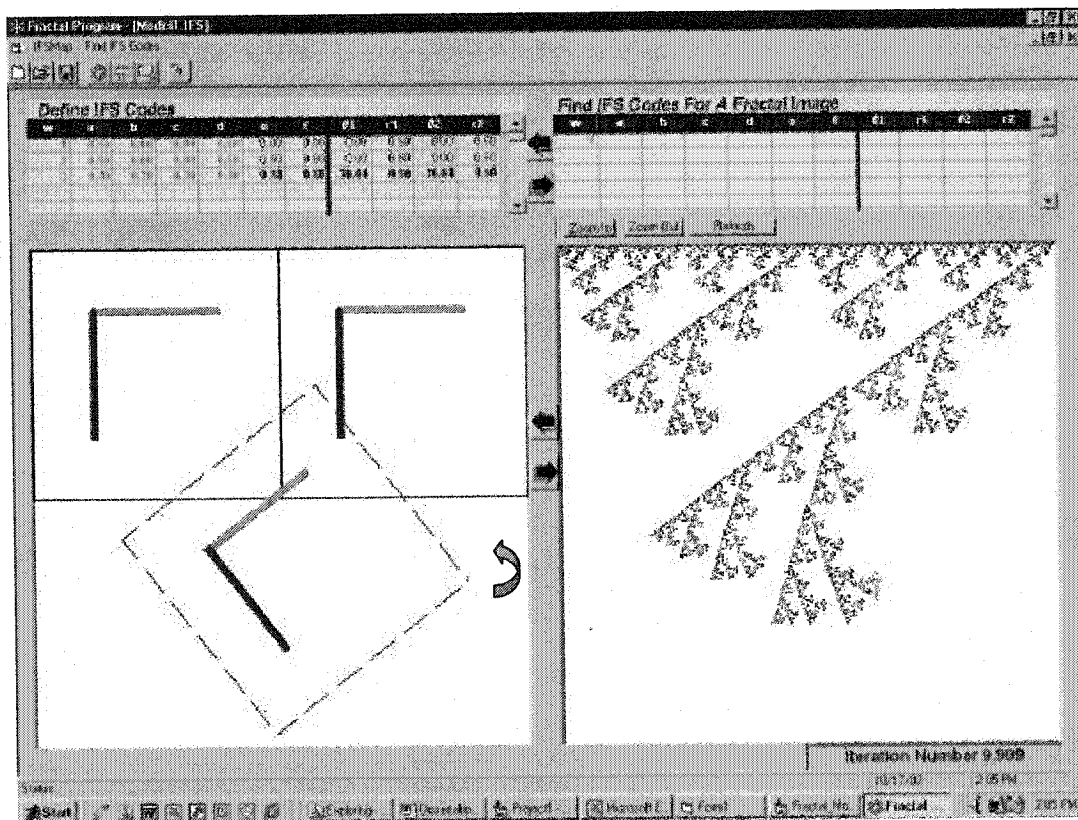
Figure 7.10 – Development of a Fractal Image (right)
from an Iterated Function System (left)

The reverse algorithm is incorporated as follows, with a simple example in Figure 7.11:

1. An image file (JPEG, GIF,BMP, etc.) is downloaded into the right window

2. A polygon that defines the boundaries (or outstanding features) of the image is drawn, by visual inspection (P_0).

3. A transformation is added ($P_1^{①}$). This is a (½x ⅓) copy of the boundary polygon, located on the center of the right window.

4. $P_1^{①}$ is moved, rotated, sheared, and/or resized to cover a portion of P_0.

128

5. Three arbitrary adjacent corners of $P_1^{\text{①}}$ (called X_1, X_2, X_3) are moved to better cover a portion of P_0.

6. As soon as each corner is relocated, a subroutine is called to recalculate IFS_1 based on the first three corners of P_0 and $P_1^{\text{①}}$, using equation (7.2).

7. Consequently, the other corners of $P_1^{\text{①}}$ are calculated by equation (7.1).

8. If a corner is not matching right, that corner and two of its adjacent corners are selected as X_1, X_2, X_3 and we go back to step 5.

9. An option is available to apply the same algorithm to $P_1^{\text{①}}$ and its image $P_1^{\text{②}}$ in order to assure self-affinement. $P_1^{\text{②}}$ can also be altered to optimize coverage of a portion of P_0 by $P_1^{\text{①}}$ and, subsequently, a portion of $P_1^{\text{①}}$ by $P_1^{\text{②}}$.

10. Add a new transformation (step 3 – $P_2^{\text{①}}$) and repeat the process until the entire image P_0 is bounded by $P_1^{\text{①}}$, $P_2^{\text{①}}$, $P_3^{\text{①}}$,..., $P_n^{\text{①}}$ (n = number of transformations).

129

Find IFS Codes For A Fractal Image

w	a	b	c	d	e	f	θ1	r1	θ2	r2
1	0.50	-0.13	0.12	0.48	0.49	0.01	13.61	0.51	15.24	0.50
2	0.36	-0.17	0.48	0.47	0.27	-0.01	53.46	0.60	19.53	0.50
3	0.77	0.11	0.03	0.47	0.04	0.48	2.24	0.77	-13.67	0.48

Zoom In | Zoom Out | Refresh
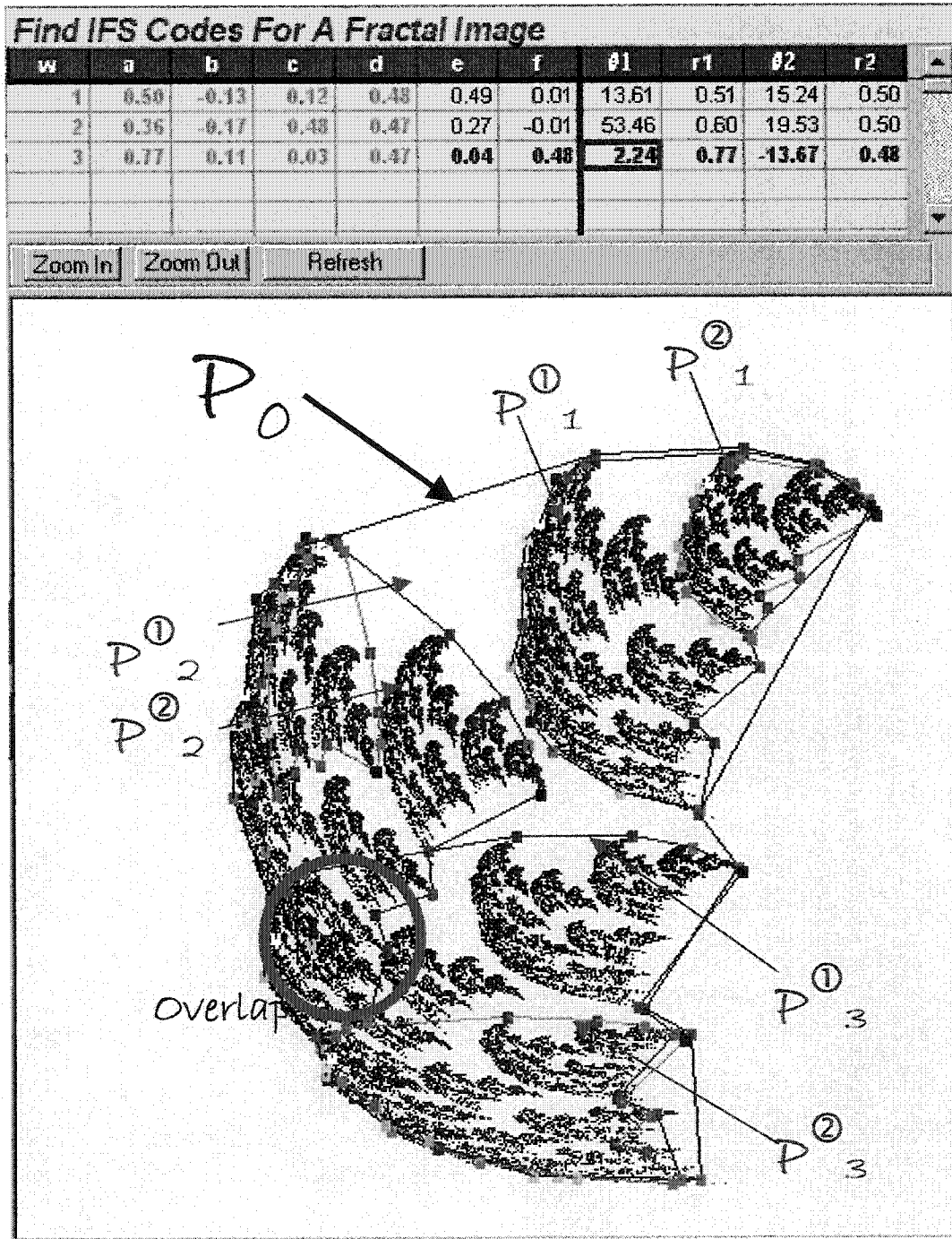
Figure 7.11 – Implementation of Reverse Agorithm in IFP. The three copies of P_0 (i.e. $P_1^①$, $P_2^①$, $P_3^①$) each cover a portion of P_0. Subsequently, $P_1^②$, $P_2^②$, and $P_3^②$ (copies of $P_1^①$, $P_2^①$, and $P_3^①$) cover a portion of each, in the same manner.

130

Transformations $IFS_1, IFS_2, IFS_3, \ldots IFS_n$ are recorded/adjusted in the right hand side spreadsheet, as soon as they are created and/or modified. These transformations can be sent back to the forward algorithm in order to develop their attractor. This attractor can be overlapped on the original image for comparison (Figure 7.12). Such a comparison could show areas of improvement. For example, Figure 7.12 shows that some rotation and/or movement of transformation could improve the attractor. Comparison of their fractal dimensions shows that the fractal dimension of the attractor is about 2.3% less the fractal dimension of the image ($D_{Attractor} = 1.610$, $D_{Image} = 1.648$).
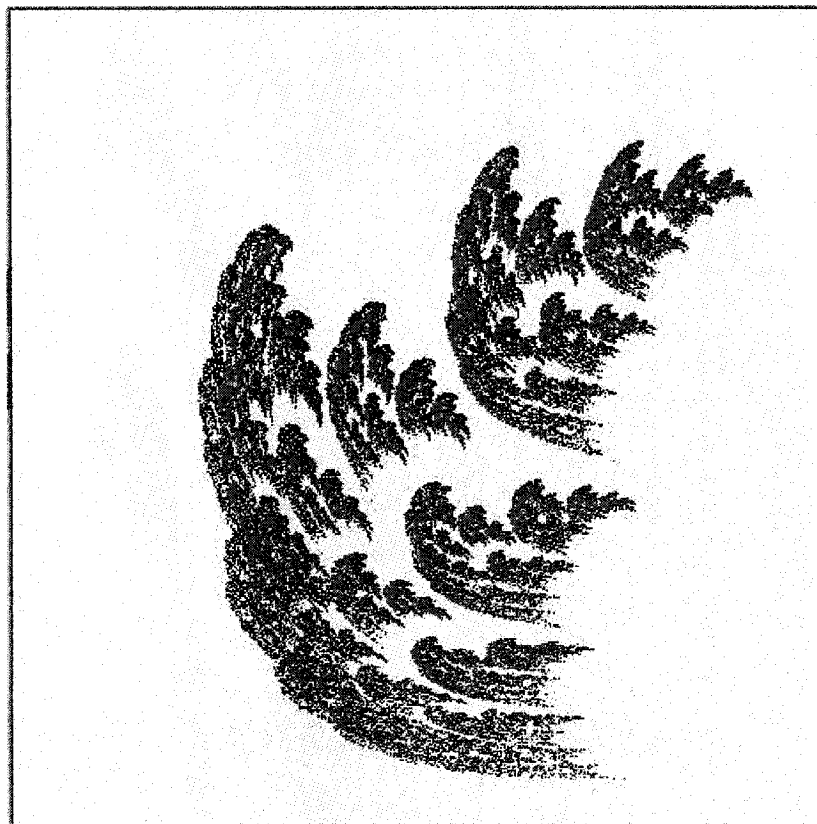
Figure 7.12 – Comparison of a fractal image (blue) with an attractor from inverse algorithm (red)

131

The proposed reverse algorithm is very effective for disconnected and just-touching fractals. With some practice, iterated function systems for any such fractals can be found quickly and accurately. More accuracy can be achieved by adjusting IFS codes, interactively, on the left window of figure 7.9 and redrawing the attractor to overlap the fractal image on the right window. It takes more practice to analyze overlapping fractals. In the above example, IFS_2 was more difficult to find due to overlapping of its important corners with IFS_3. Sometimes overlapping makes a fractal image so complicated that it becomes impossible to find a reasonable iterated function system. Fortunately, fractal network of fractures, in the form proposed here, have very limited overlapping.

VI.   <u>IFP and Fractured Rock Characterization</u>

It is important to note that a rough approximation of fractal image boundaries can be sufficiently used as the initial polygon (P_0) in the inverse algorithm. For example the fractal of Figure 7.11 can be also analyzed by triangles (Figure 7.13.a), since the "outstanding features" of this image are the three corners shown in Figure 7.13.a by red circles. Identification of such features makes it much easier and faster to find an iterated function system for a given image. The triangular approach for the above example provided the IFS codes in less than 5 minutes (Figure 7.13.b). The fractal dimension of this model is 2.1% more than the fractal image (more accurate than figure 7.10!).

132
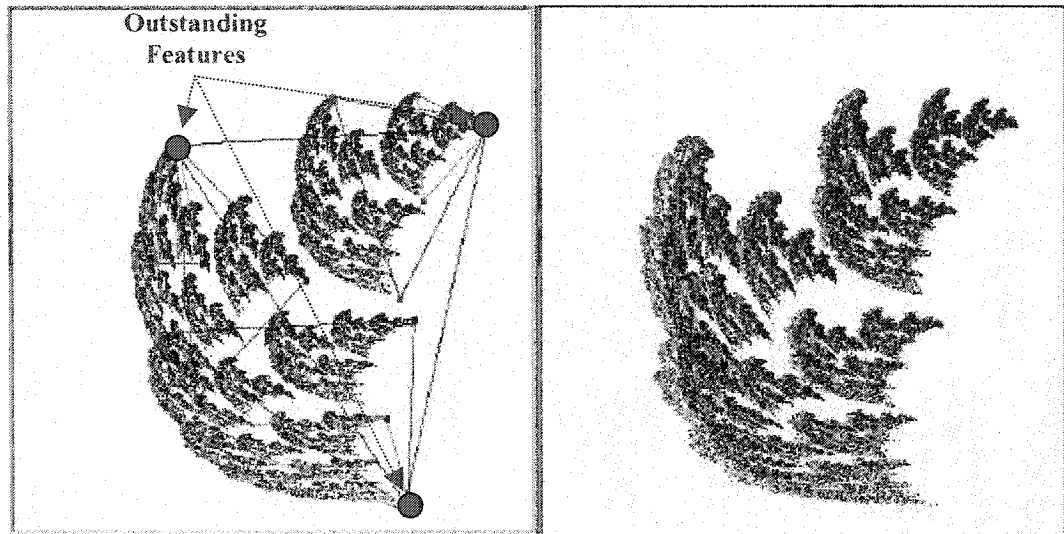
Figure 7.13 – (a) Triangular simulation of IFS codes. (b) Comparison of the fractal image (blue) with the attractor from triangular boundary (red).

The above observation is the basis of a technique that is proposed to find iterated function system for a fractal network of fractures for which only limited information is available. Consider a fracture set for which we have borehole data of Figure 7.14. Let's assume this is a fractal image (it will be proved, if we are wrong). The most outstanding feature of this fractal image is the initial fracture (the largest fracture). Figure 7.14 shows a few hypothetical fractures that can be spotted from the boreholes observations (blue dashed lines). We hypothesize the initial fracture as the large one on the center top, due to its largest thickness. Now we define the outstanding feature to be a quadrilateral based on the initial fracture and one of the other fractures (it doesn't matter which one, as long as its copies can be realizable at various scales). Here, we define the quadrilateral shown in Figure 7.14 as P_0.

133
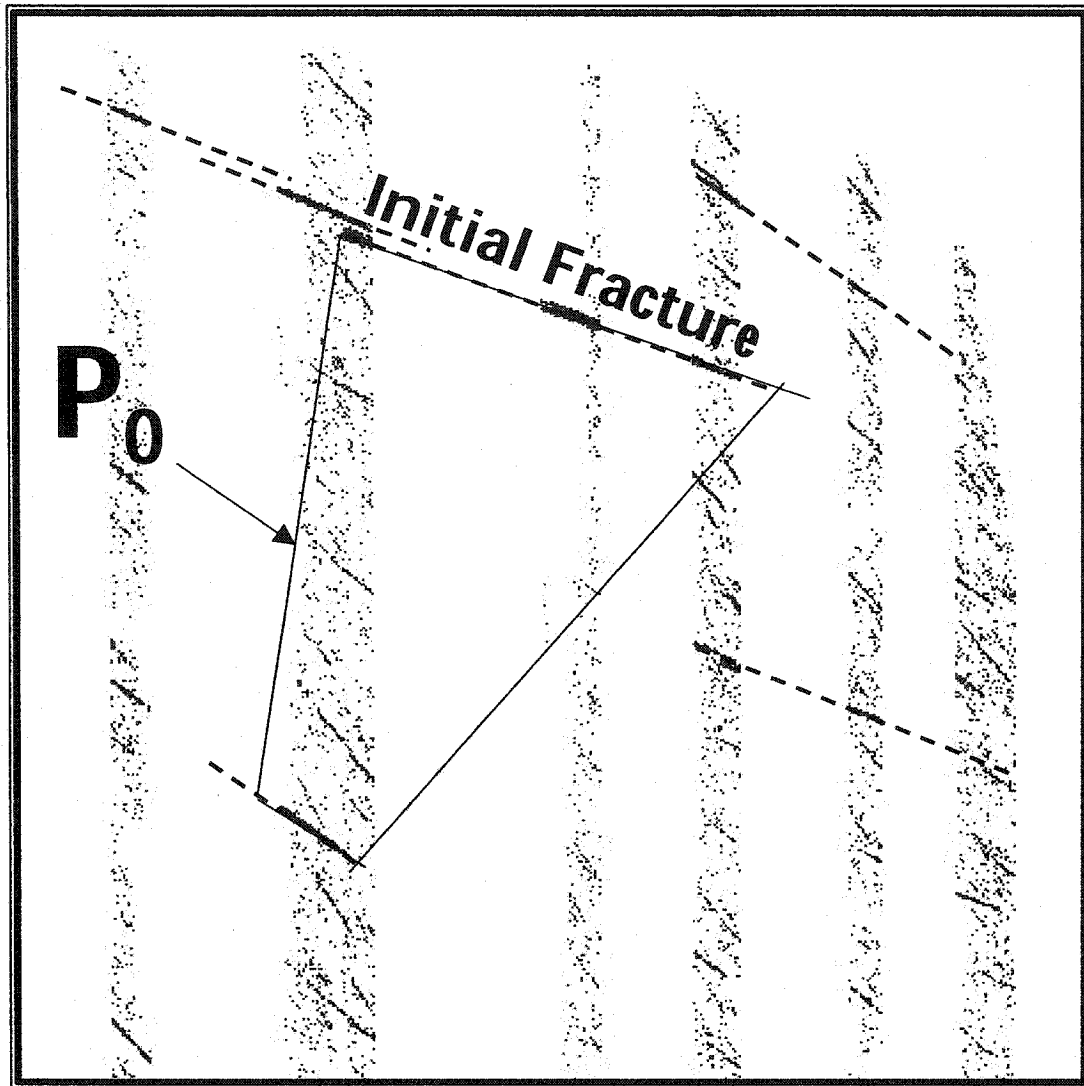
Figure 7.14 – Hypothesizing initial Fracture and Polygon P_0, based on borehole data of a fracture set.

The remaining of the work is straightforward. The reverse algorithm is used to identify altered copies of P_0 that cover various parts of P_0. Once copies of P_0 cover itself entirely, the iterated function system is identified (without condensation set), approximately. The condensation set is defined based on initial fracture properties (length, orientation, and thickness). We develop the attractor of this IFS with condensation and investigate whether it covers all borehole images. If we do not

134

succeed, the transformations need to be altered (or the initial fracture hypothesis must be changed), until the desired attractor is explored. Figure 7.15.a shows this process and Figure 7.15.b shows the best attractor that was found compared to the boreholes image. Perhaps IFS_1 needs some modifications.
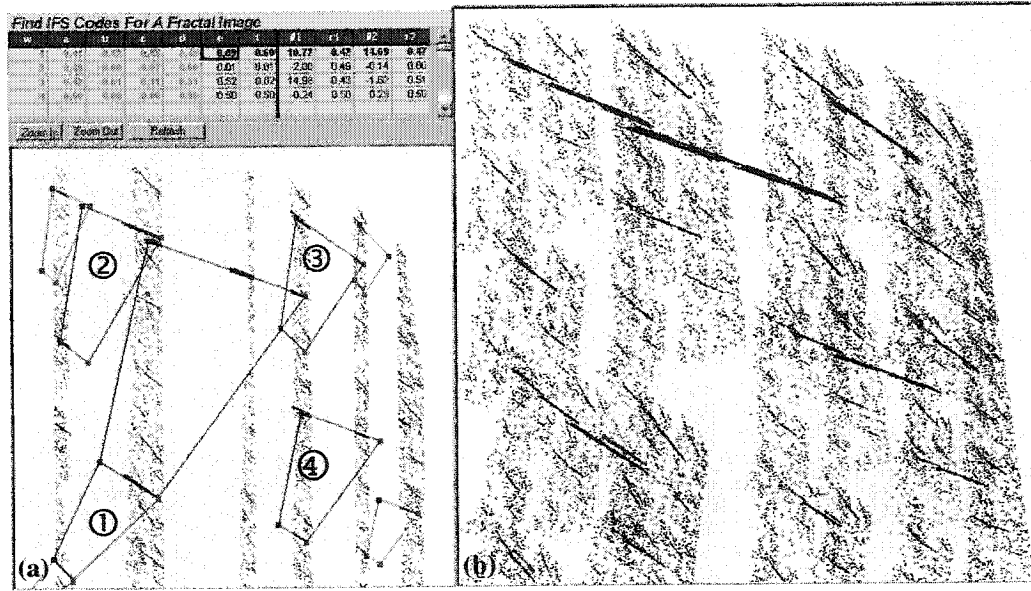
Figure 7.15 – (a) Development of IFS codes. (b) IFS attractor (blue) and boreholes image (red)

To evaluate proximity of the attractor to the original image, we need to "predict" fractal dimension of fracture set. But we have only parts of this image (borehole date). If there are n boreholes of thickness t, spread (approximately) uniformly in a region of with w, the available portion of the image would be: $\alpha = n \cdot t/w$. We can therefore predict fractal dimension of the fracture set as follows:

Fractal dimension is D=Ln($\mathcal{N}$)/Ln(n), where $\mathcal{N}$ is calculated based on the number of dots divided by maximum number of dots, counted by an image processing program.

135

Lets define a fictitious fractal dimension for the boreholes image, even though it is not a fractal: $D_\alpha = Ln(N_\alpha)/Ln(n)$. Box counting program can easily process the boreholes image and calculate D_α. We have:

$$N = \frac{\sum [\text{\# of Dots in All Cells (Attractor)}]}{Max[\text{\# of Dots (Attractor)}]}$$

$$N_\alpha = \frac{\sum [\text{\# of Dots in All Cells (Borehloes Image)}]}{Max[\text{\# of Dots (Borehloes Image)}]} \approx \frac{\alpha \times \sum [\text{\# of Dots in All Cells (Attractor)}]}{\alpha \times Max[\text{\# of Dots (Attractor)}]}$$

$$(7.3) \qquad D_\alpha = \frac{Ln(N_\alpha)}{Ln(n)} \approx \frac{Ln(N)}{Ln(n)} \Rightarrow \qquad \therefore \overset{?}{D} \approx D_\alpha$$

At every grid $n \times n$, D_α is calculated and D can be approximated by D_α, based on equation (7.3). This relation can be used to evaluate stability of the fractal dimension and confirm fractal nature of the partially known fracture set. It can be also used to compare the attractor found by the reverse algorithm with the actual fracture pattern and evaluate their proximity.

The above method is effective when the boreholes are spread uniformly in the region. In the above example where boreholes distribution is not uniform, we may not be able to predict fractal dimension very well. In the example of Figure 7.16.a, however, we have a good distribution of boreholes and fractal dimension can be predicted from boreholes images. A fractal image was developed using IFP (Figure 7.16.b – This is in fact the exact fractal that created boreholes image of Figure

136

7.16.a) and its fractal dimension (Figure 7.16.d) shows relatively good agreement with the fictitious fractal dimension of the boreholes image (Figure 7.16.c):

$$Deviation = \frac{2|D - D_\alpha|}{D + D_\alpha} = \frac{2|1.6496 - 1.6279|}{1.6496 + 1.6279} = 1.32\%.$$

A word of caution in this technique is to make sure that the mesh size should not exceed some threshold smaller or equal to the number of boreholes. In the example of Figure 7.16, there are 13 boreholes and mesh size larger than 8x8 should not be used, due to anomalies observed on the regression curve (Figure 7.16.c).
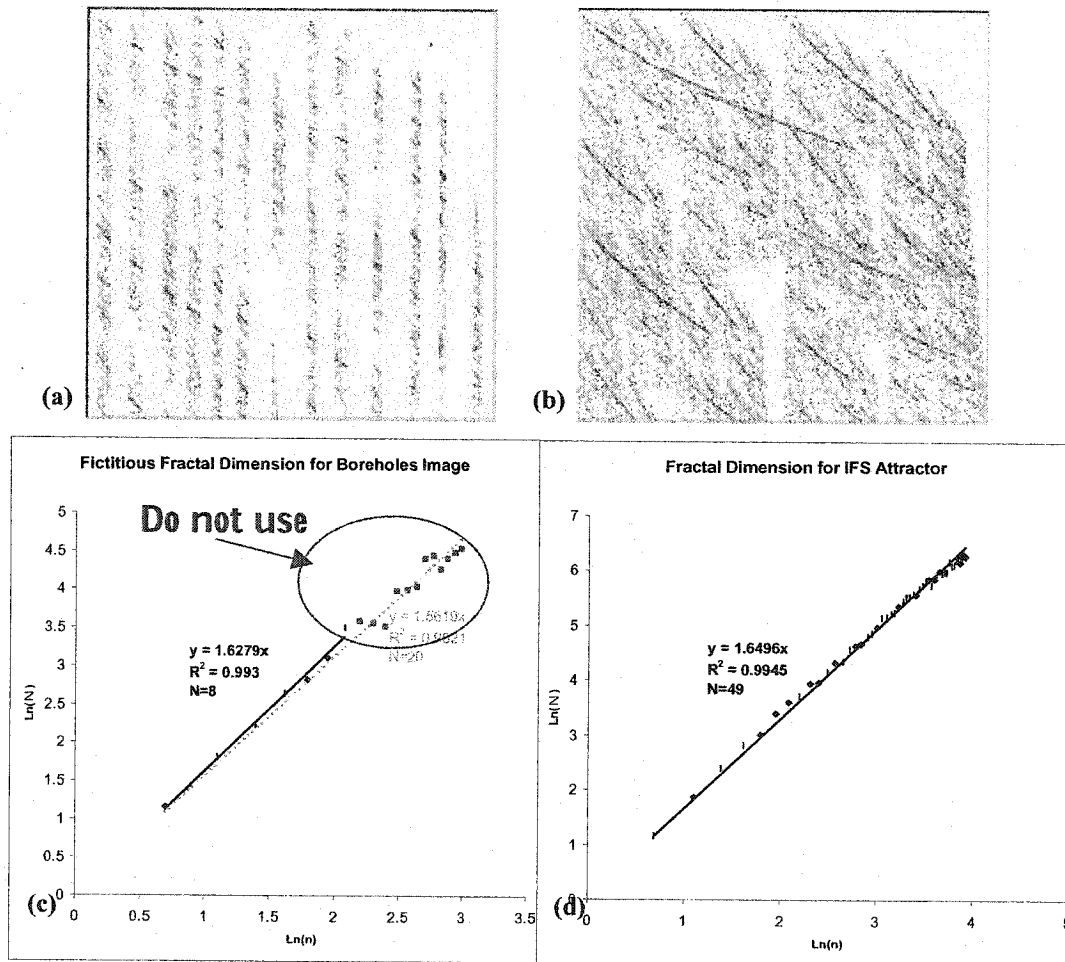
Figure 7.16 – (a) Image of Boreholes. (b) IFS Attractor for boreholes image (a). (c) Fictitious fractal dimension of the boreholes image (a). (d) Fractal dimension of the attractor (b).

137

7.2 - DEVELOPMENT OF THE PERMEABILITY TENSOR (FLOW MODEL)

I. Classical Equivalent Continuum Model

The foundation of the flow model that is developed in this study is based on the classical Equivalent Continuum Model (ECM) that was introduced by Oda (1985) for homogeneous and anisotropic fractured rock masses. In this case, steady state flow can be modeled using Darcy's law:

$$(7-4) \qquad u_i = -k_{ij} \bullet \frac{\partial \phi}{\partial x_i} = k_{ij} \bullet J_j$$

Where:

k_{ij} = Element ij of permeability tensor (ft/sec.)[11]

$\partial \phi / \partial x_i$ = Gradient of total Hydraulic head ϕ (ft) in direction i

The model was developed based on the basic assumption that each fracture can be modeled by two parallel plates that are spaced very closely (fracture aperture). The well-known equation for this model is:

$$(7-5) \qquad u_i^{(c)} = \frac{g}{12 \cdot v} \bullet t^2 \bullet J_i$$

Where:

$u_i^{(c)}$ = Average flow velocity in crack (c)
t = Crack thickness (aperture)
g = Gravitational acceleration = 32.2 ft/sec.^{2}
v = Fluid kinematic viscosity (ft^2/sec.)

---

[11] Note that, in the general form, there is a g/v multiplier in eq.7-4. Here, this multiplier is embedded in k_{ij} for simplicity.

138

In Oda (1985), fractures were assumed as circular disks of radius r, thickness t (hydraulic aperture), and orientation $\bar{n}$ (comonly used assumptions is this line of research). The probability density function of fractures properties distribution was defined as $E(\bar{n}, r, t)$. Elements of the permeability tensor were calculated by integration over the volume of region as follows:

$$(7-6) \qquad K_{ij} = \frac{1}{12}\left(P_{kk}\delta_{ij} - P_{ij}\right)$$

Where: $\qquad P_{ij} = \frac{\pi\rho}{4}\int_0^\infty \int_0^\infty \int_\Omega r^2 t^3 \bar{n}_i \bar{n}_j E(\bar{n}, r, t)d\Omega dr dt$ \qquad (Crack Tensor)

ρ = Volume density of cracks [$m^{(V)}/V$] (lb/ft^3)

Ω = The region under study

P_{kk} = Trace of matrix P ($P_{11}+P_{22}+P_{33}$)

$\delta_{ij} = 0$, $Else$ If $i = j \Rightarrow \delta_{ij} = 1$

Permeability tensor (K) and crack tensor (P) are symmetric matrices. In fact, K is similar to elasticity tensor (K_e) and the relation between permeability tensor (K), velocity (U $\qquad\qquad$ J) is analogous to the relation between elasticity tensor ($_e$), stress vector (σ), and strain vector (

Therefore, it is quite rational to discretize a heterogeneous region of fracture network, calculate permeability tensor for each small region (assuming it is

and size of its fractures (Figure 7.17), and use a

finite element or finite difference program to calculate global permeability of the

139

The above concept is the basis of a simplified equivalent continuum model that was developed and applied to fractal networks of fractures, as described in section 7.1. This model is explained next.

$$K_{24} = F(C_1, C_2, ..., C_7)$$

$$K_{Overall} = F(K_{11}, K_{12}..., K_{77})$$
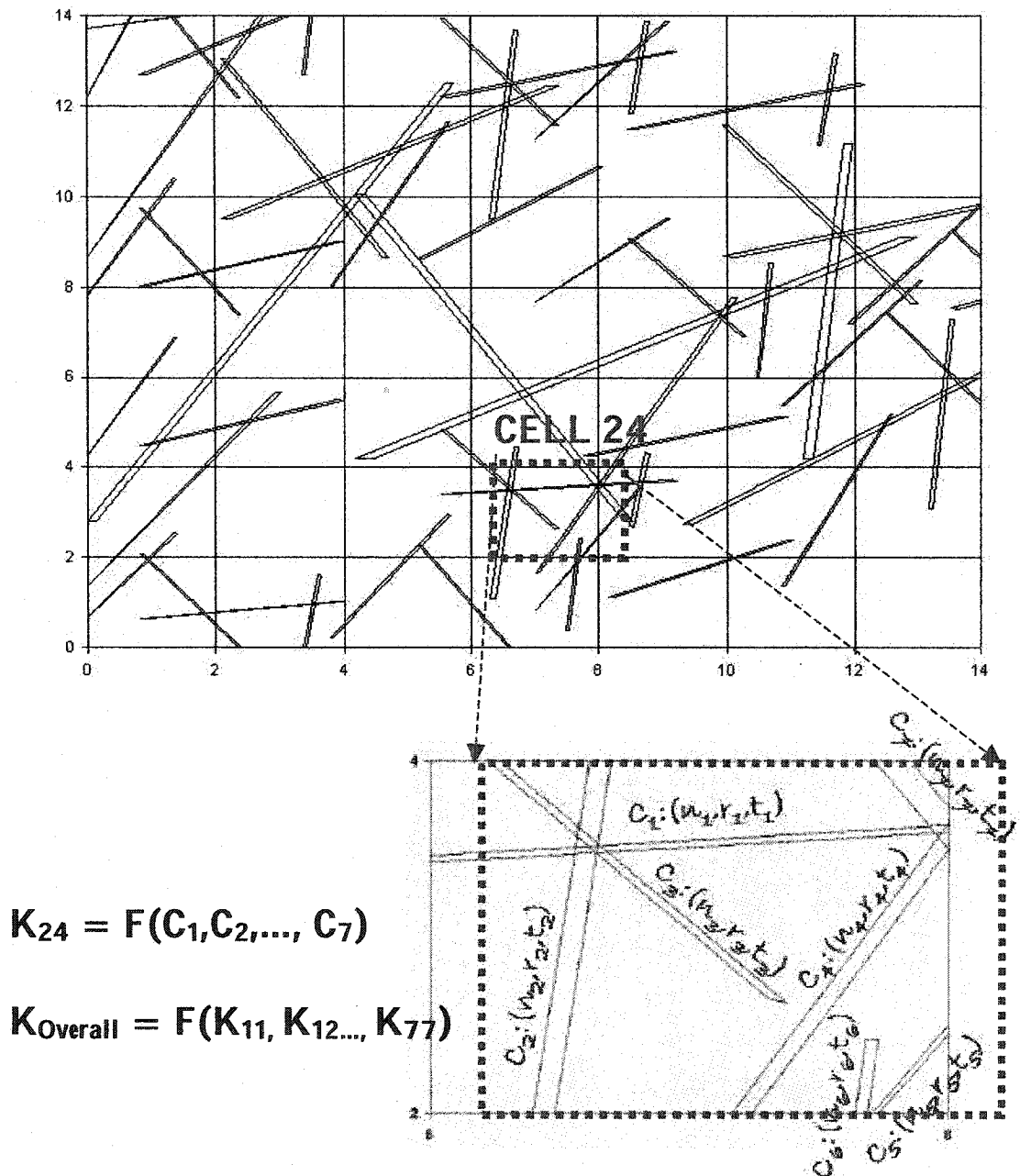
Figure 7.17 – Discretization of a heterogeneous fracture network for flow modeling

140

II. Simplified Equivalent Continuum Model (SECM)

In a non-statistical model, fractures properties are available and there is no need for the function $E(\vec{n}, r, t)$. Therefore, values of P_{ij}'s in equation 7-6 can be calculated as summations, instead of integrations. In addition, at this time, the model is developed in 2D[12] and directional vector of a crack ($\vec{n}$) can be written in terms of $\vec{n}_1$ and $\vec{n}_2$ (directional vectors of x and y). The other simplifying assumption is using parallelograms of length l and width b for fracture geometry. Some scholars have used parallelograms or polygons instead of circular disks for fracture surface (e.g. Dershowitz and Einstein – 1988).

Consider a square region of side L with n fractures of length $l^{(c)}$, orientation $\vec{n}^{(c)}$ ($\vec{n}^{(c)} = Cos\alpha^{(c)}$, $\alpha^{(c)}$ is the angle with x axis), thickness $t^{(c)}$, width b, where c is the fracture number (Figure 7.18). Flow equation for this medium is driven as follows:

---

[12] The model can be expanded to 3D space. The concept is straightforward, while the calculations and the reverse fractal algorithm become very complicated. Development of a 3D model is one of the recommendations of this study (see Chapter 10)

141
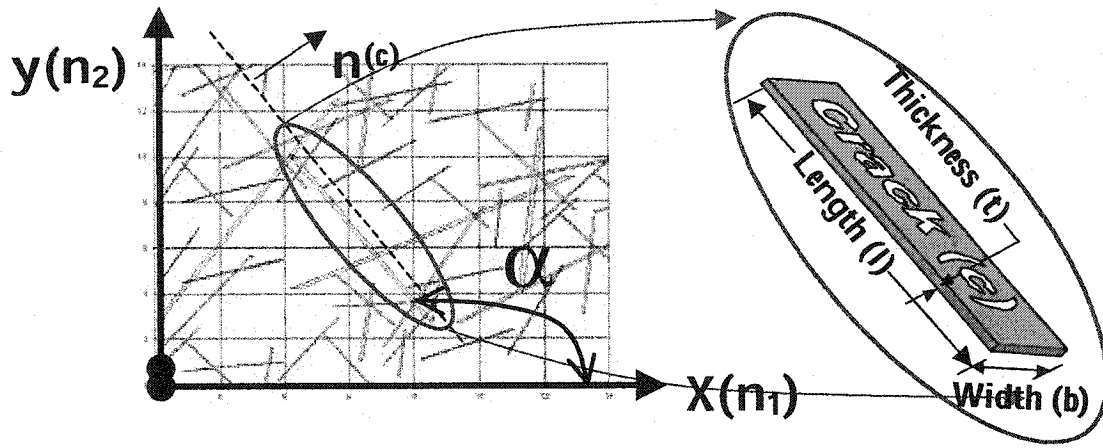
Figure 7.18 – Fractures (cracks) properties

$$\bar{u}_i * V = \sum_{c=1}^{n(\#ofCracks)} u_i^{(c)} * V^{(c)} \;;\; V = L \times L \times b \;;\; V^{(c)} = l^{(c)} \times t^{(c)} \times b \;;\; (7\text{-}5) \Rightarrow u_i^{(c)}$$

$$\Rightarrow \bar{u}_i * \left(L \times L \times b\right) = \frac{g}{12\upsilon} \sum_{c=1}^{n} \left(t^{(c)}\right)^2 * J_i * \left(l^{(c)} \times t^{(c)} \times b\right)$$

$$\Rightarrow \bar{u}_i = \frac{g}{12 \cdot \upsilon \cdot L^2} \sum_{c=1}^{n} l^{(c)} * \left(t^{(c)}\right)^3 * J_i \;;\; J_i^{(c)} = \left(\delta_{ij} - n_i \cdot n_j\right) * J_j \;;\; \vec{n}_1 = Sin\alpha \;;\; \vec{n}_2 = Cos\alpha$$

$J_i^{(c)} = i$ component of gradient of crack c

$J_j = j$ component of field gradient J

$$\Rightarrow \bar{u}_i = \left(\frac{g}{12 \cdot \upsilon \cdot L^2} \sum_{c=1}^{n} l^{(c)} * \left(t^{(c)}\right)^3 * \left(\delta_{ij} - n_i \cdot n_j\right)\right) * J_i \;;\qquad \bar{u}_i = k_{ij} * J_i$$

Therefore:

$$(7-7.a) \qquad k_{ij} = \frac{g}{12 \cdot \upsilon \cdot L^2} \sum_{c=1}^{n} l^{(c)} * (t^{(c)})^3 * (\delta_{ij} - n_i \cdot n_j)$$

Or in matrix format:

142

$$(7-7.b) \quad \overline{K}_{[2\otimes2]} = \frac{g}{12 \cdot \upsilon \cdot L^2} \sum_c \left[l^{(c)} * \left(t^{(c)} \right)^3 \right] * \begin{bmatrix} Cos^2\alpha^{(c)} & -Sin\alpha^{(c)} \cdot Cos\alpha^{(c)} \\ -Sin\alpha^{(c)} \cdot Cos\alpha^{(c)} & Sin^2\alpha^{(c)} \end{bmatrix}$$

III. Application of SECM to fractal Network of Fractures

If properties of all fractures in a medium are available, equation (7-7) can be used to calculate the permeability tensor of the equivalent porous medium. For a fractal network of fractures, these properties must be defined based on the pattern of the fractal dots. For each fracture set, assume the region is broken down by an $n \times n$ grid (Figure 7.19.a). If n is large enough, it can be assumed that hydraulic properties of each cell can be estimated by a single *representative fracture*. It remains to find properties of this fracture and apply equation (7-7) to calculate the permeability tensor of that cell.
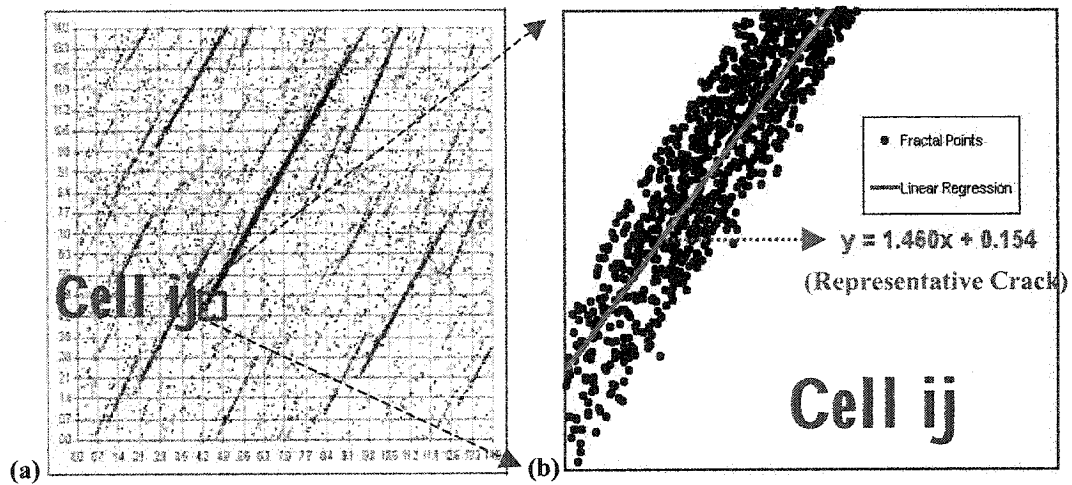
Figure 7.19 – (a) A fractal set of fractures, discretized by $n \times n$ mesh.
(b) Linear Regression for cell ij

143

To identify the representative fracture, the following three techniques were investigated. They are sorted in the order of their accuracy:

- *Regression Analysis:* Consider the blown-up cell *ij* in Figure 7.19.b. If we could find a line that is closest to all fractal points, that line would define the representative fracture. Regression analysis is a technique that finds such a line by minimizing the <u>squared "y" distance</u> of all points with respect to an imaginary line $d : y = a + b \cdot x$:

$$Minimize\left\{ f(a,b) = \sum_{i=1}^{n(\#Points)} (y_i - \hat{y}_i)^2 = \sum_{i=1}^{n} [y_i - (a + b \cdot x_i)]^2 \right\}$$

(7.8) $\begin{cases} \dfrac{\partial f(a,b)}{\partial a} = 0 \\[3mm] \dfrac{\partial f(a,b)}{\partial b} = 0 \end{cases} \Rightarrow \begin{cases} a = \dfrac{1}{n}\left(\sum y - b \cdot \sum x\right) = \bar{y} - b \cdot \bar{x} \\[3mm] b = \dfrac{n\sum x \cdot y - \sum x \cdot \sum y}{n\sum x^2 - \left(\sum x\right)^2} \end{cases}$

The regression line is shown for the particular cell *ij* in Figure 7.19.b. Although, Regression line, is not always the best trend-line. The concept of regression is based on the assumption that "y" is the "dependent" variable and "x" is the "independent" variable. In cases such as Figure 7.20, this assumption results is erroneous values of a and b. The regression line in Figure 7.20 (pink) is not a good representative of the representative fracture. To be accurate, the <u>minimum</u> distance between the points and the

144

representative line should be minimized (Figure 7.22). We introduce an approximate method, and then the exact equation.
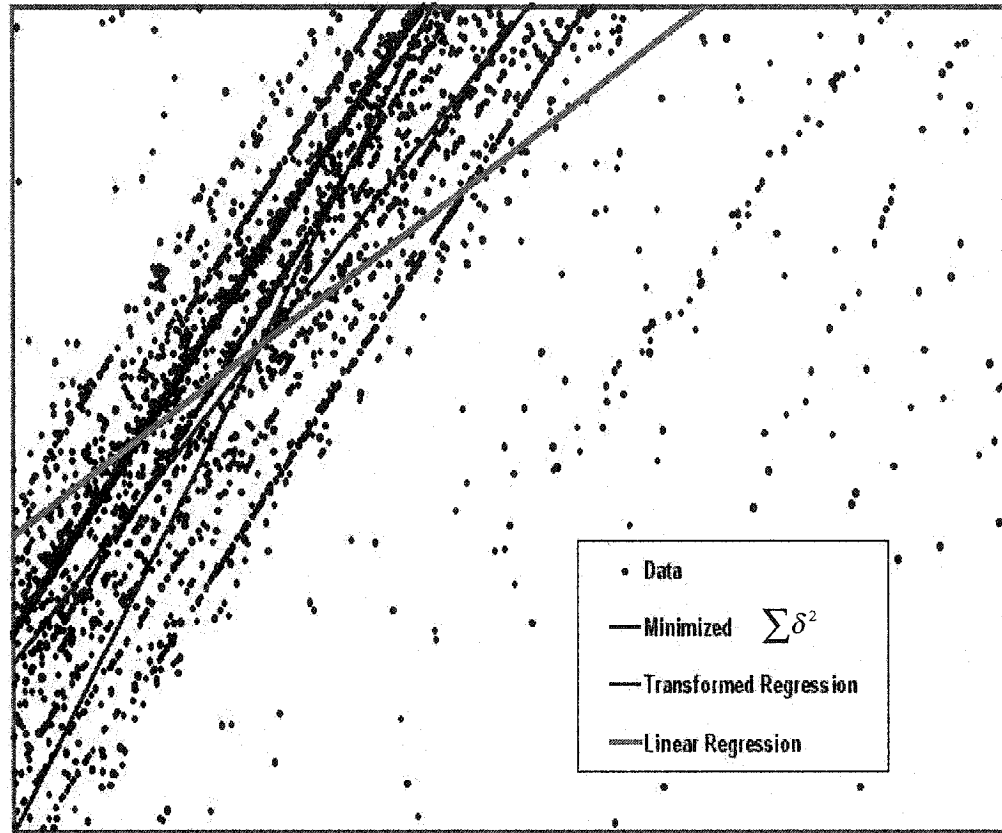
Figure 7.20 – Comparison of three methods to estimate representative crack

- *Approximate Optimization – Transformed Regression:* The notion that fractures in a set are approximately parallel, provides a tool to modify the above regression model. The idea is simple: rotate coordinate system by $-\theta$ (θ=Orientation of the initial fracture), calculate regression line in the new

145

system, and then rotate the regression line by θ and put it in the original system (Figure 7.21). The regression line is calculated as follows.

$$(7-9) \qquad b = Tan(\alpha) = Tan(\theta + \alpha') \; ; \; a = b' \times \frac{Cos\alpha'}{Cos\alpha}$$

a', b' are calculated using regular regression in the transformed coordinate system, $d: y' = a' + b' \cdot x'$.

$y = a + b \cdot x$

$y' = a' + b' \cdot x'$
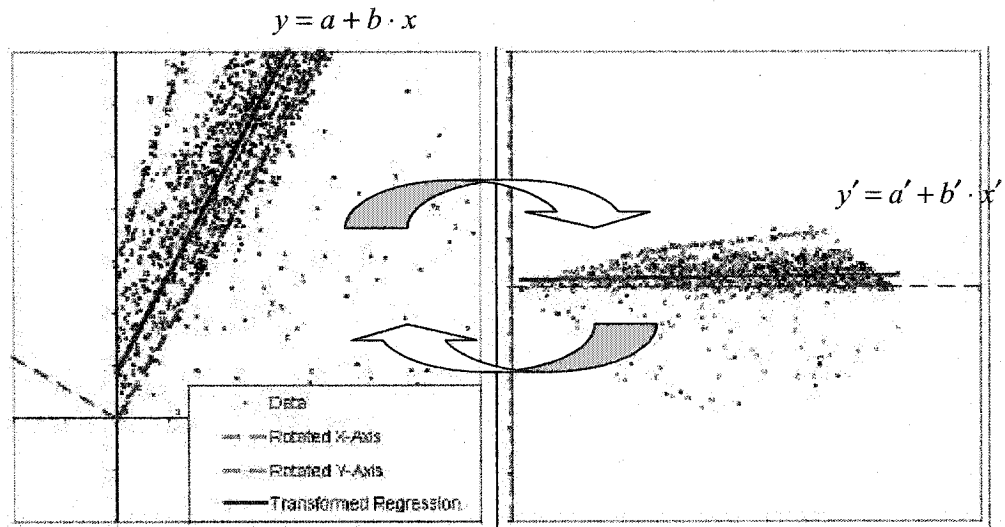
Figure 7.21 – Transformed Regression

- *Accurate Optimization – Minimized $\sum \delta^2$ Regression:* In order to find a fracture that best represents trend of the fractal points in a cell, the shortest distance from all points to this fracture (δ) should be minimized, as shown in Figure 7.22. In other words, we need to solve the following optimization problem for α and b:

146

$$Minimize\left\{f(\alpha,b)=\sum_{i=1}^{n}d_i^2=\sum_{i=1}^{n}\left(\frac{y_i-\hat{y}_i}{Cos\alpha}\right)^2=\sum_{i=1}^{n}\frac{(y_i-\hat{y}_i)^2}{1+b^2}\right\}.$$ Appendix A

provides solution to this optimization problem and it concludes that:

$$(7-10)\qquad \begin{bmatrix}\dfrac{\partial f(a,b)}{\partial a}=0\\[3mm]\dfrac{\partial f(a,b)}{\partial b}=0\end{bmatrix}\Rightarrow\begin{cases}a=\dfrac{1}{n}\left(\sum y-b\cdot\sum x\right)=\overline{y}-b\cdot\overline{x}\\[3mm]b=\pm\sqrt{U^2+1}-U\end{cases}$$

Where: $$U=\frac{\left[(\sum x)^2-(\sum y)^2\right]-n\left(\sum x^2-\sum y^2\right)}{2(\sum x\sum y-n\cdot\sum xy)}$$

It is important to note that there are always two values for b, in equation 7-10 and selection of the right value is crucial. In cases that the initial fracture is very close to horizontal ($\alpha=0°$), the error is negligible. In other cases, however, the right value must be selected. This is done by looking at the orientation of the initial fracture (sign of θ) and using it as correction factor:

$b=\theta/|\theta|\times\sqrt{U^2+1}-U$, keeping in mind that θ can only take values ($0°$ to $90°$] or [$-90°$ to $0°$).

147
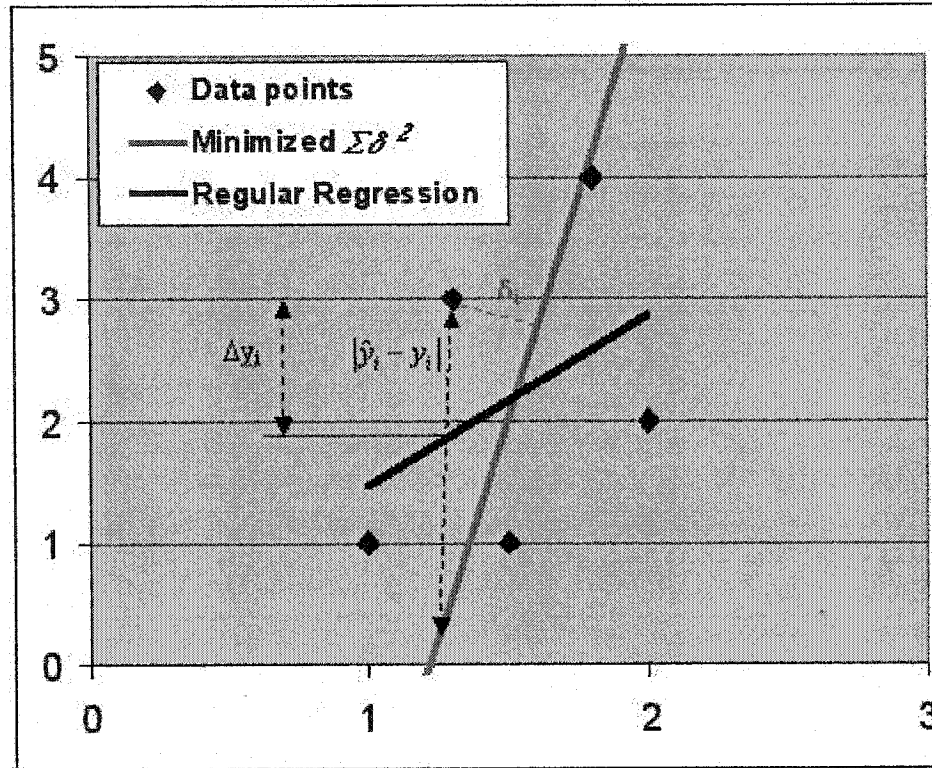
Figure 7.22 – Comparison of Minimized $\sum \delta^2$ and linear regression

In this study Minimized $\sum \delta^2$ *Regression* was applied to the fractal model. For a highly fractured region, approximate optimization may be used for faster results. Regular regression is not recommended, due to the problems discussed above.

Propertied of the representative fracture are now easy to define:

- Orientation α is defined by $Tan^{-1}b$. b is calculated by equation (7-9) or (7-10).

148

- Length l is calculated based on the assumption that the fracture meets both boundaries. This assumption is rationalized by the fact that the cells are very small. A conditional statement in a computer program can calculate l for each of the cases of Figure 7.23.
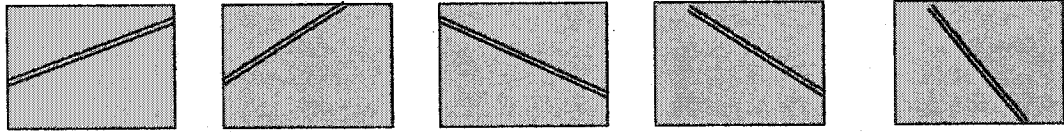
Figure 7.23 – Defining crack length: Alternative crack truncation schemes

- Fracture thickness is assumed to be the 85% confidence interval. This width is defined by $\mu \pm \sigma$, assuming normal distribution of errors $(\hat{y}_i - y_i)$. This is a widely accepted assumption for regression analysis. Higher confidence interval was considered to be too wide due to the fact that hydraulic aperture is always less that physical aperture. For an actual problem, one could find a confidence interval that is appropriate for a given roughness (JRC). A surface with JRC=0 requires 95%[+] confidence interval, while a surface with JRC=20 may use a confidence interval as low as 60%. Normal distribution tables can be used to gain a desired confidence interval by defining κ in $\mu \pm \kappa \cdot \sigma$.

A visual basic program was used to calculate properties of the representative fracture and permeability tensor of all cells, for each fracture set. The fracture network of

149

Figure 7.24 was used for the purpose of this study. Permeability tensor values for each fracture in each cell were calculated by taking the average of 20 simulation runs. Permeability tensors for all fractures in each cell were superimposed to get the global permeability tensor for that cell. The flow problem was then modeled by FLAC^{2D}, a finite difference program. A brief summary of FLAC^{2D} and simulation of the proposed problem (Figure 7.24) are discussed in the next section.
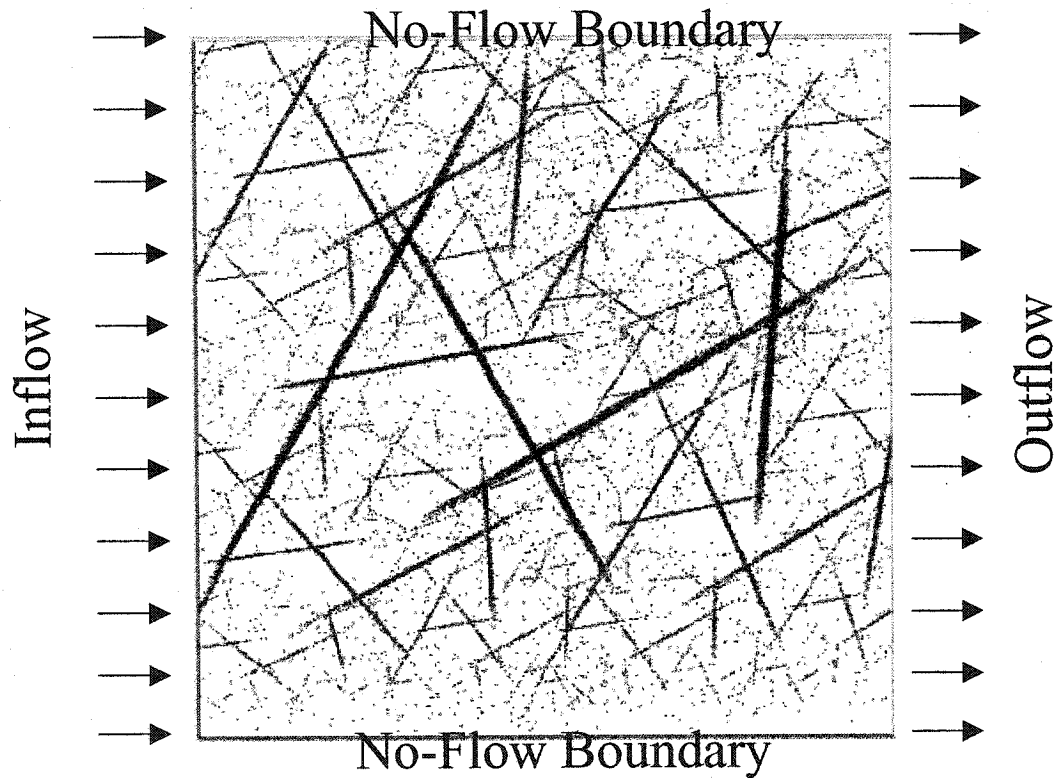
Figure 7.24 – Proposed fracture network flow problem

150

7.3 - FLOW MODELING USING FLAC^{2D} FINITE DIFFERENCE PROGRAM

I. Introduction

Fast Lagrangian Algorithm for Continua (FLAC) is a finite difference model that creates real time simulation of mechanical and hydro-mechanical behavior of earth structures. FLAC can be used to predict response of an earth structure to external factors step by step, including loads, temperature, and hydraulic forces. With an appropriate model, one could simulate a sliding block in a slope stability problem and monitor the block deformation (failure) at different times (Figure 7.25).
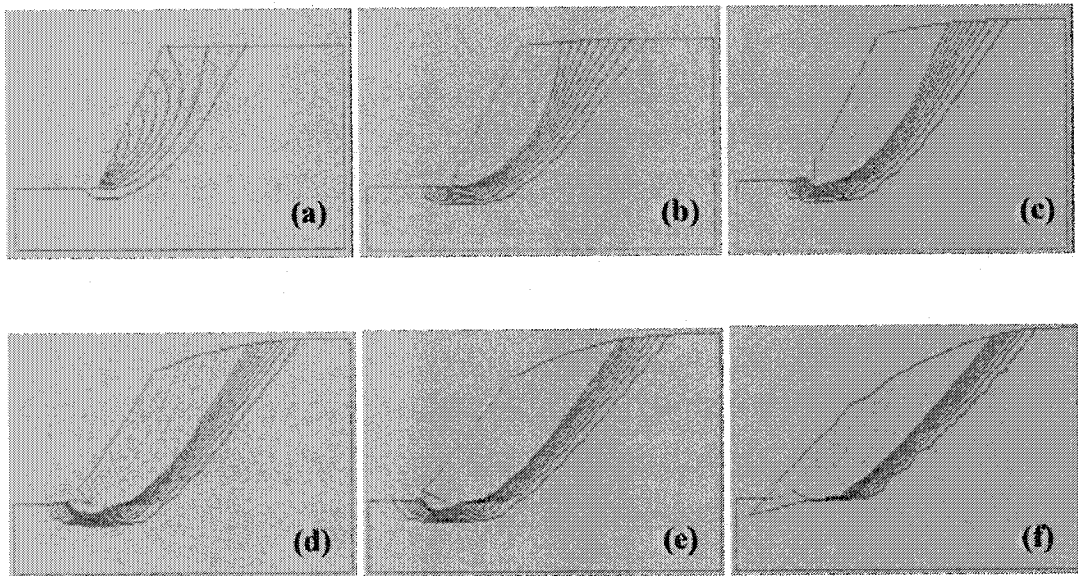
Figure 7.25 – FLAC^{2D} sliding block simulation for slope stability analysis, from initial stage (a) through failure (e)

151

As applied to this study, FLAC can simulate groundwater flow in heterogeneous and anisotropic porous media. Various boundary conditions can be applied to simulate various real life situations. Steady state and transient flow can be both modeled. Fluid saturation can be initialized, fixed, and/or calculated at the end of simulation. More complicated problems (such as hydro-mechanical coupling) can be simulated using FLAC programming language FISH, which can define new parameters and conduct desired calculations.

The objective of this study is to simulate fluid flow in a fractal network of fractures. A very simple problem is selected for this purpose. A 14x14 piece of rock containing fracture network of Figure 7.24 is subject to horizontal flow from left to right (no gravitational forces). Flow is assumed to be saturated and steady, with no hydro-mechanical coupling. A 50x50 grid discretizes the region, permeability tensor is calculated at each cell, and FLAC uses the following formulation to simulate flow.

II. Numerical Formulation of Flow in FLAC^{2D}

In FLAC, each cell of the grid that is introduced by the user is subdivided by two overlaying triangular elements, as shown in Figure 7.26.

152
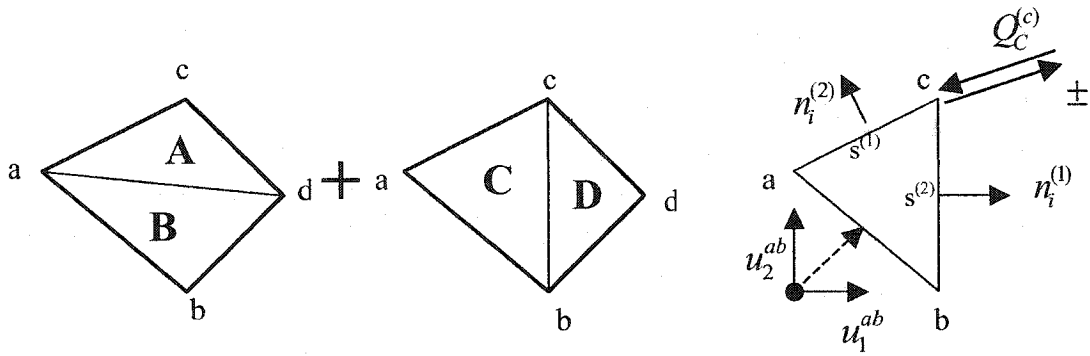
Figure 7.26 – Each element is subdivided by two overlaying triangular elements with given properties

Darcy's law is used for general formulation of flow in direction i: $u_i = k_{ij} \bullet \partial P / \partial x_j$.

Therefore, using Gauss' divergence theorem, flow equation for each triangle in direction i can be approximated by $u_i \approx \dfrac{k_{ij}}{A} \sum P \bullet n_j \bullet s$, where the summation is over the three sides of a triangle and A is the area of the triangle. Thus, components of velocity are:

$$(7-11) \qquad \begin{cases} u_1 = \dfrac{1}{A}\left[k_{11} \sum P \bullet n_1 \bullet s + k_{12} \sum P \bullet n_2 \bullet s \right] \\[4mm] u_2 = \dfrac{1}{A}\left[k_{121} \sum P \bullet n_1 \bullet s + k_{22} \sum P \bullet n_2 \bullet s \right] \end{cases}$$

Discharge (Q) into each edge of an element is calculated as:

$$(7-12) \qquad Q = u_i \bullet A_i = u_i \bullet n_j \bullet s \bullet 1.0$$

Combining equations (7-11) and (7-12), the numerical model can be re-written in matrix format as:

153

$$(7-13) \qquad \{Q\} = [M] \otimes \{P\}, \text{ with gravity: } \{Q\} = [M] \otimes \left\{ P - \left(x_i - x_i^{(1)} \right) \bullet g_i \bullet \rho_w \right\}$$

At each iteration, after calculating $Q^{(i)}$ at all nodes (i) using equation 7-13, pore pressure at all nodes (i) is decremented by:

$$(7-14) \qquad P^{(i)} := P^{(i)} - \frac{K_w \bullet \sum \left(Q^{(i)} \bullet \Delta t \right)}{n \bullet V}$$

$$If \quad \Delta t = Cte. \Rightarrow P^{(i)} := P^{(i)} - \frac{K_w \bullet \Delta t \bullet \sum Q^{(i)}}{n \bullet V} = P^{(i)} - \lambda \bullet \sum Q^{(i)}$$

Where:
K_w = Fluid bulk modulus of elasticity
Δt = Time step
n = Medium porosity
$V^{(i)}$ = Volume associated with the node i

Equations (7-13) and (7-14) are the foundation of flow simulation of FLAC^{2D}. They are applied through several iterations until the change in pore pressure (defined by equation 7-14) becomes insignificant.

It is noteworthy that the values of K_w, Δt, and n do not impact the final result. They are, however, very important in taking us to the final results. If these parameters are selected suitably, after small number of iterations, convergence will occur (changes of pore pressure become insignificant). Inappropriate values of K_w, Δt, and n result in very long simulation time.

154

III. Simplified Formulation, as applied to the proposed problem

In order to understand the way FLAC models a simple problem such as the one proposed in Figure 7.24, FLAC flow algorithm was modified for such simple problems and reprogrammed in Microsoft Excel. This provided a tool to review system behavior step by step and understand finite difference applications and limitations to fracture networks, in general. In this specific case, elements of Figure 7.26 are changed to square elements of side ε, as shown in Figure 7.27.
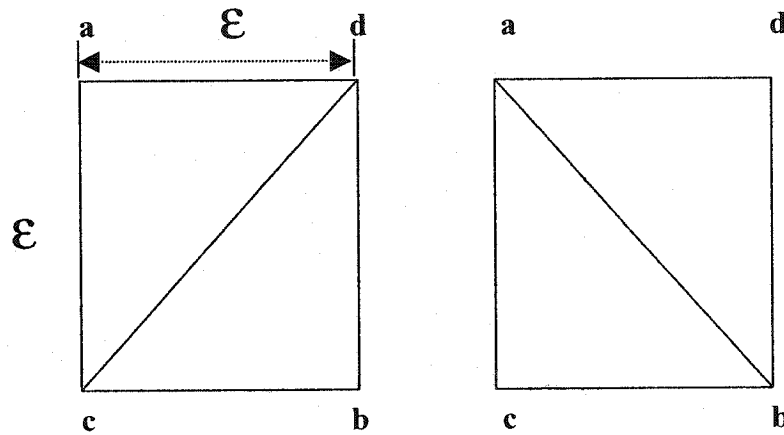
Figure 7.27 – Grid geometry for the simplified problem

Using equation (7-11) velocity vectors at an edge *ij* of a triangle are calculated. Discharge at node *i* is calculated by equation (7-12). These calculations were performed for all four triangles and superimposed to calculate the overall discharge into one node. Details of these calculations are provided in Appendix B. Flow equations are derived as follows:

155

$$(7-15) \begin{cases} \sum Q^{(a)} = \frac{1}{2}\left[\left(k_{11} - k_{12} + k_{22}\right) \bullet P^{(a)} + k_{12} \bullet P^{(b)} - k_{22} \bullet P^{(c)} - k_{11} \bullet P^{(d)} \right] \\\\ \sum Q^{(b)} = \frac{1}{2}\left[k_{12} \bullet P^{(a)} + \left(k_{11} - k_{12} + k_{22}\right) \bullet P^{(b)} - k_{11} \bullet P^{(c)} - k_{22} \bullet P^{(d)} \right] \\\\ \sum Q^{(c)} = \frac{1}{2}\left[-k_{11} \bullet P^{(a)} + k_{22} \bullet P^{(b)} + \left(k_{11} + k_{12} + k_{22}\right) \bullet P^{(c)} - k_{12} \bullet P^{(d)} \right] \\\\ \sum Q^{(d)} = \frac{1}{2}\left[-k_{22} \bullet P^{(a)} - k_{11} \bullet P^{(b)} - k_{12} \bullet P^{(c)} + \left(k_{11} + k_{12} + k_{22}\right) \bullet P^{(d)} \right] \end{cases}$$

IV. Simplified Flow Algorithm

Now that the simplified model (equation 7-15) is available, the flow algorithm for horizontal, saturated, and steady-state flow in a square mesh $n \times n$ $(\varepsilon = 1/n)$, is as follows:

1. Apply $n \times n$ mesh

2. Apply Boundary Conditions at each boundary node: P_{Left}=given, P_{Right}=given

3. Assign permeability values (k_{ij}) to all cells

4. Calculate total flow at each node using equations (7-15).

5. Apply equation (7-14) to update pore pressure (P) at all nodes. λ can be selected as an arbitrary small number. But it should be selected appropriately.

6. Repeat steps 4 and 5 until the change in pore pressure becomes insignificant.

156

The above algorithm was incorporated in Microsoft Excel in two ways:

- *Recursive Algorithm:* As shown in Figure 7.28, permeability values are entered and matrix M is calculated. The special case of $k_{11} = k_{22}$ and $k_{12} = 0$ for all cells (isotropic and homogeneous) is shown here. At step 1, pore pressure in every cell is calculated using boundary values. At each step, discharge values are calculated as a function of pore pressures and permeability values (equation 7-15) and then pore pressures are modified by the new discharge values (equation 7-14). The sheet is calculated for several times (F9 key) until there is no observable change in the values of all cells. This indicates convergence and final values are obtained.

- *Stepwise Algorithm:* Recursive algorithm is only useful to compare the final results with FLAC and confirm accuracy of equations (7-14) and (7-15). It is desired to review FLAC outputs at every step and look for any anomalies to investigate FLAC limitations (Figure 7.29).

157

Figure 7.28 – Recursive Algorithm in MS-Excel

$$M = \frac{1}{2} \times \begin{bmatrix} 2.0E\text{-}06 & 0.0E\text{+}00 & -1.0E\text{-}06 & -1.0E\text{-}06 \\ 0.0E\text{+}00 & 2.0E\text{-}06 & -1.0E\text{-}06 & -1.0E\text{-}06 \\ -1.0E\text{-}06 & -1.0E\text{-}06 & 2.0E\text{-}06 & 0.0E\text{+}00 \\ -1.0E\text{-}06 & -1.0E\text{-}06 & 0.0E\text{+}00 & 2.0E\text{-}06 \end{bmatrix}$$

$$\alpha = 1.0E\text{+}05$$
$$K_{11} = 1.0E\text{-}06$$
$$K_{22} = 1.0E\text{-}06$$
$$K_{21} = 0.0E\text{+}00$$

Pore Pressure @ Grid Points

	1	2L	2R	3L	3R	4L	4R	5
5	5.00E+06	5.00E+06		5.00E+06		5.00E+06		5.00E+06
4T	3.75E+06	3.75E+06		3.75E+06		3.75E+06		3.75E+06
4B								
3T	2.50E+06	2.50E+06		2.50E+06		2.50E+06		2.50E+06
3B								
2T	1.25E+06	1.25E+06		1.25E+06		1.25E+06		1.25E+06
2B								
1	0.00E+00	0.00E+00		0.00E+00		0.00E+00		0.00E+00

Flow @ Grid Points (PER CELL)

	1	2L	2R	3L	3R	4L	4R	5
5	0.625	0.625	0.625	0.625	0.625	0.625	0.625	0.625
4T	-0.625	-0.625	-0.625	-0.625	-0.625	-0.625	-0.625	-0.625
4B	0.625	0.625	0.625	0.625	0.625	0.625	0.625	0.625
3T	-0.625	-0.625	-0.625	-0.625	-0.625	-0.625	-0.625	-0.625
3B	0.625	0.625	0.625	0.625	0.625	0.625	0.625	0.625
2T	-0.625	-0.625	-0.625	-0.625	-0.625	-0.625	-0.625	-0.625
2B	0.625	0.625	0.625	0.625	0.625	0.625	0.625	0.625
1	-0.625	-0.625	-0.625	-0.625	-0.625	-0.625	-0.625	-0.625

Flow @ Grid Points (TOTAL)

	1	2L	2R	3L	3R	4L	4R	5
5	0.625	1.250		1.250		1.250		0.625
4T	0.000	0.000		0.000		0.000		0.000
4B								
3T	0.000	0.000		0.000		0.000		0.000
3B								
2T	0.000	0.000		0.000		0.000		0.000
2B								
1	-0.625	-1.250		-1.250		-1.250		-0.625

INFLOW= 5.0000   OUTFLOW= -5.0000   ΔFLOW= 0.0000

158

Figure 7.29 – Stepwise comparison of FLAC with MS Excel output

Step 1

	Re-Programmed In Excel (No Truncation)						From FLAC/FISH				
	1	2	3	4	5		1	2	3	4	5
5	5.00000E+06	5.00000E+06	5.00000E+06	5.00000E+06	5.00000E+06	5	5.00000E+06	5.00000E+06	5.00000E+06	5.00000E+06	5.00000E+06
4	0.00000E+00	0.00000E+00	0.00000E+00	0.00000E+00	0.00000E+00	4	0.00000E+00	0.00000E+00	0.00000E+00	0.00000E+00	0.00000E+00
3	0.00000E+00	0.00000E+00	0.00000E+00	0.00000E+00	0.00000E+00	3	0.00000E+00	0.00000E+00	0.00000E+00	0.00000E+00	0.00000E+00
2	0.00000E+00	0.00000E+00	0.00000E+00	0.00000E+00	0.00000E+00	2	0.00000E+00	0.00000E+00	0.00000E+00	0.00000E+00	0.00000E+00
1	0.00000E+00	0.00000E+00	0.00000E+00	0.00000E+00	0.00000E+00	1	0.00000E+00	0.00000E+00	0.00000E+00	0.00000E+00	0.00000E+00

Step 2

	1	2	3	4	5		1	2	3	4	5
5	5.00000E+06	5.00000E+06	5.00000E+06	5.00000E+06	5.00000E+06	5	5.00000E+06	5.00000E+06	5.00000E+06	5.00000E+06	5.00000E+06
4	1.33333E+06	6.66667E+05	6.66667E+05	6.66667E+05	0.00000E+00	4	1.33330E+06	6.66670E+05	6.66670E+05	6.66670E+05	0.00000E+00
3	0.00000E+00	0.00000E+00	0.00000E+00	0.00000E+00	0.00000E+00	3	0.00000E+00	0.00000E+00	0.00000E+00	0.00000E+00	0.00000E+00
2	0.00000E+00	0.00000E+00	0.00000E+00	0.00000E+00	0.00000E+00	2	0.00000E+00	0.00000E+00	0.00000E+00	0.00000E+00	0.00000E+00
1	0.00000E+00	0.00000E+00	0.00000E+00	0.00000E+00	0.00000E+00	1	0.00000E+00	0.00000E+00	0.00000E+00	0.00000E+00	0.00000E+00

Step 3

	1	2	3	4	5		1	2	3	4	5
5	5.00000E+06	5.00000E+06	5.00000E+06	5.00000E+06	5.00000E+06	5	5.00000E+06	5.00000E+06	5.00000E+06	5.00000E+06	5.00000E+06
4	2.13333E+06	1.24444E+06	1.15556E+06	1.06667E+06	1.77778E+05	4	2.13330E+06	1.24440E+06	1.15560E+06	1.06670E+06	1.77780E+05
3	2.66667E+05	4.44444E+04	8.88889E+04	4.44444E+04	-8.88889E+04	3	2.66670E+05	4.44440E+04	8.88890E+04	4.44440E+04	0.00000E+00
2	0.00000E+00	0.00000E+00	0.00000E+00	0.00000E+00	0.00000E+00	2	0.00000E+00	0.00000E+00	0.00000E+00	0.00000E+00	0.00000E+00
1	0.00000E+00	0.00000E+00	0.00000E+00	0.00000E+00	0.00000E+00	1	0.00000E+00	0.00000E+00	0.00000E+00	0.00000E+00	0.00000E+00

V. Considerations and Limitations of FLAC

A simple rectangular region (5" x 5") was discretized by a 5×5 grid and permeability values were applied at each cell. To impose variations in k_{ij}'s, k_{12} took a non-zero value (for simplicity it was set to $k_{11} = k_{22}$). Pore pressure of 5×10^6 psi was applied to the top boundary and zero pore pressure was applied to the bottom boundary. FLAC model was developed, pore pressures at all nodes were recorded in every step, and the results were exported into Microsoft Excel. The same problem was simulated using the simplified algorithm in Microsoft Excel. The same value of λ was used in both models to assure the same convergence speed. Figure 7.29 shows the results for P_{ij} values and compares them with each other. It is concluded that:

159

- FLAC tends to generate a numerical error as a result of rounding every P_{ij} value. In the case of this example (Figure 7.29), accumulation of these errors resulted in small deviations of final results. It was observed that more heterogeneous and/or anisotropic media (more variable k_{ij}'s) would enhance this error and *it is concluded that simulation of highly heterogeneous media by FLAC is not recommended.*

- It is observed that heterogeneity and/or anisotropy result in negative pore pressure. By default, FLAC truncates pore pressure and does not allow negative values. Changing the value of FLAC parameter ftense to a large negative number can modify this criterion. However, negative pore pressure could result in cavitations, which is not accounted for. Again, impact of negative pore pressure was not significant in this particular example. It was observed that more heterogeneous media present more difficulty to converge as a result of higher values and number of negative pore pressures. In fact, when the variations in k_{ij}'s became very significant, the finite difference equations did not converge and P_{ij} values moved to infinity in both MS Excel model and FLAC model. *In conclusion, finite difference modeling may not be appropriate for highly heterogeneous media.* In cases where fracturing is not well developed throughout a region, one should seek alternative flow modeling such as discrete network models.

160

- This kind of convergence problem was also experienced in the Yucca Mountain Project. *The 3D flow model did not converge due to "distinctly heterogeneous"[13] nature of the problem.* To overcome this problem in YMP, all fractures permeability values were enhanced 10,000 timed and matrix permeability remained unchanged. It was argued that in a true steady-state condition, the final results should not be impacted.

VI. Simulation of The Proposed Problem

The proposed model of Figure 7.24 was simulated in FLAC^{2D}. The following parameters and boundary conditions were applied:

Grid: 50 x 50 (Largest acceptable mesh in the available version of FLAC)

Size: 14 in x 14 in (largest constructible size, in the physical model)

Saturation: Fixed at 100%

Water density $(\gamma_w) = 0.03611$ lb/in^3

$H_{in} = 46$ in $\Rightarrow$ $P_{in} = \gamma_w H_{in} = 46 \times 0.03611 = 1.661$ psi

$H_{out} = 21$ in $\Rightarrow$ $P_{in} = \gamma_w H_{in} = 21 \times 0.03611 = 0.783$ psi

---

[13] Unsaturated Model and Submodels, YMP Report – page 53.

k_{ij}'s calculated by the proposed SECM model (section 7.2.III). For

FLAC, values of k_{ij}'s needed to be divided by Water density (γ_w).

In the original simulation, numerical convergence did not occur. It was concluded

that a lower-bound threshold of $k_{ij(Min)} = 5 \times 10^{-4} k_{ij(Max)}$ could cause an acceptable

convergence (see Chapter 8). This threshold was applied, the problem was simulated

and the results were compared with a physical model and the model was validated

using a sensitivity analysis, as will be discussed in the next Chapter.

7.4 - A GLANCE AT DISCRETE NETWORK MODEL AND APPLICATION
OF PERCOLATION THEORY

Earlier we discussed the need for a discrete network model in cases that equivalent

continuum model is not practical. A discrete network model (e.g. for Figure 7.24)

needs the "backbone" network only. The backbone network is the only network of

fractures that contributes to flow. Identification of the backbone can simplify DNM

significantly.

Classical percolation theory has developed an algorithm that identified the

percolating clusters and consequently the backbone network. This algorithm, with

some modifications, can be applied to a fractal network of fractures to identify the

backbone network. The classical algorithm looks at all the sites (bonds) to see

162

whether they are "open" or "close" and then looks at the neighbors of an open site (bond). In a fractal model, sites can be considered as cells of a large mesh. In this case openness is defined by the number of dots within each site (cell) and it is not binary (0, 1). A site may be "partially open". In this case, sites that have less occupancy than a percentage of maximum number of dots (e.g. 4% in Figure 7.30) are considered close. The portion of the sites that is open to flow can be translated to fracture aperture. Therefore the backbone network will consist of fractures with variable apertures throughout the region. These variations in apertures influence flow behavior in the medium.

Percolation clustering algorithm was applied to the fracture network of figure 7.24 and the result is shown in figure 7.30. All clusters that do not contribute to flow can be safely eliminated and we will be left with one backbone fracture network (Blue/dark gray cluster). Fracture apertures throughout the network can be estimated by the number of dots in each cell (site) and they are variable. This information can be used as the input to a discrete network model.

163
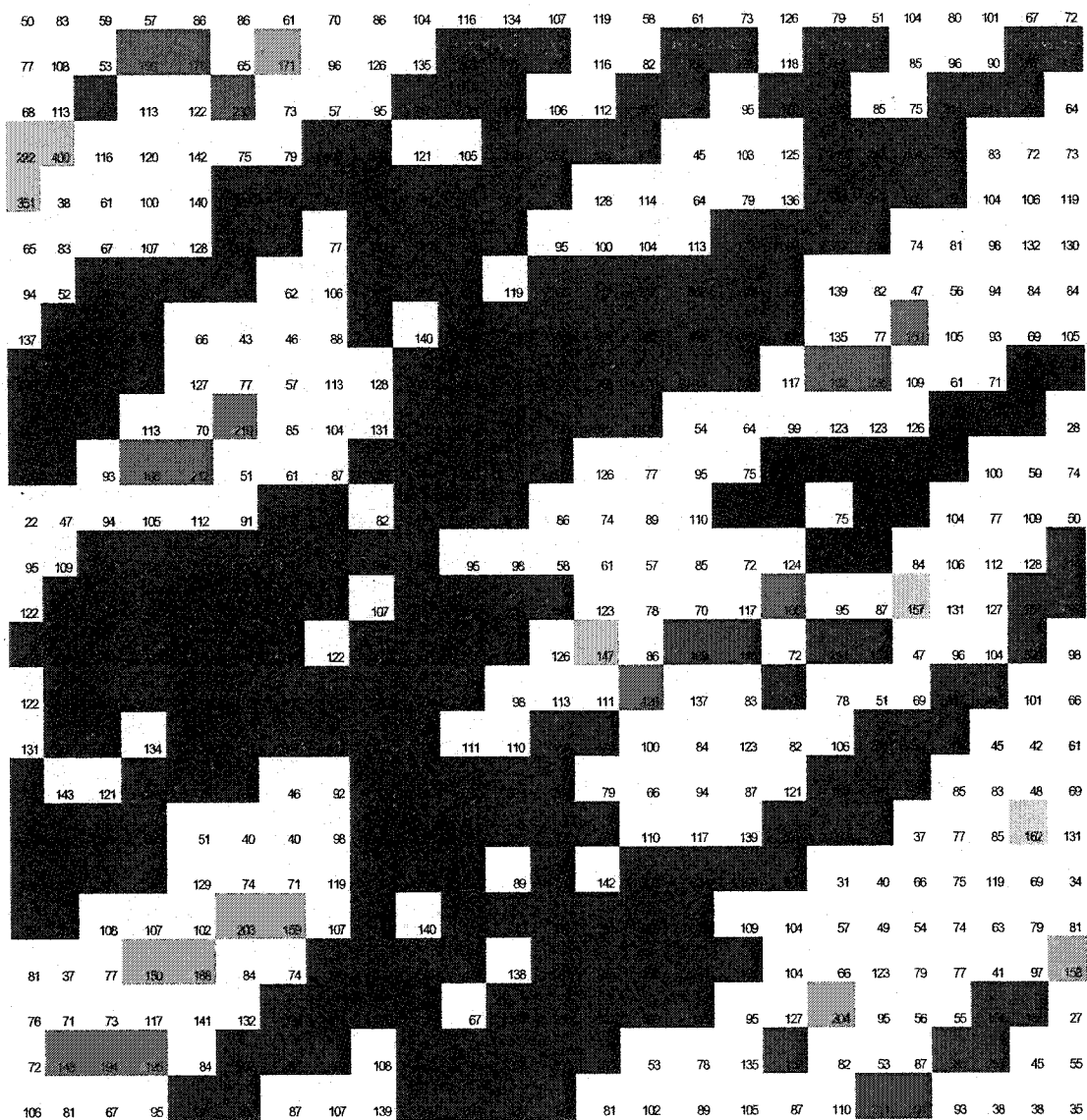
Figure 7.30 – Percolation Cluster Counting Algorithm and Fractal Network of Fractures

164

CHAPTER 8 - EXPERIMENTAL AND STATISTICAL VERIFICATION OF THE FRACTAL BASED FLOW MODEL

8.1 - EXPERIMENTAL MODEL

I. Physical Model Basis: Hele-Shaw Model

In order to verify the results of the proposed flow model (Figure 7.24), a physical model was developed and used. The basis of this model is the *Parallel-Plate Hele-Shaw Apparatus*[14]. Hele-Shaw model is a simple equipment that consists of two parallel plates that are separated by a small gap, flow intake, constant-head tank, flow outlet, reservoir, and a series of piezometers to record hydraulic head variations throughout the system (Figure 8.1). Since Hele-Shaw experiment is based on Darcy's law and its generalized form, Navier-Stokes equations, it is important to have a laminar flow through the region. Therefore a Reynolds number of more that 2,000 is not appropriate. It is proposed that the plates spacing should be less than or equal to 1 millimeter for water and a few millimeters for heavy oil. In any event, flow at the vicinity of boundaries may become turbulent and unreliable. Therefore the larger the model, the better the results.

(a) (b)
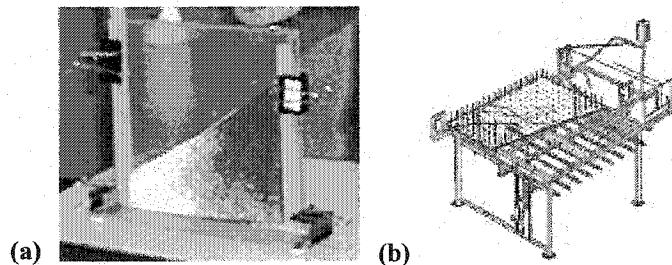
Figure 8.1 – Hele-Shaw Experiment, could be as simple as (a) or as complex as (b).

---

[14] Handbook of Ground Water Development (1990) – Appendix K

165

For the purpose of study, the Hele-Shaw model was modified as follows. Instead of using two parallel Plexiglas plates with a gap, an aluminum plate with the fractal pattern of fractures encrypted in it was covered by a Plexiglas plate, to facilitate flow monitoring.

II. Physical Model Design and Construction:

Figure 8.2.a shows the design of the lower (aluminum) plate. The fracture pattern was carved into the aluminum plate by a CNC machine. The fractal network of fractures of Figure 7.24 was developed using IFP computer program. Due to CNC machine limitations, a computer algorithm eliminated all fractal points that would not form significant fractures, since these points would not contribute to flow. Then, the coordinates of all fractal dots were translated into the CNC machine language and fractures depth was identified as 2 millimeters (see below).

Due to CNC machine movement limitations, a size of 14" x 14" was the largest practical size for the physical model. Fractures depth (aperture) in this model is equivalent to the parallel plates spacing in the Hele-Shaw model. From practical point of view and due to the small size of the model, 2 millimeters fractures depth was used. This is a little more than the "1 millimeter" that is recommended for water. Therefore possibility of turbulence flow for water was initially predicted.

166

Based on measure theory of fractals, as long as a considerably large number of very small dots are generated, flow properties are independent from the number and size of the dots (see Test #1 of section 8.3). This is, however, a restriction for the physical model. The physical model is using only 20,000 data points (5,000 per set). Therefore, the size of the dots should be proportional to their size in the printout of the computer model. This consideration dictated a mill size of 0.1" for the CNC machine. The resulting fracture pattern (Figure 8.3.b) was compared to the computer model (Figure 8.3.a) to assure that they have identical flow pathways.
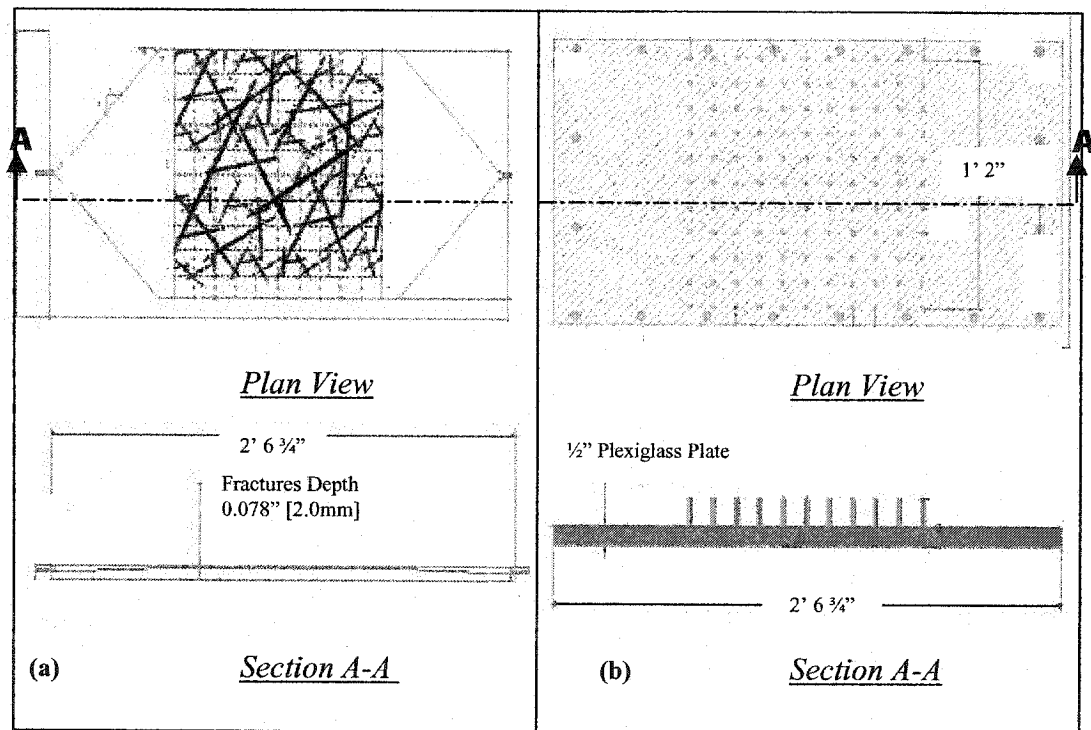
Figure 8.2 – (a) Aluminum plate with fracture pattern.
(b) Plexiglas Plate to monitor flow

167
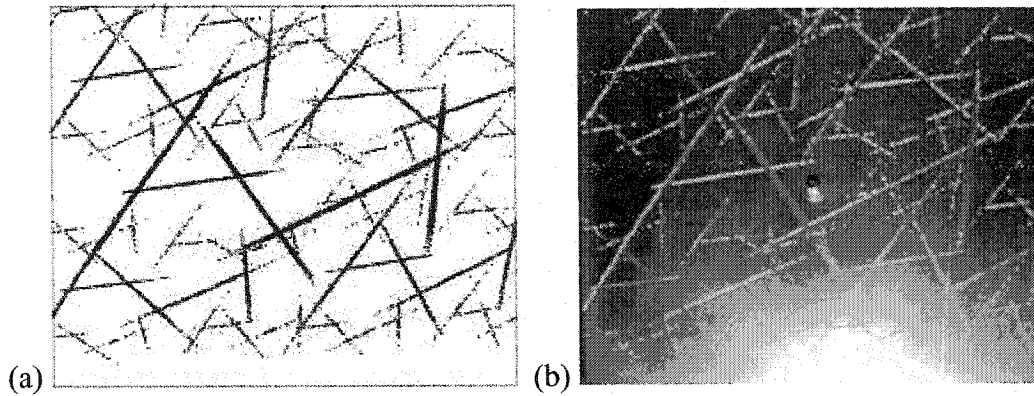
Figure 8.3 – (a) Fractal Model, eliminated isolated fractal points after 20,000 iterations.
(b) Equivalent fracture network, encrypted on an aluminum plate, using CNC machine.

III. Physical Experiment

The preliminary experiment with pure water indicated possibility of turbulence flow, as predicted. The experiment results are summarized in Figure 8.4. To verify turbulence possibility, Reynolds Number (Re) was calculated as follows:

$$\Re_e = \frac{u \bullet D}{v}$$

Where: $\Re_e$ = Reynolds Number : $\begin{cases} \Re_e \prec 2,000 \Rightarrow Laminar \\ 2,000 \prec \Re_e \prec 3,000 \Rightarrow Transitional \\ 3,000 \prec \Re_e \Rightarrow Turbulence \end{cases}$

$u =$ Fluid Velocity (in/min)

$D =$ Diameter = Diameter of the equivalent pipe. For a rectangular duct $(a \times b)$, $D = 4R_h = 4\dfrac{a \cdot b}{2(a+b)}$ [15]

$v =$ Kinematic Viscosity of fluid – for water: $v = 0.09150$ $in^2/\min$

---

[15] Roberson and Crowe (1993) – Page 449

168

For the particular case of Figure 8.4, lets consider the large intake pipe that passes through piezometers 9R and 4L. This is a duct with width 0.14^{in} and thickness 0.078^{in} (2^{mm} fractures depth). The amount of flow through this fracture is 62.5% of the total inflow, since the other intake fracture's width is 60% of this fracture (it is a copy of the initial fracture with $\rho_1 = \rho_2 = 0.6$). Therefore, Reynolds number is calculated as:

$$\left. \begin{array}{l} \textit{Measured Discharge} \quad Q = 25 \times 0.625 = 15.625 \ in^3/\min \\ \textit{Cross Section:} \quad A = 0.14^{in} \times 0.078^{in} = 0.01092 \ in^2 \end{array} \right\} \Rightarrow u = \frac{Q}{A} = \frac{15.625 \ in^3/\min}{0.01092 \ in^2} = 1,430 \ in/\min$$

$$D = 4R_h = 2\frac{a \cdot b}{a+b} = 2\frac{0.01092 \ in^2}{(0.14+0.078)^{in}} = 0.100 \ in; \ v_{water} = 0.09150 \ in^2/\min$$

Therefore: $\quad \Re_e = \frac{u \bullet D}{v} = \frac{1,430 \times 0.100}{0.09150} = 1,563 \quad \leftrightarrow \quad 2,000 \Rightarrow$ Close to Transitional

Flow

This calculation shows that if pure water is used, flow will be close to the transitional regime. In transitional zone, flow interchanges between laminar and turbulence. Therefore, laminar flow model (Darcy's law) in not applicable. This justifies the large deviation between experiment and the numerical model results (section 8.2), for pure water.

169

#	t (sec)	W (Kg)	Q (Cm³/Sec) (1)	Q (in³/min) (1)x60x(1/2.54³)
1	90	0.612	6.800	24.898
2	60	0.422	7.033	25.752
3	90	0.624	6.933	25.386
4	60	0.408	6.800	24.898
5	90	0.602	6.689	24.491
6	90	0.606	6.733	24.654
Average (μ)			6.831	25.013
Standard Deviation (σ)			0.129	0.472
Relative Deviation (σ/μ)			1.9%	1.9% O.K.

Piez.#	Reading"	h"
1L	36 1/4	46 1/4
2L	36 1/4	46 1/4
3L	31 3/4	41 3/4
4L	29 1/8	39 1/8
5L	27 3/4	37 3/4
6L	27	37
7L	22 3/8	32 3/8
8L	21	31
9L	18 1/2	28 1/2
10L	11	21
1R	11	21
2R	13 1/2	23 1/2
3R	11	21
4R	16	26
5R	17 7/8	27 7/8
6R	24 5/8	34 5/8
7R	26 1/4	36 1/4
8R	30 1/8	40 1/8
9R	31 1/2	41 1/2
10R	36 1/4	46 1/4
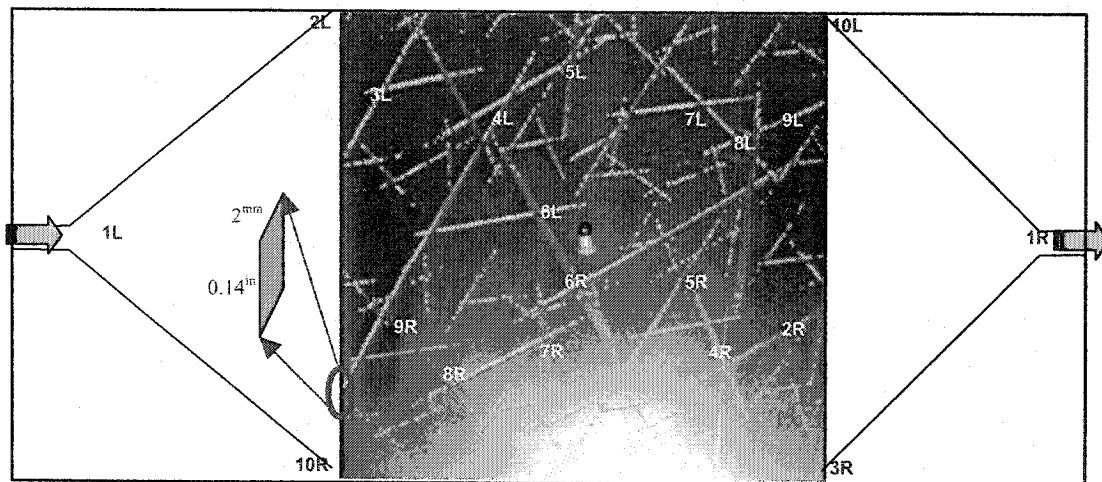
Figure 8.4 – Pure water flow physical model and experiment results

Based on the above observation, it was necessary to repeat the experiment with less viscous fluids. An additive called Hydroxypropyl methylcellulose (HPMC) was added to water at various proportions. Stewart et al. (1998) showed that solving various proportions of HMPC in water changes waters viscosity. They developed

170

Figure 8.5 that could be used to achieve a desired viscosity by mixing the right

proportions of HPMC powder. This relation was modeled by $v_{20^{0}c} = 6.92 \cdot C^{2.54}$,

where $v_{20^{0}c}$ is viscosity at 20^{0C} and C is HPMC concentration (%). Stewart et al.'s

finding was used and the experiment was repeated for the 0.5%, 1.0%, 2.0% and 3%

concentrations of HPMC. The results were used for verification of the numerical

model and sensitivity as follows.
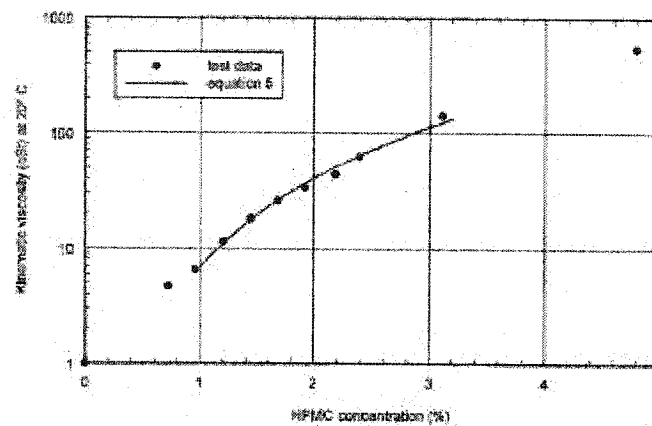
HPMC%	v (ft ^{2}/s)
0.0	1.059E-05
0.5	3.230E-05
1.0	7.530E-05
2.0	4.300E-04
3.0	1.070E-03

Figure 8.5 – Water viscosity as a function of HPMC concentration
(from Stewart et al. -1998)

8.2 - NUMERICAL MODEL VERIFICATION

I. Comparison with Physical Experiment

The physical model was used to verify the numerical model results. Various mixtures of water-HPMC were experimented and values of viscosity, discharge, and boundaries hydraulic heads were recorded. Viscosity and hydraulic head values were used as input parameters for the FLAC^{2D} model, permeability tensors for FLAC^{2D} were calculated from the proposed SECM flow model (section 7.2). To eliminate biases due to algorithm randomness, average of 20 runs, each with 300,000 iterations, was used. The problem was also analyzed using deterministic fractal algorithm and the classical equivalent continuum model (modified Oda − 1985). Alternatively, an equivalent pipe-network model was developed and analyzed. Development of the pipe network model is explained in appendix C.

Figure 8.6 summarizes the outcomes of the three models (Classical ECM, Proposed fractal model, and pipe-network), in comparison with the physical model. Comparison of the results provide the following conclusions:

172

HPMC Percentage	Viscosity υ (ft²/sec)	Observed Head DH (in)	Observed Discharge Q (in³/min)	Calculated Discharge (Modified ODA) Q (in³/min)	Error1 2(Calc.-Obs.)/(Calc.+ Obs.)	Calculated Discharge (Proposed Model) Q (in³/min)	Error2 2(Calc.-Obs.)/(Calc.+ Obs.)	Pipes Network	Reynolds Number (Observed)
0.0%	1.059E-05	25.25	25.000	162.44	146.6%	171.00	149.0%	54.81	1,563.82
0.5%	3.230E-05	15.50	15.500	32.69	71.3%	32.61	71.1%	22.76	317.89
1.0%	7.530E-05	14.50	10.000	14.50	36.7%	14.10	34.0%	10.20	87.97
2.0%	4.300E-04	13.00	0.682	2.06	100.5%	1.90	94.3%	1.72	1.05
3.0%	1.070E-03	13.25	0.659	0.84	24.6%	0.75	12.9%	0.71	0.41

Effects of HPMC Density on Discharge
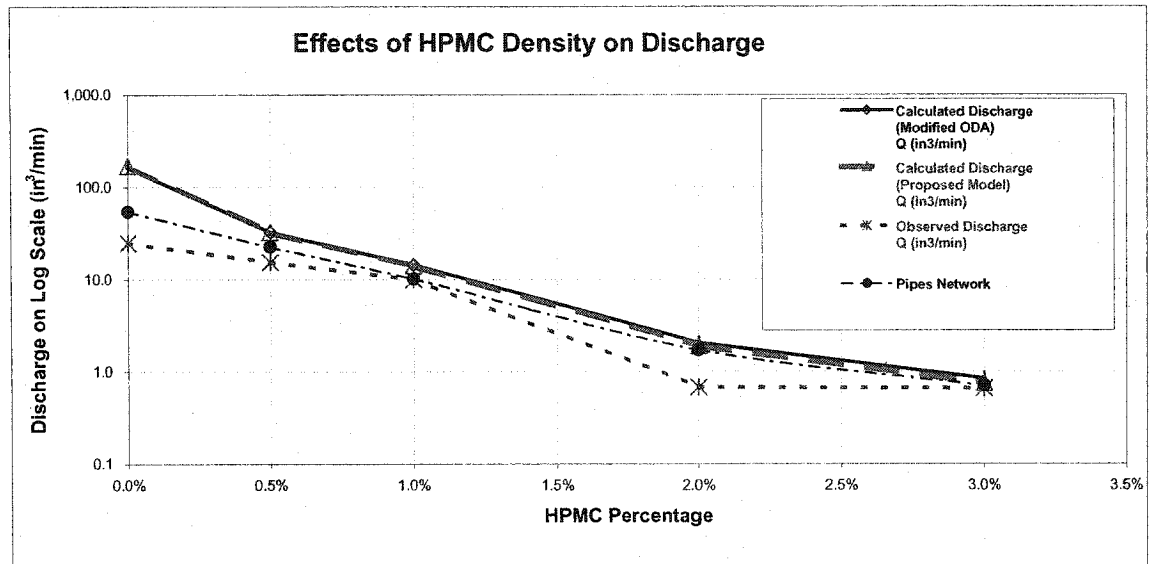
Figure 8.6 – Comparison of results between classical flow model, proposed fractal model, pipe-network model, and physical experiment. In best case (1%HPMC), observation is 32% less than estimation.

- The first observation in this graph is the proximity of the fractal model to the classical equivalent continuum model. This outcome was predictable, since both models have the same foundation and use the same laminar flow assumptions. In general (with the exception of 0% HPMC[16]), classical ECM provides a little higher discharge. While this difference is insignificant, it could relate to smoothness of fractures surfaces in the classical ECM. In the fractal model, fractures roughness is accounted for using confidence interval around the trend-line. The hydraulic aperture is therefore less than the

---

[16] The results of 0% HPMC are not reliable, since we are close to laminar/turbulence transitional flow zone.

173

mechanical aperture and smaller discharge is calculated. Selection of the right confidence interval could result in more realistic flow calculations. In addition to accounting for joints roughness, the other advantage of the proposed model compared to classical ECM is its ability of study internal behavior of the system and flow pattern, whereas classical ECM only provides macroscopic information (total flow amount throughout the system).

- Due to the large Reynolds number for the 0% HPMC experiment, the flow is not always laminar in this case. As a result, the observed discharge is considerably less that the calculated discharge by the proposed model, due to the significant head losses. As the viscosity increases (higher HPMC concentration), Reynolds number decreases and we move into laminar flow. This explains the proximity of the results at 1% HPMC. However, more concentration of HPMC results in too much viscosity, high shear stress and friction at fractures surfaces, and deviation from laminar flow regime. Note that the deflection point may be somewhere between 1% HPMC and 2% HPMC. Additional experiments could find the deflection point more accurately. For the purpose of this study 1% HPMC as the deflection point is accurate enough. Above 2% HPMC, viscosity becomes so high that discharge becomes almost independent from change in viscosity. This could be attributed to the increased discharge measurement errors as a result of high viscosity, as well as extreme friction at fractures walls.

174

- The pipe network model has very good agreement with the other two models and, again, its prediction is closest to the observation at 1% HPMC. In general, predictions of the pipe network model are above the observations, but below the other two models. Pipes network assumes that the dead-end portions of the pipes can contribute to flow. Therefore it over-estimates total discharge. However, the results are smaller than ECM, due to the fact that ECM assumes that all fractures contribute to flow. It is expected to have more agreeable results between the two models (ECM and pipe network), if the region is well fractured and the pipe network is considerably larger.

- In the best-case scenario (1% HPMC), calculated discharge from the proposed model is 29% more than the observed value (1-10/14.1). In the next part we will see that smaller number of iterations and elimination of fractal points in the physical model was responsible for this deviation.

Based on the above observations, 1% HPMC was used as the comparison benchmark. In the numerical model head distribution was calculated using FLAC/FISH program. In the physical model, hydraulic head was recorded at all piezometers. Figure 8.7 shows modeled head distribution compared to experiment observations. With the exception of 3 deviations shown by (◄), results are in agreement. Contribution of the localized error resulted in an overall error of 9.51%, which is considered acceptable (<10%). Also a correlation analysis between observed head and estimated head, showed good agreement: The regression line is

175

very close to (y=x) and the correlation coefficient is very close to 1.0:

$$R^2 = 0.9026 \Rightarrow \rho = \sqrt{R^2} = \sqrt{0.9026} = 0.95.$$

Piez. #	Estimated	Observed	ε(Obs. - Est.)
3L	43.87	44.00	0.13
4L	39.64	41.00	1.36
5L	37.41	39.00	1.59
6L	38.83	40.50	1.67
7L	34.45	37.00	2.55
8L	33.55	36.00	2.45
9L	32.23	35.00	2.77
2R	32.28	33.00	0.72
4R	34.73	34.50	-0.23
5R	34.92	35.75	0.83
6R	38.81	39.50	0.69
7R	40.35	40.50	0.15
8R	42.83	42.50	-0.33
9R	43.86	44.00	0.14
Relative Error (σ_ε / Range) =			9.51%
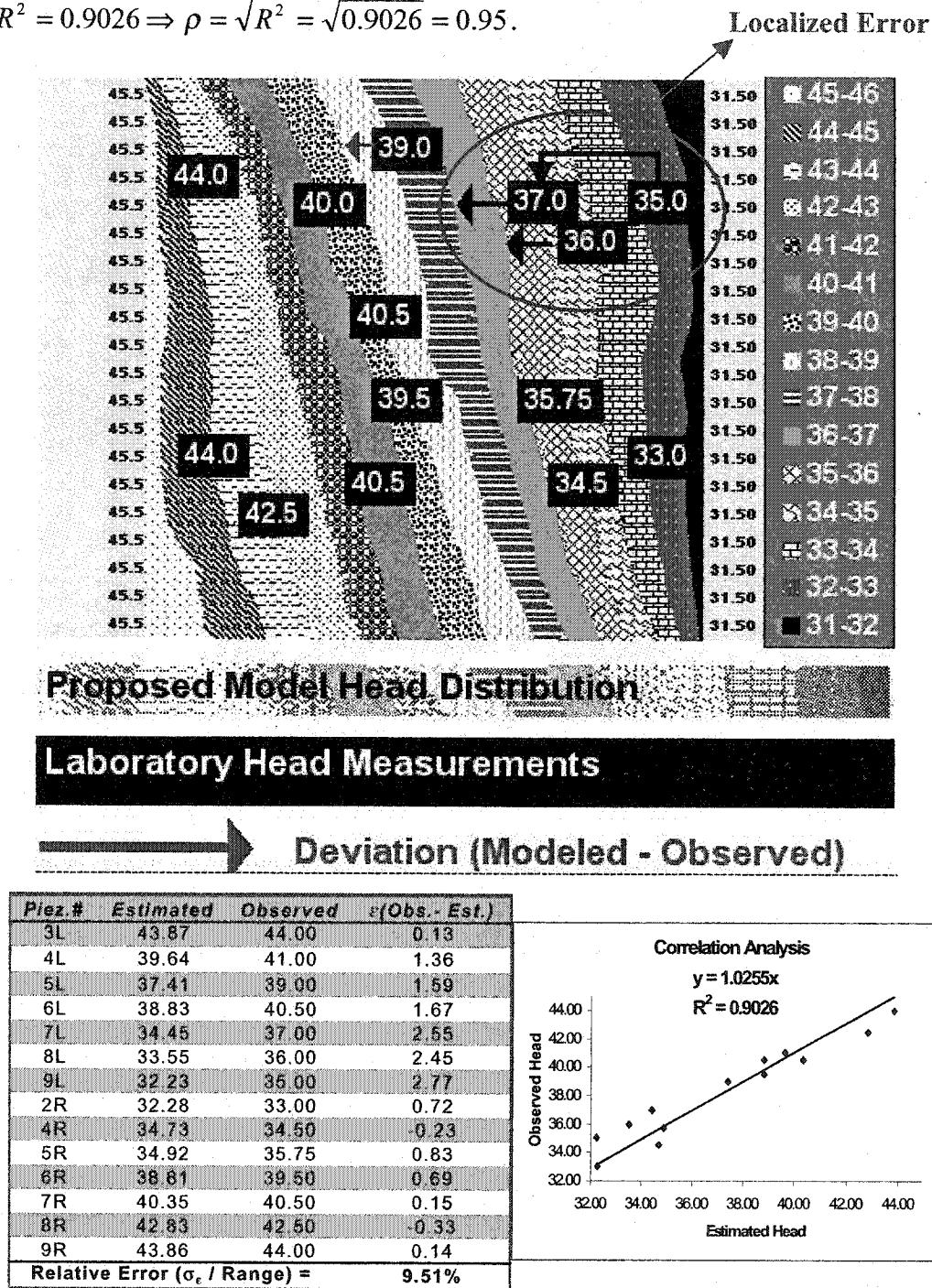
Figure 8.7 – Comparison of results error analysis for 1% HPMC

II. Sensitivity Analyses

In order to confirm fractal model stability and accuracy of the above results, a number of sensitivity tests were performed a explained below:

- *TEST #1 – Hydraulic Properties Stability*: Based on measure theorem of fractals, the shape of a fractal image remains constant in various simulation runs, after a large number of iterations. It is expected that hydraulic properties of a fractal network of fractures should remain constant, as well. Sensitivity tests were needed to validate this hypothesis and to identify the number of iterations above which hydraulic properties remain unchanged. In order for this, two tests were performed. In the first test, trend-line parameters (a and α) of an arbitrary cell in a fracture network were monitored for various iterations. It was observed that for number of iterations larger than 200,000, variations of a and α become insignificant (Figure 8.8). To confirm that the same kind of stability exists in the overall system, a second test was performed: the proposed flow problem was solved for different numbers of iterations and total discharge was calculated for each simulation. As Figure 8.9 shows, it was found that if the number of iterations per fracture set is larger than 200,000, variations of calculated discharge become insignificant (less than 1.2%). This confirms stability of hydraulic properties for a fractal network of fractures, as long as number of iterations remains very large ($\geq$200,000 per fracture set in this case). It is also

177

interesting to note that changes in finite difference equations convergence

becomes insignificant, for iterations larger than 200,000.
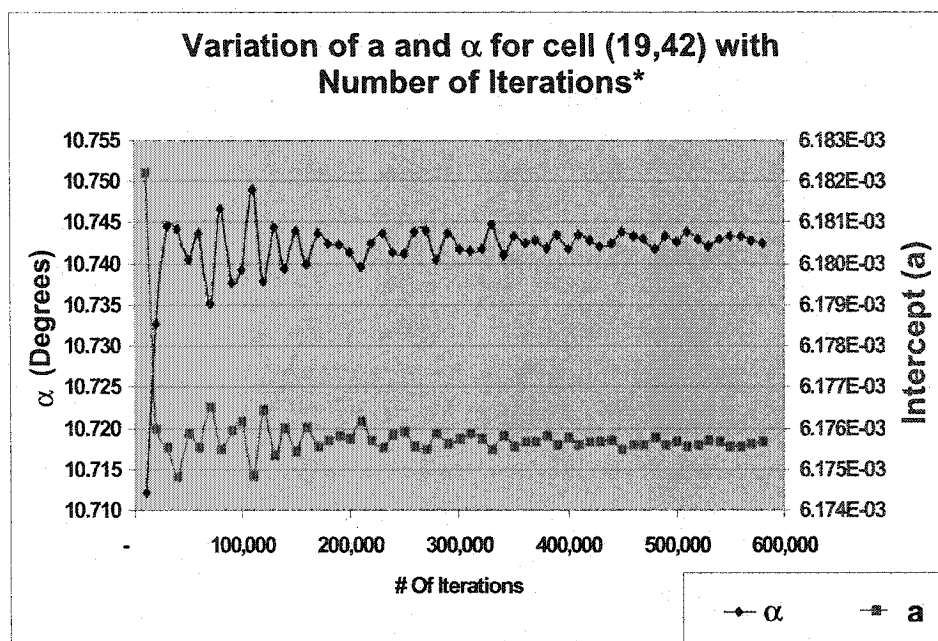
Figure 8.8 – Stability of Trend-line in an arbitrary cell
* Each point represents average of 1,000 runs
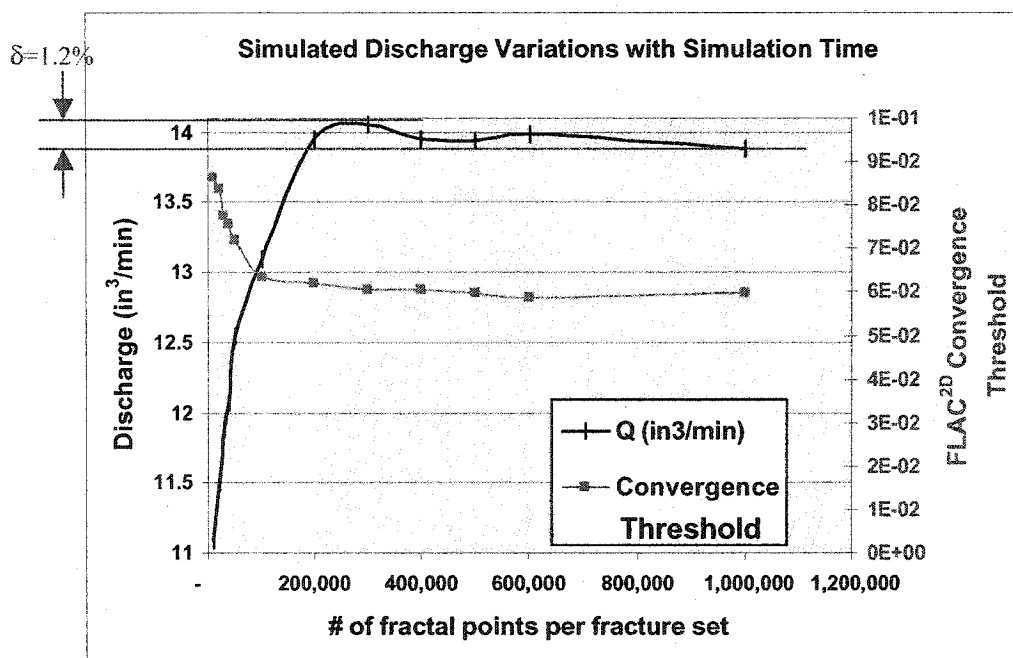
Figure 8.9 – Overall Flow Stability, independent form (large) number of iterations

178

- *TEST #2 – Limitation of Physical Model:* Based on the above finding, 300,000 iterations per fracture set was used as the basis of simulating the proposed model. The physical model, however, was simulated using 5,000 iterations per set, only, due to practical limitations. Since this number is less than the stability threshold (200,000), its impact should be taken into account. From Figure 8.9 it is readily concluded that the observed discharge would be at least 20% less that the actual value [(14-11)/14]. To get a more accurate prediction lets go back to the deterministic algorithm and apply classical equivalent continuum model (Figure 8.10). Properties of all fractures are available and overall permeability tensor is calculated using equation 7-7. Average velocity is calculated by multiplying the overall permeability tensor by the overall flow gradient ($\Delta H/\Delta L$). Discharge is calculated by multiplying velocity by the equivalent cross section (Figure 8.4): ($2^{mm} \times 11^{mm}$). This calculation was performed for two models:

1. Complete network of fractures (Figure 8.10.a) ➔ $Q_{Actual} = 14.50$ in^3/min

2. Partial network, physical model (Figure 8.10.b) ➔ $Q_{Phys. Model} = 10.0$ in^3/min
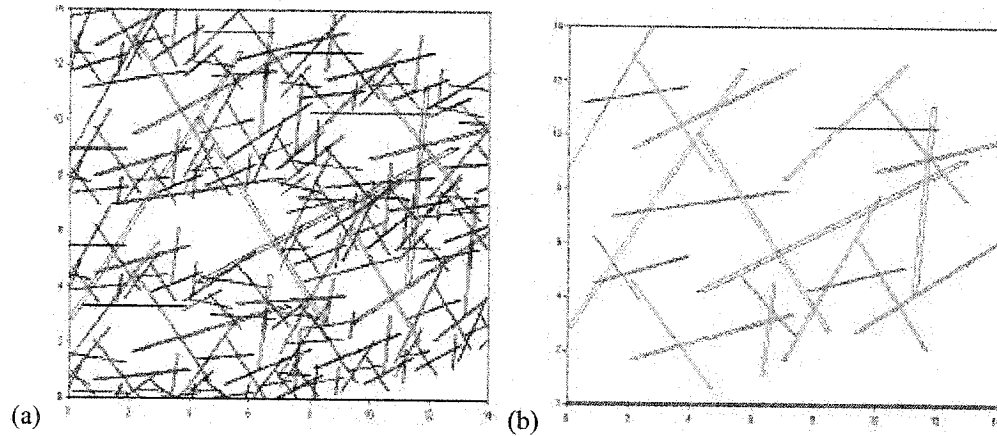
Figure 8.10 – Proposed Problem Fracture Network (deterministic fractal algorithm)
(a) Network with 250 fractures (50 per set). (b) Equivalent to physical model

It concludes that the physical model provides 69% of the discharge that is predicted by the proposed model (10/14.5). This finding provides the rational for the ~30% difference that we observed between physical model and the numerical model (refer to Figure 8.6 and related discussion.)

- *TEST #3 – Permeability Lower-Bound impact:* In order to make finite difference equations converge, it was necessary to use a lower-bound value for permeability. An appropriate value for this lower-bound should be identified. A very low value would not improve convergence and a very high value would impact the outcomes. As Figure 8.11 shows, lower-bound larger than $5\times10^{-4}\times K_{max}$ provide reasonable convergence threshold (less than 0.1). Therefore, small permeability values are truncated by: $5\times10^{-4}\times K_{max}$. Note that the technique we propose here is different from the one used for Yucca

180

Mountain Project. This technique has less impact on the final result, since the change in small K_{ij}'s is insignificant.
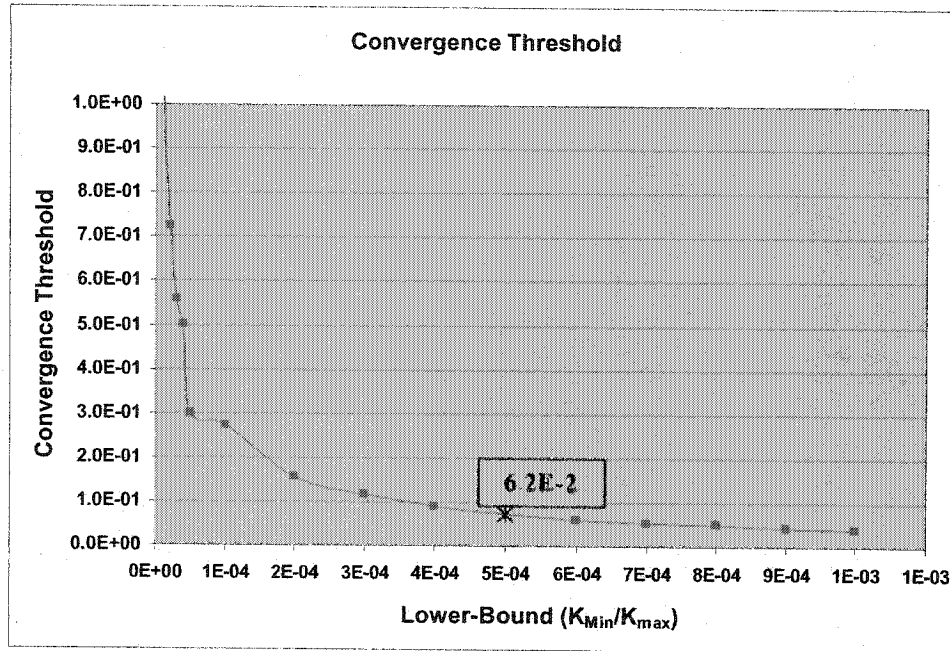
Figure 8.11 – Selection of Permeability Lower Bound

- *Test #4 – Scale effect:* Due to self-similar nature of the proposed problem, it was hypothesized that flow properties are controlled by sample size. Based on the relations: $u_i \propto \left(\sum l \cdot t^3 \right)\big/ L^2$ and $Q_i \propto u_i$, and from self-similarity we have: $l \propto L$ and $t \propto L$, therefore it is hypothesized that: $Q = c \bullet L^2$. This hypothesis was tested and a perfect correlation was found between Q and L^2. Figure 8.12 shows the result of the regression analysis, and proves that this hypothesis is correct. This finding proves that the scale problem that we experience in classical ECM modeling, for sizes smaller than representative elementary volume (REV), does not exist in a fractal model of fracture

181

networks. If the region has a true fractal nature, and if the fractal model is accurately representative of the field conditions, results of a lab scale model can be confidently extrapolated to obtain field scale predictions.

Variations of Discharge with Sample Size (Fluid = 1% HPMC Mixture)

$y = 0.065x^2$
$R^2 = 0.998882$
$S^2_{y|x} = 0.00607$

Q (in3/min)
Power (Q)
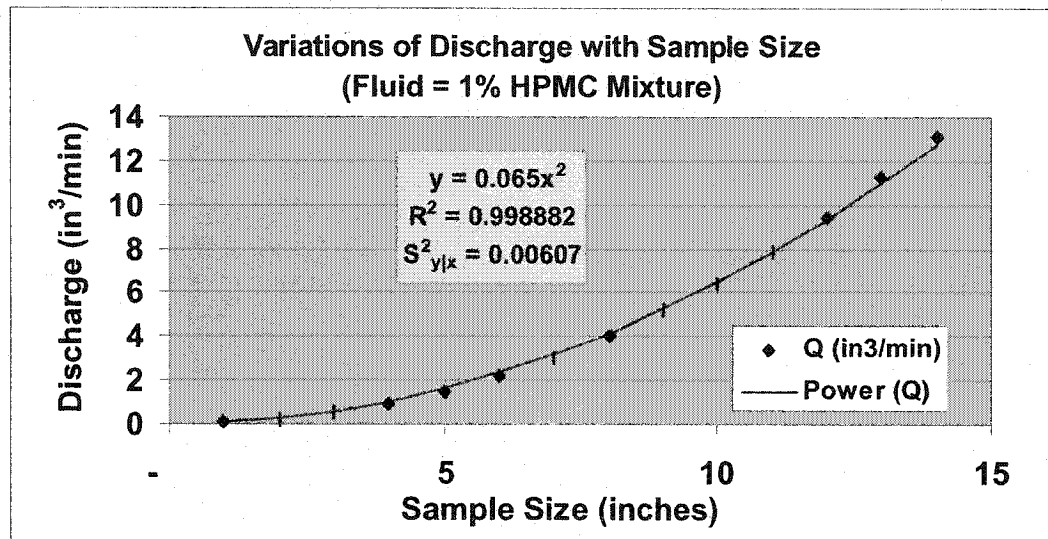
Figure 8.12 – Scale effects for a self-similar fracture network

182

CHAPTER 9 - POTENTIAL FOR PRACTICAL APPLICATIONS

9.1 - OVERVIEW OF YUCCA MOUNTAIN PROJECT

U.S. Department Of Energy (DOE) identified Yucca Mountain as a potential site to construct, operate, and close a repository for the disposal of spent nuclear fuel and high-level radioactive waste. The proposed site is located at Yucca Mountain, Nye County, Southern Nevada (100 Miles Northwest of Las Vegas). Project location and layout are presented in Figure 9.1.

Among numerous studies, it was necessary to verify hydraulic conductivity and transport properties of the region in order to predict possible contamination of groundwater through nuclear waste transport. Therefore, it became vital to develop complete flow and transport models. To estimate and calibrate models parameters, numerous site investigations were conducted. These investigations were conducted in three stages. In stage 1, flow was monitored through a large number of pre-existing boreholes (Figure 9.2). Results of this investigation provided a global estimate of flow behavior in the region. At stage 2, an exploratory tunnel was constructed that basically encircled the proposed repository site. The exploratory Study Facilities (EFS) was used to collect information on fractures patterns and conduct hydraulic tests. To better characterize the media and validates outcomes of stage 2, a new exploratory tunnel was constructed in stage 3. This tunnel would cross the repository block and it was named "enhanced characterization of repository

183

block" (ECRB) or "Cross-drift". Rock stratification and fractures properties were identified through these tunnels and hydraulic tests were conducted through various "niches" in both EFS and ECRB. All information were compiled into databases and were available on Yucca Mountain Project website (www.ymp.gov). Numerous flow and transport models were developed and the results of these models were also available on the project website.
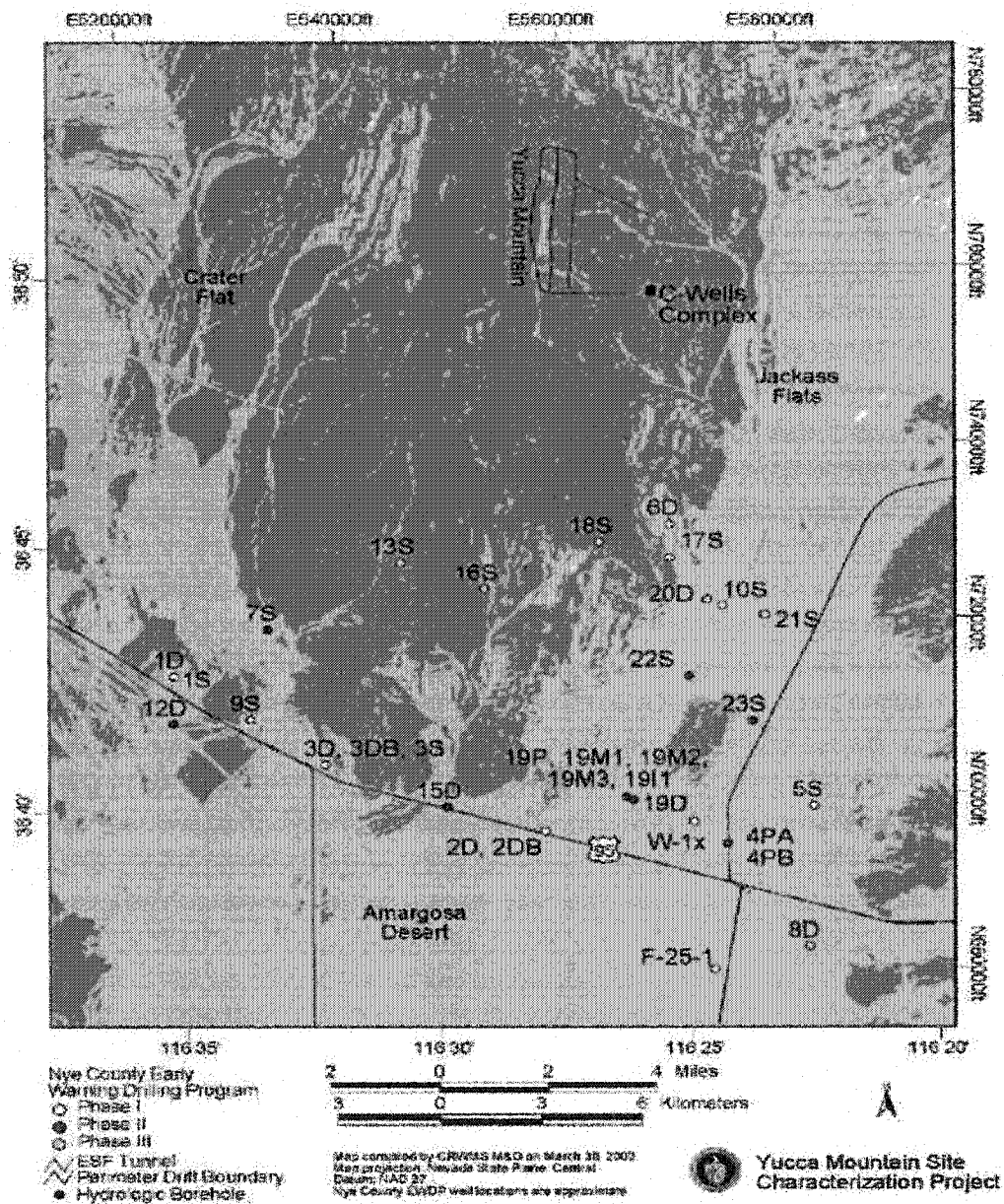
Figure 9.1 – Yucca Mountain Project Layout and Location
(Yucca Mountain Science and Engineering Report – 2001)

185
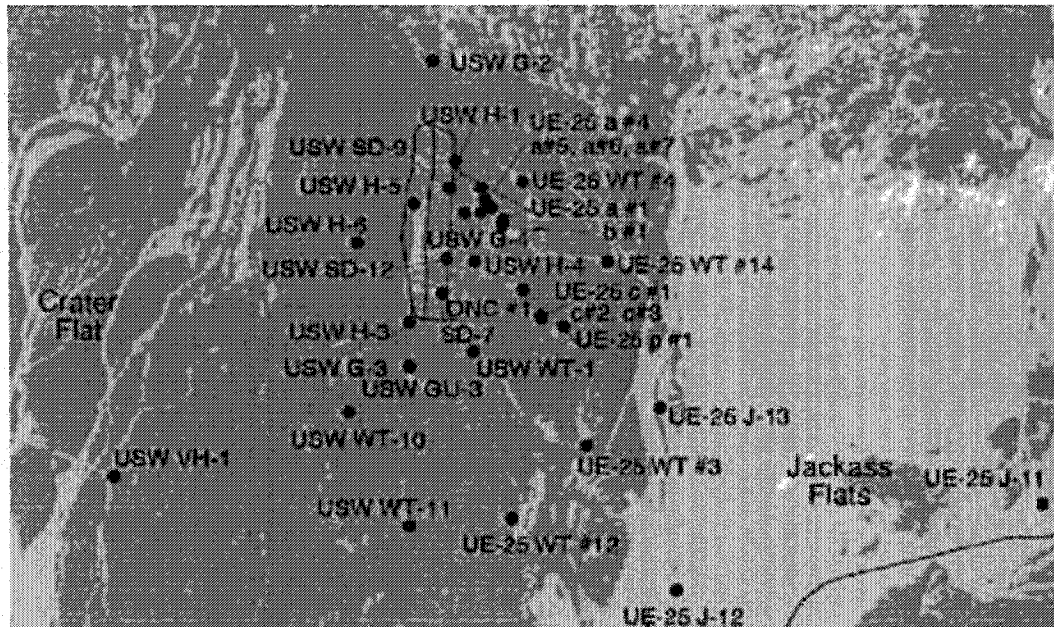
Figure 9.2 – Pre-existing Boreholes, used to conduct stage 1 investigations
(Yucca Mountain Science and Engineering Report – 2001)

9.2 - GEOLOGY

I. Regional Geology

Regional geology has been investigated through numerous boreholes and some 6 miles of tunnels, since 1950's. Yucca Mountain is believed to be formed as a result of faults moving on sides of the western United States basin (Great Basin), over the past 15 million years.

186

In general, in the area surrounding Yucca Mountain, rocks are sedimentary or metamorphic and they are not very permeable. Gneiss and Schist are the most common and oldest rocks, dating some 1.7 billion years ago. The upper layers are less metamorphosed rocks composed of quartzite, siltstone, shale, and carbonates. Carbonate layer is the only aquifer layer and the rest are aquitards and <u>rock fractures</u> <u>are the primary conductors of groundwater flow</u>. Most of the aquifer carbonates (dolomite and limestone) are identified in Spring Mountain, between Yucca Mountain and Las Vegas. These aquifers are the sources of underground water for Yucca Mountain and flow direction in the region can be predicted from status of these aquifers.

II. <u>Local Geology</u>

Most of the rocks at Yucca Mountain are tuffs which are resulted from large volcanic activities between 14 and 7.5 million years ago. These rocks are known as paintbrush group and cover the area that will embed the proposed repository. Site Stratigraphy is shown in Figure 9.3. Paintbrush group consists of three tuff layers; Tiva Canyon welded tuff, Topapah Spring welded tuff, and non-welded tuffs (below repository). Topapah Spring will be the host rock for the proposed repository.

187

(b) Detailed Stratigraphic Column

Figure 9.3 – Geological Stratigraphy at the Proposed Repository Location (Yucca Mountain Science and Engineering Report – 2001)

188
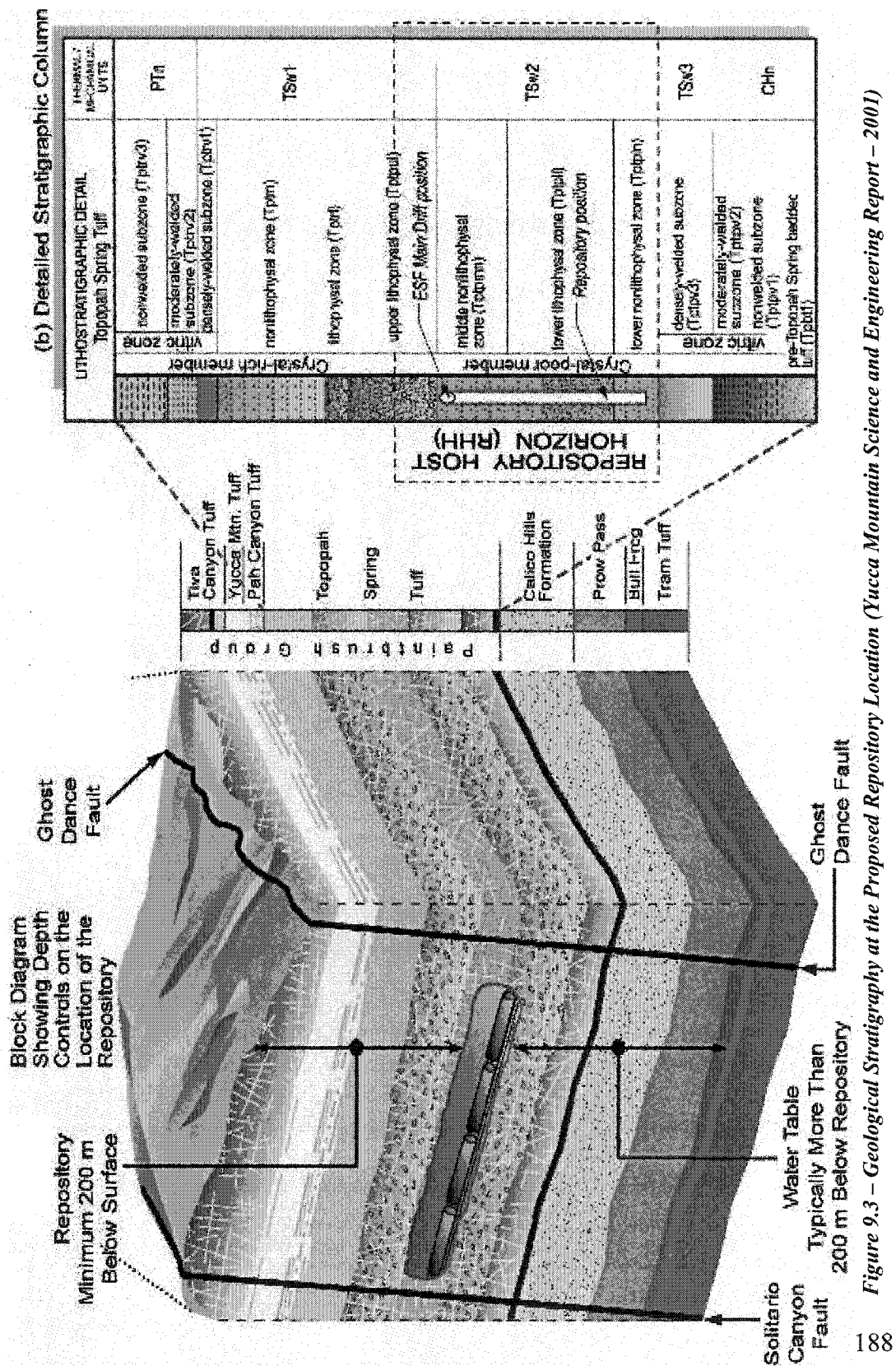
III. Hydrogeologic Units

The repository region, which is the basis of the unsaturated flow model, is divided into 5 major hydrogeologic units (Figure 9.3). Fracturing of these rocks is highly controlled by their degree of welding. These fractures are, in general, thermal fractures resulting from cooling down of the magmas. If the cooling down process was slow, the material becomes very well welded, more brittle, and highly fractured with very low matrix permeability. Quick cooling down of magmas results is non-welded and less fractures rocks with relatively more matrix permeability. A brief description of hydrologic properties of various units of the unsaturated zone (UZ) is provided here:

- *Tiva Canyon welded (TCw)* is the topmost unit that is observed at the ground surface. It is highly fractured with almost zero matrix permeability. The high density of fractures provides very well connected network of connected pathways for groundwater to flow, without seeping into rock porosities, due to low matrix permeability. Water can flow quickly and pass through this layer into the next one (PTn).

- *Paintbrush non-welded (PTn)* is predictably more porous and less fractured. During transition from TCw to PTn, groundwater flow changes from rapid fracture flow to slow matrix flow and in PTn layer flow is mainly through rock porosity and there are very few connected fractures to accelerate flow.

189

Due to its high storage capacity and slow discharge from this unit, flow of water in units underneath PTn are considered to be steady. Steady-state flow in the repository region is an important assumption that simplifies the flow model, significantly.

- *Topapa Spring welded (TSw)* is, again, well fractured and has low matrix permeability. Due to this rapid increase in permeability, the area above TSw (bottom of PTn) may be assumed to be saturated. This stored water above TSw could initiate fracture flow through TSw. Different sub-layers of TSw vary in degree of welding and abundance of lithophysae. In general, flow is dominated by fractures and matrix flow is very limited in this layer.

- *Calico Hills non-welded (CHn)* has low fracture intensity and relatively higher matrix permeability. In the lower half part of this layer, fractures become more significant and matrix permeability becomes less, due to higher degree of welding.

- *Crater Flat undifferentiated (CFu)* is non-welded to densely welded and shows significantly different flow properties at different locations. The non-welded portion of this unit has been altered from tuff to zeolite. This zeolitic portion has very low matrix permeability and slightly grater fracture permeability. This is an aquitard with very small room for water to flow (mainly through limited fractures).

190

It is interesting to see how groundwater flow changes from slow matrix flow to rapid fracture flow and back. These changes result in storage of water at various elevations and possibility of considering some parts of the flow as saturated and/or steady state to simplify the flow model.

9.3 - VARIOUS MODELS AND FLOW MODEL

I. Saturated and Unsaturated Zone Models

Numerous models were developed to verify appropriateness of the Yucca mountain site to host a nuclear repository. The study was conducted at two scales (Figure 9.4). An unsaturated zone was defined and an unsaturated zone (UZ) model was developed to investigate flow of rainfall water through the repository and transport of nuclear waste into the underground water. The saturated zone (SZ) that covers a larger region would look into possibility of transporting the nuclear waste out of the region, after (and if) it reached the underground water.

Figure 9.5 provides a summary of various models for unsaturated zone to study climate, rainfall infiltration rate, flow, transport, and seepage through the potential repository site, and many other factors. In line with the objective of this study, a brief summary of the UZ flow model is provided next.

191
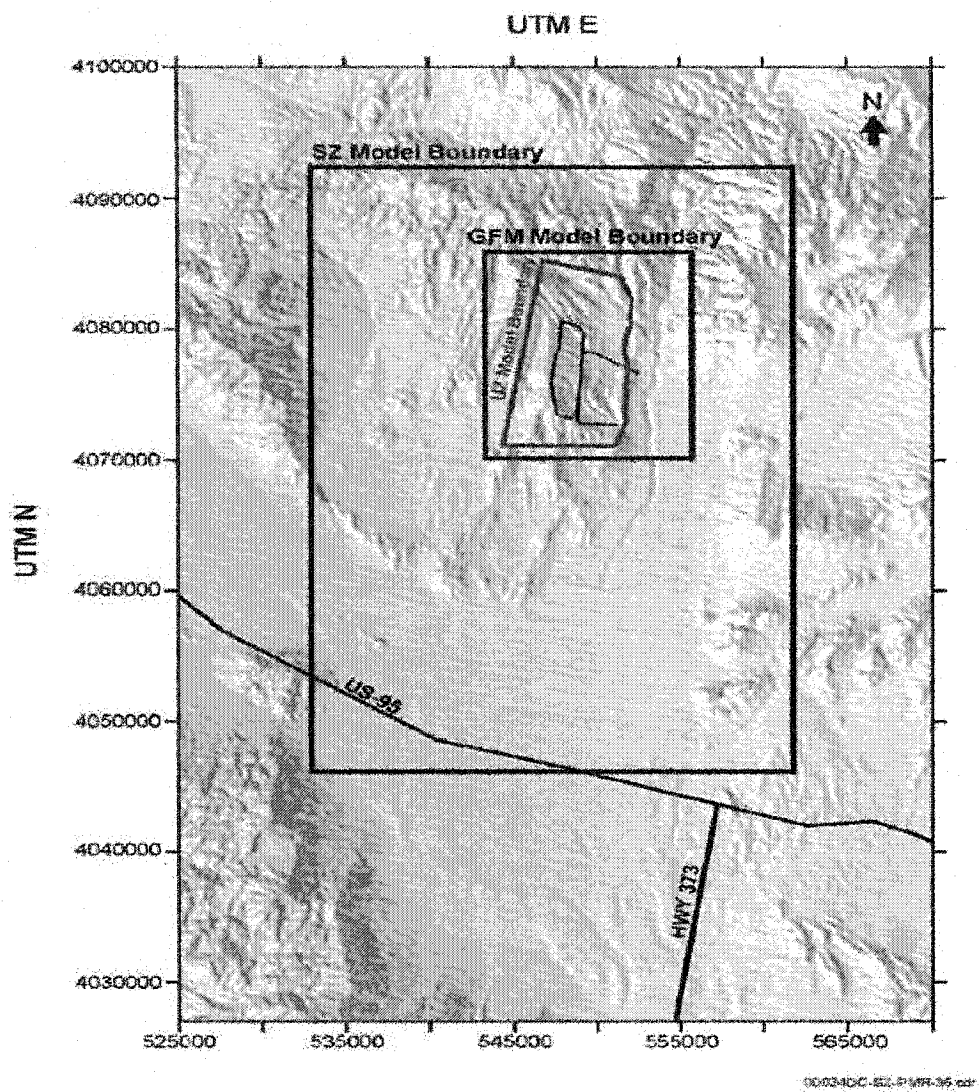
Figure 9.4 – Saturated and Unsaturated Zones Boundaries
(Yucca Mountain Science and Engineering Report – 2001)

192
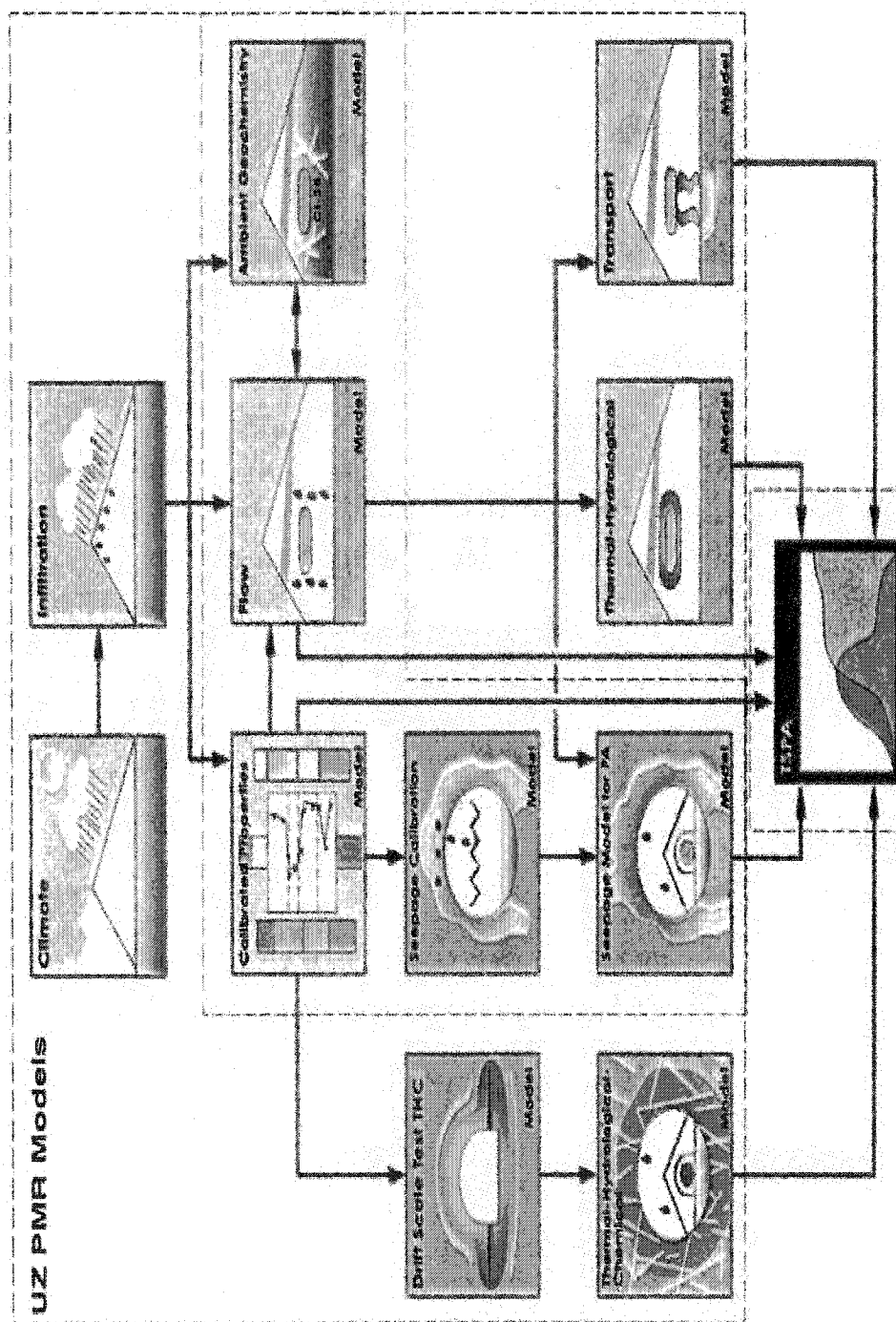
*Figure 9.5 – Various Unsaturated Zone Models
(Yucca Mountain Science and Engineering Report – 2001)*

193

II. Unsaturated Zone Flow Model and Outcomes

The essential assumptions of the UZ flow model were based on geological and hydrogeological findings:

- Steady-State Flow due to permeability barriers

- Fixed Saturation and pressure at bottom boundary

- No-Flow Lateral Boundaries (Media bounded by impermeable faults)

The input parameters consisted of fracture data, collected from Data Line Scanning (DLS) at exploratory tunnels (ESF and ECRB), Flow data and initial saturation data, collected at various niches inside the exploratory tunnels. Some examples of available fracture data are shown in Figures 9.6 and 9.7.
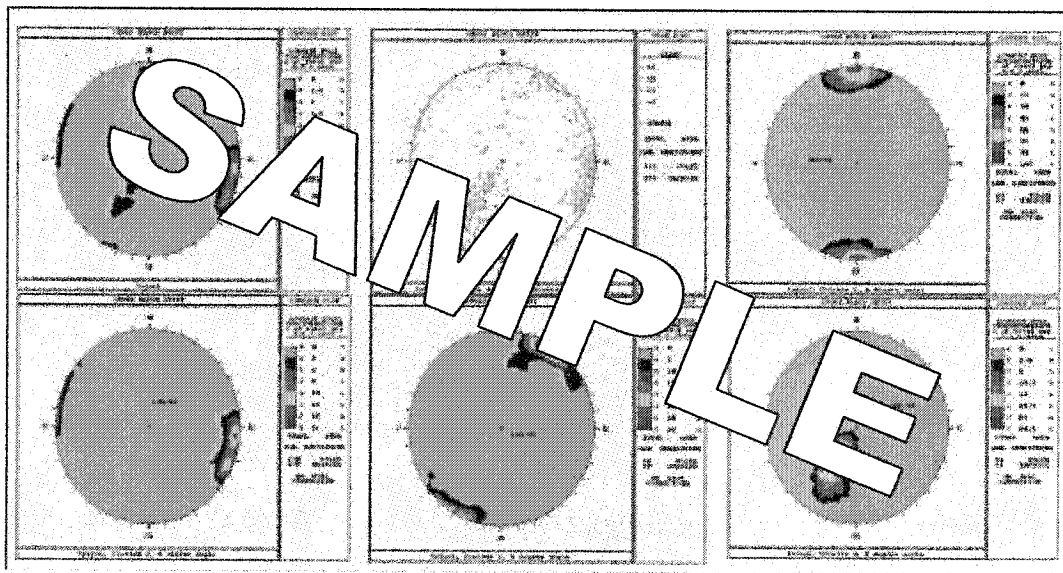
Figure 9.6 – Fracture Orientation Data: Tptpul Contour Plot for Clusters 1 through 3
(Yucca Mountain Science and Engineering Report – 2001)

194

Cross Drift Fracture Apertures
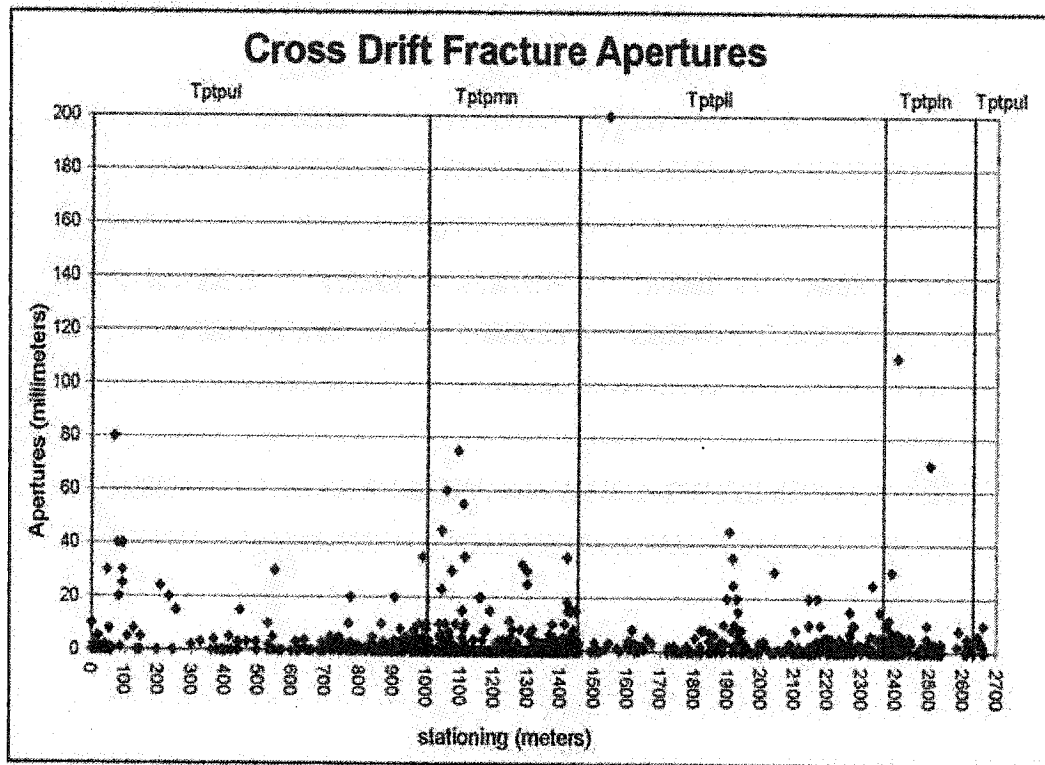
*Figure 9.7 – Fracture aperture data: DLS investigations at Cross-Drift tunnel
(Yucca Mountain Science and Engineering Report – 2001)*

A 3 dimensional equivalent continuum model (ECM) was used to simulate the problem. A dual-porosity model was used for this purpose. The region was discretized as shown in Figure 9.8 (plan), permeability tensors were calculated for each mesh, and a finite difference program (TOUGH2) was used to estimate flow and equivalent permeability of each layer of the unsaturated zone. Seven scenarios were applied to account for effects of perched water (lack, bypassing, or flow-

195

through) and account for various infiltration scenarios (present day lower-bound, mean and upper-bound). The simulation results showed good agreements with hydrologic investigations.
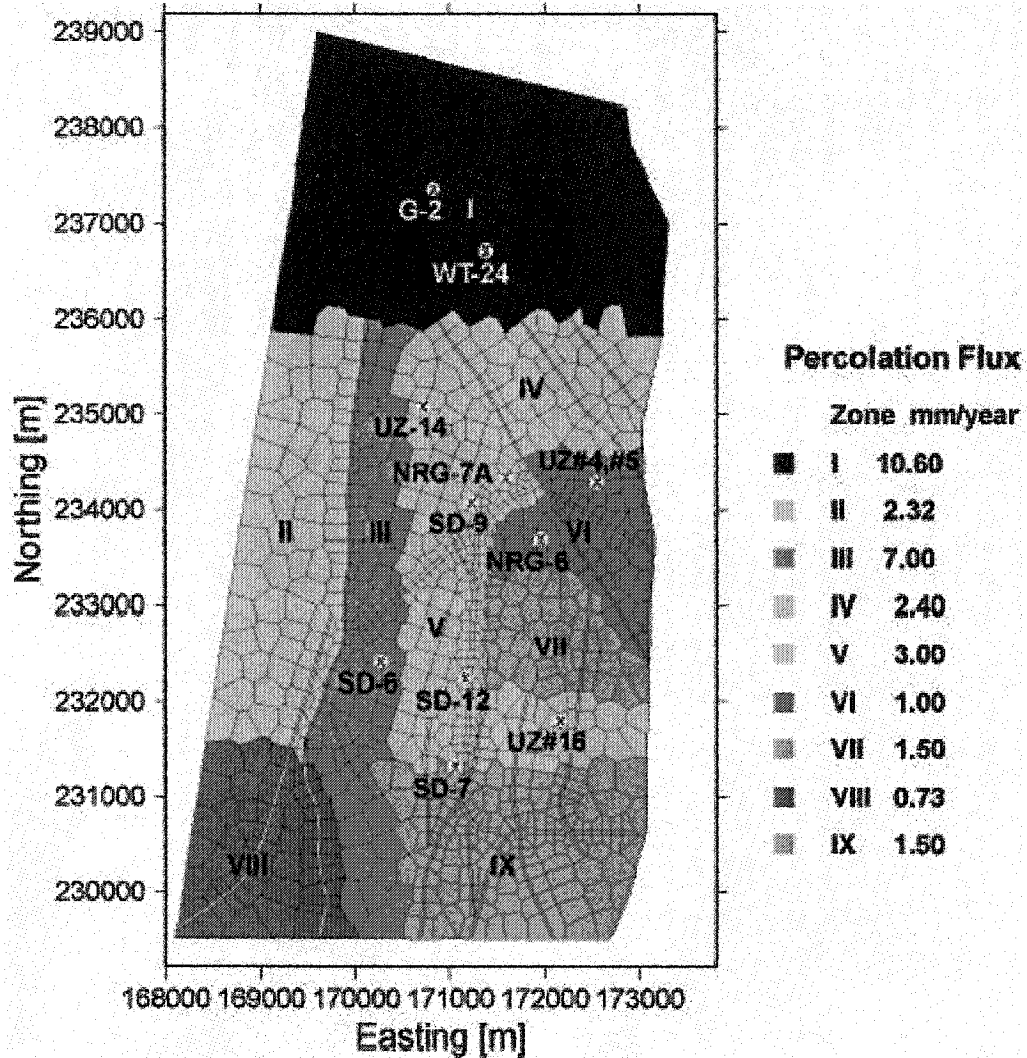
Figure 9.8 – Repository region discretization and sample output (Yucca Mountain Science and Engineering Report – 2001)

196

The numerical model of Yucca Mountain Project was more complicated than just Darcy's law. Richards' equation was used to account for partial saturation and van Genuchten model provided capillary functions. Detailed discussion of the simulation process and results verification is provided in "Unsaturated Model and Submodels" report of Yucca Mountain Project, which can be requested from www.ymp.gov.

9.4 - APPLICATION TO THIS STUDY

It has been shown that fracture patterns at Yucca Mountain have a self-similar nature. Upon data availability, it would be interesting to develop a fractal model for the above problem and compare the results with the previous models and field observations. One limitation of the model proposed in this study is non-applicability to unsaturated flow problems. It would be necessary to modify the model to account for partial saturation.

An initial step was taken in this study and a fractal model for one fracture set was developed. Data on one fracture set at the cross drift (ECRB) tunnel that went through Tptpul layer (see Figure 9.3) was downloaded from the project web site. The pattern of this fracture set is presented in Figure 9.9.

197

DLS Data for Fracture Set #3 Through
TPTPUL Layer of Cross-Drift Tunnel
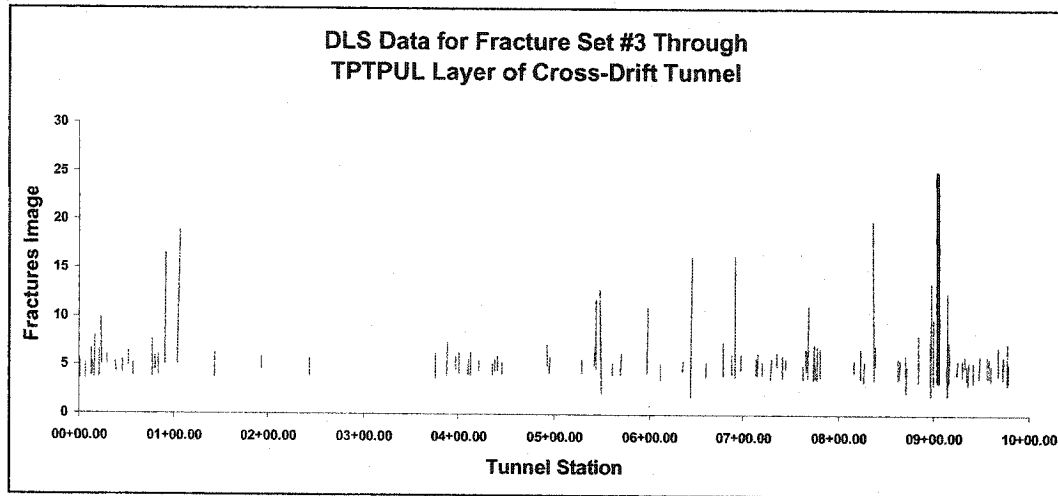
Figure 9.9 – Sample fractures image from Cross-Drift tunnel
(Yucca Mountain Science and Engineering Report – 2001)

Considering the largest fracture (shown in black) as the initial object, we seek the IFS Code that generates a pattern that looks like Figure 9.9. ρ_1 and e can be predicted using shadow theorem of fractals, based on the observed clustering of fractures. Distribution of fractures centers on x-axis is shown in Figure 9.10. Based on the observed clustering, the cantor set on the x-axis must result in the following transformation:

$$[0.00 \quad 1.00] \xrightarrow{\sim Map} \{ [0.00 \quad 0.11] , [0.14 \quad 0.24] , [0.38 \quad 0.45] , [0.50 \quad 0.79] , [0.82 \quad 0.98] \}$$

Therefore, IFS codes in x direction can be easily defined:

$$w_i = ax + b \qquad \Rightarrow \qquad [0.00 \quad 1.00] \xrightarrow{Map} [b \quad a + b]$$

198

$$\Rightarrow \begin{cases} w_1 : [0.00 \quad 1.00] \xrightarrow{\quad Map \quad} [0.00 \quad 0.11] \Rightarrow a = 0.11 \quad , \quad b = 0.00 \\ w_2 : [0.00 \quad 1.00] \xrightarrow{\quad Map \quad} [0.14 \quad 0.24] \Rightarrow a = 0.10 \quad , \quad b = 0.14 \\ w_3 : [0.00 \quad 1.00] \xrightarrow{\quad Map \quad} [0.38 \quad 0.45] \Rightarrow a = 0.07 \quad , \quad b = 0.38 \Rightarrow \therefore \\ w_4 : [0.00 \quad 1.00] \xrightarrow{\quad Map \quad} [0.50 \quad 0.79] \Rightarrow a = 0.29 \quad , \quad b = 0.50 \\ w_5 : [0.00 \quad 1.00] \xrightarrow{\quad Map \quad} [0.82 \quad 0.98] \Rightarrow a = 0.16 \quad , \quad b = 0.82 \end{cases} \begin{cases} w_1 = 0.11x + 0.00 \\ w_2 = 0.10x + 0.14 \\ w_3 = 0.07x + 0.38 \\ w_4 = 0.29x + 0.50 \\ w_5 = 0.16x + 0.82 \end{cases}$$
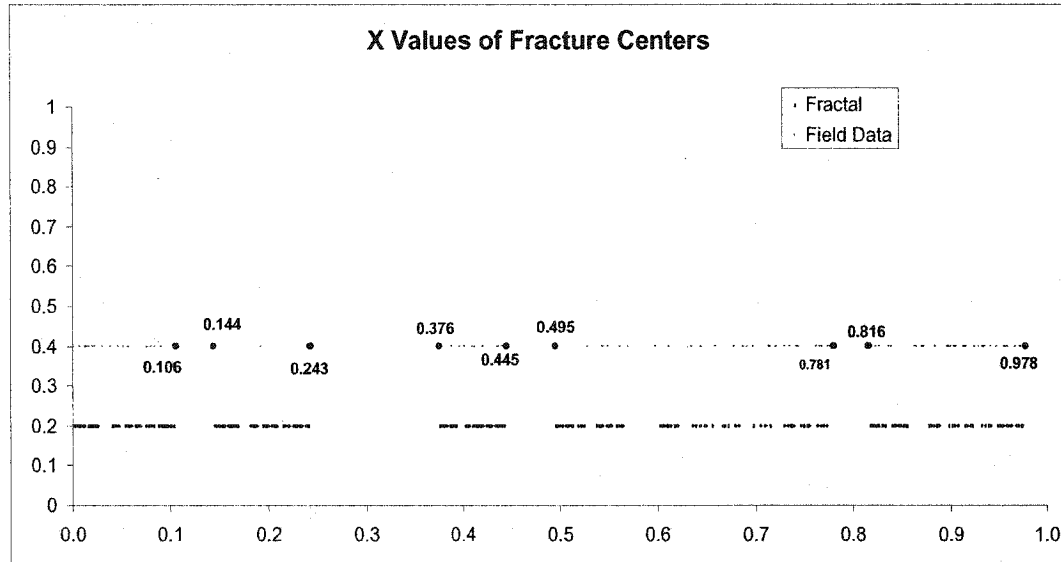
Figure 9.10 – Application of Shadow Theorem to identify IFS Codes in x direction

The cantor set from the above IFS code is shown as blue (dark) dots in figure 9.10. IFS codes in y direction are identified in a similar manner. Although, The accuracy in y direction is much less, since fractures centers are too close in y direction and their overlapping results in some difficulties (Figure 9.11).

199

Y Values of Fracture Centers

- Fractal
- Field Data
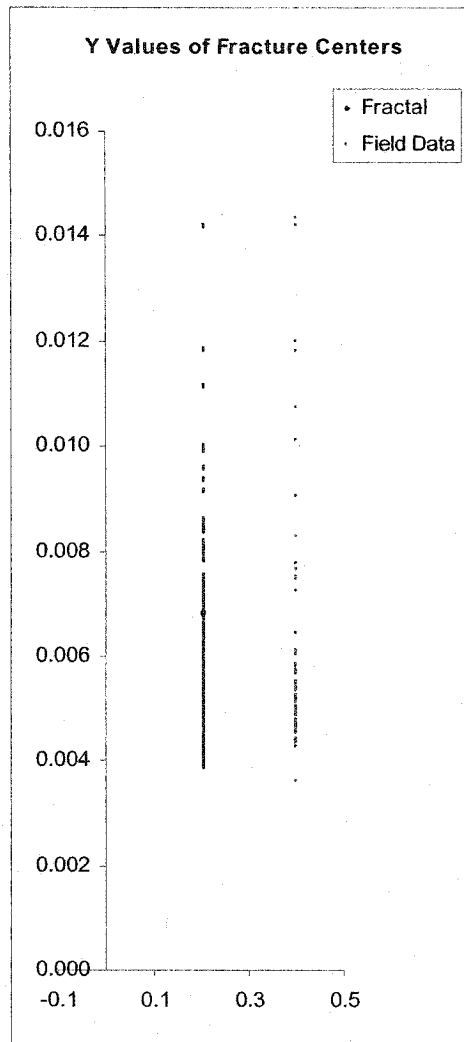
Figure 9.11 – Application of Shadow Theorem to identify IFS Codes in y direction. Accuracy is much less than x direction, due to overlapping between v=0.004 and v=0.008.

The other IFS parameters were identified arbitrarily, by a dynamic link with statistical distribution of fractures length, spacing, and orientation. Kolmogorov-Smirnov (K-S) parameter gets updated instantly at each alteration of IFS codes and shows whether statistical distributions are acceptable. After some trials, the IFS codes were identified that would produce a fracture set similar to Figure 9.9 with acceptable statistical properties (K-S value, mean, and standard deviation), as shown in Figure 9.12.

200
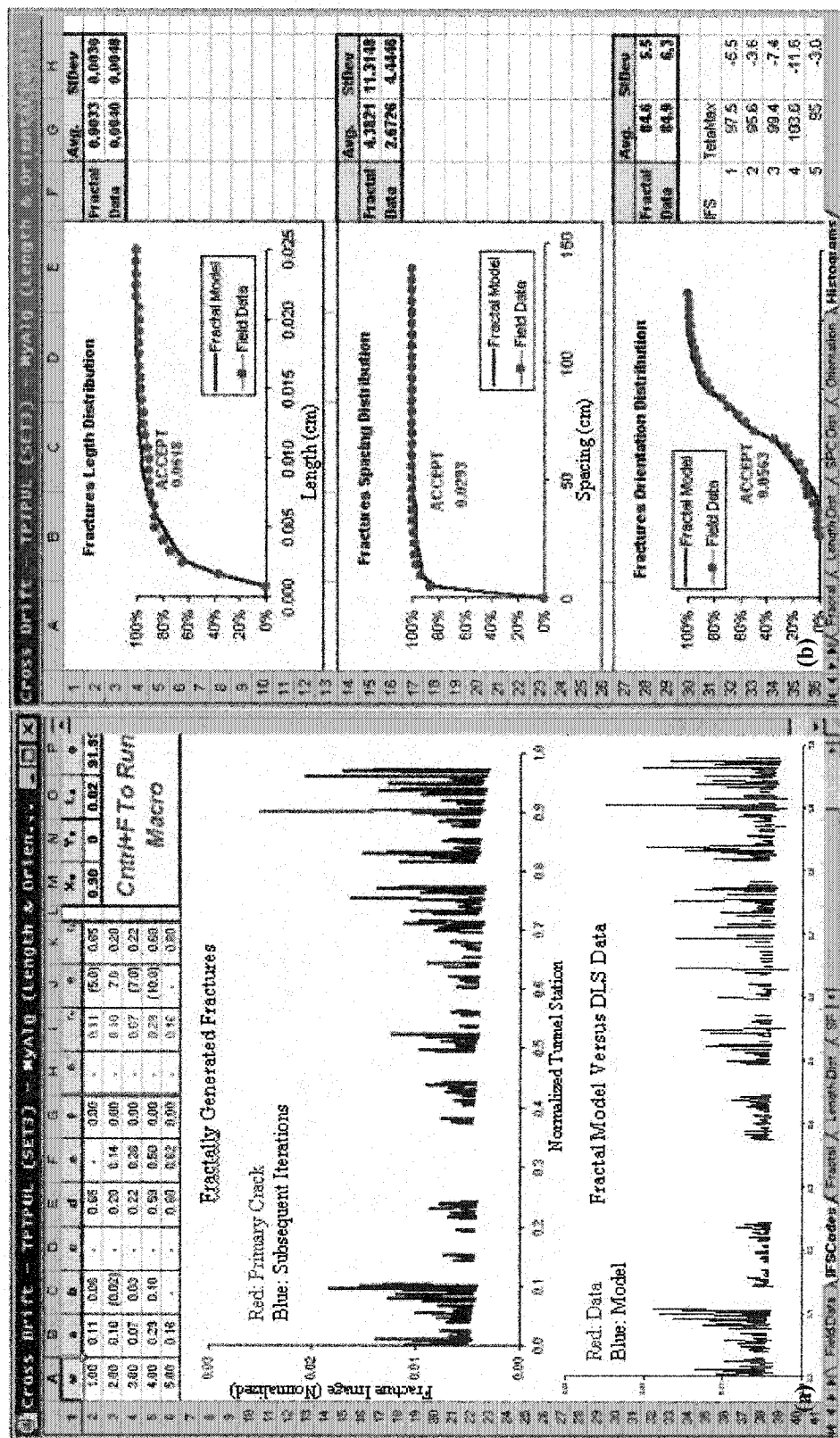
Figure 9.12 – (a) Comparison of the fractures images with the proposed fractal model.
(b) Statistical tests for fractures length, spacing, and orientation.

The above example shows the potential of the proposed fractal model to simulate real world problems. It is noteworthy that it is almost impossible to create a fractal pattern that would look exactly like the given fracture set (see Figure 9.12a closely). It is, however, reasonable to assume that flow properties of the model are similar to the ones of the real problem, since the largest factures (the major contributors to flow) are in relatively good agreement. In any event, this model is much more realistic than a pure statistical model: Numerous fracture sets could be generated with the same statistical properties as Figure 9.12.b, but with patterns totally different from Figure 9.12.a.

It would be interesting to develop a complete fractal fracture network model, continue with the flow model, and compare the results with the previous models and field data. This goal was not achieved due to restrictions on the information of Yucca Mountain Project. This could be a good contribution to this work in future (see Chapter 10).

CHAPTER 10 - CONCLUSIONS AND RECOMMENDATIONS

10.1 - REPORT SUMMARY

Several researchers have acknowledged limitations of the classical models to characterize fractured media and study fluids flow in a network of fractures. Among various limitations of the classical statistical models, this report identified the following as the most important ones:

- Extensive data collection is necessary in order to develop a reliable statistical model and intensive computations are required.

- Statistical methods are associated with scale dependence. Identification of an appropriate scale (REV) is very difficult and, sometimes, impractical.

- Statistical model do not provide stable results. Various simulations of the same problem with the exact same assumptions and parameters may result in totally different flow outcomes.

- Fractures appear to have predefined paths to grow and they appear in clusters that are denser on some areas. Fractures are not developed in a random manner.

203

- Fracture parameters interactions cannot be accounted for effectively, using the current statistical techniques.

The above limitations of current models were the primary motivation for this work. Modern techniques such as hydrologic inversion and percolation theory were reviewed and their contributions and limitations were discussed. Need for a more practical model was identified – a model that provides a realistic image of the fracture network and provides reliable flow predictions, based on limited filed observations.

Both fracture mechanics and field investigations confirm the fact that there is a good chance for fracture networks to be either self-similar or self-affined. Therefore it is quite rational to seek a fractal model that characterizes fractured media appropriately. Such a deterministic model can overcome all the above limitations and will provide a much more realistic image of the fracture network.

This study was intended to find an alternative tool to characterize fractured rocks that appear to have self-similar nature. Self-similarity of a fracture network can be identified by the limited information available from field investigations. This study showed that, with some modifications to box counting theorem of fractals, the image of a uniform series of boreholes can be analyzed for possible self-similarity.

204

With very limited information about a fracture network (which is proven to be fractal), we could develop the complete network, using iterated function systems (IFS). All we need is the 6 parameters of each transformation in the iterated function system that can be derived using 6 equations form polygonized image boundaries (or outstanding features).

Based on essential fractal theorems, an inverse algorithm was proposed and a graphical program was developed that takes the image of boreholes in a fractured region and searches for the most appropriate iterated function system, an IFS whose attractor is closest to the original image. Proximity of the two images can be evaluated by fractal dimension and by Haudorff metric. Hausdorff metric, may not be very practical, since it requires lengthy computations. Fractal dimension is a quick and easy alternative for this purpose. It was acknowledged that fractal dimension is not as accurate as Haudorff metric and it may occasionally provide incorrect evaluations, mainly because of two reasons:

1. Box counting is a visual inspection technique and it is approximate
2. Different fractal images can have the same fractal dimension

The first limitation was overcome, to some extend, using computer image processing in place of visual inspection. It was shown that this approach provides a good

estimation of fractal dimension for complicated images. The second limitation is not preventable. It was however argued that non-identical fractal images that have the same fractal dimension are usually very different; they are very "far" from each other. In the proposed inverse algorithm, the attractor of the IFS is "close" to the fractal image, at least visually. Therefore, there is little room for it to be mistaken with another fractal image.

In the second phase of this study, an effort was made to develop a flow model that uses information on a fractal network of fractures. The classical equivalent continuum model was used as the basis. The flow region was discretized by large number of small cells and the equivalent porous medium was calculated for each cell, assuming a single fracture per fracture set, in each cell. Properties of this single fracture were estimated using a new regression model and the permeability tensor was developed for each cell, for each fracture set. All permeability tensors were superimposed and the entire problem was translated into an anisotropic and heterogeneous porous medium.

In order to analyze flow behavior in the equivalent porous medium, a finite difference program, $FLAC^{2D}$, was used. It was shown that for highly heterogeneous media, finite difference equations do not converge. This is to some degree related to the program limitations but it is also associated with the heterogeneous nature of such media, as acknowledged in the Yucca Mountain Project. It was observed that

206

permeability values had a big range of variations throughout the region. A lower-bound truncation was applied to cause convergence to occur, without significant impact on the outcomes.

A physical model was developed using very small number of fractal dots (due to practical limitations) and calculations showed that this model should provide 70% of the complete model. The experiment was repeated for various fluids and the one that provides a laminar flow was identified (water with 1% HPMC). Flow was calculated and head distribution was measured in this model and the results had very good agreements with predictions.

To prepare for future work, Yucca Mountain Project (YMP) was selected as one that has a very good potential to be analyzed using the proposed flow model. As an example, One fracture set from Cross-Drift tunnel explorations was used and, with the help of shadow theorem of fractals, IFS codes were identified that produced fractures similar to the observations, both visually and statistically. Numerous investigations for both fracture and flow characterization of Yucca Mountain have provided lots of information. This information could be used to develop a fractal network of fractures, study flow behavior, and compare the results with numerous previous models and with field observations. All YMP data and reports were originally available at www.ymp.com. However, in the midst of this study the site

was restricted and it became impractical to collect necessary information, for the purpose of this work.

To confirm model accuracy and stability, various sensitivity analyses verified the hypotheses that were applied to the proposed model:

1. Despite the <u>randomness</u> of the implemented fractal algorithm, deterministic nature of a fractal network of fractures was emphasized based on fractal concepts and was proven by demonstrating flow properties stability.

2. While the physical model was far from the numerical model for fracture network, their differences were captured and it was shown that the observed differences agreed with the predicted differences.

3. The solution to the convergence problem with finite difference modeling of fractures networks was analyzed and the most appropriate lower-bound truncation was estimated.

4. It was shown that self-similarity results in a predictable flow behavior at various scales and properties of the filed scale problem can be extrapolated from the lab scale model, confidently.

10.2 - STUDY CONCLUSIONS

Fractal modeling of fracture networks has a great potential for application. While the above work is at a conceptual stage, it shows that limited data could be used to simulate a fractured region, realistically. The proposed flow model is very simple and easy to use and the results showed very good agreement with the physical experiment. The followings are the main conclusions of this work:

- ❖ It is quite possible for a fractured rock to have a fractal nature. Box counting theorem of fractals can be used to verify this fractal nature. It is possible that different fracture sets belong to different fractal families (specially when they have different geological origins). In such cases, self-similarity may not be readily observable and it is recommended to analyses each fracture set separately.

- ❖ Borehole data from field investigations on a fracture set can be used to predict fractal nature of the complete set, based on the portion of the image of fractures that is provided by the boreholes.

- ❖ An inverse fractal algorithm can be applied to the partial image of a fractal object and predict the complete image. This partial image could be an image

209

of some borehole data. Proximity of the model to the image can be estimated

using fractal dimension or, more accurately but tediously, Hausdorff metric.

❖ Discretized nature of fractal network of fractures can be used to develop a

simple flow model, calculate permeability tensors, and analyze the flow

problem using a finite difference program such as FLAC^{2D}.

❖ There is a great potential for the proposed model to be applied to real

projects. A preliminary analysis on Yucca Mountain Project showed that an

observed network of fractures can be modeled using shadow theorem of

fractals.

10.3 - RECOMMENDATIONS FOR FUTURE APPLICATIONS AND FURTHER STUDY

This work is considered as initiation of a new technique for hydraulic

characterization of fractured media – a model that overcomes limitations of the

classical models. It is necessary for each fracture set of a region to have a self-

similar or self-affined nature, in order for this fractal model to be applicable. Field

observations and rock fracture mechanics have both proven that this requirement is

usually satisfied. This study opens various avenues of research to improve

applications of fractal theory to hydraulic characterization of fractured media. The

210

following improvements to the proposed model are some interesting areas of research:

- ❖ This two dimensional model can be escalated to three dimensions. The process is very straightforward. The algorithms however may be more complicated and computationally more intense. The most challenging part of a 3D model is development of a 3D graphical program to apply the inverse algorithm. It may be appropriate to apply the algorithm to each plane separately, while observing changes in the other planes (something like the 3-pane view in AutoCAD).

- ❖ As we showed in chapter 9, Shadow algorithm has good potential to be integrated into the inverse algorithm and improve the model. Selecting x and y axes appropriately, one could project the 2D image of borehole data on the two axes, apply collage theorem to each 1D image, and aggregated the 1D IFS's to get the complete IFS. Similar approach may be used for a 3D model.

- ❖ It was shown that the inherent relationship between rock mass parameters can be captured by selection of the right IFS transformations (Figure 6.5 and the related discussion in Page 7-3). It would be interesting to develop generic numerical models in an inverse direction. That is, having the relation

211

between rock mass parameters, what should be the relation between IFS parameters and how to define those transformations.

❖ In the same line of thought, it would be interesting to find a systematic approach to arrive at a desired statistical distribution for a fracture parameter by selecting the right IFS codes. The example provided in Figure 6.17 was created arbitrarily. IFS parameters were altered by trial-error and instant changes in statistical distribution were observed. This process was repeated until a good match was found. Additional work may find numerical models to replace trial error.

❖ For simplicity and consistency with the physical model, the flow model was developed assuming fracture surfaces have a parallelogram shape. Using disk shape fractures, however, provides a more realistic model. The flow model can be easily modified to get more realistic outputs for more realistic problems.

❖ It was shown that fractal dimension could be used to verify proximity of the model to a given boreholes image. It is more accurate to use Hausdorff metric for this purpose. Calculation of Hausdorff metric based on the distance between millions of pairs of points is quite time consuming and

212

impractical. A new algorithm can help us to make Hausdorff metric more useful.

* It is crucial to apply the proposed model to a practical problem. While this model was verified by laboratory experiment, evaluation of a real project such as YMP provides good insight for future applications and improvements. Specifically, the scale effect hypothesis that was validated using a sensitivity analysis, is interesting to be evaluated on the field.

* We observed a major limitation of equivalent continuum model: Highly heterogeneous fracture networks whose permeability tensors vary significantly throughout a region, are not appropriately modeled by ECM. Alternative discrete network models (DNM) should be developed for such systems. Similar to ECM, properties of each cell can be estimated using information on fractal dots. It was shown that a cluster counting algorithm of percolation theory could be used to identify the backbone of this fracture network. This would significantly simplify development of a discrete network model. More work is necessary to study applications of DNM to the proposed fractal network of fractures.

* It is also useful to study a less heterogeneous fracture network to eliminate convergence problem in the finite difference model. Therefore, a more

213

accurate sensitivity analysis can be conducted to study lower-bound effects on flow properties.

❖ Automation of the inverse algorithm would be a great improvement to this work. After defining the boundary (or outstanding features) polygon (P_0) of a fractal image, an image processing algorithm may analyze the fractal object, and find polygons similar to P_0 but shrunk, rotated, and/or sheared, that define boundaries of portions of the object. The algorithm may become very complicated but it is worth investigating.

❖ Self-similarity of fracture initiation and propagation process has been widely acknowledged and many numerical models are available, as discussed in this chapter 5. It is interesting to seek a relationship between the history of filed stresses and the iterated function system that would result in the observed fracture pattern. Specifically the "beam" approach is very similar to IFS model: a series of beams are rotated and sheared to cause new cracks. These rotations and shears may be considered as IFS parameters. Ideally, a real time simulation could be developed to look at the entire fracturing process, through the history of the rock fracturing.

214

REFERENCES

Acuna, Jorge (1993). Numerical Construction and Fluid Flow simulation in Network of Fractures Using Fractal Geometry. *Ph.D. Dissertation, Department of Petroleum Engineering, University of Southern California, August 1993.*

Acuna, J. A. and Yortsos, Y. C. (1991). Numerical Construction and Flow Simulation in Network of Fractures Using Fractal Geometry. Paper SPE-22703 presented at *the 66th Annual Technical Conference, Socienty of Petroleum Engineering, Dallas, Oct. 6-9.*

andersson, Johan and Thunvik, Roger (1986). Predicting Mass Transport in Discrete Fracture Networks With the Aid of Geometrical Field Data. *Water Resources Research, Vol. 22, No. 13, pp. 1941-1950, December 1986.*

Ashby M. F. and Sammis, C. G. (1990). The Damage Mechanics of Brittle Solids in Compression. *PAGEOPH, Vol. 133, No. 3, 1990.*

Balberg, I. (1987). Recent Developoments in Continuum Percolation. *Philos. Magazine. Vol. 56, No. 6, pp. 993-1003, 1987.*

Balberg I., Berkowitz B., Drachsler G. E. (1991). Application of a Percolation Model to Flow in Fractured Hard Rocks. *Journal of Geophysical Research, Vol. 96, No. B6, pp. 10,015-10,021, June 10, 1991.*

Barker J. A. (1988). A Generalized Radial Flow model for Hydraulic Tests in Fractured Rock. *Water Resources Research, Vol. 24, No. 10, pp. 1796-1804, October 1988.*

Barnsley, Michael F. (1993). Fractals Everywhere, Second Edition. *Morgan Kaufmann, an Imprint of Academic Press.*

Barton, C. C. and Hsiesh, P. A. (1989). Physical and Hydrologic-Flow Properties of Fractures.Field Trip Guidbook T385. *Washington D.C.: Americal Geophysical Union.*

Berkowitz B., Balberg I. (1991). Percolation Approach to the Problem of Hydraulic Conductivity in Porous Media. *Transport in Porous Media, Vol. 9, pp. 272-286, 1992.*

215

Berkowitz B., Braester C. (1991). Dispersion in Sub-Representative Elementary Volume Fracture Networks: Percolation Theory and Random Walk Approaches. *Water Resources Research, Vol. 27, No. 12, pp. 3159-3164, December 1991.*

Berkowitz, Brian; Balberg, Isaac (1993). Percolation Theory and Its Application to Groundwater Hydrology. *Water Resources Research, Vol. 29, No. 4, pp. 775-794, April 1993.*

Billaux D., Chiles J. P., Hestir K., Long J. (1989). Three-Dimensional Statistical Modeling of a Fractured Rock Mass – An Example From Fanay-Augeres Mine. *Int. J. of Rock Mech. Min. Sci. & Geomech. Abstr. Vol. 26, No. 3/4, pp. 281-299, 1989.*

Cacas M.C., Ledoux E., De Marsily G., Tillie B., Barbereau A., Calmels P., Gaillard B., Margritta R. (1990). Modeling Fracture Flow with a Stochastic Discrete Fracture Network 1. The Flow Model, 2. The Transport Model. *Water Resources Research, Vol. 26, pp. 479-500, March 1990.*

Carter B. J., Lajtai E. Z., Perukhov A. (1989). Primary and Remote Fracture Around Underground Cavities. *International Journal for Numerical and Analytical Methods in Geomechanics, Vol. 15, pp. 2-40, 1991.*

Chang, J. and Yortsos, Y. C. (1990). Pressure Transient Analysis of Fractal Reservoirs. SPE Formation Evaluation, p. 631.

Charlaix, E.; Guyon E.; Roux, S. (1987). Permeability of a Random Array of Fractures of Widely Varying Appertures. *Transp. Porous Media. No. 2, pp. 31-43, 1987.*

Chelidze T. L. (1982). Percolation and Fracture. *Physics of the Earth and Planetary Interiors, Vol. 28, pp. 93-101, 1982.*

Chen, Guoliang and Harpalani, Satya (1995). Study of Fracture Network in Coal. Fractured and Jointed Rock Masses. *A.A. Balkema/Rotterdam/Brookfield/1995.*

Committee on Fracture Characterization and Fluid Flow, U.S. National Committee for Rock Mechanics (1996). Rock Fractures and Fluid Flow, Contemporary Understanding and Applications. *National Academy Press, Washington, D.C. 1996.*

Conceptual and Numerical Models for UZ Flow and Transport. *U.S. Department of Energy, Office of Civilian Radioactive Waste Management, March 2000 (www.ymp.gov).*

Cook R. F., Warren S. Groundwater Control for the Los Angeles Metro System Beneath the Santa Monica Mountains. *Geo-Engineering For Underground Facilities.*

Cook, P. (1999). In Situ Pneumatic Testing at Yucca Mountain. *International Journal of Rock Mechanics and mining Science, Vol. 37, pp. 375-367, 2000.*

Cushman, John H. (1991). On Diffusion in Fractal Porous Media. *Water Resources Research, Vol. 27, No. 4, pp. 643-644, April 1991.*

DeGragoria, A. J. (1985). A Predictive Monte Carlo Simulation of Two-Fluid Flow Through Porous Media at Finite Mobility Ratio. *Phys. Fluids, Vol. 28, No. 10, 2933-2935, 1985.*

Dershowitz, W. (1995). Interpretation and Synthesis of Discrete Fracture Orientation, Size, Shape, Spatial Stricture and Hydraulic Data by Forward Modeling. Fractured and Jointed Rock Masses. *A.A. Balkema/Rotterdam/Brookfield/1995.*

Dershowitz, W. S. and Einsein, H. H. (1988). Characterizing Rock Joint Geometry with Joint System Models. *Rock Mechanics and Rock Engineering. Vol. 21, pp. 21-25, 1988.*

Development of Numerical Grids for UZ Flow and transport Modeling. *U.S. Department of Energy, Office of Civilian Radioactive Waste Management, September 1999 (www.ymp.gov).*

Dienes, J. K. (1982). Permeability, Percolation, and Statistical Crack Mechanics. *Rock Mechanics.*

Doolin, David M. and Mauldon Matthew (1995). Anisotropy and Heterogeneity in Conasauga Group Rocks near Oak Ridge Reservation, Tennessee. *May 30, 1995.*

Doyen, Philippe M. (1988). Permeability, Conductivity, and Pore Geometry of Sandstone. *J. of Geophysical Research, Vol. 93, No. B7, pp. 7729-7740, July 10, 1988.*

Dzik, E. J. and Lajtai, E. Z. (1996). Primary Fracture Propagation from Circular Cavities Loaded in Compression. *International Journal of Fracture 79: 49-64, 1996.*

217

Eberhardt E., Stead D., Stimpson B., Lajtai, E. Z. (1998). The Effect of Neighboring Cracks on Elliptical Crack Initiation and Propagation in Uniaxial and Triaxial Stress Fields. Engineering fracture mechanics, Vol. 59, No. 2, pp. 103-115, 1998.

Ehlen, J. (2000). Fractal Analysis of Joint Patterns in Granite. *International Journal of Rock Mechanics and Mining Sciences, Vol. 37, pp. 909-922, 2000.*

Fast Lagrangian Analysis of Continua (FLAC) Reference Manual. *Itasca Consulting Group (1999), Thresher Square East, 708 South Third Street, Suite 310, Minneapolis, Minnesota 55415 USA.*

Geology of the ECRB Cross Drift – Exploratory Studies Facility, Yucca Mountain Project, Yucca Mountain, Nevada. *U.S. Department of Energy, Office of Civilian Radioactive Waste Management, 1999 (www.ymp.gov).*

Gervinais, Farbice and Gentrier, Sylvie; Chiles, Jean Paul (1995). Geostatistical Analysis and Hierarchical Modeling of a Fracture Network in a Stratified Rock Mass. Fractured and Jointed Rock Masses. *A.A. Balkema/Rotterdam/Brookfield/1995.**

Ghorbanpoor, Al and Zhang, Jiping (1990). Boundary Element Analysis of Crack Growth for Mixed-Mode Center Slant Crack Problems. *Engineering Fracture Mechanics, Vol. 36, No. 5, pp. 661-668, 1990.*

Golden J. M. (1980). Percolation Theory and Models of Unsaturated Porous Media. *Water Resources Research, Vol. 16, No. 1, pp. 201-209, February 1980.*

Griffiths D. V. and Ferton, Gordon A. (1998). Probablistic Analysis of Exit Gradients due to Steady Seepage. *Journal of Geotechnical and Geoenvironmental Engineering, Sep. 1998.*

Grossmann, Nuno Feodor (1995). About Distribution of the Trace Length of a Joint set. Fractured and Jointed Rock Masses. *A.A. Balkema/Rotterdam/Brookfield/1995.*

Gueguen, Y. and Dennis, J. (1989). Transport Properties of Rocks From Statistics and Percolation. *Math. Geol. Vol. 21, No. 1, pp. 1-13, 1989.*

---

[*] This book is a compilation of numerous short rock mechanics research papers in the areas of Characterization & Statistics, Modeling of Mechanical Behavior, Physical Properties, Fluid Flow, and Underground Openings and Slopes.

218

Gueguen, Y.; David, C.; Darot, M. (1986). Models and Time Constants for Permeability Evolution. *Geophysics Research Letters. Vol. 13, No. 5, pp. 460-463, 1986.*

Guo, H.; Aziz, N. I.; Schmidt, L. C. (1990). Linear Elastic Crack Tip Modeling By the Displacement Discontinuity Method. *Engineering Fracture Mechanics. Vol. 36, No. 6, pp. 933-943, 1990.*

Hall, Randolph W. (1991). Queuing Methods For Services and Manufacturing. *Prentice Hall, Englewood Cliffs, NJ 07632.*

Handbook of Ground Water Development / Roscoe Moss Company. New York: Wiley, 1990.

Hazzard, James F. and Young, R. Paul (2000). Micromechanical Modeling of Cracking and Failure in brittle Rocks. *Journal of Geophysical Research, Vol. 105, No. B7, pp. 16,683-16,697, July 10, 2000.*

Heping, Xie and Pariseau, William G. (1995). Fractal Estimation of Joint Roughness Coefficients. Fractured and Jointed Rock Masses. *A.A. Balkema / Rotterdam / Brookfield / 1995.*

Herbert, A. W. and Lanyon, G. W. (1995). Discrete Fracture Network Modeling of Flow and Transport within a Fracture Zone at Stripa. Fractured and Jointed Rock Masses. *A.A. Balkema/Rotterdam/Brookfield/1995.*

Herrmann H. J. (1991). Shapes of Different Cracks Obtained Under Shear. *Fractals' Physical Origin and Properties.*

Hestir, Kevin and Long, Jane C. S. (1990). Analytical Expressions for the Permeability of Random Two-Dimensional Poisson Fracture Networks Based on Regular Lattice Percolation and Equivalent Media Theories. *Journal of Geophysical Research, Vol. 95, No. B13, pp. 21,565-21,581, December 10, 1990.*

Hudson, John A.; Brown, Edwin T.; Fairhurst, Charles; Hoek, Evert (1993). Comprehensive Rock Engineering Principals and, Practices, and Projects (Volume I). *Pergamon Press.*

King, Geoffrey C. P. and Sammis, Charles G. (1992). The Mechanisms of Finite Brittle Strain. *PAGEOPH, Vol. 138, No. 4, 1994.*

219

Kominek, Di John   (1977-1993).   Brief History of Fractal Image Compression. http://www.khet.net/gmc/docs/musum/en_compressioneFractale.html.

Kulatilake P.H.S.W., UM J. (1998). Requirements for Accurate Quantification of Self-Affine Roughness Using The Roughness-Length Method. *International Journal of Rock Mechanics and Mining Sciences, Vol. 36, pp. 5-18, 1999.*

La Pointe, P. R. (1988).   A Method to Characterize Fracture Density and Connectivity Through Fractal Geometry. *Int. J. of Rock Mech. Min. Sci. & Geomech. Abstr. Vol. 25, No. 6, pp. 421-429, 1988.*

La Pointe, P. R. and Hudson, J. A. (1985).   Characterization and Interpretation of Rock Mass Joint Patterns. *The Geological Society of America: Special Paper 199.*

Lajtai E. Z., Carter B. J., Ayari M. L. (1990).   Criteria for Brittle Fracture in Compression. *Engineering Fracture Mechanics. Vol. 37, No. 1, pp. 59.74, 1990.*

Lajtai E. Z., Carter B. J., Scott Duncan E. J. (1991). Mapping the State of Fracture Around Cavities. *Engineering Geology, Vol. 31, pp. 277-289, 1991.*

Li, Song and Lajtai E. Z. (1998).   Modeling the Stress-Strain Diagram for Brittle Rock Loaded in Compression. *Mechanics of Materials, Vol. 30, pp. 243-251, 1998.*

Long, Jane C. S. and Witherspoon, Paul A. (1985). The Relationship of the Degree of Interconnection to Permeability in Fracture Networks. *Journal of Geophysical Research, Vol. 90, No. B4, pp 3087-3098, 1985.*

Mahinthakumar, Kumar and Saied Faisal (1997). Multigrid and Krylov Solvers for Large Scale Finite Element Groundwater Flow Simulations on Distributed Memory Parallel Platforms. *Prepared by the Center for Computational Sciences, Oak Ridge National Laboratory, Oak Ridge, Tennessee 37831 for the U.S. Department of Energy, July 1997.*

Mandelbrot B. (1982).   The Fractal Geometry of Nature. *W.H. Freeman and Co., San Francisco, 1982.*

Marrett, Randall; Ortega, Orlando J.; Kelsey, Celinda M. (1999).   Extent of Power-Law Scaling for Natural Fractures in Rock. *Geology, Vol. 27, No. 9, pp. 799-802, September 1999.*

Martel S. J., Peterson Jr. J. E. (1991). Interdisciplinary Characterization of Fracture Systems at the US/BK Site, Grimsel Laboratory, Switzerland. *Int. J. of Rock Mech. Min. Sci. & Geomech. Abstr. Vol. 28, No. 4, pp. 295-323, 1991.*

Mathab, A.; Xu, S.; Grosso, P. (1995). Use of Alternative Distributions for Characterizing Joint Extent and Spacing. Fractured and Jointed Rock Masses. *A.A. Balkema/Rotterdam/Brookfield/1995.*

Muralha, Jose (1995). Fractal Dimension of Joint Roughness Surfaces. Fractured and Jointed Rock Masses. *A.A. Balkema/Rotterdam/Brookfield/1995.*

Myer L. R.; Cook N. G. W.; Goodman R.E. (1995). Fractured and Jointed Rock Masses. *A.A. Balkema/Rotterdam/Brookfield/1995.*

Nishioka, T. and Atluri, S. N. (1983). Path-Independent Integrals, Energy Release Rates, and General Solutions of Near-Tip Fields in Mixed-Mode Dynamic Fracture Mechanics. *Engineering Fracture Mechanics. Vol. 1, pp. 1-22, 1983.*

Nordqvist, A.; Tsang, Yvonne, W.; Tsang, Chin-Fu; Dverstorp, Bjorn; andersson Johan (1995). A Variable-Aperture Fracture Network Model for Flow and Transport in Fractured Rock at Different Scales. Fractured and Jointed Rock Masses. *A.A. Balkema/Rotterdam/Brookfield/1995.*

Oda, M. (1985). Permeability Tensor for Discontinuous Rock Masses. *Geotechnique 35, No. 4, 483-49.*

Odling, Noelle (1995). The Development of Network Properties in Natural Fracture Patterns: An Example from the Devonian Sandstone of Western Norway. Fractured and Jointed Rock Masses. *A.A. Balkema/Rotterdam/Brookfield/1995.*

Ortega, Orlando and Marrett, Randall (1999). Prediction of Macrofracture Properties Using Microfracture information, Mesaverde Group Sandstones, San Juan Basin, New Mexico. *Journal of Structural Geology, Vol. 22, pp 571-588, 2000.*

Popove, Egor P. (1990). Engineering Mechanics of Solids. *Prentice Hall, Englewood Cliffs, NJ 07632.*

Rouleau, A. and Raven, K. G. (1995). Site Specific Simulation of Groundwater Flow and Transport Using a Fracture Network Model. Fractured and Jointed Rock Masses. *A.A. Balkema/Rotterdam/Brookfield/1995.*

Robinson, P. C. (1983). Connectivity of Fracture Systems – A Percolation Theory Approach. *J. Phys. A. Math. Gen. Vol. 16, No. 3, pp. 605-614, 1983.*

Robinson, P. C. (1984). Numerical Calculation of Critical Densities for Lines and Planes. *J. Phys. A. Math. Gen. Vol. 17, No. 14, pp. 2823-2830, 1984.*

Roberson, John A. and Crowe, Clayton T. (1995). Engineering Fluid Mechanics, Fifth Edition. *John Wiley & Sons, Inc.*

Ross, Benjamin (1986). Dispersion in Fractal Fracture Networks. *Water Resources Research, Vol. 22, No. 5, pp. 823-827, May 1986.*

Sahimi, Muhammd (1994). Applications of Percolation Theory. *Taylor & Francis Ltd 1994.*

Sammis, C. G. and Ashby, M. F. (1986). The Failure of Brittle Porous Solids Under Compressive Stress States. *Acta Metall.Vol. 34, No. 3, pp. 511-526, 1986.*

Silliman, S. E. and Wright, A. L. (1988). Stochastic Analysis of Paths of High Hydraulic Conductivity in Porous Media. *Water Resources Research. Vol. 24, No. 11, pp. 1901-1910.*

Snow, D. (1965). A Parallel Plate Model of Fractured Permeable Media. Ph.D. dissertation. University of California, Berkley.

Stewart, Douglas P.; Chen, Yie-Ruey; Kutter, Bruce L. (1998). Experience with the Use of Methylcellulose as a Viscous Pore Fluid in Centrifuge Models. *Geotechnical Testing Journal GTJODJ. Vol. 21, No. 4, pp. 365-369, December 1998.*

Swenson, Daniel (1986). Development of the Near-Tip Stress and Displacement Fields for a Moving Crack Without Using Complex Functions. *Engineering Fracture Mechanics. Vol. 24, No. 2, pp. 315-321, 1986.*

Torelli, L. (1972). Computer Simulation of Dispersion Phenomena Occurring During Flow Through Porous Media, Using a Random Maze Model. *Pure Applied Geophysics. Vol. 96, No. 4, pp 57-88, 1972.*

Torelli, L. and Schiedeger, A. E. (1971). Random Maze Models of Flow Through Porous Media. *Pure Applied Geophysics. Vol. 89, No. 6, pp 32-44, 1971.*

Unsaturated Flow Model and Submodels. *U.S. Department of Energy, Office of Civilian Radioactive Waste Management, March 2000 (www.ymp.gov).*

Vannucchi, Paola and Tobin, Harold (2000). Deformation Structures and Implications for Fluid Flow at the Costa Rica Convergent Margin, ODP Sites 1040 and 1043, Leg 170. *Journal of Structural Geology, Vol. 22, pp. 1087-1103, 2000.*

Wakabayashi, Naruki and Fukushige Ikuo (1995). Experimental Study on theRelation Between Fractal Dimension and Shear Strength. Fractured and Jointed Rock Masses. *A.A. Balkema/Rotterdam/Brookfield/1995.*

Wawersik W. R. (1999). The Value of Laboratory Experiments for Code Validations. *International Journal of Rock Mechanics and Mining Sciences, Vol. 37, pp. 307-316, 2000.*

Weinberger, Ram (1999). Initiation and Growth of Cracks During Desiccation of Stratified Muddy Sediments. *Journal of Structural Geology, Vol. 21, pp.379-3876, 1999.*

Wong Po-zen (1988). The Statistical Physics of Sedimentary Rocks. *Physics Today, December 1988.*

Xie, Heping; Wang, Jin-An; Kwasniewski M. A. (1998). Multifractal Characterization of Rock Fracture Surfaces. *Int. J. of Rock Mech. Min. Sci. Vol. 36, pp. 19-27, 1999.*

Yuan, Y. G.; Lajtai, E. Z.; Ayari, M. l. (1993). Frature Nucleation from a Compression-Parallel, Finite-Width Elliptical Flaw. *International Journal of Rock Mechanics and Mining Sciences &Geomechanical Abstracts , Vol. 30,No. 7, pp. 873-876, 2000.*

Yucca Mountain Science and Engineering Report, Technical Information Suggesting Site Recommendation Consideration. *U.S. Department of Energy, Office of Civilian Radioactive Waste Management, May 2001 (www.ymp.gov).*

APPENDIX A - MINIMIZED $\sum \delta^2$ TREND-LINE CALCULATIONS

The objective is to minimize the <u>perpendicular</u> distances of all points from the trend-line. As shown in Figure A.1 this distance can be calculated as:

$$\delta_i = \frac{y_i - \hat{y}_i}{Cos\alpha} = \frac{y_i - \hat{y}_i}{\sqrt{1+b^2}}$$
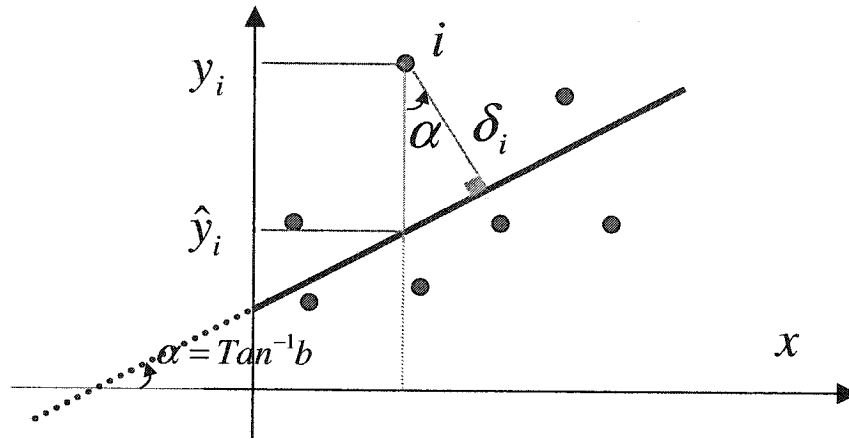
Figure A.1 - δ_i **as a function of** $y_i, \hat{y}_i, \alpha$

Therefore, the Objective function has the following form:

$$Minimize \quad f(a,b) = \sum_{i=1}^{\#Po\,int(n)} \delta_i^2 = \frac{(y_i - \hat{y}_i)^2}{1+b^2} = \frac{[y_i - (a+b\cdot x_i)]^2}{1+b^2}$$

To minimize this function, we should take its derivatives with respect to a and b and make them zero:

$$(1) \quad \frac{\partial f}{\partial a} = 0 \Rightarrow \frac{-2}{1+b^2}\sum(y-a-bx) = 0 \Rightarrow \sum y - na - b\sum x = 0 \Rightarrow a = \frac{1}{n}\left(\sum y - b\sum x\right)$$

224

(2) $\dfrac{\partial f}{\partial b} = 0 \Rightarrow \sum\left[-x\left(1+b^2\right)\left(y-a-bx\right)-b\left(y-a-bx\right)^2\right]=0$

$\Rightarrow \sum\left[x\left(1+b^2\right)\left(y-a-bx\right)\right]+b\sum\left(y^2+a^2+b^2x^2-2bxy-2ay-2abx\right)$

$\Rightarrow b^2\sum xy-b^3\sum x^2-ab^2\sum x+\sum xy-b\sum x^2-a\sum x+\ldots$

$\ldots+b\sum y^2+b^3\sum x^2+na^2b-2b^2\sum xy-2ab\sum y+2ab^2\sum xy=0$

Multiply by n and replace na by $\left(\sum y-b\sum x\right)$ from (1):

$\Rightarrow n\sum xy-nb\sum x^2-\left(\sum y-b\sum x\right)\sum x+nb\sum y^2+b\left[\left(\sum y\right)^2+\left(b\sum x\right)^2-2b\sum x\sum y\right]+\ldots$

$\ldots-nb^2\sum xy-2b\sum y\left(\sum y-b\sum x\right)+b^2\sum x\left(\sum y-b\sum x\right)=0$

$\Rightarrow n\sum xy-nb\sum x^2-\sum x\sum y-a\left(\sum x\right)^2+nb\sum y^2+b\left[\left(\sum y\right)^2+b\left(\sum x\right)^2-2b\sum x\sum y\right]+\ldots$

$\ldots-nb^2\sum xy-2b\sum y\left(\sum y-a\sum x\right)+b^2\sum xy\left(\sum y-a\sum x\right)=0$

$\Rightarrow n\sum xy-nb\sum x^2-\sum x\sum y-b\left(\sum x\right)^2+nb\sum y^2+b\left(\sum y\right)^2+b^3\left(\sum x\right)^2-2b^2\sum x\sum y+\ldots$

$\ldots-nb^2\sum xy-2b\left(\sum y\right)^2+2b^2\sum x\sum y+b^2\sum x\sum y-b^3\left(\sum x\right)^2=0$

Which can be reorganized as: $A\bullet b^2+B\bullet b+C=0$ where:

$A=\sum x\sum y-n\sum xy$

$B=\left(\sum x\right)^2-\left(\sum y\right)^2-n\left(\sum x^2-\sum y^2\right)$

$C=n\sum xy-\sum x\sum y=-A$

Therefore: $b=\dfrac{-B\pm\sqrt{B^2-4AC}}{2A}=\dfrac{-B}{2A}\pm\sqrt{\dfrac{B^2+4A^2}{4A^2}}=-U\pm\sqrt{U^2+1}$

where: $U=\dfrac{-B}{2A}=\dfrac{n\left(\sum x^2-\sum y^2\right)-\left(\sum x\right)^2-\left(\sum y\right)^2}{2\left(\sum x\sum y-n\sum xy\right)}$

$\therefore$ This concludes the proof.

APPENDIX B – SIMPLIFIED FLAC^{2D} ALGORITHM

In general, Fluid Flow velocity through an edge ab of a triangular cell ∇abc is calculated as:

$(B-1)$
$$\begin{cases} u_1 = \dfrac{1}{2A}\left[-K_{11}\left(P^b + P^a\right)\left(x_2^b - x_2^a\right) + K_{12}\left(P^b + P^a\right)\left(x_1^b - x_1^a\right)\right] \\[2mm] u_2 = \dfrac{1}{2A}\left[-K_{21}\left(P^b + P^a\right)\left(x_2^b - x_2^a\right) + K_{22}\left(P^b + P^a\right)\left(x_1^b - x_1^a\right)\right] \end{cases}$$

and contribution of Δabc to discharge at node a is estimated by:

$(B-2)$ $\qquad Q^a_{\nabla abc} = \left[-u_1\left(x_2^b - x_2^c\right) + u_2\left(x_1^b - x_1^c\right)\right]/2$

Consider square elements of the Figure B.1. In triangle Δabc, for example, equation B-1 is:

$$\begin{cases} u_1^{ab} = \dfrac{1}{2\left(\varepsilon^2/2\right)}\left[-K_{11}\left(P^b + P^a\right)\left(-\varepsilon\right) + K_{12}\left(P^b + P^a\right)\left(\varepsilon\right)\right] = \dfrac{1}{\varepsilon}\left(K_{11} + K_{12}\right)\left(P^b + P^a\right) \\[2mm] u_2^{ab} = \dfrac{1}{2\left(\varepsilon^2/2\right)}\left[-K_{21}\left(P^b + P^a\right)\left(-\varepsilon\right) + K_{22}\left(P^b + P^a\right)\left(\varepsilon\right)\right] = \dfrac{1}{\varepsilon}\left(K_{21} + K_{22}\right)\left(P^b + P^a\right) \end{cases}$$
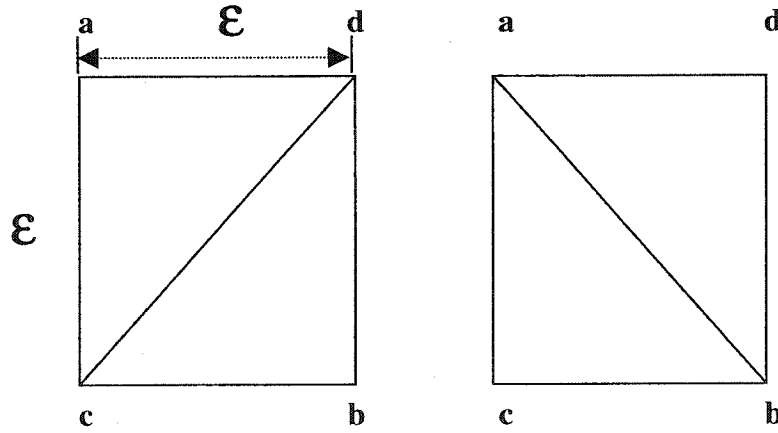

Figure B.1 - Square Elements for the Simplified FLAC Algorithm

and equation B-2 becomes: $Q^a_{\Delta abc} = \left[-u_1(0) + u_2(\varepsilon)\right] = \varepsilon \cdot u_2$

The calculations for each of the triangles $\Delta abc, \Delta adb, \Delta adc, \Delta dbc$ is simplified as follows:

Δabc :

$$\begin{cases} u_1^{ab} = \dfrac{1}{\varepsilon}(K_{11} + K_{12})(P^a + P^b) \\ u_2^{ab} = \dfrac{1}{\varepsilon}(K_{21} + K_{22})(P^a + P^b) \end{cases} \qquad \begin{cases} u_1^{ca} = \dfrac{1}{\varepsilon}(-K_{11})(P^c + P^a) \\ u_2^{ca} = \dfrac{1}{\varepsilon}(-K_{21})(P^c + P^a) \end{cases}$$

$$\begin{cases} u_1^{bc} = \dfrac{1}{\varepsilon}(-K_{12})(P^b + P^c) \\ u_2^{bc} = \dfrac{1}{\varepsilon}(-K_{22})(P^b + P^c) \end{cases}$$

Therefore total velocity into ∇abc is calculated as:

$$(B-3.a) \qquad \begin{cases} \sum u_1^{\Delta abc} = \dfrac{1}{\varepsilon}\Big[K_{12}P^a + K_{11}P^b + (-K_{11} - K_{12})P^c\Big] \\ \sum u_2^{\Delta abc} = \dfrac{1}{\varepsilon}\Big[K_{22}P^a + K_{21}P^b + (-K_{21} - K_{22})P^c\Big] \end{cases}$$

and contribution of Δabc to discharge at the three nodes a, b, c is:

$$(B-3.b) \qquad Q^a = u_2 \varepsilon/2 \ ; \ Q^b = u_1 \varepsilon/2 \ ; \ Q^c = (-u_1 - u_2)\varepsilon/2$$

Δadb :

$$\begin{cases} u_1^{ad} = \dfrac{1}{\varepsilon}(K_{12})(P^a + P^d) \\ u_2^{ad} = \dfrac{1}{\varepsilon}(K_{22})(P^a + P^d) \end{cases} \qquad \begin{cases} u_1^{db} = \dfrac{1}{\varepsilon}(K_{11})(P^d + P^b) \\ u_2^{db} = \dfrac{1}{\varepsilon}(K_{21})(P^d + P^b) \end{cases}$$

$$\begin{cases} u_1^{ba} = \dfrac{1}{\varepsilon}(-K_{11} - K_{12})(P^a + P^b) \\ u_2^{ba} = \dfrac{1}{\varepsilon}(-K_{21} - K_{22})(P^a + P^b) \end{cases}$$

227

Therefore total velocity into Δadb is calculated as:

$$(B-4.a) \quad \begin{cases} \sum u_1^{\Delta adb} = \dfrac{1}{\varepsilon}\left[-K_{11}P^a - K_{12}P^b + (K_{11} + K_{12})P^d\right] \\[4mm] \sum u_2^{\Delta adb} = \dfrac{1}{\varepsilon}\left[-K_{21}P^a - K_{22}P^b + (K_{21} + K_{22})P^d\right] \end{cases}$$

and contribution of Δadb to discharge at the three nodes a, d, b is:

$$(B-4.b) \quad Q^a = -u_1\,\varepsilon/2 \;\; ; \;\; Q^b = -u_2\,\varepsilon/2 \;\; ; \;\; Q^d = (u_1 + u_2)\varepsilon/2$$

$\underline{\Delta adc:}$

$$\begin{cases} u_1^{ad} = \dfrac{1}{\varepsilon}(K_{12})(P^a + P^d) \\[4mm] u_2^{ad} = \dfrac{1}{\varepsilon}(K_{22})(P^a + P^d) \end{cases} \qquad \begin{cases} u_1^{dc} = \dfrac{1}{\varepsilon}(K_{11} - K_{12})(P^d + P^c) \\[4mm] u_2^{dc} = \dfrac{1}{\varepsilon}(K_{21} - K_{22})(P^d + P^c) \end{cases}$$

$$\begin{cases} u_1^{ca} = \dfrac{1}{\varepsilon}(-K_{11})(P^c + P^a) \\[4mm] u_2^{ca} = \dfrac{1}{\varepsilon}(-K_{21})(P^c + P^a) \end{cases}$$

Therefore total velocity into Δadc is calculated as:

$$(B-5.a) \quad \begin{cases} \sum u_1^{\Delta adc} = \dfrac{1}{\varepsilon}\left[(K_{12} - K_{11})P^a - K_{12}P^c + K_{11}P^d\right] \\[4mm] \sum u_2^{\Delta adc} = \dfrac{1}{\varepsilon}\left[(K_{22} - K_{21})P^a - K_{22}P^c + K_{21}P^d\right] \end{cases}$$

and contribution of Δadc to discharge at the three nodes a, c, d is:

$$(B-5.b) \quad Q^a = (-u_1 + u_2)\varepsilon/2 \;\; ; \;\; Q^c = -u_2\,\varepsilon/2 \;\; ; \;\; Q^d = u_1\,\varepsilon/2$$

$\underline{\Delta dbc:}$

228

$$\begin{cases} u_1^{db} = \dfrac{1}{\varepsilon}(K_{11})(P^d + P^b) \\ u_2^{db} = \dfrac{1}{\varepsilon}(K_{21})(P^d + P^b) \end{cases} \qquad \begin{cases} u_1^{bc} = \dfrac{1}{\varepsilon}(-K_{12})(P^b + P^c) \\ u_2^{bc} = \dfrac{1}{\varepsilon}(-K_{22})(P^b + P^c) \end{cases}$$

$$\begin{cases} u_1^{cd} = \dfrac{1}{\varepsilon}(-K_{11} + K_{12})(P^c + P^d) \\ u_2^{cd} = \dfrac{1}{\varepsilon}(-K_{21} + K_{22})(P^c + P^d) \end{cases}$$

Therefore total velocity into Δdbc is calculated as:

$$(B-6.a) \qquad \begin{cases} \sum u_1^{\Delta dbc} = \dfrac{1}{\varepsilon}\left[(K_{11} - K_{12})P^b - K_{11}P^c + K_{12}P^d\right] \\ \sum u_2^{\Delta dbc} = \dfrac{1}{\varepsilon}\left[(K_{12} - K_{22})P^b - K_{21}P^c + K_{22}P^d\right] \end{cases}$$

and contribution of Δdbc to discharge at the three nodes b, c, d is:

$$(B-6.b) \qquad Q^b = (u_1 - u_2)\varepsilon/2 \;\; ; \;\; Q^c = -u_1\varepsilon/2 \;\; ; \;\; Q^d = u_2\varepsilon/2$$

Replacing u_1, u_2 in equations B-3.b, B-4.b, B-5.b, B-6.b with their values from equations B-3.a, B-4.a, B-5.a, B-6.a and summing discharges at the 4 nodes, we conclude:

229

$$\therefore \begin{cases} \sum_{All\Delta} Q^a = \left[(K_{11} - K_{12} + K_{22})P^a + K_{12}P^b - K_{22}P^c - K_{11}P^d \right]/2 \\[2em] \sum_{All\Delta} Q^b = \left[K_{12}P^a + (K_{11} - K_{12} + K_{22})P^b - K_{11}P^c - K_{22}P^d \right]/2 \\[2em] \sum_{All\Delta} Q^c = \left[-K_{11}P^a - K_{22}P^b + (K_{11} + K_{12} + K_{22})P^c - K_{12}P^d \right]/2 \\[2em] \sum_{All\Delta} Q^d = \left[-K_{22}P^a - K_{11}P^b - K_{12}P^c + (K_{11} + K_{12} + K_{22})P^d \right]/2 \end{cases}$$

Or in Matrix Form:

$$\begin{Bmatrix} Q^a \\ Q^b \\ Q^c \\ Q^d \end{Bmatrix} = \begin{bmatrix} K_{11} - K_{12} + K_{22} & K_{12} & -K_{22} & -K_{11} \\ K_{12} & K_{11} - K_{12} + K_{22} & -K_{11} & -K_{22} \\ -K_{11} & -K_{22} & K_{11} + K_{12} + K_{22} & -K_{12} \\ -K_{22} & -K_{11} & -K_{12} & K_{11} + K_{12} + K_{22} \end{bmatrix} \times \begin{Bmatrix} P^a \\ P^b \\ P^c \\ P^d \end{Bmatrix}$$

Discharge at these four nodes is also calculated by the neighboring cells. The total discharge at a node is the summation of the contributions of all cells surrounding that node.

APPENDIX C – PIPE NETWORK MODEL FOR FRACTURE FLOW PROBLEM

Consider the fracture network of the proposed problem (Figure C.1). In the physical experiment, dyeing material was used to identify the backbone fracture network (Figure C.2.a) and the corresponding pipe network model was developed using the deterministic algorithm as shown in figure C.2.b and selecting the backbone fractures (red/light) only.
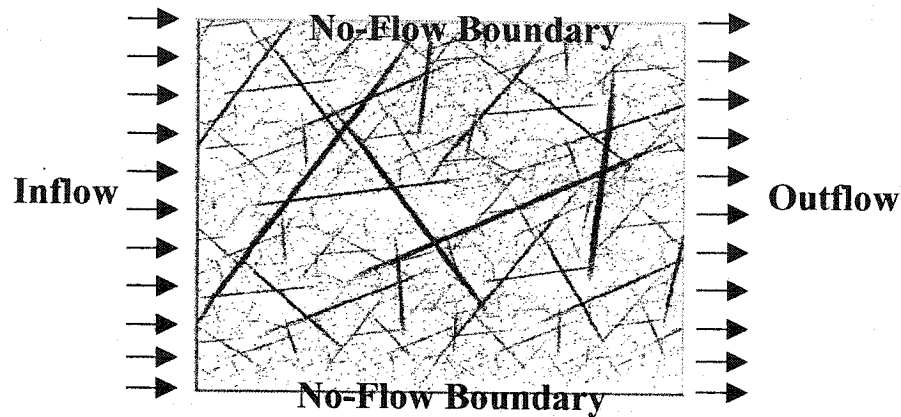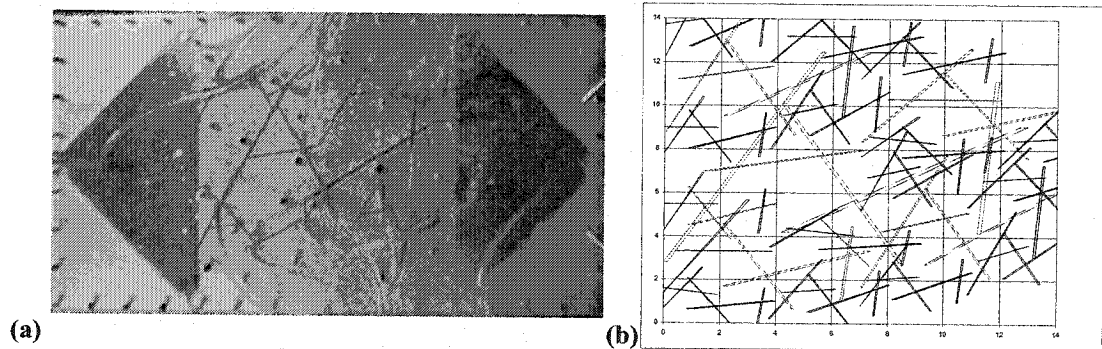

Figure C.1 – Proposed Fracture Flow Problem (Duplicate of Figure 7.24)

(a)   (b)

Figure C.2 – (a) Identification of the Backbone fracture network in the lab.
(b) Simulation of the Backbone (Pink) fractures using Deterministic Algorithm

231

To solve the network problem, we consider one of the flow paths in the pipe network of figure C.2.b and write Bernoulli equations. Figure C.3 identifies one of these paths in black color and its fractures properties.
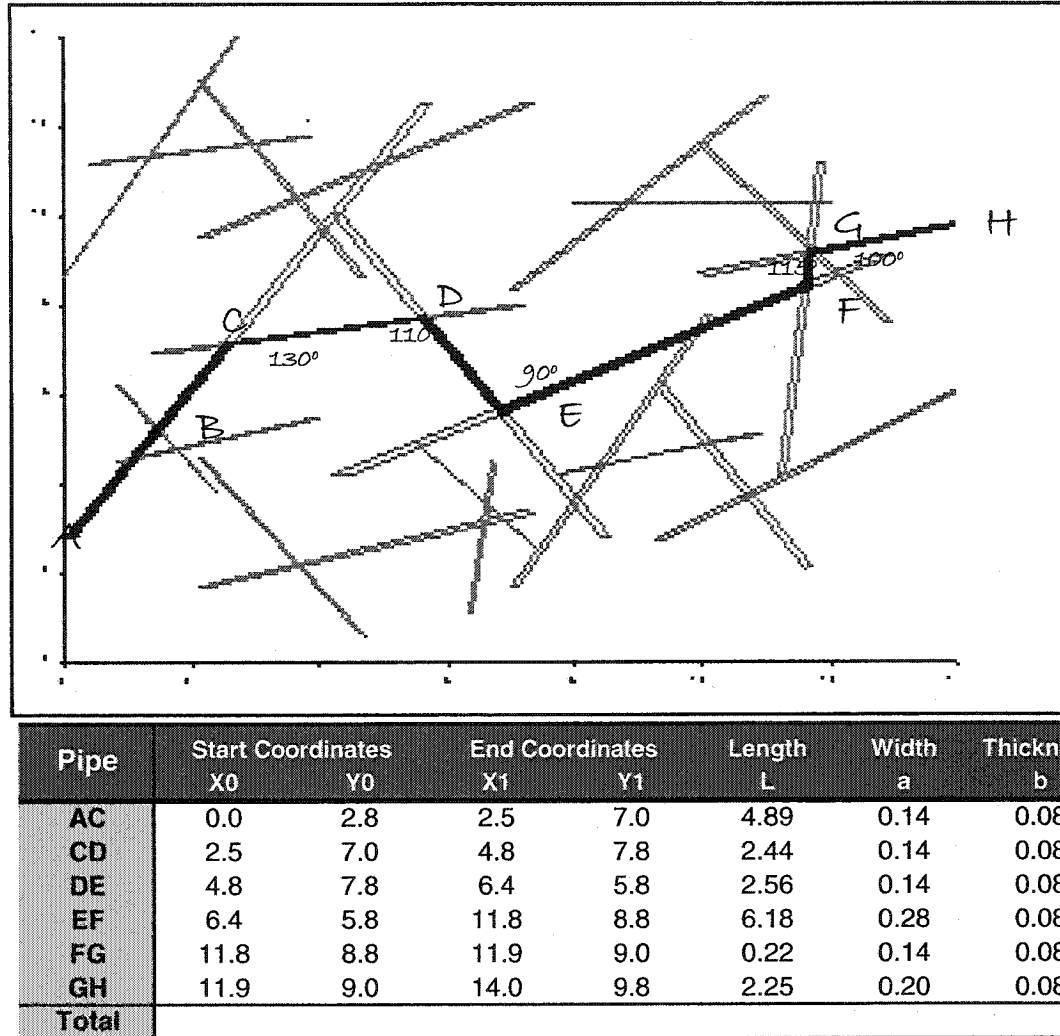

Pipe	Start Coordinates X0	Y0	End Coordinates X1	Y1	Length L	Width a	Thickness b
AC	0.0	2.8	2.5	7.0	4.89	0.14	0.08
CD	2.5	7.0	4.8	7.8	2.44	0.14	0.08
DE	4.8	7.8	6.4	5.8	2.56	0.14	0.08
EF	6.4	5.8	11.8	8.8	6.18	0.28	0.08
FG	11.8	8.8	11.9	9.0	0.22	0.14	0.08
GH	11.9	9.0	14.0	9.8	2.25	0.20	0.08
Total							

Figure C.3 – (a) One flow path (Black). (b) Properties of the fractures of flow path AH

Bernoulli equilibrium between A and H results:

$$\frac{P_A}{\gamma_w} + \frac{u_A^2}{2g} = \frac{P_H}{\gamma_w} + \frac{u_H^2}{2g} + \sum_{All\ Pipes}\left(K_L \frac{u_{Avg}^2}{2g} + \frac{fL}{D} \times \frac{u_{Avg}^2}{2g} \right)$$

where:

232

$P_A =$ Pore Pressure at Entrance (A)

$u_A =$ Velocity at entrance (A): (Discharge Q) /(Pipe AC cross section)

$P_H =$ Pore Pressure at Exit (H)

$u_H =$ Velocity at Exit (H): (Discharge Q) /(Pipe GH cross section)

$K_L =$ Loss coefficients at pipes intersections (=1.1 for $90°$ intersection)

$f =$ Pipe friction coefficient. For Laminar flow: $f = 64/\mathrm{Re} = 64v/(u \cdot D)$

$L =$ Pipe Length from figure C.3.b

$D =$ Pipe Hydraulic Diameter $= (a \cdot b)/(a + b)$, where a is 85% of the

value from figure C.3.b (to account for roughness) and b is 0.08^{in} (plates

spacing).

Total head loss between A and H can be calculated using the above Bernoulli

    equation:

$$\Delta h_{AH} = \frac{P_H}{\gamma_w} - \frac{P_A}{\gamma_w} = \frac{u_H^2}{2g} + \left[\frac{u_{Avg}^2}{2g} \sum_{All\ Pipes} \left(K_L + \frac{fL}{D} \right) \right] - \frac{u_A^2}{2g}$$

Therefore, knowing Δh_{AH} from the lab experiment, discharge Q can be back-

calculated (using Excel "Tools/Goal Seek" feature) . This model was applied

to all 5 experiments and the results follow in the next pages.

It is noteworthy that the results of the pipe network for the 0% HMPC may be

incorrect, since the above model is based on laminar flow assumption, while

we observe Reynolds numbers very close to 2,000 in this case (refer to page 8-

9). This may be responsible for the discrepancy we observe for pure water, as

discussed in chapter 8.